UNIVERSITÉ PARIS 13, SORBONNE PARIS CITÉ
INSTITUT GALILÉE
LABORATOIRE DE PHYSIQUE DES LASERS

Thèse présentée par

Mathieu de Goër de Herve

Pour obtenir le grade de

Docteur de l'Université Paris 13,
Sorbonne Paris Cité

Sujet :

Superfluid dynamics of annular Bose gases

Soutenue le 23 octobre 2018 devant le jury composé de :

M.	Robert SMITH	Rapporteur
M.	Christoph WESTBROOK	Rapporteur
M.	Vanderlei BAGNATO	Examinateur
M.	Gabriel DUTIER	Examinateur
Mme	Patrizia VIGNOLO	Examinatrice
Mme	Hélène PERRIN	Directrice de thèse

Contents

Acknowledgements

Un anneau pour les confiner tous.
Un anneau pour les condenser.
Un anneau pour les piéger tous
Et dans le vide les faire tourner.

Le nombre de personnes qui m'ont accompagné et soutenu pendant ma thèse, ou qui ont contribué d'une façon ou d'une autre à ce qu'elle se fasse, est fort conséquent, et je vais ici essayer de remercier ces personnes de façon aussi exhaustive que possible.

Je commencerai bien sûr par Hélène Perrin pour générosité, sa patience et sa grande disponibilité en dépit de la quantité de travail effrayante qu'elle abat, pour m'avoir supporté et avoir réussi à (presque) me cadrer[1] pendant ces trois années malgré ma tendance à partir dans tous les sens, ainsi que pour le détail et l'exigence de ses relectures y compris au coeur des vacances d'été.

Then, thank you very much to Robert Smith and Christoph Westbrook for having accepted to review my thesis, which happened to be thicker that initially expected, and to Vanderlei Bagnato, Gabriel Dutier and Patrizia Vignolo for being part of my committee. I am grateful for the interest you showed to my work.

Une thèse c'est long, et pas toujours très drôle au quotidien lors des longues journées passées seul en manip. Suivra donc dans ces remerciements l'équipe dans laquelle j'ai travaillé, qui a fortement contribué à rendre ce quotidien plus agréable par sa gentillesse. Merci à Aurélien Perrin et Laurent Longchambon pour leur immense bienveillance qui m'a aidé à prendre plus confiance dans mon travail et pour les discussions passées à refaire le monde, à Romain Dubessy pour son humour et l'idée du vortex géant, à Thomas Badr pour sa tranquilité bienveillante. Merci à Camilla qui m'a précédé sur la manip pour nos longues discussions, à Dany et Joe que j'ai vus travailler sur la manip Sodium, la "petite soeur" de Rubidium. Thank you Avinash for your kindness and your impressive quietness. Merci enfin et bon courage à Yanliang Guo, qui prend désormais la relève sur l'expérience.

Un grand merci également à l'équipe administrative du LPL, et en particulier à Maryse Medina, pour sa disponibilité, son efficacité et sa gentillesse, ainsi qu'aux ateliers du laboratoire pour leur aide (merci en particulier à Fabrice Wiotte et Haniffe Mouhamad pour avoir

1. J'en profite d'ailleurs pour lui dédier cette note de bas de page (elle saura pourquoi).

fabriqué notre formidable nouveau DDS!). Et merci à tout le laboratoire pour la grande gentillesse de ses membres, l'ambiance qui y règne et les nombreuses et intéressantes discussions que j'ai pu avoir. Merci à Martin pour les échanges musicaux et pour m'avoir accompagné au Triton, à Franck pour les soirées passées à taper ensemble ; à Kaci[2], Christelle et à tous les autres doctorants et post-doctorants que j'ai pu côtoyer.

Plus généralement, merci à toute la communauté des atomes froids. J'ai eu la chance de rencontrer durant ces trois années de nombreuses personnes à la fois passionnantes et d'une grande gentillesse[3], et les occasions de partir en conférence ont toujours été extrêment agréables. Merci en particulier à Raphaël[4], Manel, Jean-Loup, Éric, Elliott, Firat, Hugo, Robin, et à tous les collègues thésards que j'ai croisés et recroisés à ces occasions.

Merci à Randall Munroe, Gilles Roussel, Carlos Eiene et Jorge Cham pour m'avoir accompagné pendant les longues heures passées à bricoler et faire tourner mon expérience.

Et merci à Jean-Claude Raimbault et Antoine Moreau pour m'avoir transmis leur amour de la physique, à Hélène Coudert pour m'avoir accompagné tout au long de mon aventure dans le monde de la physique, à Jérôme Beugnon et à Jacob Sherson pour m'avoir fait découvrir le monde fascinant des atomes froids.

J'ai également eu la chance d'être fort bien entouré durant les moments passés hors du laboratoire. Je remercie immensément la Rand'home pour ces quatre années passées à habiter ensemble, et les nombreux repas que nous avons pris en commun. Merci à Jonas pour le carrot-cake, les aiguillettes de kiwi et le temps passé à s'occuper du jardin ensemble, à Jeanne pour sa gentillesse, son enthousiasme débordant et sa cuisine, à Riwan pour les nombreux jeux qu'il m'a fait découvrir, les séances de grimpe et sa contribution à ma notion de ponctualité, à Mireille pour m'avoir accompagné jusqu'au début de cette thèse, à Hachino pour son humour formidable, à Clémence qui a rejoint la maison tardivement mais dont la compagnie fut toujours des plus agréables et pour sa bonne humeur perpétuelle, à Élise pour les discussions dans le hall d'entrée de la maison, à Léa et Julien. C'est promis, je ne devrais normalement plus rentrer systématiquement après 20h30.

Merci à Trolin, 20-100, Boîte, Marion, Ara, Zelda et à tout le département A♡ pour les folies qu'on a pu faire ensemble, les gros dej' et la statue de deux mètres de haut qui a occupé mon plafond pendant presque toute ma thèse. Merci à Pauline et Théodore, Vincent, Chicco, Hypérion, Flavien et Claire pour les dimanches passés à jouer. Merci également à tous ceux qui ont accompagné ma passion pour la musique qui a occupé une bonne partie de mon temps hors thèse. Merci à la Bête Aveugle, Marc, Nico, Bastien pour avoir fait du boucan avec moi ; merci à Daniel, Bruno, Andrew et Jean pour m'avoir appris et aidé à mettre ce boucan en forme, merci à Tom de m'avoir introduit au monde des jams, et merci à mes voisins et à Jonas pour avoir toléré le temps conséquent que j'ai passé à faire du bruit. Et un immense merci à l'équipe du Triton pour tous les concerts que j'y ai vécu et leur travail formidable.

Finalement, merci à Hélène pour les longues randonnées suédoises, parfaites pour faire une pause entre deux années d'expériences. Merci à Matthieu pour les discussions musicales. Et merci à toute ma famille pour son soutien, et pour le formidable niveau de non-sens et de délire qui m'a accueilli à chacun de mes retours.

2. Bon courage pour la fin!
3. J'ai l'impression de répéter ce mot en boucle depuis le début de ces remerciements. J'imagine que c'est bon signe et laisserai passer pour cette fois mon aversion à la trop grande répétition des mots dans un même texte...
4. Que je remercie aussi pour m'avoir introduit *dans* les commandes de sa manip, selon ses dires.

General Introduction

In 1937, when cooling down liquid helium, Kapitza [1], Allen and Misener [2] observed that its viscosity suddenly dropped to almost zero (later proven to be exactly zero), which suggested a new state of matter described a "superfluid". London, one year later, established the link with the "Bose-Einstein condensation" phenomenon proposed by Einstein in 1924 [3–5], which was up to there rather considered as a pathologic limit of the Bose statistics. Quantum mechanics predicts that particles are also waves, which extend over a typical size $\lambda_{\mathrm{dB}} = h/\sqrt{2\pi M k_{\mathrm{B}} T}$, where M is the mass of the particles and T the temperature. Bose-Einstein condensation occurs when at low enough temperature the spatial extent of the particles grows up to reaching the interparticle distance: what was once an ensemble of individual particles then begins to behave as a giant matter wave whose flow properties are again extremely different. In this way, superfluidity provided for the first time a manifestation of quantum effects at a macroscopic scale – and even reached later astrophysical scales [6, 7].

Although initially described as "the ability of a fluid to flow without friction" superfluidity is somehow defined by the ensemble of its properties [8]. Among these properties, one can cite the existence of a critical speed above which the "frictionless flow" is not true anymore [9], or the possibility for the current to flow virtually indefinitely when the flow velocity lies below the critical speed [10, 11]. Possibly even more astonishing are the rotation properties of these systems. In a superfluid, the particles behave like a giant wave, characterized by an amplitude and a phase whose gradient gives the fluid velocity. This implies that a superfluid is irrotational, and setting it into rotation requires quantized vortices to enter the system, introducing singularities in the fluid where the density vanishes in order to allow it to rotate [12–15].

Many remarkable experiments have been performed with superfluid helium. The advent of gaseous Bose-Einstein condensates provided later a new system allowing to study superfluidity in the dilute regime. These systems are to superfluid helium what gases are to liquids: while in superfluid helium the atomic density is large and the interactions strong, in dilute superfluids the density is low and the interactions much weaker. This lower density allows to describe the system very accurately through simple mean-field theories. In addition, these systems are usually well isolated and come with a extremely broad palette of manipulation tools and possibilities to shape the potential landscape of the systems. In this way, these "quantum gases" open a path to a better understanding of phenomena in a variety of domains which extend, in fact, way beyond the sole superfluidity.

However, as the atomic density is much smaller in dilute gases than in liquids, the tem-

perature required in order for the atoms to "overlap" is also considerably smaller: while the critical temperature to achieve superfluidity in helium is around 2 K, the temperature necessary to reach quantum degeneracy in cold atom clouds ranges typically between 100 nK and 1 µK. This was made possible by the development of laser cooling techniques. Starting from the eighties, the techniques allowing to manipulate matter using light beams and magnetic field displayed an amazingly fast development, from laser cooling of ions [16, 17] and neutral atoms [18] to atom traps [19–21], finally enabling evaporative cooling of the atoms down to the obtention of a Bose-Einstein Condensate (BEC), 70 years after its prediction [22, 23]. These developments led to two Nobel prizes in 1997 [24–26] and 2001 [27, 28].

Since the experimental achievement of the first dilute BECs, the field of ultracold atoms completely exploded, the control onto the systems getting finer and finer, allowing for example to load ultracold atoms into "eggbox-like" potentials formed by optical lattices [29] and then image and manipulate them at the single-atom level [30–32]; to achieve new exotic quantum sytems like quantum droplets [33–35], synthetic magnetic fields [36–38] or supersolids [39, 40]; to perform measurements with an unprecedented precision, allowing to test fundamental concepts of physics [41–43]; or to apply the concepts of quantum optics to atoms instead of photons [44–46]. The study of superfluidity in such systems also displayed extremely fast progress, and for example the existence of a critical velocity [47] and collective modes [48–50] were demonstrated only a few years after the first dilute BECs. On the side of rotating superfluids, the observation of the first vortices [51, 52], of large vortex lattices [53] and of the existence of a Lowest Landau Level [54] – demonstrating in this way a remarkable analogy with the Quantum Hall Effect [55] – were achieved one after the other in less than five years; phase-engineering allowed to observe and study vortices carrying multiple charge [56], and ring-shaped traps to study superfluid flow within wave guides [57–59].

Among the tools that come with quantum gases, there is also the possibility to generate very strong confinements and access in this way regimes of lower dimensionality [60]. In these regimes, the thermal and quantum fluctuations play an important role, encouraging the presence of phase disorder in the systems. In two dimensions, for example, this leads to a new phase transition between a superfluid state and a normal phase called the Berezinskii-Kosterlitz-Thouless (BKT) transition [61, 62] whose interplay with possible condensation of the gas is highly subtle [63, 64]; in 1D there is a wide variety of possible phases depending on the number of atoms and their relative interations [65], among which the most surprising is probably the Tonks regime, in which bosons behave like fermions [66]. Exploring the superfluid properties in these regimes presents therefore a significant interest [67–69].

While vortices provide a way to allow rotation in superfluids by creating regions where the fluid density cancels, it is not the only method. A natural geometry for studying superfluid flow is the ring geometry: persistent currents can be stabilized along the waveguide formed by the potential. Such systems allowed for example to study the quantization of such a flow [58] and its hysteretic behavior [59], or the appearance of a flow after a sudden quench below the critical temperature due to the "Kibble-Zurek" effect [70, 71]. It also suggests the possibility to achieve an atomic analogue to the SQUIDs[5] [72, 73], which raises a significant interest.

Another strategy allowing to have a hole in the gas around which the superfluid will rotate relies on the centrifugal force. A gas rotating faster than the frequency of its trap will be expelled from the center of the trap; the addition of nonharmonic confinement to prevent the atoms from escaping then gives rise to a "dynamical" ring potential whose shape is tailored

5. Superconducting QUantum Interference Devices – it is a magnetometer made of a ring-shaped supraconductor with two parallel Josephson junctions.

by the rotation itself. Such a geometry, when reaching large rotation rates, should enable to generate a so-called giant vortex configuration, in which all the atoms are flowing along a 1D ring, all the vortices of the cloud having migrated within the central hole [74–76]. A first attempt to reach this regime, more than 10 years ago, was unsuccessful [77]; despite the absence of recent experimental work on this topic it continues to attract theoretical interest [78–80].

The work presented in this document aims at studying the rotational properties of superfluidity in the two aformentioned cases of annular geometry, as well as their connection to the lower dimensional regimes. It is divided into three parts: after a common general part, the second part deals with the realization of a ring-shaped trap, suitable for studying persistent currents and superfluid flow, with a technique that could possibly allow to enter the 2D or even 1D regimes. The third part deals with the regime of fast-rotating superfluids: by rotating a gas fast enough in a non-harmonic trap, we are able to generate an effective Mexican hat potential and generate a "dynamical" ring-shaped gas, which incidentally happens to be quasi-2D. The overall structure of this thesis will be the following:

- The **first part** aims at presenting the tools needed to properly understand the details associated to the production, manipulation and observation of our systems. Chapter 1 will describe the general properties and behavior of trapped quantum gases. The second chapter will then detail from a theoretical point of view the central technique of our experiments: the realization of RF-dressed adiabatic potentials. Chapter 3 will finally present the general experimental details of our setup, from the production of the BEC to the imaging procedures.

- The **second part** is dedicated to the work realized on the topic of superfluid flow in ring-shaped gases. The fourth chapter will present the theoretical details about superfluid flow in annular traps and about the way we realize such a trap. Chapter 5 will then describe the experimental obtention of a BEC in the ring trap, and chapter 6 will be dedicated to the preparation and detection of a superfluid flow in this annular BEC.

- Finally, the **third part** of my thesis will present the work on the topic of fast-rotating superfluids and the obtention of an annular gas whose shape is due to its own rotation. The 7^{th} chapter will detail the theory that lies behind rotating superfluid and the interest towards fast rotation. Chapter 8 will then present the experimental achievements on this topic, from the obtention of a "dynamical ring" to the possible observation of thermal melting of vortex lattices.

The first part contains all the details that are common to the following two parts. Parts two and three have both their own detailed introduction as well as a chapter dedicated to the theoretical details useful to understand them, and can therefore be read independently from each other.

Part I

Preliminaries

Chapter 1

Bose-Einstein condensation, superfluidity and rotation

This chapter aims at presenting the basic concepts and theoretical tools needed to describe Bose-Einstein condensates (BECs). Starting from the principle of Bose condensation, I will first describe the physics of a BEC at rest. I will then extend it to its out-of-equilibrium behavior and show how it leads to the concept of superfluidity as well as the consequences on the rotation of the gas. This will lead me to introduce the two central ideas on which parts 2 and 3 of this document are based. Finally, I will conclude this chapter by describing the case of two-dimensional gases and the Berezinskii-Kosterlitz-Thouless transition.

1.1 Bose-Einstein Condensation

1.1.1 Bose-Einstein condensation in an harmonic trap

Principle of BEC

Let us begin by considering a gas of N bosons, supposed for now non-interacting, at thermal equilibrium at temperature T. Described in grand-canonical ensemble and denoting μ the chemical potential of the system, the average number of bosonic particles in a given state j with energy E_j reads:

$$N_j = \frac{1}{e^{(E_j-\mu)/k_\mathrm{B}T} - 1}. \tag{1.1}$$

N_j must obviously be positive, which sets the condition $\mu < \min(E_j)$. Denoting E_0 the energy of the ground state (supposed nondegenerate) and defining the origin of energies to have $E_0 = 0$, this condition becomes:

$$\mu < E_0 = 0. \tag{1.2}$$

In addition to that, counting the total number of atoms in excited states N_exc leads to the expression:

$$N_\mathrm{exc} = \sum_{j>0} \frac{Z}{e^{E_j/k_\mathrm{B}T} - Z}, \tag{1.3}$$

where $Z = \exp(\mu/k_{\mathrm{B}}T)$ is called the fugacity. The condition (1.2) leads to $Z < 1$, and thus sets an upper bound on the population of the excited states:

$$N_{\mathrm{exc}} < N_{\mathrm{exc}}^{(max)}(T) = \sum_{j>0} \frac{1}{e^{E_j/k_{\mathrm{B}}T} - 1}. \tag{1.4}$$

In other words, if $N > N_{\mathrm{exc}}^{(max)}(T)$, all the additional particles *must* be in the ground state, which can eventually attain macroscopic population. This corresponds to the phenomenon called *Bose-Einstein condensation* (BEC).

Depending on the geometry and dimensionality, the sum $N_{\mathrm{exc}}^{(max)}(T)$ may or note converge, indicating whether this quantum[1] degeneracy of the ground state can be achieved.

Bose-Einstein condensation in harmonic traps

A significant part of the work described here was achieved in harmonic traps, and I will therefore specifically describe this case.

Let us consider that the atoms are now confined in an harmonic trap with frequencies ω_x, ω_y, ω_z. The energies of the single particle states then write:

$$E_{n_x,n_y,n_z} = (n_x + \tfrac{1}{2})\hbar\omega_x + (n_y + \tfrac{1}{2})\hbar\omega_y + (n_z + \tfrac{1}{2})\hbar\omega_z. \tag{1.5}$$

The sum (1.4) then becomes a triple sum over (n_x, n_y, n_z). Turning this sum into an integral[2] using density of states allows one to calculate the maximal population of the excited states [81]:

$$N_{\mathrm{exc}}^{(max)}(T) = \zeta(3)\left(\frac{k_{\mathrm{B}}T}{\hbar\omega_{\mathrm{ho}}}\right)^3, \tag{1.6}$$

where $\omega_{\mathrm{ho}} = (\omega_x\omega_y\omega_z)^{1/3}$ is the geometric average of the trapping frequencies and $\zeta(n)$ is the Riemann ζ function.

When dealing with ultracold atoms experiments, we usually prefer to think in terms of transition temperature. Such a temperature can be estimated by supposing that $N = N_{\mathrm{exc}}^{(max)}(T_c)$ at the transition (i.e. the population in the ground state is still negligible, and the total number of particles just reaches the maximum allowed in the excited states). Equation (1.6) can then be rewritten:

$$k_{\mathrm{B}}T_c = \hbar\omega_{\mathrm{ho}}\left(\frac{N}{\zeta(3)}\right)^{1/3} = 0.94\hbar\omega_{\mathrm{ho}}N^{1/3}. \tag{1.7}$$

Below this temperature, quantum degeneracy is achieved, and the fraction of atoms in the ground state can be deduced from:

$$\frac{N_0}{N} = 1 - \left(\frac{T}{T_c}\right)^3. \tag{1.8}$$

1. As opposition to thermal degeneracy, which would correspond to the temperature being so low that excited states cannot be thermally populated.
2. This is relevant if the energies in the system are much larger than the level spacings, especially $k_{\mathrm{B}}T \gg \hbar\omega_{ho}$, and if the number of atoms in the system is large.

Condensate wavefunction and correlation function

Let us now try to describe the atomic state in such a system; we will write $\hat{\Psi}(\mathbf{r})$ the field operator creating a particle at position $\mathbf{r}$. One can decompose the state of the system in the basis of the single-particle states φ_i, with creation operators $\hat{a}_i$:

$$\hat{\Psi}(\mathbf{r}) = \sum_i \varphi_i(\mathbf{r})\hat{a}_i. \tag{1.9}$$

The number of particles in the single-particle ground state φ_0 can then be written as $N_0 = \langle \hat{a}_0^\dagger \hat{a}_0 \rangle$. If the system is condensed, the population of the ground state is macroscopic: supposing that the total number of particles in the system is large, one has therefore $N_0 \gg 1$. It is then relevant to treat the field classically and ignore the noncommutativity between $\hat{a}_0$ and $\hat{a}_0^\dagger$, writing $\hat{a}_0 \approx \sqrt{N_0}$ [82]. The field operator can then be rewritten as:

$$\hat{\Psi}(\mathbf{r}) = \sqrt{N_0}\varphi_0 + \sum_{i\neq 0} \varphi_i(\mathbf{r})\hat{a}_i, \tag{1.10}$$

and for $T \ll T_c$, as most atoms are in the ground state the atomic state is approximately $\sqrt{N_0}\varphi_0(\mathbf{r})$ (and φ_0 then depends, of course, on the considered system). The field operator is then replaced by a c-number.

Writing the field operator is also useful to provide a more general definition of Bose-Einstein condensation. The first order correlation function can be written as the one-body density matrix:

$$g_1(\mathbf{r}, \mathbf{r}') = \langle \hat{\Psi}^\dagger(\mathbf{r})\hat{\Psi}(\mathbf{r})' \rangle. \tag{1.11}$$

In the case of a uniform gas, Penrose and Onsager showed that the population of the ground state is given by $\lim_{|\mathbf{r}-\mathbf{r}'|\to\infty} g_1(\mathbf{r}, \mathbf{r}') = N_0/V$, with V the volume of the gas [83]. The Bose-Einstein condensation is therefore equivalent to the the existence of a non-zero limit of the first order correlation at large distances. This criterion provides, in fact, a more general definition of the condensation that can be generalized to any system, from the limit $|\mathbf{r} - \mathbf{r}'| \to \infty$:

- If $g_1(\mathbf{r}, \mathbf{r}')$ tends towards a non-zero limit, the system is condensed. One can also speak of "off-diagonal long-range order", as it involves the non-diagonal terms of the density matrix.
- If $g_1(\mathbf{r}, \mathbf{r}')$ goes down to zero, the gas is non-condensed.

In fact, intermediate cases can also happen: especially, for finite-size systems, the correlation function can tend towards zero on a distance that is larger than the size of the system, leading to the so-called quasicondensation where the system is coherent while strictly speaking condensation does not occur (as can happen in the 2D case, see section 1.3). More generally, in the non-condensed case, the distance over which the correlation function goes to zero can be used to define a "correlation length" which describes the size over which the system is coherent, which can sometimes be non-negligible compared to the size of the system.

1.1.2 Interacting Bose-Einstein Condensate

Let us come back to our harmonic trap. In the previous section, we deduced that in the absence of interactions for $T \ll T_c$ the atomic state could be described by the c-number $\sqrt{N}\varphi_0(\mathbf{r})$, $\varphi_0(\mathbf{r})$ being for harmonic traps the wavefunction of the ground state of the harmonic oscillator.

However, this picture happens to be completely wrong in the vast majority of experimentally obtained cases (fig. 1.1). This is due to the presence of interactions between atoms, which significantly modifies the condensate's behavior even in the weakly interacting case. In the case of repulsive interactions (which will be the case during this whole document), it is indeed favorable for the atoms to populate different (single-particle) states in order to reduce the density: the real ground state in which condensation will occur is therefore modified by the interactions between atoms. We can however suppose that the approach described in section 1.1.1 still holds, and describe the field classically: $\hat{\Psi}(\mathbf{r}) = \psi(\mathbf{r})$ (with $\int |\psi|^2 = N$). This approximation supposes that the populated states contain many atoms each, so that we can neglect the noncommutativity of the single-particle annihilation and creation operators. The susbsequent question is then: what is the equation that governs $\psi(\mathbf{r})$?

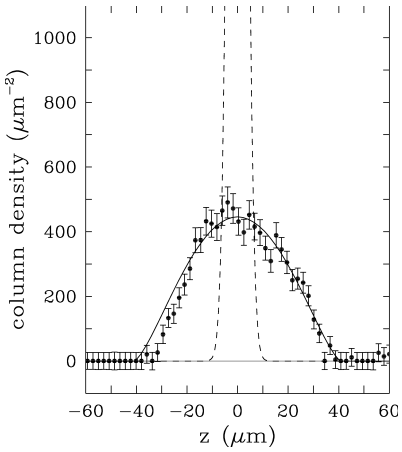

Figure 1.1 — Density distribution of a sodium condensate in a harmonic trap: the non-interacting description (dashed line), corresponding to the gaussian distribution of the harmonic oscillator's ground state, differs very significantly from experimental results. The Thomas-Fermi profile (solid line) shows a good agreement with the data. The presence of repulsive interactions significantly broadens the cloud, reducing the local density. Figure from [81], data from [84].

Let us describe the interactions first. For ultracold temperatures and dilute gases, interactions are essentially low-energy binary collisions ("s-wave" collisions), for which the exact shape of interaction potential does not matter: all the interaction can be summarized by a single parameter, the scattering length a [82]. The effective interaction potential between two particles can therefore be described by a Dirac potential with only one amplitude parameter [81]:

$$V_{\text{int}}(\mathbf{r} - \mathbf{r}') = g_{\text{int}}\delta(\mathbf{r} - \mathbf{r}'), \tag{1.12}$$

where g_{int} is the coupling constant, which reads:

$$g_{\text{int}} = \frac{4\pi\hbar^2 a}{M}, \tag{1.13}$$

M being the atomic mass.

For such interactions, applying the Heisenberg equation to $\hat{\Psi}(\mathbf{r})$ and then replacing, again, $\hat{\Psi}(\mathbf{r})$ by $\psi(\mathbf{r})$ leads to [81]:

$$\left(-\frac{\hbar^2\nabla^2}{2M} + V_{\text{ext}}(\mathbf{r}) + g_{\text{int}}|\psi(\mathbf{r},t)|^2\right)\psi(\mathbf{r},t) = i\hbar\frac{\partial\psi}{\partial t}(\mathbf{r},t). \tag{1.14}$$

This equation, called "Gross-Pitaevskii equation" (GP equation), describes well the behavior of most trapped atomic gases. It takes the form of a non-linear Schrödinger equation ; the first term corresponds to kinetic energy of the condensate, the second one to the trapping energy, and the third one to the interaction energy. Describing the ground state wavefunction classically corresponds, in fact, to a mean-field approximation: the GP equation describes the behavior of a single atom in the field created by the $N-1 \approx N$ other atoms.

By separating the time and spatial dependence of the condensate wavefunction like one would do to write the time-independent Schrödinger equation, $\psi(\mathbf{r},t) = \psi(\mathbf{r})\exp(-i\mu t/\hbar)$, we can write the stationnary Gross-Pitaevskii equation, describing the ground state of the system at rest[3]:

$$\left(-\frac{\hbar^2\nabla^2}{2M} + V_{\text{ext}}(\mathbf{r}) + g_{\text{int}}|\psi(\mathbf{r})|^2\right)\psi(\mathbf{r}) = \mu\psi(\mathbf{r}). \tag{1.15}$$

For a large number of particles with repulsive interactions (i.e. $g_{\text{int}} > 0$, or $a > 0$), the kinetic term usually becomes very low and can be neglected – this is called the Thomas-Fermi approximation. For a harmonic trap, the density variations happen on a typical size $d_{\text{ho}} = \sqrt{\hbar/M\omega_{\text{ho}}}$, called the harmonic oscillator length, which also gives the typical size of the cloud: comparing the kinetic term and the interaction term in the previous equation, we find that this approximation will be relevant for $Na \gg d_{\text{ho}}$. The previous equation can then be rewritten as:

$$n(\mathbf{r}) = |\psi(\mathbf{r})|^2 = \frac{\mu - V_{\text{ext}}(\mathbf{r})}{g_{\text{int}}}. \tag{1.16}$$

We see that the density distribution "mimics" the potential landscape, filling the trap up to the chemical potential $\mu = g_{\text{int}}n_{\max}$ (see figure 1.2). For a harmonic trap, it leads to the following density distribution:

$$n(\mathbf{r}) = n(0)\left(1 - \frac{x^2}{R_x^2} - \frac{y^2}{R_y^2} - \frac{z^2}{R_z^2}\right), \tag{1.17}$$

where the right hand side is positive, and 0 everywhere else. The R_j, called *Thomas-Fermi radii*, are defined for the axes of the harmonic trap as: $R_j^2 = 2\mu/M\omega_j^2$, and give the total extent of the cloud along the directions of the trap. This profile is the one describing the density distribution of figure 1.1.

In this regime, the chemical potential of a 3D cloud trapped in a harmonic potential thus writes [81]:

$$\mu_{3D} = \frac{1}{2}M\omega_{\text{ho}}^2 R_{\text{ho}}^2 = \frac{\hbar\omega_{\text{ho}}}{2}\left(\frac{15Na}{a_{\text{ho}}}\right)^{2/5}. \tag{1.18}$$

Finally, one may note that equation (1.17) leads to a discontinuity of the derivative of the density where density cancels, and thus to an infinitely high kinetic energy on the edges of the cloud. In fact, the Thomas-Fermi approximation does not hold in regions where the density

3. It is also possible to derive it directly from a variational method [82].

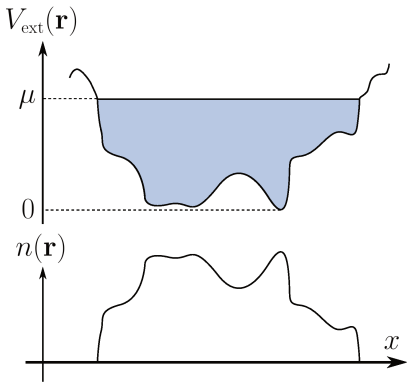

Figure 1.2 — In the Thomas-Fermi approximation, the density distribution mirrors the potential landscape. Top: potential landscape, bottom: density distribution.

is very low. An estimation of the size over which the kinetic term is non negligible, denoted ξ, can be done by comparing the kinetic energy for an evolution on a distance ξ with μ:

$$\xi = \sqrt{\frac{\hbar^2}{2M\mu}} = \frac{1}{\sqrt{8\pi a n}}. \tag{1.19}$$

ξ, called the *healing length*, describes the typical minimal size on which the atomic density can vary from n to 0. Similarly, on the edges of the condensate the Thomas-Fermi profile will in fact be smoothened by the kinetic term.

1.2 Out-of-equilibrium behavior of BECs

The previous section described the behavior of a BEC at rest, however, like most phase transitions the Bose condensation leads to very significant changes in the dynamical behavior as compared to the case of a thermal gas. We therefore also need theoretical tools to describe the out-of equilibrium behavior of such a system. In particular, this will lead us to show that a Bose-condensed gas, in the presence of interactions, is superfluid.

1.2.1 The Bogoliubov approach

Bogoliubov spectrum

An interesting approach to begin with corresponds to supposing that most of the condensate is at rest, and look for small fluctuations around this equilibrium position. With this in mind, a relevant description of the wavefunction can be written as:

$$\psi(\mathbf{r}, t) = [\psi_0(\mathbf{r}) + \delta\psi(\mathbf{r}, t)]e^{-i\mu t/\hbar}. \tag{1.20}$$

Here, ψ_0 is the wavefunction of the BEC at rest – i.e. the solution of the stationary GP equation as described in section 1.1.2, and the corresponding density will be noted $n(\mathbf{r})$. The quantity $\delta\psi(\mathbf{r}, t)$ is the deviation from the condensate at rest, and is supposed to be much smaller than $\psi(\mathbf{r})$. Under these conditions, the GP equation can be linearized by removing

all high order terms, leading to [85]:

$$i\hbar\frac{\partial}{\partial t}\delta\psi = -\frac{\hbar^2\nabla^2}{2M}\delta\psi + g_{\text{int}}n(\mathbf{r})[\delta\psi^* + 2\delta\psi] - \mu\delta\psi. \tag{1.21}$$

Solving this equation leads to the *excitation spectrum* of the sytem, and the results obviously depends on the geometry of the system (due to the $n(\mathbf{r})$ term). For a uniform system with density n, it leads to the so-called Bogoliubov spectrum:

$$E_k = \sqrt{\frac{\hbar^2k^2}{2M}\left(\frac{\hbar^2k^2}{2M} + 2g_{\text{int}}n\right)} = \frac{\hbar^2k^2}{2M}\sqrt{1 + \frac{2}{(k\xi)^2}}, \tag{1.22}$$

where E_k is the energy of an elementary excitation of the system, corresponding to a plane wave with wavevector k; the spectrum is plotted on figure 1.3. For low-energy excitations, it is proportional to k, corresponding to a phononic excitation: $E_k = \hbar ck$, where $c = \sqrt{g_{\text{int}}n/M}$ is the speed of sound in the gas. For high-energy excitations, it is quadratic, describing free-particle excitations shifted by the condensate chemical potential: $E_k = g_{\text{int}}n + \hbar^2k^2/2M$. These two domains correspond to excitations with wavelength larger or smaller than the healing length of the condensate.

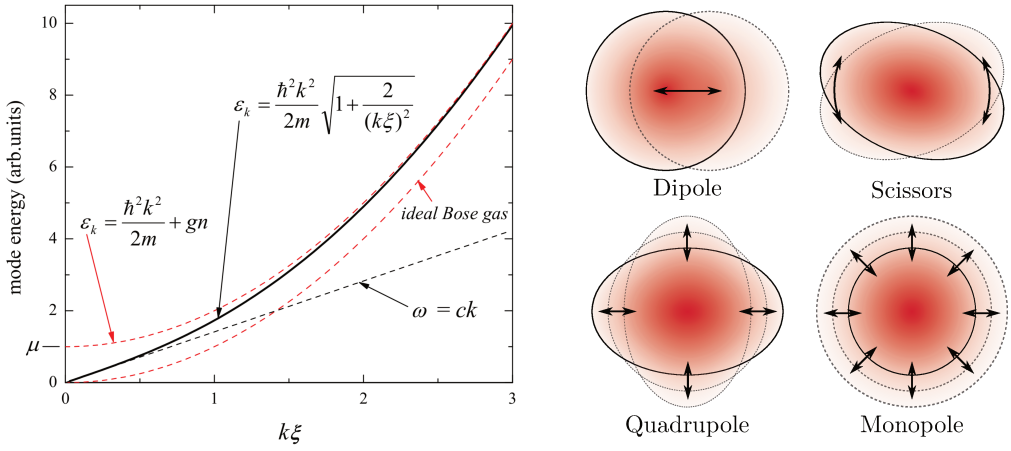

Figure 1.3 — Left: Bogoliubov excitation spectrum (black solid line), plotted with the two phonon-like (black dashed line) and particle-like (red dashed line) excitation limits. Figure taken from [85]. Right: illustration of the first collective modes in highly oblate (or quasi-2D) trapped gases – in which case the oscillation happens in-plane.

For a non-uniform gas, computing the excitation spectrum can lead to various results depending on the gas geometry. In particular, whereas in the case of uniform gas the low-energy excitations are plane waves, for trapped gases it takes the form of collective excitations called *collective modes* [82]. In the simplest case of a harmonically trapped gas, we can mention for example the dipole mode (center of mass oscillation at the bottom of the trap), the monopole "breathing" mode (corresponding to the oscillation of the cloud radius), the quadrupole mode (oscillation of the cloud radii in phase opposition), or the scissors mode (oscillation of the orientation), which are represented on figure 1.3 in the case of an oblate

gas. All these modes have their own excitation spectrum and eigenfrequencies and can give a significant insight into the physics of trapped gases. A lot of work on the study of these modes has been achieved in our team in the case of 2D gases [86,87]; a more detailed description will be presented in chapter 7.

Critical velocity

Once we know the excitation spectrum of the gas, we can wonder how to create these excitations. Let us consider the case of momentum transfer from an object moving with a velocity v relative to an homogeneous fluid, for example a point-like impurity moving with velocity v within the fluid at rest[4]. Writing the conservation of momentum and energy for creating an excitation of energy E_k and momentum $\hbar k$ leads to the inequality [82]:

$$v > \frac{E_k}{\hbar k}. \tag{1.23}$$

In other words, for a given excitation there can be threshold for velocity under which creating this excitation is not allowed. If *all* excitations have such a threshold, it implies the existence of a velocity threshold below which no excitation can be created *at all* (fig. 1.4). This "critical velocity" then expresses as:

$$v > v_c = \min_k \left(\frac{E_k}{\hbar k} \right). \tag{1.24}$$

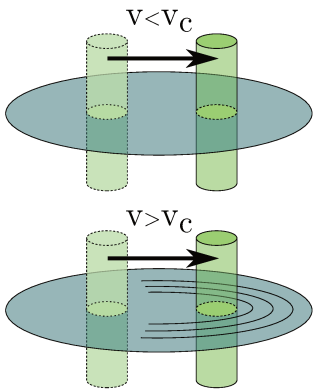

Figure 1.4 – Illustration of the notion of critical velocity. An obstacle moving within the fluid below critical velocity cannot create excitations, and the fluid does not interact with it. Above the critical velocity, creating excitations is possible, allowing interactions.

The existence of a non-zero critical velocity means that a defect moving slowly enough will not interact with the fluid. In particular, it means that the viscosity for the motion of this defect is stricty zero. This is the definition of *superfluidity* as expressed by Landau [88].

For the uniform gas, this velocity is easily deduced from (1.22):

$$v_c = \sqrt{g_{\text{int}} n / M}, \tag{1.25}$$

4. The case initially considered by Landau was a superfluid flowing with velocity v along a capillary, and the momentum transfer from the container to the fluid.

which is the speed of sound in the gas c. One may note that for non-interacting gases ($g = 0$), the critical velocity vanishes: repulsive interactions are necessary to achieve superfluidity.

This approach is however limited as it considers only the excitations that are described by the Bogoliubov approach; especially, the possibility to nucleate vortices in the fluid can significantly lower the real critical velocity [12]. In the non-uniform case, computing properly all the possible excitations to which an impurity can couple is quite troublesome and there is often no model allowing to compute v_c precisely.

1.2.2 Hydrodynamic formulation

Larger displacements and excitations of the condensate are also described by the time-dependent Gross-Pitaevskii equation (1.14), but it would be useful to have a description of the fluid that corresponds more to what we are used to ; in particular we would like to have an expression for the fluid velocity.

Multiplying equation (1.14) by ψ^* and substracting its complex conjugate, we find:

$$i\hbar\left(\psi^*\frac{\partial}{\partial t}\psi + \psi\frac{\partial}{\partial t}\psi^*\right) = \frac{\hbar^2}{2M}\left(\psi^*\nabla^2\psi - \psi\nabla^2\psi^*\right), \tag{1.26}$$

which also writes:

$$\frac{\partial}{\partial t}|\psi|^2 = \frac{\hbar}{2Mi}\boldsymbol{\nabla}\cdot(\psi^*\boldsymbol{\nabla}\psi - \psi\boldsymbol{\nabla}\psi^*). \tag{1.27}$$

Since $|\psi(\mathbf{r},t)|^2 = n(\mathbf{r},t)$, this equation can thus be written under the form of the continuity equation for a classical compressible fluid:

$$\frac{\partial n}{\partial t} + \boldsymbol{\nabla}\cdot(n\mathbf{v}) = 0, \tag{1.28}$$

where the velocity v of the fluid is defined as:

$$\mathbf{v} = \frac{\hbar}{2Mi|\psi|^2}\left(\psi^*\boldsymbol{\nabla}\psi - \psi\boldsymbol{\nabla}\psi^*\right). \tag{1.29}$$

Writing the wavefunction as amplitude and phase[5]:

$$\psi(\mathbf{r},t) = \sqrt{n(\mathbf{r},t)}\exp(iS(\mathbf{r},t)) \tag{1.30}$$

thus leads to the expression of the local velocity of the superfluid:

$$\mathbf{v}(\mathbf{r},t) = \frac{\hbar}{M}\boldsymbol{\nabla}S(\mathbf{r},t). \tag{1.31}$$

Multiplying equation (1.14) by ψ^*, adding its complex conjugate and injecting (1.30) leads to the equation:

$$\frac{1}{2}M\mathbf{v}^2 - \frac{\hbar^2}{2M\sqrt{n}}\nabla^2(\sqrt{n}) + g_{\text{int}}n + V_{\text{ext}} + M\frac{\partial}{\partial t}\left(\frac{\hbar S}{M}\right) = 0, \tag{1.32}$$

5. A more rigorous writing of the phase is $\varphi(\mathbf{r},t) = \mu t + S(\mathbf{r},t)$, but the phase μt is uniform over the whole cloud and is thus not implied in its superfluid dynamics. However, it can be useful to keep in mind that $S(\mathbf{r},t)$ is the *deviation* from the phase of the stationary state.

or, equivalently, to the *Euler equation* for a quantum fluid [85]:

$$\boldsymbol{\nabla}\left(\frac{1}{2}M\mathbf{v}^2 - \frac{\hbar^2}{2M\sqrt{n}}\nabla^2(\sqrt{n}) + g_{\text{int}}n + V_{\text{ext}}\right) + M\frac{\partial \mathbf{v}}{\partial t} = 0. \tag{1.33}$$

This equation is equivalent to the classical Euler equation, describing the evolution of an inviscid flow (as expected for a superfluid), with the addition of a term involving explicitly $\hbar$, corresponding to a "quantum pressure". The combination of equations (1.28) and (1.33) is in fact equivalent to the Gross-Pitaevskii equation, simply separating it into amplitude and phase. These hydrodynamic equations are the ones that allow, for example, to compute the collective modes in the case of a trapped gas [89].

1.2.3 Rotating superfluids

Equation (1.31) is crucially important, as it directly links the superfluid velocity to the phase. It also shows that the superfluid flow is *irrotational*: $\boldsymbol{\nabla} \times \mathbf{v} = 0$, which leads to important consequences when trying to describe to rotation of a superfluid.

One has to note that an irrotational flow doesn't necessarily imply the absence of rotation of the fluid: it means that *locally*, the fluid doesn't rotate, but the ensemble motion of a condensate can still allow rotation and non-zero angular momentum (an example will be discussed in chapter 7). However, this configuration usually allows the cloud to carry only a small angular momentum: a large angular momentum would require large anisotropies and large ensemble motion, which is usually unstable and decays to form quantized vortices [90,91]. It is these vortices which "hold" the rotation of a superfluid.

Quantized vortices

A very important relation when dealing with rotating superfluids can be obtained by calculating the circulation of the superfluid velocity along a closed loop: since this velocity is given by (1.31), it corresponds to calculating the phase difference between a point and itself. The wavefunction having to be single-valued this difference then has to be an integer multiple of 2π. The circulation then has to be quantized, as noted by Onsager and Feynman [12,92]:

$$\oint_{\mathcal{C}} \mathbf{v}(\mathbf{r},t)\cdot \mathrm{d}\mathbf{l} = \frac{\hbar}{M}\Delta_{\mathcal{C}}S = \ell \times 2\pi\frac{\hbar}{M}, \ell \in \mathbb{Z}. \tag{1.34}$$

However, due to Stokes' theorem and the irrotationality of the superfluid velocity, this circulation is necessarely equal to zero if the velocity can be continuously defined on the surface enclosed by the contour. A non-zero circulation thus requires the atomic density to vanish somewhere on this surface to allow the presence of a phase singularity, that is, a vortex. A quantized vortex can be seen simply as a node in the condensate wave function, around which the phase rotates by a multiple of 2π (see figure 1.5): in this way, the superfluid flow can rotate around it while keeping its irrotational character. Note that the two-dimensional and three-dimensional cases differ here: in 2D, the vortex is a *point* around which the fluid rotates, while in 3D the vortices are *lines*, which allows for example vibrations of vortices or vortex rings.

While in principle any multiple of 2π is possible, a configuration with $|\ell| < 1$ is in practice unstable: a vortex with a phase winding larger than 2π spontaneously breaks into several vortices with 2π phase winding each [56,93], which repel each other.

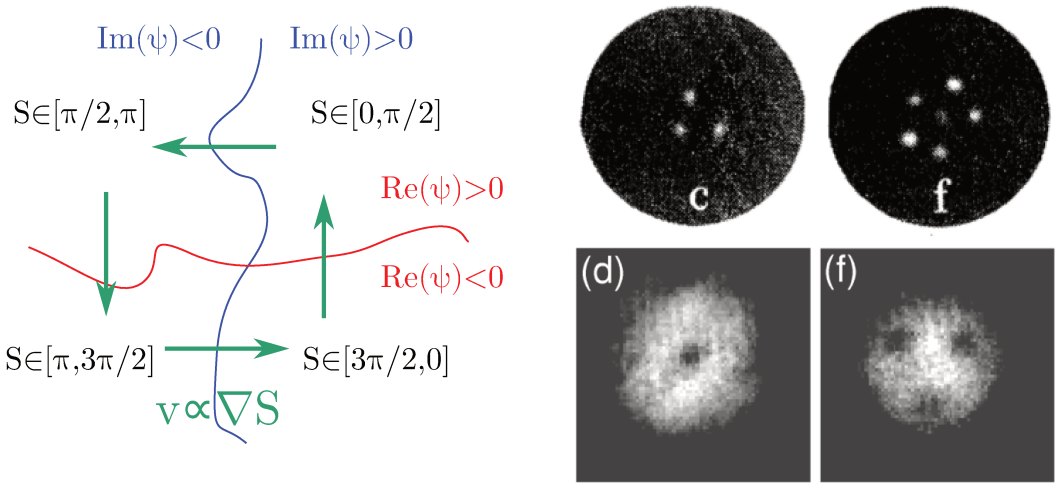

Figure 1.5 — Left: principle of a vortex (in two dimensions). Let us suppose that the atomic density cancels somewhere: both real part and imaginary part of the wavefunction then have to cancel somewhere; I draw as a red line the border between positive and negative real part and as a blue line the border between positive and negative imaginary part. Following equation (1.31), we see that the fluid now rotates around the crossing between both regions, which corresponds to a node in the wavefunction. Right: experimental pictures of vortices, in superfluid helium (top, from [15]) and in a dilute BEC (bottom, from [52]); the fluid rotates around each of these vortices at the same time.

Beyond quantized vortices

Vortices provide a way to indroduce angular momentum in a cloud by locally creating a zero of the density. However, if the density vanishes locally in the cloud for some other reason, circulation around the corresponding region is also allowed. Two ways to produce such configurations will be studied in this thesis, corresponding to parts two and three:

- The trap can have an annular shape: in this case, the fluid at rest already has a hole in its center. In such a configuration, it is possible to create a persistent flow along the ring, and due to relation (1.34) the circulation of the flow along the ring is quantized.

- In the case of a very fast rotation, a centrifugal barrier can appear at the center of the gas, leading to the appearance of a hole around which the fluid rotates. The gas will also adopt a ring shape, but this time the effect will be dynamical, as the hole somehow sustains itself through the rotation it creates.

1.3 2D systems and the BKT transition

I will now conclude this chapter by discussing the case of 2D gases, as it provides one of the motivations for the work presented in part II and describes a significant part of what happens in part III.

1.3.1 The quasi-2D regime in a vertically harmonic trap

First, how do we enter the 2D regime? The first criterion is that the gas should have all dynamics frozen in the vertical direction: the particles all have to be in the same vertical state. This is achieved when both the gas temperature and the chemical potential have to be too low for the first excited vertical state to be populated. For a vertical harmonic confinement, this condition corresponds to $k_{\mathrm{B}}T, \mu < \hbar\omega_z$. Note that this is very different from Bose-Einstein condensation: this time, we have a *thermal* degeneracy of the ground state (but only in the vertical direction).

The second criterion deals with interactions: if the vertical size of the gas is smaller than the scattering length, the collisions have to be treated in 2D; if the gas is harmonically trapped with all atoms in the vertical ground state, this corresponds to $d_z < a$ (d_z being the vertical oscillator length). The gas can then be considered as truly 2D.

While the first criterion can be fulfilled with available experimental techniques, the second one is considerably more difficult to verify (and in our experiments, d_z is typically 50 to 100 times larger than a). If only the first criterion is satisfied, the gas is said *quasi-2D*: the vertical motion of the particles is frozen, but the collisions are still described by 3D physics. In this case, one can show that the interactions between atoms can still be described using a Dirac potential, but with a modified coupling constant:

$$g_{2D} = \frac{g_{\mathrm{int}}}{\sqrt{2\pi} d_z} = \frac{\hbar^2}{M}\tilde{g}, \tag{1.35}$$

where $\tilde{g}$ is a dimensionless coupling constant, expressed as:

$$\tilde{g} = \sqrt{8\pi}\frac{a}{d_z}. \tag{1.36}$$

In the case of a condensed gas (whose validity will be described in the next section), the Gross-Pitaevskii equation will then stay valid (both in its time-dependent and stationnary versions), simply replacing g_{int} by g_{2D} and replacing the 3D wavefunction ψ by its value averaged along z (and replacing the space density n by a surface density ρ). Note that in the experiments described in this document, $\tilde{g}$ is typically of the order of 0.1.

1.3.2 (Quasi) condensation in 2D

Let us now discuss the possibility of condensation in 2D. For a uniform (quasi-)2D gas, the sum (1.4) does not converge, meaning that no condensation can occur. However, Berezinskii [61] and Kosterlitz and Thouless [62] predicted that an interacting 2D gas should undergo a phase transition towards a superfluid state, now called the BKT transition, at a critical phase-space density $\mathcal{D} = \rho\lambda_{\mathrm{dB}}^2$ that was later computed to be equal to [94]:

$$\mathcal{D}_c = \ln(380/\tilde{g}). \tag{1.37}$$

Remarkably, at the transition the superfluid phase-space density $\mathcal{D}_s$ presents a universal jump from 0 to 4, see section 1.3.3. This transition does not allow a long-range order to appear in the gas and the correlation function g_1 still goes down to zero at long distance, but while this decay is exponential for large temperatures, it is only algebraic for $\mathcal{D} > \mathcal{D}_c$, allowing a more extended phase coherence that is sufficient for superfluidity; in the case of finite-size systems this coherence can even extend on the whole system size. Such a gas is called a *quasicondensate*, that is a condensate with a nonuniform, fluctuating phase [95].

The case of harmonically trapped quasi-2D gases is even more subtle. In the non-interacting case, the density of states is modified and real condensation has been demonstrated to occur at a critical atom number [96]:

$$N_{\mathrm{c}}^{0} = \frac{\pi^2}{6}\left(\frac{k_{\mathrm{B}}T}{\hbar\omega_{\perp}}\right)^2, \tag{1.38}$$

where $\omega_{\perp}$ is the radial trapping frequency. This corresponds to the critical temperature

$$k_{\mathrm{B}}T_c = \hbar\omega_{\perp}\frac{\sqrt{6N}}{\pi}. \tag{1.39}$$

However, one can show that in this case, the density at the center of the trap diverges (even though the total number of particles is conserved) [63]: in the presence of repulsive interactions, this is not possible and true condensation does not occur. Instead, a BKT transition occurs again, for a particle number slightly higher than the one required for condensation in the non-interacting case [97]:

$$\frac{N_{\mathrm{c,real}}}{N_{\mathrm{c}}^{0}} \approx 1 + \frac{3\tilde{g}}{\pi^3}\ln^2\left(\frac{\tilde{g}}{16}\right) + \frac{3\tilde{g}}{8\pi^2}\left[15 + \ln\left(\frac{\tilde{g}}{16}\right)\right]. \tag{1.40}$$

This increased critical atom number corresponds, somehow, to the additional atoms one has to put in the trap in order to reach the critical phase-space density in its center, due to repulsive interactions. It has been remarkably verified in the group of Z. Hadzibabic [64] (see figure 1.6). The BKT transition (in the interacting case) and the BEC transition (in the non-interacting case) connect in the limit $\tilde{g} \to 0$.

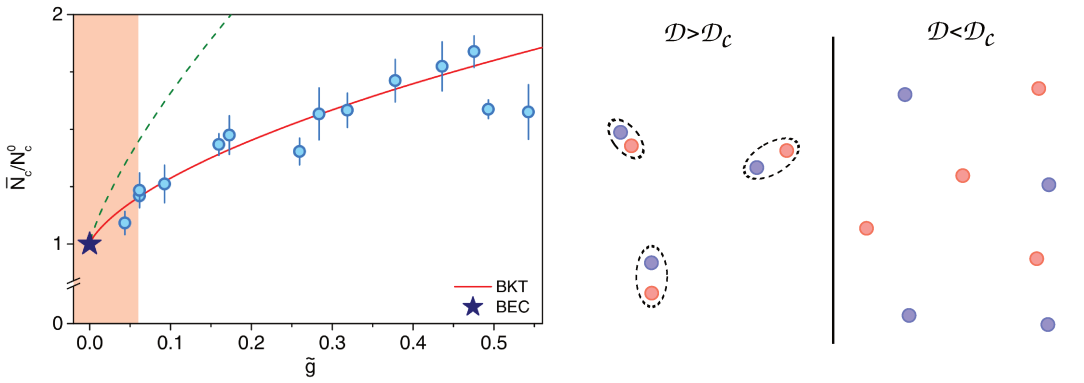

Figure 1.6 — Left: measurement of the critical atom number for the BKT transition, taken from [64], depending on the interaction parameter $\tilde{g}$. The solid line corresponds to the prediction of equation (1.40). Right: underlying mechanism for the transition: for $\mathcal{D} > \mathcal{D}_c$ (or equivalently $\mathcal{D}_s > 4$), the thermally activated vortex-antivortex pairs stay bound together: their impact on the gas is only local. For $\mathcal{D} < \mathcal{D}_c$, they are not bound anymore and vortices freely proliferate in the gas, destroying the phase order.

1.3.3 The BKT mechanism

The mechanism allowing the appearance of superfluidity in a 2D gas is particularly elegant. It deals with the presence of vortices within the gas: since a vortex causes a winding in the phase of the wavefunction, the proliferation of free vortices in the gas would destroy the phase order, and prevent the occurence of superfluid behavior. In 2D, the thermal fluctuations can cause the nucleation of vortex-antivortex pairs, that is, pairs of vortices with opposite charge. If the vortex and antivortex stay close to each other, they will cause a local perturbation, but their respective effects will cancel far away from the pair. Therefore, the existence of a quasi long-range order will depend on whether the vortex-antivortex pairs can unbind or not. Using thermodynamic considerations, Kosterlitz and Thouless [62] showed that the average elongation of the pair $\langle(\mathbf{r}_v - \mathbf{r}_a)^2\rangle$ expresses from the phase-space density of the superfluid $\mathcal{D}_s$ as:

$$\langle(\mathbf{r}_v - \mathbf{r}_a)^2\rangle = \xi^2 \frac{\mathcal{D}_s - 2}{\mathcal{D}_s - 4}. \tag{1.41}$$

This expression is defined only for $\mathcal{D}_s > 4$: for lower phase-space density, the vortex-antivortex pair can unbing freely, while for a phase-space density larger than 4 the distance between them will be of the order of a few ξ (see figure 1.6). The appearance of superfluidity in the gas therefore requires the phase-space density $\mathcal{D}_s$ *of the superfluid* to be larger than 4; the condition (1.37) in fact corresponds to the phase-space density $\mathcal{D}$ *of the whole gas* required to reach $\mathcal{D}_s = 4$. It also leads to a so-called "universal jump " of the superfluid density from $\mathcal{D}_s = 0$ to $\mathcal{D}_s = 4$ at the transition.

It is also interesting to quantify the order in the system by computing the effect of phase and density fluctuations. One can show that for $\mathcal{D} \ll 1$, the density fluctuations are strongly suppressed [94]. Concerning the phase fluctuations, while the short-wavelength phase fluctuations are prohibited in the superfluid regime, the long-wavelength phase fluctuations still have an impact, and lead to a decay of the correlation function g_1 at long distance [63]:

$$g_1(\mathbf{r}, 0) \approx \rho \left(\frac{\lambda_{dB}}{r}\right)^{1/\mathcal{D}_s}. \tag{1.42}$$

However, while g_1 decays exponentially in the thermal regime, it is here always larger than $\rho(\lambda/r)^{-1/4}$ and can easily have a significant value at the edges of the gas.

Chapter 2

Trapping atoms with RF-dressed potentials

The central tool in our experiment is the use of radiofrequency-dressed (RF-dressed) adiabatic potentials to trap and manipulate atomic clouds [98, 99]. RF-dressed traps give access to highly versatile and precisely tunable traps, that enable interesting trapping geometries. Still, it isn't as common as techniques like optical dipole trapping and the underlying mechanism is quite subtle. This chapter is intended to give the theoretical bases required for a good understanding of the work presented in this thesis, as well as the "RF-dressing for dummies" document I would have liked to find when starting to deal with these traps. It will, for a significant part, be inspired of the review of Hélène Perrin and Barry Garraway [100], towards which people looking for a complete description should go.

RF-induced adiabatic potentials were first proposed in 2001 by O. Zobay and B.M. Garraway [98]. The idea was to couple different Zeeman substates in an inhomogeneous static magnetic field to create avoided crossings and trap atoms on isomagnetic surfaces, and it was initially intended to generate two-dimensional (2D) atom traps. The first experimental realization of such a trap was achieved at LPL in 2003 [99, 101], but the 2D character was achieved later, in 2013 [102], and has been used for example to study the collective modes of 2D superfluids [68, 103, 104]. In addition to low-dimensional trapping, this method also showed useful to generate exotic trap geometries, for example double well potentials [105]. Combining it with optical potentials enables even more geometries to be achieved, for example ring potentials [106, 107] or lattice potentials [108]. Finally, the fast control available with such traps allows one to modulate the control parameters and produce time-averaged potentials [109, 110]. Among the current projects under development involving RF-dressed potentials, one can cite the realization of a Sagnac interferometer using a ring-shaped TAAP potential [111] or the project of realizing a bubble trap in space, in the absence of gravity [112]. A more detailed review of the last developments in the field can be found in [113].

2.1 Introduction to RF dressing

Let us now enter the core of the problem. I will first try to explain the physical principle on which RF-dressed traps rely. The problem can be expressed quite simply:

"How can we trap atoms at an arbitrary position using an inhomogeneous static magnetic field and an oscillating magnetic field?"

2.1.1 Trapping an atom in an inhomogeneous magnetic field

To begin with, we can try to answer a simplified version of the question: how can we trap atoms in an inhomogeneous static magnetic field?

Let us consider an atom in a state with total angular momentum F evolving in a static magnetic field $\mathbf{B}_0(\mathbf{r}) = B_0(\mathbf{r})\mathbf{e}_z$. In the following, I will call "spin" the total angular momentum, sum of nuclear spin, electronic spin and orbital angular momentum.

The angular momentum operator of the atom will be denoted $\hat{\mathbf{F}}$. The field defines a quantization axis, and we can find a basis to diagonalize both $\hat{\mathbf{F}}^2$ and the projection of $\hat{\mathbf{F}}$ along $\mathbf{e}_z$, denoted $\hat{F}_z$. For the sake of simplicity, I will for now use a two level system, i.e. $F = 1/2$. The eigenstates of the system will then be written $|\pm\rangle_z$, with eigenvalues:

$$\hat{F}_z|\pm\rangle_z = \pm\frac{1}{2}\hbar|\pm\rangle_z, \qquad \hat{\mathbf{F}}^2|\pm\rangle_z = \hbar^2 F(F+1)|\pm\rangle_z. \tag{2.1}$$

These two eigenstates correpond to the spin being oriented in the same (or opposite) direction as the magnetic field. The hamiltonian of the system writes:

$$\hat{H} = \frac{g_F\mu_\mathrm{B}}{\hbar}\mathbf{B}_0\cdot\hat{\mathbf{F}} = \frac{g_F\mu_\mathrm{B}}{\hbar}B_0\hat{F}_z, \tag{2.2}$$

with μ_B the Bohr magneton and g_F the Landé factor of the atomic state. The energy of the eigenstates is then $E_\pm = \pm g_F\mu_\mathrm{B}B_0/2$: if the field is inhomogeneous, supposing $g_F > 0$, the $|+\rangle_z$ state will be attracted towards regions where the field has a lower modulus ("low-field seeker"), and the $|-\rangle_z$ state towards high magnetic fields (high-field seeker). If $g_F < 0$ it is simply the opposite situation.

This already allows us to trap an atom: depending on its state and on the sign of g_F one has to realize a maximum or minimum of the magnetic field. However, Wing's theorem forbids the existence if a maximum in the modulus of a static magnetic field [114]: it is thus necessary to trap atoms in a low-field seeking state.

Things become a little more complex if the field orientation is not uniform (which corresponds to realistic cases, where it is needed to trap atoms along all directions). The atom will be trapped provided it stays in the *local* state that is attracted towards the field minimum, i.e. if it *adiabatically* follows the field orientation. It is thus necessary to take care when trapping low-field seeker atoms: if the minimum of the magnetic field is too weak, the atoms may not follow the field orientation, which results in atoms escaping the trap, called Majorana losses [115].

One can also show that the spin will precess around the axis of the static field, with frequency: $\omega_0(\mathbf{r}) = |g_F|\mu_\mathrm{B}|\mathbf{B}_0(\mathbf{r})|/\hbar$, called the Larmor frequency. The eigenenergies $E_\pm$ of the states can then be simply written $E_\pm = \pm\hbar\omega_0(\mathbf{r})/2$.

2.1.2 Trapping an atom anywhere in an inhomogeneous magnetic field

It is somehow possible to explain the most basic principle of RF-dressed potentials classically, by reformulating a little bit our question: how is it possible to stabilize a magnet at an arbitrary position in an inhomogeneous magnetic field?

The answer is: flip it. By flipping the magnet, the forces exerted on it are changed to their opposite. If the magnet is regularly flipped, it should be possible to keep it at a stable position, the magnet going back and forth around its average position.

We thus need to think about a way to "flip" the atomic spin. A mechanism allowing to do that is the phenomenon of nuclear magnetic resonance [116], which won Rabi his Nobel prize in 1944. By applying on the atoms an oscillating magnetic field orthogonal to the local static, directing magnetic field, it is possible to resonantly flip the atomic state if the frequency of the oscillating field is equal to the Larmor frequency defined by the static field.

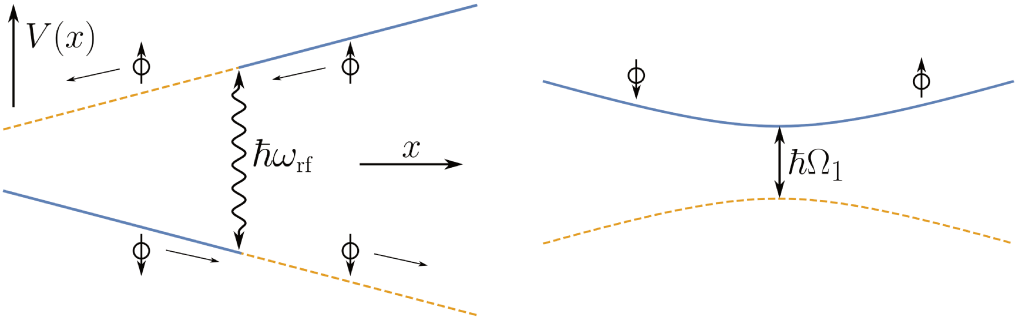

Figure 2.1 — Basic principle of RF-dressed adiabatic potentials. Left: bare potentials (for a linear variation of $\omega_0(\mathbf{r})$). The whole system is exposed to an RF field; in places where its frequency is equal to the local energy difference between the Zeeman states it is able to flip the atomic spin. Atoms in the blue regions are attracted towards resonance and can be trapped, whereas atoms in the yellow (dashed) regions are expelled from resonance. Right: corresponding adiabatic potential close to resonance, with the shape $\frac{\hbar}{2}\sqrt{(\omega_0(\mathbf{r})-\omega_{\mathrm{rf}})^2+\Omega_1^2}$. The atoms now continuously evolve between $|+\rangle_z$ and $|-\rangle_z$ states. The energy splitting between levels on resonance is equal to $\hbar\Omega_1$.

We can then go back to the previous question of a spin evolving in an inhomogeneous magnetic field (that we will still, for now, consider always aligned along $\mathbf{e}_z$): since the local magnetic field amplitude varies, the Larmor frequency will now also vary in space. We also add an oscillating magnetic field orthogonal to $\mathbf{e}_z$ (that I will in the following call "RF field", since it is what we use in practice), with uniform amplitude B_1 and frequency ω_{rf}, and we suppose that the local Larmor frequency is equal to ω_{rf} at some position.

An atom in state $|+\rangle_z$ located at a place where the Larmor frequency $\omega_0(\mathbf{r})$ is higher than ω_{rf} will be attracted towards lower magnetic fields: the Larmor frequency will then decrease during its displacement, and it will at some point come into resonance with ω_{rf}. The oscillating field is then able to flip its spin. Since the atom has some velocity, it will cross the resonance and arrive on the other side, but its state then became $|-\rangle_z$: the potential landscape it feels becomes inverted and it is now attracted towards places with higher $\omega_0(\mathbf{r})$... which will cause it to cross resonance again, and get flipped again while going back to the other side of the resonance (see figure 2.1).

In the end, the atom gets trapped around the resonance $\omega_0(\mathbf{r}) = \omega_{\mathrm{rf}}$, or, equivalently, on

the **isomagnetic region** defined by:

$$B_0(\mathbf{r}) = \frac{\hbar\omega_{\mathrm{rf}}}{\mu_{\mathrm{B}}|g_F|}. \tag{2.3}$$

2.1.3 Adiabaticity and Landau-Zener paradigm

This description allows to explain how atoms can be trapped close to resonance, but doesn't tell anything on their behavior around the resonance itself: we need a mathematic treatment of what happens when atoms cross it to understand things properly.

Let us add to the system of section 2.1.1 an oscillating magnetic field $\mathbf{B_1} = B_1\cos(\omega_{\mathrm{rf}}t)\mathbf{e}_x + B_1\sin(\omega_{\mathrm{rf}}t)\mathbf{e}_y$; we can define similarly to $\omega_0(\mathbf{r})$ the frequency $\Omega_1 = |g_F|\mu_{\mathrm{B}}|\mathbf{B_1}|/\hbar$, and the interaction of the atom with this field writes, if $g_F > 0$: $\hat{V_1} = \Omega_1\left[\cos(\omega_{\mathrm{rf}}t)\hat{F}_x + \sin(\omega_{\mathrm{rf}}t)\hat{F}_y\right]$ with $\hat{F}_x$, $\hat{F}_y$ the projections of $\hat{\mathbf{F}}$ along $\mathbf{e}_x$, $\mathbf{e}_y$. In the basis rotating at ω_{rf} around $\mathbf{e}_z$:

$$|\tilde{\pm}(t)\rangle_z = \exp\left[\frac{-i\omega_{\mathrm{rf}}t}{\hbar}\hat{F}_z\right]|\pm\rangle_z = e^{\mp i\omega_{\mathrm{rf}}t/2}|\pm\rangle_z, \tag{2.4}$$

the total hamiltonian of the system writes:

$$\hat{H} = \frac{\hbar}{2}\begin{bmatrix}-\delta(\mathbf{r}) & \Omega_1\\ \Omega_1 & \delta(\mathbf{r})\end{bmatrix} \tag{2.5}$$

where $\delta(\mathbf{r}) = \omega_{\mathrm{rf}} - \omega_0(\mathbf{r})$ is the detuning between the oscillating field and the local Larmor frequency.

However, the complete description of the evolution of an atom in a space-dependent potential can easily become complex since the position and momentum operators $\hat{\mathbf{R}}$, $\hat{\mathbf{P}}$ do not commute. For simplicity, we will keep a semi-classical description, and consider that:

- δ and Ω_1 depend exclusively on space.
- $\mathbf{r} = \langle\hat{\mathbf{R}}\rangle$ and $\Delta\mathbf{R} = 0$: the atoms are point-like, and their time evolution then depends only of their position.
- the atomic motion happens at a constant velocity: $\mathbf{r}(t) = \mathbf{v}t$.

We will thus consider that what happens to the atoms can be described as a sweep of the parameters δ and Ω_1:

$$\delta(\mathbf{r}(t)) = \delta(\mathbf{v}t) \leftrightarrow \delta(t) \tag{2.6}$$

$$\Omega_1(\mathbf{r}(t)) = \Omega_1(\mathbf{v}t) \leftrightarrow \Omega_1(t). \tag{2.7}$$

The considered hamiltonian will then be (2.5), but this time considering time-dependent Ω_1 and δ:

$$\hat{H} = \frac{\hbar}{2}\begin{bmatrix}-\delta(t) & \Omega_1(t)\\ \Omega_1(t) & \delta(t)\end{bmatrix}. \tag{2.8}$$

At an instant t, $\hat{H}$ can be diagonalized with a unitary operator $\hat{U}^\dagger$:

$$\hat{H}_A = \frac{\hbar}{2}\begin{bmatrix}-\Omega(t) & 0\\ 0 & \Omega(t)\end{bmatrix} = \hat{U}^\dagger(t)\hat{H}\hat{U}(t). \tag{2.9}$$

The instantaneous eigenenergies are then:

$$E_{\pm}(t) = \pm\frac{\hbar}{2}\Omega(t) = \pm\frac{\hbar}{2}\sqrt{\delta^2(t) + \Omega_1^2(t)}. \tag{2.10}$$

Writing $\psi(t)$ and $\psi_A(t)$ the atomic state in the respective bases where $\hat{H}$ and $\hat{H}_A$ are diagonal, with $\psi(t) = \hat{U}(t)\psi_A(t)$, the Schrödinger equation:

$$i\hbar\frac{\partial}{\partial t}\psi(t) = \hat{H}(t)\psi(t) \tag{2.11}$$

becomes for $\psi_A(t)$:

$$i\hbar\frac{\partial}{\partial t}\psi_A(t) = \hat{H}_A(t)\psi_A(t) - i\hbar\hat{U}^\dagger\frac{\partial}{\partial t}\hat{U}\psi_A(t). \tag{2.12}$$

We see, then, that the atom will "follow" the eigenstates of $\hat{H}_A(t)$ if the last part of equation (2.12) stays small. For the hamiltonian (2.8), this correction term has the form [100]:

$$\frac{\hbar}{2}\begin{bmatrix} 0 & \gamma(t) \\ \gamma^*(t) & 0 \end{bmatrix}. \tag{2.13}$$

$\gamma(t)$ is the correction corresponds to non-adiabatic coupling between the eigenstates of $\hat{H}_A$, with $\gamma(t)$ given by:

$$\gamma(t) = -i\frac{\dot{\delta}(t)\Omega_1(t) - \delta(t)\dot{\Omega}_1(t)}{\Omega^2(t)}. \tag{2.14}$$

Following the eigenstates of $\hat{H}_A$ then supposes the condition [117]

$$|\gamma(t)| \ll \Omega(t). \tag{2.15}$$

Let us then go back to the description of an atom evolving in an inhomogeneous static magnetic field and an oscillating field. If we suppose that the oscillating field has a homogeneous amplitude such that $\dot{\Omega}_1 = 0$, this condition then rewrites:

$$|\dot{\delta}| \ll \Omega^2, \tag{2.16}$$

which is called the adiabaticity condition.

In these conditions, the Landau-Zener model [118, 119] expresses the probability of non-adiabatic transition when crossing the resonance:

$$P = \exp\left(-\pi\frac{\Omega_1^2}{|\dot{\delta}|}\right). \tag{2.17}$$

Let us finally sum up what we have seen until now: for an atom evolving in an inhomogeneous magnetic field in the presence of an oscillating field, the energy of the atom in the upper state at time t is $E(t) = \frac{\hbar}{2}\sqrt{\delta^2(t) + \Omega_1^2(t)}$, which equivalently means that the *effective* energy landscape felt by the atom can be expressed as $E(\mathbf{r}) = \frac{\hbar}{2}\sqrt{\delta^2(\mathbf{r}) + \Omega_1^2(\mathbf{r})}$, with δ the detuning between the local Larmor frequency and the oscillating field frequency and Ω_1 the local Rabi coupling, provided that the *adiabaticity condition* $|\dot{\delta}| \ll \Omega^2$ is respected (for an atom in motion and a time-independent $\delta(\mathbf{r})$, it becomes $|\mathbf{v}\cdot\boldsymbol{\nabla}\delta| \ll \Omega^2$).

2.2 Formalism of RF-dressed traps

Up to now, I explained the principles on which RF-dressed adiabatic potentials rely, but we now need a more detailed treatment, that would allow us to fully describe a trap for ultracold atoms based on this method. In particular, we need to be able to describe the case of more than 2 spin states (which is always the case when working with bosons[1]), and to be able to take into account the local polarization of the oscillating field (the previous treatment corresponds to circular polarization). This description is detailed in sections III and IV of [100], that I will present here in a simplified version.

2.2.1 Classical field treatment of magnetic resonance

Like previously, we want to describe the behavior of an atom placed in the combination of a static magnetic field $\mathbf{B}_0 = B_0\mathbf{e}_z$ and an arbitrary classical magnetic field oscillating at RF frequency $\mathbf{B}_1(t) = B_x\cos(\omega_{\rm rf}t)\mathbf{e}_x + B_y\cos(\omega_{\rm rf}t)\mathbf{e}_y + B_z\cos(\omega_{\rm rf}t)\mathbf{e}_z$.

Using a quantization axis $\mathbf{e}_z$, there is a basis where $\hat{\mathbf{F}}^2$ and F_z are diagonal. We will consider all atoms to be in the same F state, and the spin eigenstates will then be written $|m\rangle_z$, with $F_z|m\rangle_z = m\hbar|m\rangle_z$ and $m \in \{-F, -F+1, ..., F-1, F\}$.

The magnetic interaction between the static field and the atomic spin reads:

$$\hat{H}_0 = \frac{g_F\mu_{\rm B}}{\hbar}\mathbf{B}_0\cdot\hat{\mathbf{F}} \tag{2.18}$$

and we can write the Larmor frequency as:

$$\omega_0 = |g_F|\mu_{\rm B}B_0/\hbar. \tag{2.19}$$

For an arbitrary polarization, it is more practical to describe the RF field using complex notation, as $\mathbf{B}_1(t) = \boldsymbol{\mathcal{B}}_1 e^{-i\omega_{\rm rf}t} + c.c.$, with $\boldsymbol{\mathcal{B}}_1$ the complex field amplitude:

$$\boldsymbol{\mathcal{B}}_1 = \frac{B_x}{2}e^{-i\phi_y}\mathbf{e}_x + \frac{B_y}{2}e^{-i\phi_y}\mathbf{e}_y + \frac{B_z}{2}e^{-i\phi_z}\mathbf{e}_z, \tag{2.20}$$

or, writing $\boldsymbol{\epsilon}$ the complex polarization of the field ($|\boldsymbol{\epsilon}| = 1$):

$$\boldsymbol{\mathcal{B}}_1 = \mathcal{B}_1\boldsymbol{\epsilon}. \tag{2.21}$$

We choose to describe the RF field in the spherical basis $(\mathbf{e}_+, \mathbf{e}_-, \mathbf{e}_z)$, with

$$\mathbf{e}_+ = -\frac{1}{\sqrt{2}}(\mathbf{e}_x + i\mathbf{e}_y), \qquad \mathbf{e}_- = \frac{1}{\sqrt{2}}(\mathbf{e}_x - i\mathbf{e}_y). \tag{2.22}$$

The component along $\mathbf{e}_z$ of the RF field is aligned with the static field, and provided $B_z \ll B_0$, its effect is negligible [120,121][2]. We will thus only consider orthogonal components, and write the RF amplitude as

$$\boldsymbol{\mathcal{B}}_1 = B_+\mathbf{e}_+ + B_-\mathbf{e}_- \tag{2.23}$$

with $B_\pm = \mathbf{e}_\pm^*\cdot\boldsymbol{\epsilon}\mathcal{B}_1$. In the spherical basis, we can write $\hat{\mathbf{F}}\cdot\mathbf{e}_\pm = \mp\frac{1}{\sqrt{2}}\hat{F}_\pm$, with $\hat{F}_\pm$ the raising and lowering operators defined as $\hat{F}_\pm = \hat{F}_x \pm i\hat{F}_y$.

1. F=0 is not relevant, being insensitive to magnetic fields.
2. B_z comparable to B_0 leads to a modification of the Landé factor when calculating the RF coupling to B_x and B_y.

Using these definitions, the coupling between the RF and the atomic spin can be written as:

$$\hat{V}_1 = \frac{g_F \mu_B}{\hbar} \boldsymbol{\mathcal{B}}_1 \cdot \hat{\mathbf{F}}\ e^{-i\omega_{\mathrm{rf}} t} + h.c. \tag{2.24}$$

$$= \frac{g_F \mu_B}{\hbar} \left[-\frac{1}{\sqrt{2}} B_+ \hat{F}_+ + \frac{1}{\sqrt{2}} B_- \hat{F}_- \right] e^{-i\omega_{\mathrm{rf}} t} + h.c. \tag{2.25}$$

And defining the (complex) coupling amplitudes as:

$$\Omega_\pm = \mp\sqrt{2} \frac{|g_F| \mu_B}{\hbar} B_\pm, \tag{2.26}$$

it can be expressed more nicely as:

$$\hat{V}_1 = s \left[\frac{\Omega_+}{2} \hat{F}_+ + \frac{\Omega_-}{2} \hat{F}_- \right] e^{-i\omega_{\mathrm{rf}} t} + h.c. \tag{2.27}$$

Here, we introduced $s = g_F/|g_F|$ the sign of the Landé factor.

We can then, finally, write the total hamiltonian $\hat{H} = \hat{H}_0 + \hat{V}_1$:

$$\hat{H} = s\omega_0 \hat{F}_z + s \left[\frac{\Omega_+}{2} e^{-i\omega_{\mathrm{rf}} t} \hat{F}_+ + \frac{\Omega_+^*}{2} e^{i\omega_{\mathrm{rf}} t} \hat{F}_- + \frac{\Omega_-}{2} e^{-i\omega_{\mathrm{rf}} t} \hat{F}_- + \frac{\Omega_-^*}{2} e^{i\omega_{\mathrm{rf}} t} \hat{F}_+ \right]. \tag{2.28}$$

The first term corresponds to precession of the spin around $\mathbf{e}_z$, and the four next terms correspond to transitions between the different $|m\rangle_z$ substates.

Like for section 2.1.3, we will now look at what happens in the basis rotating at frequency $s\omega_{\mathrm{rf}}$ around $\mathbf{e}_z$, with rotated states $|\psi\rangle_{\mathrm{rot}} = \exp(-\frac{is\omega_{\mathrm{rf}} t}{\hbar} \hat{F}_z)|\psi\rangle$. In this basis, denoting $\delta = \omega_{\mathrm{rf}} - \omega_0$, the hamiltonian now reads:

$$\hat{H}_{\mathrm{rot}} = -s\delta \hat{F}_z + s \left[\frac{\Omega_+}{2} e^{i(s-1)\omega_{\mathrm{rf}} t} \hat{F}_+ + \frac{\Omega_+^*}{2} e^{-i(s-1)\omega_{\mathrm{rf}} t} \hat{F}_- \right] + s \left[\frac{\Omega_-}{2} e^{-i(s+1)\omega_{\mathrm{rf}} t} \hat{F}_- + \frac{\Omega_-^*}{2} e^{i(s+1)\omega_{\mathrm{rf}} t} \hat{F}_+ \right]. \tag{2.29}$$

Depending on the sign of s, the first two terms or the last two terms will be static, whereas the two other terms will evolve at very high frequency $\pm 2\omega_{\mathrm{rf}}$. We can then suppose that the two non-resonant terms, evolving much faster than the rest of the system, will average to 0, and consider only the two static terms, in what is called the Rotating Wave Approximation (RWA). This approximation is valid in the limit where $|\delta|, \Omega_\pm \ll \omega_{\mathrm{rf}}$.

We will then denote $\Omega_1 = \Omega_s$; in both cases $\Omega_1 = -\sqrt{2} g_F \mu_B B_s/\hbar$. Writing $\Omega_1 = |\Omega_1| e^{i\phi}$ and transforming into the states rotated by $s\omega_{\mathrm{rf}} t + \phi$ instead of just $s\omega_{\mathrm{rf}} t$, the effective hamiltonian then becomes:

$$\hat{H}_{\mathrm{eff}} = -s\delta \hat{F}_z + s \frac{|\Omega_1|}{2} (\hat{F}_+ + \hat{F}_-) \tag{2.30}$$

$$= s(-\delta \hat{F}_z + |\Omega_1| \hat{F}_x). \tag{2.31}$$

Then we can finally rewrite:

$$\hat{H}_{\mathrm{eff}} = \Omega \hat{F}_\theta, \tag{2.32}$$

where we defined:

$$\Omega = \sqrt{\delta^2 + \Omega_1^2}, \tag{2.33}$$

$$\hat{F}_\theta = \cos(\theta)\hat{F}_z + \sin(\theta)\hat{F}_x, \tag{2.34}$$

$$\theta = \arccos\left(\frac{-\delta}{\Omega}\right) + \frac{s-1}{2}\pi. \tag{2.35}$$

$\hat{F}_\theta$ is the projection of $\hat{\mathbf{F}}$ along a new axis in the $x-y$ plane: $\mathbf{e}_\theta = \cos(\theta)\mathbf{e}_z + \sin(\theta)\mathbf{e}_x$. In other words, everything happens as if the atom was evolving in a static magnetic field oriented along $\mathbf{e}_\theta$. We can define a new set of eigenstates in the rotating basis:

$$|m\rangle_\theta = e^{-i\theta\hat{F}_y/\hbar}|m\rangle_z, \tag{2.36}$$

and the eigenenergies of the corresponding states are:

$$E_m = m\hbar\Omega. \tag{2.37}$$

We thus see that the dressing corresponds to creating a minimum of an *effective* magnetic field to trap the atoms.

Close to the resonance, we can now write the adiabaticity criterion simply as:

$$|\dot{\theta}| \ll \Omega. \tag{2.38}$$

If this criterion is fulfilled, the spin adiabatically follows the orientation of the *effective* local magnetic field $\mathbf{e}_\theta$. Going from one side of the resonance to the other one, this corresponds to a complete flip of the spin, with a continuous rotation of the spin orientation.

2.2.2 Adiabatic potentials for RF-dressed atoms

The previous description corresponds to a uniform magnetic field and is thus unsufficient to describe a trap. We also need to take into account the spatial dependence of all parameters: static field amplitude and orientation, RF polarization and amplitude. The basic principle, however, still holds: provided the atoms adiabatically follow the local states $|m\rangle_{\theta(\mathbf{r})}$, they will feel an effective potential landscape whose value is:

$$V_m(\mathbf{r}) = m\hbar\Omega(\mathbf{r}) = m\hbar\sqrt{\delta^2(\mathbf{r}) + \Omega_1^2(\mathbf{r})}. \tag{2.39}$$

For practical reasons, the extreme adiabatic state $|m = F\rangle_\theta$ will always be used for trapping: for $F \leq 1$ it is the only state that is trapped, and for $F > 1$ having all atoms in the maximally polarized state avoids spin-changing collisions, which would result in atom losses [122]. In the following, all occurences of m will then be replaced by F.

General principles

The expression (2.39) already allows us to get a good insight on what happens for this kind of potential:

- The $\delta(\mathbf{r})$ dependence, which is generally the strongest, indicates that the atoms will be trapped in the place where $\delta(\mathbf{r}) = 0$, i.e. where the RF is resonant with the Larmor frequency. For a given RF frequency, this corresponds to an isomagnetic surface. The strength of the confinement depends on the local magnetic gradient (which is, by definition, orthogonal to the surface). Writing $\alpha = |\boldsymbol{\nabla}\omega_0|$ this gradient (in units of frequency), we can deduce the trapping frequency [100]:

$$\omega_{\text{transverse}} = \alpha\sqrt{\frac{F\hbar}{M\Omega_1}} \tag{2.40}$$

  where M is the atomic mass. This confinement can easily be quite strong in practice, between several hundred Hz and a few kHz, and can be used to reach low-dimensional regimes. The atoms evolve on an isomagnetic surface, in general bubble-shaped.

- On the other hand, on resonance the $\Omega_1(\mathbf{r})$ dependency will also structure the shape of the potential close to resonance. The variations in Rabi coupling being usually much smoother than the variations in the Larmor frequency, it in fact structures the fine shape of the potential, modifying the local confinement on the isomagnetic surface (cf eq. (2.40)) and attracting the atoms to the regions with lower coupling: the potential restricted to the resonant surface writes $F\hbar\Omega_1(\mathbf{r})$. This can become a problem for staying within adiabaticity conditions, but the presence of gravity can often be used to prevent atoms from reaching the regions where Ω would be too low to ensure adiabaticity. On the other hand, tailoring the local coupling can be used to modify the trap, for example to create a double well [105], to excite specific collective modes [68] or to induce rotation in the trapped cloud (cf chapters 6 and 8).

A few more useful expressions

To go beyond these general principles, we need to be able to compute exactly the value of the potential (2.39) in a given experimental configuration. The whole question is thus: what are the expressions of $\delta(\mathbf{r})$ and $\Omega_1(\mathbf{r})$? Let us write, as previously, the static field and RF field:

$$\mathbf{B}_0 = B_0(\mathbf{r})\mathbf{u}(\mathbf{r}), \tag{2.41}$$

$$\mathbf{B}_1(\mathbf{r},t) = B_1(\mathbf{r})\boldsymbol{\epsilon}(\mathbf{r})e^{-i\omega_{\text{rf}}t} + c.c. \tag{2.42}$$

where $\mathbf{u}(\mathbf{r}) = \mathbf{B}_0(\mathbf{r})/|\mathbf{B}_0(\mathbf{r})|$ is the unitary vector giving the local orientation of the magnetic field.

$\delta(\mathbf{r})$ can be very simply expressed as

$$\delta(\mathbf{r}) = \omega_{\text{rf}} - |g_F|\mu_{\text{B}}B_0(\mathbf{r})/\hbar. \tag{2.43}$$

The expression of $\Omega_1(\mathbf{r})$ is more subtle. We have seen that it depends on the *local* component of $\mathbf{B}_1(\mathbf{r},t)$ along the *local* spherical polarization σ^s. This component can be expressed, using the *local* spherical basis $(\mathbf{e}_+(\mathbf{r}),\ \mathbf{e}_-(\mathbf{r}),\ \mathbf{u}(\mathbf{r}))$ defined by the local magnetic field orientation, as $\mathcal{B}_1(\mathbf{r})\mathbf{e}_s^*(\mathbf{r})\cdot\boldsymbol{\epsilon}(\mathbf{r})$. The local coupling is then

$$\Omega_1(\mathbf{r}) = -\sqrt{2}\frac{g_F\mu_{\text{B}}}{\hbar}\mathcal{B}_1(\mathbf{r})\ \mathbf{e}_s^*(\mathbf{r})\cdot\boldsymbol{\epsilon}(\mathbf{r}) \tag{2.44}$$

$$= -\Omega_{\text{rf}}\ \mathbf{e}_s^*(\mathbf{r})\cdot\boldsymbol{\epsilon}(\mathbf{r}), \tag{2.45}$$

with $\Omega_{\mathrm{rf}} = \sqrt{2}|g_F \mu_{\mathrm{B}} \mathcal{B}_1|/\hbar$. Ω_{rf} is the maximal coupling one can expect to achieve for a given RF field amplitude $\mathcal{B}_1$ (it can be attained only with a circularly polarized RF field). Using the properties of the spherical basis, $\Omega_1(\mathbf{r})$ can also be expressed as [100]:

$$|\Omega_1(\mathbf{r})| = \frac{\Omega_{\mathrm{rf}}}{2}|\boldsymbol{\epsilon} \times \mathbf{u} + is\mathbf{u} \times (\boldsymbol{\epsilon} \times \mathbf{u})| \tag{2.46}$$

$$= \frac{\Omega_{\mathrm{rf}}}{2}\sqrt{1 - |\boldsymbol{\epsilon} \cdot \mathbf{u}|^2 + |\boldsymbol{\epsilon} \times \mathbf{u}|^2 + 2is\mathbf{u} \cdot (\boldsymbol{\epsilon} \times \boldsymbol{\epsilon}^*)}. \tag{2.47}$$

In the particular case of a RF field that is circularly polarized σ^s around the z axis, it can be simplified:

$$|\Omega_1(\mathbf{r})| = \frac{\Omega_{\mathrm{rf}}}{2}[1 + u_z(\mathbf{r})], \tag{2.48}$$

with $u_z(\mathbf{r}) = \mathbf{u} \cdot \mathbf{e}_z$.

In the other interesting case of a field that is linearly polarized along z axis, it reads:

$$|\Omega_1(\mathbf{r})| = \Omega_{\mathrm{rf}}\sqrt{\frac{1 - u_z(\mathbf{r})^2}{2}}. \tag{2.49}$$

With this, we should now be able to describe any trap based on RF dressing.

2.3 The dressed quadrupole trap

Now that the principles have been properly introduced, I will make one step further towards experimental application and describe in detail the trap we use in our experiment, the dressed quadrupole trap.

The quadrupole field is the simplest way to obtain a magnetic trap, obtained with a pair of coils in anti-Helmholtz configuration. The obtained magnetic field is linear, and reads:

$$\mathbf{B}_0(\mathbf{r}) = b'(x\mathbf{e}_x + y\mathbf{e}_y - 2z\mathbf{e}_z). \tag{2.50}$$

The corresponding local Larmor frequency is then:

$$\omega_0(\mathbf{r}) = \alpha\sqrt{x^2 + y^2 + 4z^2}, \tag{2.51}$$

with α the value of the horizontal magnetic gradient b' in frequency units:

$$\alpha = |g_F|\mu_{\mathrm{B}} b'/\hbar. \tag{2.52}$$

For a given value of the RF frequency ω_{rf}, the atoms are trapped on the isomagnetic surface defined by $\omega_0(\mathbf{r}) = \omega_{\mathrm{rf}}$, which corresponds to an ellipsoid (fig. 2.2):

$$x^2 + y^2 + 4z^2 = r_b^2. \tag{2.53}$$

r_b is then the radius at the equator of this "bubble trap", and its value is:

$$r_b = \frac{\omega_{\mathrm{rf}}}{\alpha}. \tag{2.54}$$

Adding gravity, supposed to be aligned with the axis of the quadrupole trap $\mathbf{e}_z$, and neglecting for now the details of polarization (i.e. considering uniform coupling Ω_1), we can guess that the atoms will then fall to the bottom of this bubble due to gravity, giving a

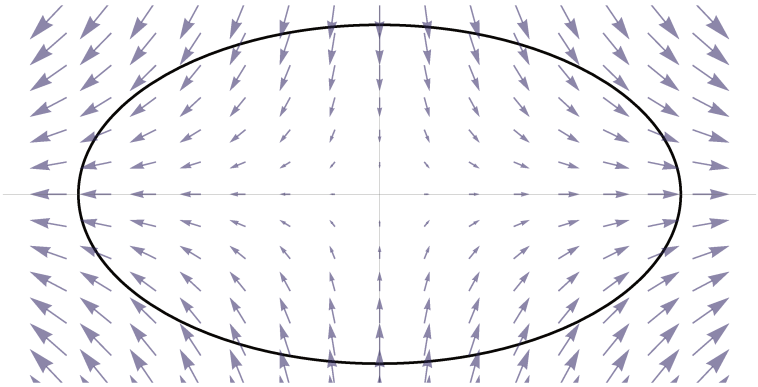

Figure 2.2 — Quadrupole vector field (blue arrows) and the corresponding isomagnetic surface (black line), on which the atoms are trapped.

pancake-shaped cloud with some residual curvature. We can already give an estimate of the trapping frequencies at the bottom of the bubble, neglecting for now the contribution of gravity and coupling inhomogeneities (considering the potential minimum stays on resonance):

$$\omega_\perp \approx \sqrt{\frac{g}{2r_b}}, \tag{2.55}$$

$$\omega_z = 2\alpha\sqrt{\frac{F\hbar}{M\Omega_1}}. \tag{2.56}$$

The radial trapping frequency is the pendulum frequency with radius $2r_b$, corresponding to the local radius of curvature at the bottom. The vertical trapping frequency is the magnetic trapping on resonance, expressed from (2.40) (the vertical gradient being 2α). We have to mention that these frequencies make sense only close to the minimum, the trap geometry being not at all harmonic.

To lighten future expressions, I will now define the generalized distance to the center of the quadrupole field:

$$\ell_b(r,z) = \sqrt{r^2+4z^2}, \tag{2.57}$$

r being the radial coordinate: $r = \sqrt{x^2+y^2}$.

The direction of the magnetic field, necessary to compute the local coupling, reads [100]:

$$\mathbf{u} = \frac{x\mathbf{e}_x + y\mathbf{e}_y - 2z\mathbf{e}_z}{\sqrt{x^2+y^2+4z^2}} = \frac{r\ \mathbf{e}_r - 2z\ \mathbf{e}_z}{\ell_b(r,z)}. \tag{2.58}$$

Let us now compute the exact potential in two situations, the most commonly used in experiment: the circular and linear polarizations.

2.3.1 Circular polarization

The atoms, once at the bottom of the bubble, feel a magnetic field aligned along the z axis ($\mathbf{u} = \mathbf{e}_z$). The coupling at this position is maximized for a σ^s polarization aligned with z:

$$\boldsymbol{\epsilon} = -\frac{1}{\sqrt{2}}(s\ \mathbf{e}_x + i\mathbf{e}_y). \tag{2.59}$$

The equation (2.48) then leads to the expression of the local coupling:

$$|\Omega_1(\mathbf{r})| = \frac{\Omega_0}{2}\left(1 - \frac{2z}{\ell_b(r,z)}\right) \tag{2.60}$$

where Ω_0 is the Rabi coupling obtained at the bottom of the bubble, which happens to be the maximal Rabi coupling[3].

As mentioned previously (section 2.2.2), the potential on the resonant surface is equal to $F\hbar\Omega_1(\mathbf{r})$. Since $\Omega_1 = 0$ at the top of the bubble, the atoms are naturally attracted towards this point which corresponds to a minimum of potential. However, having the atoms reach this point is very detrimental to the experimentalist, because the absence of coupling means that atoms passing there cannot follow the dressed state and get their spin flipped[4], resulting in their loss from the trap. This point thus acts as a "hole" from which the atoms will escape the trap: it is absolutely necessary to keep a "coupling gradient" weaker than gravity to ensure that the atoms stay at the bottom of the equator (fig. 2.3) [102, 123].

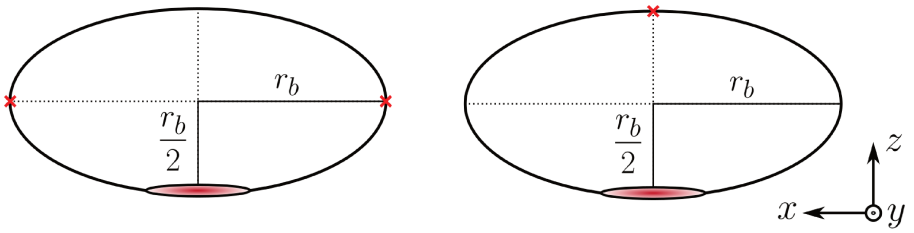

Figure 2.3 — Scheme of the dressed quadrupole trap, seen from the side. Atoms fall to the bottom of the bubble due to gravity. At one or two points of the surface (red crosses), the coupling cancels, creating "holes" from which the atoms can escape. Left: linear polarization configuration, with two holes at the equator; right: circular polarization configuration, with one hole at the top.

This condition can be expressed as:

$$F\hbar\Omega_0 < Mgr_b, \tag{2.61}$$

or, writing $\beta = F\frac{\hbar\alpha}{Mg}$ the ratio between magnetic gradient and gravity:

$$\Omega_0 < \frac{\omega_{\mathrm{rf}}}{\beta}. \tag{2.62}$$

On the other hand, $\beta > 1$ is required so that the magnetic gradient is strong enough to compensate gravity (otherwise, atoms will simply fall off the trap). This means that the maximum Rabi coupling should be significantly smaller than the RF frequency – which is also required to ensure RWA.

3. In previous documents about dressed quadrupole traps, Ω_0 was defined as the maximal Rabi coupling on the bubble, which happened to also be the Rabi coupling at the bottom of the bubble. However, for the generalization of the dressed quadrupole trap to any polarization that will follow in this chapter, defining Ω_0 as the coupling at the bottom happens to be more convenient. I think it is also a more relevant definition anyway, because with this definition Ω_0 can always be experimentally measured, since it is the coupling at the position of the atoms.
4. The spin flip happens in the dressed state basis. Related to the static magnetic field, the problem is rather that their spin is *not* flipped while crossing the resonance.

Due to gravity, the potential minimum is shifted slightly below the resonant ellipsoid, and is located at $(x = 0, y = 0, z = -R)$, with R being equal to [102]:

$$R = \frac{r_b}{2}\left(1 + \frac{1}{\sqrt{4\beta^2 - 1}}\frac{\Omega_0}{\omega_{\mathrm{rf}}}\right). \tag{2.63}$$

Around the potential minimum at the bottom of the bubble, it is then possible to make a second order development of the potential and get the oscillation frequencies:

$$\omega_\perp = \sqrt{\frac{g}{4R}}\left[1 - \frac{F\hbar\Omega_0}{2MgR}\sqrt{1 - \frac{1}{4\beta^2}}\right]^{1/2}, \tag{2.64}$$

$$\omega_z = 2\alpha\sqrt{\frac{F\hbar}{M\Omega_0}}\left(1 - \frac{1}{4\beta^2}\right)^{3/4}. \tag{2.65}$$

These frequencies are similar to (2.55), (2.56), but with factors taking into account the fact that the potential minimum is shifted due to gravity (the "pendulum" is now slightly longer). The value of $\omega_\perp$ is also slightly reduced due to the attraction to the zero of coupling at the top of the bubble. This trap is isotropic in the $x - y$ plane.

For convenience, one can define the dimensionless quantity:

$$\gamma = \frac{F\hbar\Omega_0}{MgR}\sqrt{1 - \frac{1}{4\beta^2}}, \tag{2.66}$$

which describes the typical ratio between the coupling gradient and gravity (the factor $(1 - 1/4\beta^2)^{1/2}$ present here is quite inelegant, but putting it here simplifies a lot subsequent formulas). In most experimental cases $\beta \gg 1$ and inequality (2.61) simply corresponds to $\gamma < 2$. With this definition, $\omega_\perp$ can simply be rewritten as:

$$\omega_\perp = \sqrt{\frac{g}{4R}}\left[1 - \frac{\gamma}{2}\right]^{1/2}. \tag{2.67}$$

2.3.2 Linear polarization

The other simple interesting case corresponds to the simplest one that can be obtained experimentally, the linear polarization:

$$\boldsymbol{\epsilon} = \mathbf{e}_x. \tag{2.68}$$

From (2.49), we can again deduce the local coupling:

$$|\Omega_1(\mathbf{r})| = \Omega_0\sqrt{1 - \frac{x^2}{\ell_b(r,z)^2}}, \tag{2.69}$$

where Ω_0 is the maximum Rabi coupling. This time, $|\Omega_1| = \Omega_0$ in the $y - z$ plane, and $\Omega_1 = 0$ on the two extreme points at the equator: $x = \pm r_b, y = z = 0$, where the local static field is aligned with the RF field.

The position of the potential minimum is identical to (2.63) and this time, the trapping frequencies are [102]:

$$\omega_x = \sqrt{\frac{g}{4R}}\left[1 - \frac{F\hbar\Omega_0}{MgR}\sqrt{1 - \frac{1}{4\beta^2}}\right]^{1/2} = \sqrt{\frac{g}{4R}}\left[1 - \gamma\right]^{1/2}, \tag{2.70}$$

$$\omega_y = \sqrt{\frac{g}{4R}}, \tag{2.71}$$

$$\omega_z = 2\alpha\sqrt{\frac{F\hbar}{M\Omega_0}}\left(1-\frac{1}{4\beta^2}\right)^{3/4}. \tag{2.72}$$

Again, the frequencies are slightly modified due to gravity. The coupling being homogeneous in the whole $y-z$ plane, ω_y is this time simply equal to the pendulum frequency, while the correction to ω_x due to the attraction of the holes is twice stronger than in the circular polarization case, the holes now being at half height of the bubble. This configuration gives an anisotropic trap in the $x-y$ plane.

Again, gravity must be strong enough to prevent the atoms from reaching the two points with zero coupling; this condition can be deduced from (2.70) as $\gamma < 1$. Compared to the circular polarization case, the minimum of coupling is this time at the equator and the constraint on Ω_0 is then twice stronger.

2.3.3 Elliptical polarization and control of the fine shape of the bubble

Using expression (2.47) allows us to compute the exact potential shape for any polarization of the RF wave. Before giving exact results, it is still possible to describe the general behavior or the trap:

- There are two holes somewhere on the bubble, where the coupling cancels. For a σ^s polarization with respect to the z axis, the two holes merge at the top of the bubble, for a σ^{-s} they merge at the bottom of the bubble (which makes this configuration impossible to use for trapping atoms). For an elliptical horizontal polarization, the holes are placed somewhere in between, in the same vertical plane cutting the bubble in two halves.

- Keeping atoms trapped will, again, suppose the condition:

  $$F\hbar\Omega_0 < Mgh_{\text{hole}}, \tag{2.73}$$

  with h_{hole} the height of the lowest hole with respect to the bottom of the bubble and $\Omega_0 = |\Omega_1(x=0,\ y=0,\ z=-R)|$ the coupling at the bottom of the bubble, where atoms should be located if gravity wins.

- Supposing that the atoms stay at the bottom of the bubble, the potential minimum will stay at the same position (2.63), and the oscillation frequencies will be the same as previously: trapping on resonance corrected due to gravity vertically, pendulum frequency $\sqrt{g/4R}$ corrected from the attraction of the holes radially. For a non-circular polarization, the trap will be anisotropic and its axes will be the same as those of the polarization ellipse.

Let us give another useful result: supposing that the polarization plane is orthogonal to the quadrupole axis (i.e. in the horizontal plane), we can write any polarization as:

$$\boldsymbol{\epsilon} = \cos(\Theta)\mathbf{e}_x + e^{i\Phi}\sin(\Theta)\mathbf{e}_y. \tag{2.74}$$

The coordinates of the holes are then

$$\begin{cases} x &= r_b\sin(\mathrm{t})\cos(\phi) \\ y &= r_b\cos(\mathrm{t})\sin(\phi) \\ z &= \frac{r_b}{2}\cos(\mathrm{t}) \end{cases}. \tag{2.75}$$

(t,ϕ) are the polar coordinates of the holes, taking into account the vertical "flattening" of the bubble by a factor of two as compared to the sphere; they are defined through [124]:

$$\tan(2\phi) = \tan(2\Theta)\cos(\Phi), \tag{2.76}$$

$$\cos(\mathrm{t}) = \frac{\sin(2\Theta)\sin(\Phi)}{1+\sqrt{1-\sin^2(2\Theta)\ \sin^2(\Phi)}}. \tag{2.77}$$

Equation (2.76) gives two solutions within $[0, 2\pi]$, ϕ and $\phi+\pi$. It corresponds to the orientation of the semi-major axis of the polarization ellipse with respect to the x axis. Equation (2.77) gives the vertical position of the holes in the bubble (fig. 2.4); for a circular polarization ($\Phi = \pm\pi/2$ and $\Theta = \pi/4 + n\pi$, $n \in \mathbb{Z}$) we find $\cos(\mathrm{t}) = \pm 1$ meaning the holes are at the top (or the bottom) of the ellipsoid whereas for a linear polarization ($\phi = 0 + n\pi$, $n \in \mathbb{Z}$), $\cos(\mathrm{t}) = 0$ meaning the holes are at the equator. In these conditions, and supposing $\beta \ll 1$ for simplicity, the height of the holes with respect to the bottom reads: $h_{\mathrm{hole}} = R(1+\cos(\mathrm{t}))$, and the condition (2.73) can be rewritten simply as $\gamma < 1 + \cos(\mathrm{t})$.

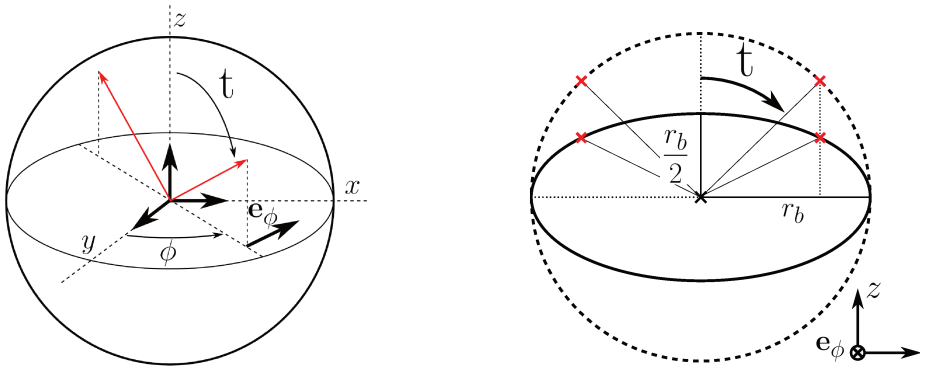

Figure 2.4 — Left: position of the holes (red arrows) on the "unflattened" bubble, in spherical coordinates (t, ϕ) for an arbitrary polarization located in the horizontal plane. t and ϕ can be modified independently by tuning the RF polarization. Right: position of the holes (red crosses) in the plane oriented along the semi-major axis of the RF polarization. Continuous black line: real profile of the bubble, dashed line: unflattened bubble, on which t is defined. For a linear polarization, $\mathrm{t} = \pi/2$, for a circular polarization $\mathrm{t} = 0$ or $\mathrm{t} = \pi$ (depending on the sign of the polarization).

By giving the azimuthal position of the holes, (2.76) also gives the symmetry axis of the bubble. A good control of (Θ, Φ) thus allows to tune the orientation of the trap as desired.

2.3.4 Detailed parametrization of arbitrary polarization

I will here go beyond the previous section, by giving analytical results that can be interesting when working with arbitrary polarization. This section will generalize the results of sections 2.3.1 and 2.3.2 to any elliptical polarization in the horizontal plane.

For an arbitrary polarization in the horizontal plane written as (2.74), the local Rabi coupling reads from (2.47) [124]

$$\Omega^2 = \frac{\Omega_{\mathrm{rf}}^2}{2}\left(1 - \frac{r^2 + (x^2-y^2)\cos(2\Theta) + 2xy\sin(2\Theta)\cos(\Phi)}{2\ell_b^2} - \frac{2z}{\ell_b}\sin(2\Theta)\sin(\Phi)\right). \quad (2.78)$$

The central term describes the anisotropy in the $x-y$ plane; it is convenient to recast it in the frame oriented along the polarization axes: $x' = \cos(\phi)x + \sin(\phi)y$ and $y' = \sin(\phi)x - \cos(\phi)y$, with ϕ defined in (2.76):

$$\Omega^2 = \frac{\Omega_{\mathrm{rf}}^2}{2}\left(1 - \frac{r^2 - 2\sqrt{\eta(1-\eta)}(x'^2 - y'^2)}{2\ell_b^2} - \frac{2z}{\ell_b}(2\eta - 1)\right) \quad (2.79)$$

where η is defined by:

$$\eta = \frac{1 + \sin(2\Theta)\sin(\Phi)}{2}. \quad (2.80)$$

η defines the anisotropy of the coupling in the $x-y$ plane, but also the coupling at the bottom of the bubble:

$$\Omega_0 = \sqrt{\eta}\Omega_{\mathrm{rf}} \quad (2.81)$$

η takes values between 0 and 1, being equal to 1 (or 0) for a circular polarization and 1/2 for a linear polarization.

The trapping frequencies then expresses from a second order development:

$$\omega_{x'} = \sqrt{\frac{g}{4R}}\left[1 - \frac{\gamma}{2}\left(1 - \sqrt{\frac{1}{\eta} - 1}\right)\right]^{1/2}, \quad (2.82)$$

$$\omega_{y'} = \sqrt{\frac{g}{4R}}\left[1 - \frac{\gamma}{2}\left(1 + \sqrt{\frac{1}{\eta} - 1}\right)\right]^{1/2}, \quad (2.83)$$

$$\omega_z = 2\alpha\sqrt{\frac{F\hbar}{M\Omega_0}}\left(1 - \frac{1}{4\beta^2}\right)^{3/4}, \quad (2.84)$$

and we find the results expected in the previous section for $\eta = 1$ or $\eta = 1/2$. The anisotropy of the trap can then be expressed as:

$$\varepsilon = \frac{|\omega_{y'}^2 - \omega_{x'}^2|}{\omega_{y'}^2 + \omega_{x'}^2} = \frac{\gamma\sqrt{\frac{1}{\eta} - 1}}{2 - \gamma}. \quad (2.85)$$

One has to take care here that γ implicitely depends on η, as it depends on the Rabi coupling at the bottom of the bubble Ω_0, which depends itself on η following equation (2.81).

To help interpreting these results, it is possible to relate η to the position of the holes on the bubble:

$$\eta = \frac{1}{2}\frac{(1 + \cos(\mathrm{t}))^2}{1 + \cos^2(\mathrm{t})} \quad \Rightarrow \quad \sqrt{\frac{1}{\eta} - 1} = \frac{1 - \cos(\mathrm{t})}{1 + \cos(\mathrm{t})}, \quad (2.86)$$

allowing to rewrite $\omega_{x'}$, $\omega_{y'}$:

$$\omega_{x'} = \sqrt{\frac{g}{4R}}\left[1 - \frac{\gamma}{1 + \cos(\mathrm{t})}\right]^{1/2}, \quad (2.87)$$

$$\omega_{y'} = \sqrt{\frac{g}{4R}}\left[1 - \frac{\gamma\cos(\mathrm{t})}{1+\cos(\mathrm{t})}\right]^{1/2}. \tag{2.88}$$

Along the semi-major axis of the polarization, $\omega_{x'}$ is the pendulum frequency reduced by the attraction of the holes: the correction term involves the ratio between the energy of the hole attraction $F\hbar\Omega_0$ (difference in coupling energy between the bottom and the hole) and the gravitational energy necessary to reach the hole $MgR\,[1+\cos(\mathrm{t})]$. On the other hand, for $\omega_{y'}$ the factor $\cos(\mathrm{t})$ shows that the correction can decrease *or increase* the pendulum frequency. We also see that the condition for the existence of the trapping frequencies is $\gamma < 1+\cos(\mathrm{t})$, as expected.

Finally, for a given anisotropy (i.e. given η), within this parametrization it is possible to give the values of $(\Theta,\ \Phi)$ corresponding to an arbitrary orientation of the trap ϕ (allowing us for example to dynamically rotate the trap) [125]:

$$\Theta(\eta,\phi) = \frac{1}{2}\arccos\left(2\sqrt{\eta(1-\eta)}\cos(2\phi)\right), \tag{2.89}$$

$$\Phi(\eta,\phi) = \arccos\left(2\sqrt{\eta(1-\eta)}\frac{\sin(2\phi)}{\sin(2\Theta(\eta,\phi))}\right) \tag{2.90}$$

$$= \arccos\left(\frac{2\sqrt{\eta(1-\eta)}\sin(2\phi)}{\sqrt{1-4\eta(1-\eta)\cos^2(2\phi)}}\right). \tag{2.91}$$

Chapter 3

Experimental setup: from the rubidium oven to the bubble trap.

All the experiments described here take as a starting point the RF-dressed "bubble" trap whose theoretical description has been given in detail in the previous chapter. In this chapter, I will first outline the experimental scheme that leads to the formation of an ultracold atomic gas in such a trap, and I will then describe more in detail the device that allows for controlling precisely our bubble trap – a DDS ("Direct Digital Synthesizer "), which has been modified during my PhD. Finally, I will describe the imaging setup that has been used to take experimental pictures.

The construction of our experimental setup has begun more than ten years ago now, and three PhD theses have already been written on it [86, 87, 126]; a reader wishing to have all details on the experiment should go towards these.

3.1 The experimental setup

3.1.1 Overall system

The experiment is built around three chambers placed under vacuum. The first one is a 2D MOT used as a source of pre-cooled atoms. It sends atoms to a second chamber made of steel, in which a 3D MOT is formed. These two steps happen continuously when the experiment is in standby. When an experimental sequence is launched, the atoms from the 3D MOT are transfered to a magnetic trap whose coils are placed on a mechanical translation. These coils are then displaced to bring the atoms in a third, final chamber – a glass cell, in which the cooling of atoms down to degeneracy and the subsequent experiments will happen (fig. 3.1).

The whole experiment is controlled by a script in which all successive experimental steps are described, which is then interpreted by a C++ program. Details can be found in [128]. We use 4 computers: one controls the experimental setup through analog and digital output cards from National Instruments[1], two computers control the imaging cameras and display the corresponding pictures, and one is used to analyze the pictures and generate the scripts used to control the DDS (cf 3.3).

1. Two PCI-6733 cards, one PCI-6713 and one DIO-32 card.

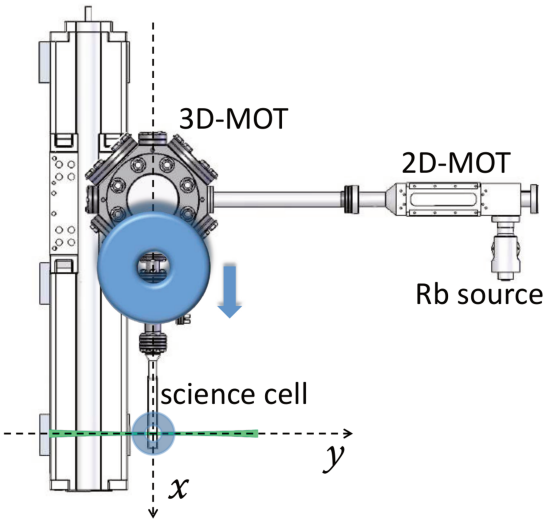

Figure 3.1 – Sketch of the experimental setup seen from above. Represented here are the vacuum chambers of the 2D MOT and the 3D MOT and the science cell. The transport coils (thick blue) can move from the MOT chamber to the science cell to transfer the atoms in a second pair of quadrupole coils (light blue), where most of the experiment happens. The notations of the "x axis" and "y axis" of the experiment are considered as a reference thoughout this manuscript. In green is the "plug" laser beam used during evaporative cooling. Figure from [127].

3.1.2 Rubidium 87

In our experiment, we work with rubidium 87 atoms. Rubidium is a soft metal, with a fusion point at 39.3 °C. Rubidium has been widely used for studying Bose condensates: it is an alkali atom with a simple electronic structure, it has collisional properties that are favorable for reaching BEC, and it has a cycling transition (D_2 line, see fig. 3.2) easily accessible with cheap lasers, which makes it the "default" atom to work with for people who are not looking for specific properties (e.g. Feshbach resonances or large spin).

3.1.3 The lasers

We use six lasers on our experiment:

- An extended cavity laser diode (NarrowDiode, from Radiant Dyes) locked on the $|^5S_{1/2}, F = 2\rangle \rightarrow |^5S_{1/2}, F = 3\rangle$ transition, used for probing the atoms and as a frequency reference for the other 780 nm lasers.
- A telecom 1560 nm laser, amplified then frequency-doubled, which gives us a high-power (2 W) 780 nm laser used for laser cooling. It has been developped in our team by Paul-Eric Pottie; more details can be found in [126].
- Two Sanyo 780 nm laser diodes on the $|^5S_{1/2}, F = 1\rangle \rightarrow |^5S_{1/2}, F = 2\rangle$ transition. One is on resonance with the transition and is used to repump the atoms in the MOT and for imaging, the second one is detuned to achieve partial repumping of the atoms during the imaging process (cf section 3.4).

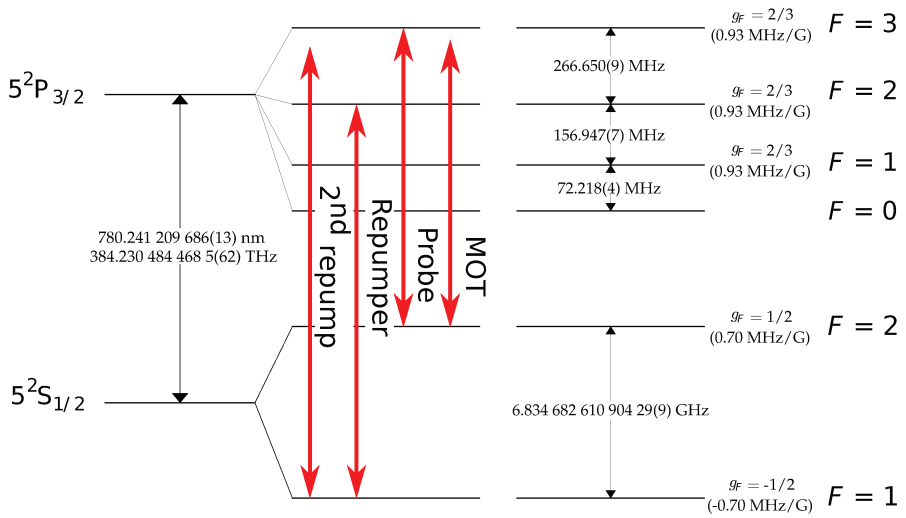

Figure 3.2 — Hyperfine structure of the ^{87}Rb D_2 transition and frequency of the 780 nm laser beams.

- Two high power green lasers at 532 nm. They are blue-detuned compared to the D_2 line, and thus repel the atoms. One is an Azur Light System 10 W laser, used to generate the plug beam (cf 3.2.3) and the stirrer (cf section 6.1.1). The second one is a Coherent Verdi 5 W laser and is used to generate a light sheet beam used to make ring-shaped trap (see part II).

3.2 Experimental sequence

3.2.1 2D + 3D MOT

The experimental sequence starts from a built-in 2D MOT, developed by the SYRTE laboratory. A cell containing rubidium is heated around 70 °C to release a rubidium vapor which is transversally cooled by two retroreflected beams in the presence of a magnetic field gradient. This creates a line of trapped atoms with a low transverse temperature. A "pushing" laser beam tuned on resonance and aligned along this line continuously sends these atoms through a differential pressure tube towards the second chamber. This system serves as an efficient source of atoms for the 3D MOT.

In this second chamber, three pairs of independent, contrapropagating beams slightly detuned from the atomic resonance cool down atoms and trap them to the center of a magnetic quadrupole field generated by a pair of coils in anti-Helmholtz configuration, realizing a 3D MOT. A repump beam mixed with the cooling beams and tuned on the $^5S_{1/2}, F = 1 \rightarrow ^5P_{3/2}, F = 2$ sends atoms which fall in the state $|^5S_{1/2}, F = 1\rangle$ back to the cycling transition. We typically load 10^9 Rb atoms in the MOT in approximately 10 s.

The 2D+3D MOT runs continuously between experimental sequences; when the sequence starts the push beam is shut down and we work with the atoms that are present in the 3D MOT at that time.

3.2.2 Magnetic transport

The first step of the sequence aims at transfering the atoms from the MOT to a quadrupole trap that can be mechanically displaced to the science cell (the coils of this quadrupole trap are the ones that are used to generate the MOT, but the trapping configuration is not the same). We start by ramping up the current in these coils to compress the MOT and increase the atomic density while increasing the detuning of the MOT beams to reduce the repulsion between atoms coming from multiple scattering events. The current in the coils is then turned off and the detuning is increased again to cool down the atoms during an optical molasses phase. At the end of this phase, the repump beam is shut down so that all atoms get depumped to the state $|^5S_{1/2}, F = 1\rangle$, which is the state with which we work in all the experiment. Finally, all beams are shut down and the current is ramped up again to generate a quadrupole magnetic trap in which atoms are loaded. We trap the atoms that are in the $|F = 1, m = -1\rangle$ state; atoms in $m = 0$ and $m = +1$ are lost.

The coils are then physically displaced over a distance of around 30 cm up to the position of the final quadrupole coils, bringing the atoms into the science cell. The current in the magnetic transport coils is then ramped down and the current in the final quadrupole coils is ramped up to transfer the atoms in this new magnetic trap, and the transport coils are sent back to their initial position. After transfer, we have around 10^8 atoms trapped, with a temperature of 150 µK.

The final steps of the experiment happen in this science cell, a glass cell manufactured by Starna with inner (outer) dimensions 10×10 (12.5×12.5) mm, under ultra-high vacuum (10^{-11} mbar).

$\mathrm{J \cdot mol^{-1} \cdot K^{-1}}$

The final quadrupole trap is realized by two conical coils placed above and below the cell, which generate a horizontal gradient $b'_0 = 1.98\,\mathrm{G \cdot cm^{-1} \cdot A^{-1}}$. The power supply we use[2] can deliver up to 110 A and 15 V, with a rise/fall time of a few milliseconds; switches allow fast shutting down of the current in the coils (around 150 µs [126], useful especially for time-of-flight imaging). The coil wire is hollow and water circulates inside to dissipate the heat in the coils.

3.2.3 The plugged quadrupole trap

Bose-Einstein condensation of rubidium requires, like for most atoms, evaporative cooling to increase the phase-space density. Using an RF knife in a magnetic trap is usually an efficient way to perform this step: shining an RF field at a given frequency on the atoms couples the different Zeeman substates and atoms get expelled from the trap if they reach resonance with the RF, enabling to eliminate atoms whose energy is too high. Such RF evaporation allows one to reduce the atomic cloud's temperature and increase the density at the center of a trap. However, in the case of a quadrupole trap, the magnetic field vanishes at the center of the trap and the atoms that arrive there get lost due to Majorana losses (cf. 2.1.1): the increase of density at the center of the trap leads to strong atom losses. This problem has been solved using various methods, for example using time averaging (TOP traps) to trap the atoms in a minimum of the *average* magnetic field while the real zero of the magnetic field stays far away from the atoms [129] or using hybrid optical-magnetic traps [23, 130, 131] where the atoms are maintained away from the place where the magnetic field vanishes by dipole beams.

2. Delta elektronika 15-100

In our experiment, we use this second approach, using a "plug" beam to expel atoms from the center of the trap [86, 127]. A 10 W, 532 nm blue-detuned beam is focused on the center of the quadrupole. It is oriented along the y axis of the experiment (cf fig. 3.1), and even though it covers the center of the trap it is slightly off-centered. This creates a unique effective potential minimum slightly away from the center, where a condensate can be trapped without suffering too much from losses.

Once this laser is on, we perform a ramp of the RF knife frequency to achieve evaporative cooling. A first evaporation ramp, going from 50 MHz to 4 MHz in 13.6 s, is performed at high magnetic field gradient: $b' = 216\,\mathrm{G}\cdot\mathrm{cm}^{-1}$ horizontally, corresponding to 110 A in the quadrupole coils; then the magnetic field gradient is reduced to $b' = 55\,\mathrm{G}\cdot\mathrm{cm}^{-1}$ to further reduce Majorana losses (the optical plug gets more efficient to expel atoms from the center). A final evaporation is then realized in 5 s, going from 2 MHz to 300 kHz, and we achieve Bose-Einstein condensation. This method allows to achieve a quasi-pure BEC with around 2×10^5 atoms, however it is more favorable for the following experiments to stop evaporation before this stage, at 350 kHz, to keep more atoms, about 5×10^5.

3.2.4 The dressed trap

Hardware presentation

On the sides of the science cell, two RF antennas generate RF fields along the x and y directions, allowing to generate an RF field with any polarization in the horizontal plane as described in section 2.3 (fig. 3.3). During my thesis, a third antenna has been placed below the cell to generate RF fields along the vertical axis; details will be given in chapter 5. A good stability of the RF phase is mandatory for achieving large lifetimes in RF-dressed traps [132]: this is obtained by using digital frequency synthetizers (DDS). We control the voltage and relative phase of each antenna; the obtained RF coupling is calibrated directly with the atoms by using RF spectroscopy so that we directly control the effective coupling felt by the trapped atoms. More details about the DDS and control of the RF are given in section 3.3.

Transfer procedure

Once the atoms are condensed, we transfer them from the plugged trap to the dressed quadrupole trap described in chapter 2. For that, we need to "dress" the atomic state adiabatically, so that the atoms stay in the *effectively* trapped state (which corresponds, once the atoms are trapped on the resonance, to a mixture of all three Zeeman substates).

In a first step, the amplitude of the RF field is ramped up far below resonance, to fullfill the adiabaticity condition (2.38) (we need to start with a large Ω, which can be achieved only through large δ since $\Omega_1 = 0$ at the beginning of the ramp). In the plugged trap, the atoms are located at a place that is resonant for RF frequency around 250 kHz; the RF field amplitude is ramped up from 0 to typically 50 kHz in 5 ms at a frequency of 175 kHz: the resonant surface is then within the plug beam and inaccessible to the atoms. Moreover, the second harmonic of the RF frequency, at $2\times175 = 350$ kHz, is beyond the resonance frequency (and corresponds to the final value of the evaporation ramp) so that the cloud is unaffected by possible harmonics that would be generated by the RF synthesizer.

The RF frequency is then ramped up with a constant amplitude[3] from its initial frequency,

3. In fact, the amplitude is not really constant: the voltage applied to the antennas keeps a constant amplitude but the antennas' admittance depends on the RF frequency. This dependence is however smooth.

below resonance, to a frequency above resonance (from 175 kHz to 770 kHz in 120 ms). During this ramp, the size of the bubble grows; the atoms reach resonance and are then "caught" by the bubble: while the bubble continues to get bigger, the potential minimum is now on the bubble.

Finally, the RF frequency is slowly ramped (up or down) to its final value (typically 0.3 to 1.2 MHz), in 175 ms. During the whole RF ramp procedure, the plug beam is slowly turned off. In the end, the potential minimum lies at the bottom of the bubble, where atoms get a pancake shape (fig. 3.3). The slow final step aims at minimizing the oscillations at the end of the transfer: from figure 3.3 we see that the atomic cloud has a lateral motion during the transfer from the plugged trap; it then has to be realized slowly enough to avoid a strong dipole motion [86]. At the end of this transfer procedure, we have typically 4 to 5×10^5 atoms trapped, with a temperature around 150 nK and a condensed fraction around 30 to 50 percent.

The position of the plug beam is very critical for both the efficiency of the evaporation in the plugged quadrupole trap and the success of the transfer procedure (it affects a lot the amplitude of the residual dipole motion). Its position is controlled by two piezoelectric actuators placed on the last mirror on the plug beam path; it is optimized every day by maximizing the number of condensed atoms we have in the dressed trap after transfer.

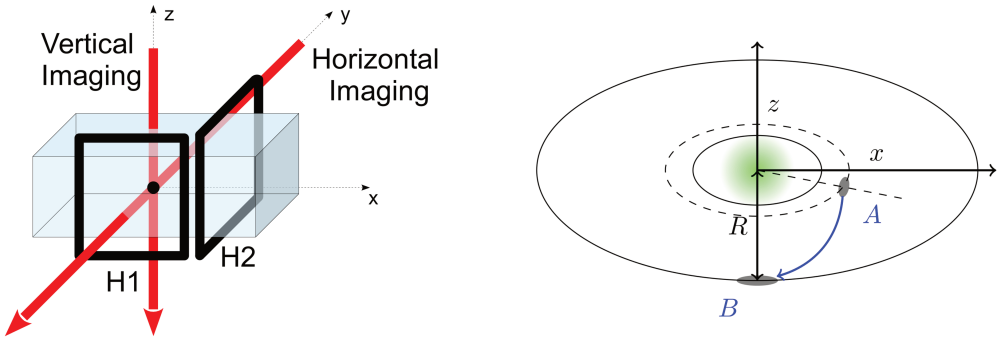

Figure 3.3 — Left: sketch of the antennas position around the glass cell. Both antennas are made of 10 loops of copper wire; they are square-shaped with 16 mm sides. Antenna H1 is placed 16.5 mm away from the atoms, its inductance and capacity are 3.83 µH and 39.2 pF; antenna H2 is placed 12.0 mm away from the atoms (it is wrapped around the cell) and its inductance and capacity are 3.22 µH and 35.0 pF [133]. One can also see both axes used to image the atoms. Right: sketch of the dressing procedure, as seen from the side. Atoms initially placed in A in the plugged quadrupole trap are caught by the growing bubble and transfered in B while the plug (in green) is turned off. Figures are taken from [86, 102].

Controlling the bubble geometry

The bubble trap is highly versatile and its parameters can be adjusted easily and dynamically (cf section 2.3):

- The radius of the bubble (typically 10 to 100 µm vertically) can be adjusted by changing the current in the coils or the RF frequency.

- The radial trapping frequencies at the bottom of the bubble (typically 20 to 50 Hz) are also controlled by the current and frequency (which modify the pendulum frequency), and slightly modified by the RF amplitude and polarization.
- The control of the RF polarization also allows us to tune the trap's horizontal anisotropy [102] (defined as $\varepsilon = |\omega_y^2 - \omega_x^2|/(\omega_y^2 + \omega_x^2)$; typically 0 to 0.5) and orientation [68].
- The vertical frequency depends strongly on the magnetic gradient and can thus be tuned easily by changing the current in the quadrupole coils. It also depends on the square root of the Rabi coupling. It can reach high values (typically 0.5 to 2 kHz), allowing to reach the quasi-2D regime [102].
- Finally, the temperature of the trapped gas can be adjusted by using an additional RF field ("RF knife") slightly detuned compared to the RF dressing frequency [100].

Even though I cited the RF amplitude as allowing to adjust the trap parameters, it has to be changed with caution since it determines the Landau-Zener loss rate in the trap [134]; even small changes can lead to prohibitive reduction of the atomic lifetime (which can, for low gradient and sufficiently high Rabi coupling, reach three minutes).

The RF knife

It can be useful to detail a little more the use of the RF knife, as its use in a dressed trap can be quite subtle. The overall idea is to apply a second, weak RF field to the trap with frequency ω_{knife}, which leads to "double dressing" [113, 135]. It leads not only to an additional dressing on the surface resonant with the knife frequency, but also to multi-photon resonances, especially at $2\omega_{\text{rf}} - \omega_{\text{knife}}$. In practice, we use a knife frequency slightly higher than ω_{rf}: $\omega_{\text{knife}} = \omega_{\text{rf}} + \delta\omega_{\text{knife}}$, with $\delta\omega_{\text{knife}} > 0$. This leads to two additional resonances at a distance $\pm\delta\omega_{\text{knife}}$ from the "main" dressing (see figure 3.4). Supposing that the Rabi coupling at the two secondary resonances is weak, this sets a depth for the trap:

$$U_{\max} = F\hbar(\omega_{\text{knife}} - \omega_{\text{rf}} - \Omega_1(\mathbf{r})). \tag{3.1}$$

This scheme therefore allows to perform RF evaporation ramps in the trap, or to set a maximal temperature to prevent heating. However, even if the Rabi coupling at the knife resonance is small, it is not necessarily homogeneous on the whole trap: in particular, the antenna generating the RF knife field is placed on the side of the trap, and the knife is therefore linearly polarized. This can lead to small anisotropic trap deformations; in particular, when the atoms are placed at the equator of the bubble (in the ring-shaped trap, see part II), the coupling vanishes at two points (see section 2.3.2), and the evaporation will not be uniform in the trap.

3.3 The new DDS

During my PhD, we decided to change the DDS used to control the dressing RF field until then [86]. This decision came from two joined needs:

- The stability of the internal clock of the microcontroller in this DDS wasn't very good, leading to jitter in the timings of the dressing sequences. This was preventing us from using the DDS to generate complex patterns; especially our new DDS allows us to rotate the atoms with the trap itself (cf 6.1.3 and 8.2.1).

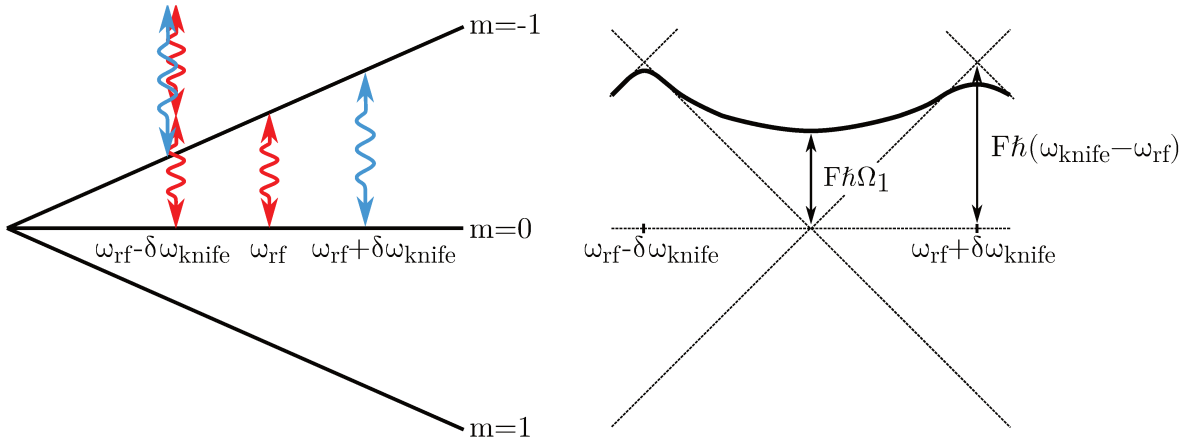

Figure 3.4 — Left: resonances in the presence of two RF frequencies, one for dressing and one for the knife. The solid lines correspond to the Zeeman substates in the quadrupole trap: two single-photon resonances happen when the frequency splitting is equal to ω_{knife} and ω_{rf}, and a three-photon transition at $2\omega_{\text{rf}} - \omega_{\text{knife}} = \omega_{\text{rf}} - \delta\omega_{\text{knife}}$. Note that other multiphoton resonances happen, but they are further away from the main resonance. Right: dressed state in which the atoms are trapped. The presence of the RF knife opens the trap on both sides of the resonance, imposing a maximal trap height. The Rabi coupling of these secondary resonances is not equal on the two sides of the transition (the coupling of the single-photon resonance is equal or larger to the coupling of the three-photon resonance [113]). Both are however much weaker than the Rabi coupling for the dressing at ω_{rf} (they are exagerated on the figure to make them visible).

- Due to misalignments effects in the RF field, we needed to put a third dressing antenna on the experiment, synchronized with the two main antennas (cf section 5.2.2). The old DDS had only two outputs and didn't allow us to do that, whereas the new one has eight parallel output and allows us to control the third antenna (and leaves us the possibility to implement many more things with the remaining outputs).

The synthesizer is home-made and has been realized in our electronics workshop. In this section, I will give the technical details about this new device and the way we control it.

3.3.1 Hardware

The structure of the DDS is presented on figure 3.5. The device is composed of three parts:

- The DDS itself (in fact, a pair of identical DDS chips[4]). It converts a 10 MHz clock signal given by an external frequency synthesizer[5] into eight (4 per DDS) analog periodic signals (sine waves with possibility of modulation, even if we use only sine outputs), phase, amplitude and frequency. The signal synthesis is achieved numerically, ensuring the continuity of the RF phase. The DDS has a 32-bit frequency resolution, 10-bit amplitude control resolution and 14-bit phase offset resolution and can operate for a clock frequency of up to 500 MHz.

4. AD9959 from Analog Devices.
5. a Stanford DS345, also used to perform spectroscopy in the trap.

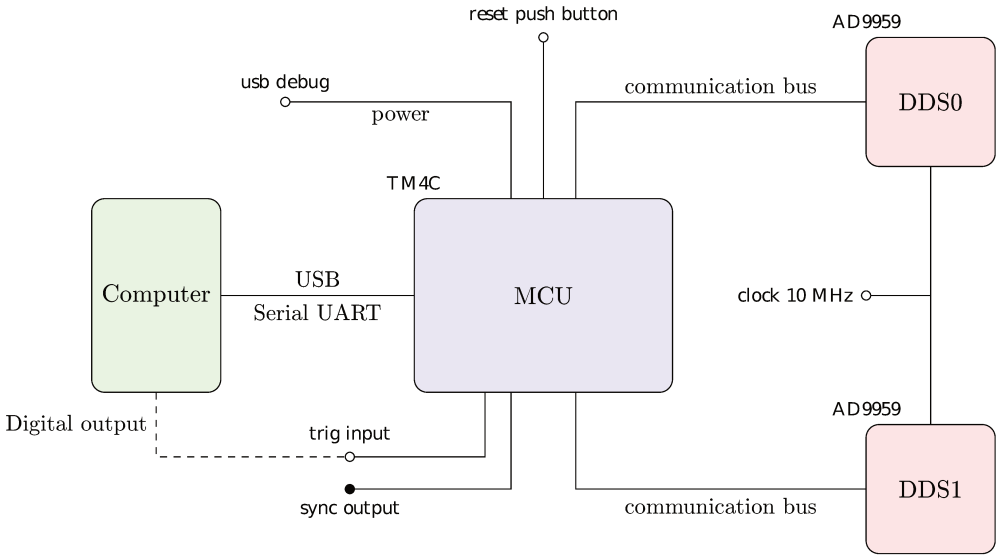

Figure 3.5 – General layout of the DDS system, see text (figure from [136]).

- A microcontroller unit (MCU)[6], used to control the DDS. Operating the DDS chip itself is beyond capabilities of the computer controlling the experiment[7]; instead the MCU is programmed in advance using the computer and triggered during the experimental sequence. It has an 80 MHz update rate, allowing update of the DDS outputs with a refresh rate of a few microseconds depending on the output which is modified (phase, frequency, amplitude).

- A box of amplifiers[8] (not represented in the figure) is used to transform the output signal of the DDS into a usable signal with sufficient amplitude, which is then sent to the dressing antennas. All the inputs of the amplifier are equipped with an individual switch[9], allowing fast switching of each RF signal. The amplifiers have a fixed gain; adjusting the gain can be done by putting external damper components downstream. Splitting the DDS/MCU part from the amplifier part allows future update of both parts independently.

We noticed that the switches implemented before the amplifiers were causing large spikes (several volts on a few milliseconds) when commuted to allow RF passing through (i.e. closed), even with an input signal set to zero. This comes, a priori, from the fact that the switches are designed for fast commutation, typically aroung 1 MHz-1 GHz (tests realized for regular, fast commutation show no spikes). In our case, they can stay opened during several tens of seconds; it is possible that we have accumulation of static electricity during this time that get released when commuting. It is necessary to take care about it when turning on the RF, for such spikes can lead to disastrous effects when sent to the atoms. Specifically, it means that

6. TM4C123GH6PMI chip from Texas Instrument, mounted onto a TM4C123G launchpad evaluation board.
7. Some digital boards can allow such operation [137], but they are expensive, more difficult to implement and have a lower update rate.
8. Gali-84+ from Mini-Circuits.
9. RSW-2-25P from Mini-Circuits.

we close the switches a few seconds before turning on the RF, during the evaporation ramp, while the atoms are still hot and not too much sensitive.

3.3.2 Control of the DDS

The DDS is controlled by the computer through two connections. The first one, a USB connection, allows us to transfer instructions from the computer to the microcontroller. However, it is slow and unable to give precise control during experimental sequences. It is therefore supported by a digital TTL command controlled by one of the digital outputs of the computer: the instructions are loaded into the MCU through USB, then triggered by the TTL.

The MCU has two modes of operation:

- "Ramp" mode: we specify the desired output states at specific times and the corresponding time steps, and the MCU computes the whole ramp from these points. This is used, for example, to generate the dressing ramps used to transfer the atoms from the plugged quadrupole trap to the bubble trap.
- "Pattern" mode: this mode allows to perform more complex tasks. A file containing *all* the successive states the output has to take and the corresponding time steps is loaded into the MCU, which will then read and apply them. This allows to perform arbitrary RF patterns (within the limits of the microcontroller internal memory - around 25 kB), it is used for example to rotate the bubble.

In both cases, we use MATLAB programs to compute and write the scripts that will be send to the DDS during experimental sequences. In one sequence, we can use up to 4 ramps and 4 patterns; however the MCU memory can only keep one of each in memory. Using several ramps or several patterns requires to load them *during* the sequence, using USB communication. This can take up to several hundreds of milliseconds (depending on the amount of information to transfer) with a jitter in the communication duration of a few milliseconds: it has to happen during non-critical parts of the experimental sequence (e.g. waiting times).

3.3.3 Calibration of the DDS

The command of the DDS is digital: the control of the RF amplitude is done by choosing a value between 0 and 1024 (the DDS has a 10-bit amplitude resolution), which leads to a certain power level at the output of the DDS; the signal is then amplified and sent to antennas with a certain impedance (which depends on the RF frequency – this dependence can modify the relative phase between the antennas). We therefore need a calibration to be able to translate the desired effect on the atoms into the instruction we have to give to the microcontroller.

Spectroscopy in the dressed trap

For a given configuration of the dressed trap, it is possible to measure the Rabi coupling at the position of the atoms by performing spectroscopy in the trap. By shining a weak RF field at a frequency ω_{probe}, it is possible to couple the different local *dressed* states $|m\rangle_{\theta(\mathbf{r})}$ (cf section 2.2), which are separated by $|\Omega_1(\mathbf{r})|$. This coupling leads to losses from the trap: the measurement of $|\Omega_1(\mathbf{r})|$ at the position of the atoms (i.e. Ω_0 in relevant experimental cases) is done by finding the probe frequency that maximizes the losses. It is usually possible to measure Ω_0 within a 0.5 kHz precision. The optimal precision is achieved using very cold gases (to minimize Doppler broadening), very weak probe intensities (to minimize power

broadening) and adjusting the probing duration to maximize contrast in the signal without clipping the signal (i.e. avoiding to remove all atoms from the trap). An example of such a spectroscopy measurement can be found on figure 3.6.

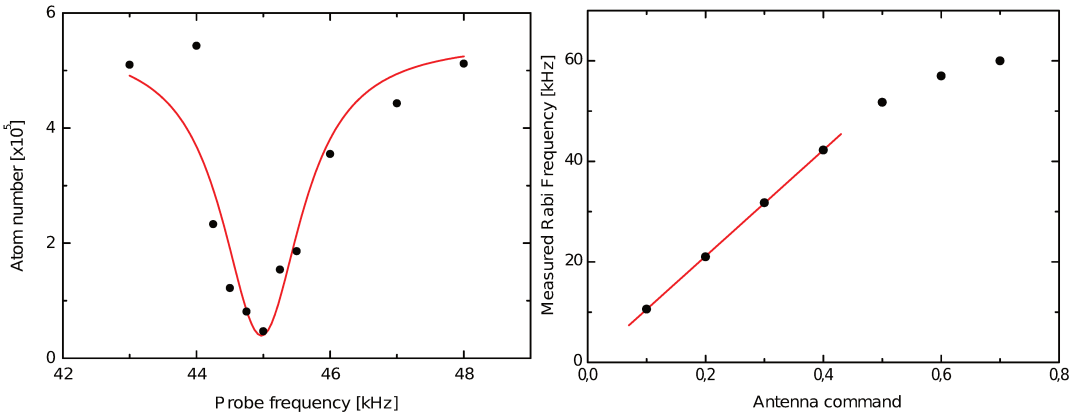

Figure 3.6 — Left: Example of a spectroscopy line measured at the bottom of the bubble; the corresponding Rabi coupling is 45.00(25) kHz. The red curve shows a Lorentzian fit of the data; however the line shape is often asymmetric and it is most of the time simpler to locate precisely the resonance by taking close points around the maximum of absorption rather than measuring the whole line. Right: Example of the calibration of H1 antenna's response at 1.2 MHz; the antenna's command is a value between 0 and 1. For low command values, the measured coupling increases linearly with the command; for high values non-linearities in the amplifier lead to a reduction of the obtained Rabi frequency. The red line shows the fit of the linear response. The slope is 105.8(4) kHz: at this dressing frequency (i.e. 1.2 MHz), the resolution on the antenna's amplitude control (i.e. the maximal achievable precision on the obtained Rabi coupling) is then 105.8/1024 = 103.3(4) Hz.

Calibration of the antennas

The calibration of the antennas is achieved by realizing dressed traps with only one antenna for different dressing amplitudes. Using only one antenna leads to a linear polarization configuration, where the maximal coupling is reached at the bottom (i.e. where the atoms are); RF spectroscopy then allows to measure the maximal achievable Rabi coupling for a given amplitude, and to calibrate the command/coupling relationship. It is better to make such a calibration at high magnetic gradient, to reduce the displacement of atoms due to gravity (which causes a shift of the measured resonance). An example of such a calibration is presented on figure 3.6.

Once such a calibration is done, it is possible to directly command the antennas in Rabi coupling units and ask for the desired result. This also allows to compute the resolution we can achieve on the final coupling (typically 100 to 200 Hz on each antenna). Such a calibration has to be done for each antenna, for all values of the dressing frequency at which we want to work.

3.4 Imaging the atomic cloud

Let us finally discuss our main diagnostic tool: the production of pictures from the atomic clouds. There are three main techniques that are used to image ultracold atoms systems: the fluorescence imaging, the phase contrast imaging, or the absorption imaging. In our experiment, we use the third one. The overall idea is to shine onto the atoms a resonant probe beam, and compare the corresponding picture to a picture of the probe in the absence of the atoms: in this way, we can measure the atomic density from the shade that the cloud creates (see figure 3.7). As the atoms exchange many photons during the process, the cloud however heats up a lot and gets destroyed; this technique is therefore destructive and a new cloud has to be prepared for each experimental picture we want to take.

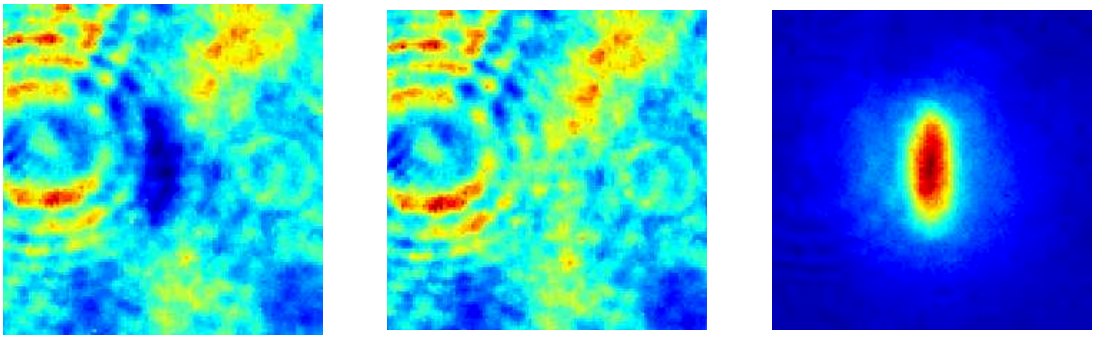

Figure 3.7 – Left: picture of the probe beam in the presence of the atoms. The light being resonant, the atoms scatter photons from the beam, creating a shade on the picture. By comparing this picture with the picture of the probe taken in the absence of the atoms (center), one can reconstruct the atomic density and generate a picture of the atoms (right). The quality of the final picture is extremely sensitive to the good alignment of the probe beam between both primary pictures: for that reason, we use a fringe reduction algoritm to compute the probe "ideal" picture [138].

We have the possibility to make a picture of the atoms in the trap (*in situ* pictures) or after a time-of-flight expansion (TOF): the trap is turned off, and the atoms fall and expand freely during a certain duration before the picture gets taken. In the first case, we measure the space distrubution; in the second, we can measure the momentum distribution (if the TOF is long enough to allow neglecting the initial size of the cloud). Both provide complementary diagnostic tools; we can note that the in situ imaging of the cloud requires to use a high intensity probe: the consequences will be detailed in the next section. However, the measured distribution is integrated along the imaging axis: we thus have two imaging systems that allow us to image the atoms from above (integrated along z) and from the side (integrated along x) – these axes are presented on figure 3.3.

3.4.1 High intensity absorption imaging

The description of the interaction of the probe with the atoms can be quite complex if we take into account all possible atomic levels, but quite simple if we consider only a two-level atom, through the Bloch equations. We image the atoms using a resonant laser on the

$F = 2 \rightarrow F = 3$ transition, and considering that these are the only levels that get populated significantly the two-level system seems a relevant approach. Let us note ω_{at} the pulsation of the transition, λ_{at} the corresponding wavelength, and Γ its width; the absorption cross section and saturation intensity read respectively:

$$\sigma_0 = \frac{3\lambda_{\text{at}}^2}{2\pi}; \qquad I_{\text{sat}} = \frac{\hbar\omega_{\text{at}}^3\Gamma}{12\pi c^2}. \tag{3.2}$$

Supposing that the probe propagates along the z axis, the absorption of the probe beam while it crosses through the cloud will behave as:

$$\frac{\mathrm{d}I}{\mathrm{d}z} = -n(\mathbf{r})\sigma(I)I, \tag{3.3}$$

where I is the probe intensity and $\sigma(I)$ the real cross-section, which depends on the probe intensity. In practice, we measure the atomic density integrated along the beam propagation axis: $n(x,y) = \int n(\mathbf{r})dz$. In the case of non-saturating imaging ($I \ll I_{\text{sat}}$), we find the usual Beer-Lambert absorption law, and $n(x,y)$ can be deduced from the intensity of the probe after absorption by the atoms I_f and the initial intensity I_i following:

$$\sigma_0 n(x,y) = -\ln\left[\frac{I_f(x,y)}{I_i(x,y)}\right]. \tag{3.4}$$

The quantity $\sigma n(x,y) \equiv od(x,y)$ is called the *optical density*, and it is what is measured in practice.

When we try to image dense clouds – for example to image the in situ density profile, working with low probe intensities can lead to a complete absorption of the beam profile (leading to infinite densities when using equation (3.4)), to collective effects like multiple scattering, or to systematic errors in the measured densities because the atoms in front of the probe absorb most of the probe photons, and the atoms in the back of the cloud are therefore exposed to lower intensities (leading to a z dependence of I in equation (3.3)). To image such clouds, there are two strategies: either repump a small fraction of the atoms in the scattering state $F = 2$, artificially reducing the optical density in this way, or use high probe intensities in order to saturate the atomic transitions. In this latter case, the cross section of the atoms writes:

$$\sigma(I) = \frac{\sigma_0}{\alpha^* + I/I_{sat}}, \tag{3.5}$$

where α^* is a dimensionless correction parameter that is used to take into account the deviation from the ideal two-level system due for example to the polarization of the imaging beam or the presence of other levels. It corresponds to considering an *effective* absorption intensity $\alpha^* I_{\text{sat}}$ instead of its ideal value [139]. In this case, the optical density reads:

$$\sigma_0 n(x,y) = -\alpha^* \ln\left[\frac{I_f(x,y)}{I_i(x,y)}\right] + \frac{I_i(x,y) - I_f(x,y)}{I_{\text{sat}}} \tag{3.6}$$

$$\equiv -\alpha^* d_{\log} + d_{\text{diff}}. \tag{3.7}$$

The first term corresponds to the low-intensity limit (i.e. the Beer-Lambert law); the second term to the high-intensity limit: if the atomic transition is completely saturated, each atom absorbs photons at a rate $\Gamma/2$, regardless of the beam intensity, and the atomic density is thus directly proportional to the number of "missing photons".

The parameter α^* is obtained experimentally, by calibrating the imaging system. A first method to calibrate this parameter has been developed by G. Reinaudi [139], and later extended by L. Chomaz [140]. In this latter approach, the parameter α^* is allowed to depend on the optical density of the cloud, to correct for possible collective effects. We used this method in our experiment, and observed a weak linear dependence of α^* with the optical density: $\alpha^*(od) = \alpha_0 + \alpha_s od$, with $\alpha_0 = 1.89$ and $\alpha_s = 0.39$ (the details about this calibration can be found in [87]). In this case, the atomic density can finally be computed through the relation:

$$\sigma_0 n = \frac{\alpha_0 d_{\log} + d_{\text{diff}}}{1 - \alpha_s d_{\log}}. \tag{3.8}$$

Finally, one can note that specific care about the probe pulse intensity and duration has to be taken when working with high intensity probe beams: indeed, when the atoms exchange many photons, they can get accelerated and get out of resonance, or get depumped in $F = 1$, and a too long probe pulse leads to a systematic underestimation of the atom number, as the number of atoms able to scatter photons decreases with time. The details about the choice of the probe parameters can be found in appendix B. One has also to take care that high intensity absorption imaging can amplify parasit fringes in the image with respect to its low-intensity counterpart. Indeed, while a modulation of the probe intensity imprinted on the beam after it interacts with the atoms will be washed out in the logarithmic term of the optical density, it will stay in the differential term. A weak interference effect on the camera, for example, can be highly detrimental for very high intensity pictures while images taken with a lower probe intensity will be less affected.

3.4.2 Experimental setup

Imaging along the horizontal axis

To perform our horizontal images, we use a collimated probe beam with a 2.7 mm waist. After the atoms, it passes through a single telescope with a total magnification $G = 2.17$, and then goes onto a iXon 885D EMCCD camera, from Andor. It has a 1004×1002 pixel matrix, with a 8 mm pixel size. A quarter waveplate ensures that the imaging beam is circularly polarized, and a magnetic field aligned with the imaging axis is turned on during the probe pulse to polarize the atoms. A 532 nm polarizing beamsplitter is placed after the cell to deflect the plug beam that is also aligned along this axis and avoids to focus the 10 W beam onto the camera (while letting the 780 nm light through), and an interferential filter prevents any green light to reach the camera. Since the experiments are done with the atoms in the $F = 1$ state, a repumper beam is used to bring the atoms back to $F = 2$ before sending the probe pulse (it is locked on resonance with the $F = 1 \rightarrow F = 2$ transition, see figure 3.2). We use this setup to image the clouds after a long time-of-flight (typically 15 to 25 ms), for example to measure the atomic temperature and optimize the cooling of the atomic cloud.

Imaging along the vertical axis

The vertical imaging setup is made of a pair of telescopes providing a magnification around 8. We use a Luca-R EMCCD from Andor, with a 1004×1002 pixel matrix and a 8 mm pixel size. The resolution of the system is 4 µm, allowing us to perform precise profile measurements of in-trap clouds. The whole imaging setup (camera + telescopes) is mounted on a three-axis micrometric translation; this allows, in particular, to adjust the vertical focus plane. The

depth of focus of the system is approximately 70 µm, comparable or smaller than the vertical radius of the bubble trap: for example, imaging a cloud at the bottom of the bubble or imaging a ring-shaped gas at the equator of the bubble (see part II) requires to shift the position of the system; this also allows us to image atomic clouds from above after a time-of-flight expansion. Similarly to the horizontal imaging, we use a collimated probe beam with a 0.7 mm waist, circularly polarized using a quarter waveplate, and we use a vertically aligned magnetic field to polarize the atoms during the imaging process. Even with our high-intensity aborption procedure, the density of the cloud can be too large for a correct imaging. To avoid this problem, we use a second repumper beam that is far detuned from the $F = 1 \rightarrow F = 2$ transition (typically 250 MHz away, for a linewidth around 6 MHz), that allows us to repump only a fraction of the cloud. In this way, we can image a cloud with the same profile, with only a multiplicative factor on the atom number (which can be measured by comparing with the horizontal imaging). Using a far-detuned repumper is necessary to achieve a uniform repumping: indeed, the photons of a repumper on resonance would be directly absorbed by the first encountered atoms, and rempump in this way only the front side of the cloud and not its back.

3.4.3 Stern-Gerlach procedure

Shutting down the trap to perform a time-of-flight expansion can require some caution when working with RF-dressed atoms. Indeed, when the atoms are in a dressed trap, their state is a mixture of the different Zeeman substates (see 2.2.1). When the RF is switched off, the atomic state will get projected along the eigenstates of the local *bare* magnetic field, leading to the separation of the atomic cloud into three clouds in the $m = -1, 0, 1$ Zeeman substates. Therefore, any stray field gradient present while the trap is switched (for example due to residual eddy currents) will accelerate the $m = 1$ and the $m = -1$ clouds along opposite directions. After a long time-of-flight – we usually use $dt_{\mathrm{TOF}} = 23$ ms, even a small acceleration during the switch-off can lead to a small separation of these three clouds, with a separation that can be comparable to the cloud's size. When working with high currents in the quadrupole trap, we usually see that at the end of the time-of-flight there are three clouds that overlap (see figure 3.8). To avoid this effect, one can keep on purpose the magnetic gradient on while the RF is switched off: the $m = 1$ and $m = -1$ clouds will then be strongly accelerated, and after TOF the three clouds completely separate: we can then image precisely the $m = 0$ cloud, that has been left unaffected by the gradient.

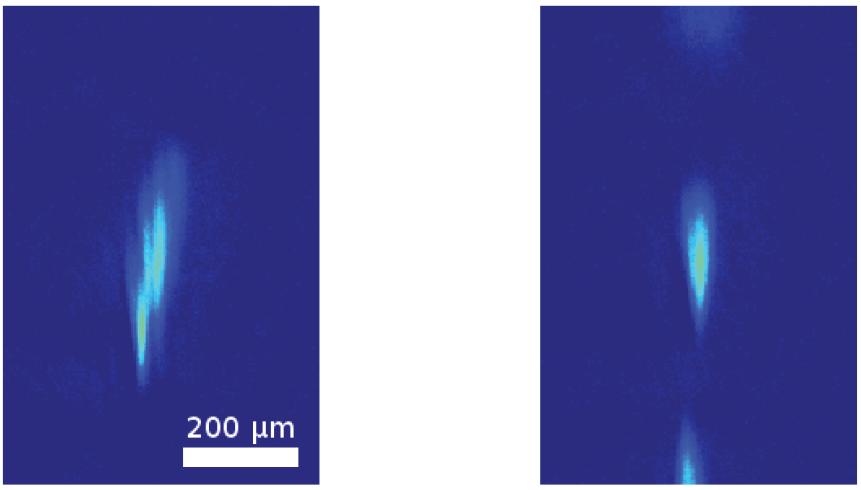

Figure 3.8 — Left: Picture of an atomic cloud produced in the dressed trap at high gradient ($218\,\mathrm{G}\cdot\mathrm{cm}^{-1}$ horizontally) and 1.2 MHz dressing frequency, taken after a 23 ms time-of-flight and observed with the horizontal imaging setup. We see three clouds overlapping, corresponding to the three $m = -1, 0, 1$ Zeeman substates (see text). Right: picture of a cloud produced in identical conditions, except that the magnetic gradient was left on during the first 0.1 ms of the TOF expansion: the $m = 0$ state is unaffected, while the $+1$ and -1 states were expelled (they still can be seen on the edges of the picture).

Part II

Ultracold atoms in a ring-shaped trap

Introduction

Superfluidity implies rotational properties that are very different from those of a conventional fluid, as described in chapter 1, and a superfluid with a ring geometry is an interesting system as it can bear rotation without necessiting singularities (i.e. vortices) to be present in the bulk of the fluid; the Feynman-Onsager criterion (1.34) here remarquably implies that the circulation of the flow along the ring is quantized. The ring geometry also allows to fully exploit the inviscid character of the superfluid flow, since a superfluid can flow within a ring trap in principle indefinitely (in practice, for experimentally accessible dilute superfluids[10] the lifetime of the flow will be limited by the lifetime of the trapped atoms).

Proposals for realizing ring geometries for ultracold atoms came soon after the experimental achievement of Bose-Einstein condensation. We can distinguish two kinds of proposals: one aims at realizing atom interferometry based on the Sagnac effect, and relies on large size traps (ring radius of typically hundreds of micrometers) [111, 141, 142]. The ring is then thought as an "atomic waveguide" in which small atomic wavepackets will evolve: a large radius allows to maximize the interferometric sensitivity but having a continuous superfluid gas in the whole trap is then challenging. The second approach aims at studying superfluidity in the presence of rotation as described previously, with traps small enough to allow reaching condensation in the whole system [57–59].

In this second approach, the first ring-shaped BEC and the first observation of a persistent flow were achieved in the W.D. Phillips group in 2007 [57]; a few years later the same group (now led by G.K. Campbell), as well as the Hadzibabic group, studied the flow quantization [58,143]; they also studied intensively the effect of a weak barrier present in the ring [144–147] and demonstrated the hysteretic behavior of the superfluid flow [59]. More generally, there is now a field of research aiming at realizing "atomtronic" circuits, studying atomic transport properties in a way analogous to the transport of electrons in electronic circuits, in which ring-shaped traps completely find their place, for example trying to realize atomic equivalent of SQUIDs[11] [72, 73, 148].

Finally, we can also mention that the ring geometry was used to perform quantum simulation, trying to simulate for example astrophysical systems: the Dalibard group studied in this way the Kibble-Zurek effect [71, 149] as originally proposed by W. Zurek [70], and the Campbell group recently studied the supersonic expansion of a quantum system [150] in analogy with the universe expansion.

10. as opposed to dense superfluids, i.e. superfluid helium. The dilute character corresponds to $\sqrt{na^3} \ll 1$.
11. Superconducting QUantum Interference Devices.

A significant part of my work was dedicated to the experimental realization of a ring trap suitable for studying superfluidity in an annular geometry, and this is what I will present in this second part. This part is divided into three chapters: chapter 4 will present the theory of superfluid flow in ring traps and the interest of such a geometry, and then present the method we to use to make the ring trap. Chapter 5 will detail the realization of the trap. An initial version of it had been built by the previous PhD student who worked on the experiment, Camilla de Rossi [87], and my contribution consisted in the improvement of this setup. Finally, chapter 6 will present the production and dectection of a superfluid flow in the annular gas.

Chapter 4

A ring trap for ultracold atoms: how and why

This chapter aims at laying down the theoretical background that will be useful for understanding this part of my thesis. It will be divided into two sections: in a first section, I will present the general theory of ring-shaped superfluids and superfluid flow. The second section will then detail the principle and characteristics of the method we use to obtain a ring-shaped BEC.

4.1 Superfluidity in ring traps

4.1.1 1D, single atom description

I will start with a simple description of a single atom[1] in a ring trap with radius r_0, considering only a 1D case (i.e. a "wire" ring), as described in [151]: the position of the atom is defined only by its azimuthal angle ϕ and the atomic state will then be written as $\psi(\phi)$. As the ring is closed on itself, ψ is periodic with period 2π: $\psi(\phi + 2\pi) = \psi(\phi)$.

Considering a constant potential along the ring, the hamiltonian only contains kinetic energy and writes:

$$\hat{H} = -\frac{\hbar^2\nabla^2}{2M} = -\frac{\hbar^2}{2Mr_0^2}\frac{\mathrm{d}^2}{\mathrm{d}\phi^2}; \tag{4.1}$$

its eigenstates and eigenenergies are then:

$$\psi_\ell(\phi) = \frac{1}{\sqrt{2\pi r_0}}e^{i\ell\phi}, \qquad E_\ell = \frac{\hbar^2}{2Mr_0^2}\ell^2. \tag{4.2}$$

These states correspond to a phase winding of $\ell \times 2\pi$ along the ring, and thus verify the quantization of flow circulation (1.34). From the eigenstates, we can deduce the angular velocity of the flow in the ring. The local velocity reads from (1.31):

$$\mathbf{v}(\phi) = \frac{\hbar}{M}\boldsymbol{\nabla}(\ell\phi) = \frac{\hbar}{Mr_0}\ell\mathbf{e}_\phi, \tag{4.3}$$

1. This also describes a pure, non-interacting BEC.

and the angular velocity for state ℓ is therefore:

$$\Omega_\ell = \ell \times \frac{\hbar}{Mr_0^2} \tag{4.4}$$

$$= \ell \times \Omega_q. \tag{4.5}$$

We see that the rotation frequency is quantized, with rotational quantum $\Omega_q = \hbar/Mr_0^2$. Having the whole cloud rotating at Ω_ℓ corresponds to an angular momentum $\ell\hbar$ per atom.

Due to this quantization, we can guess that if the gas undergoes forced rotation at a frequency $n\Omega_q$, the corresponding ground state will be the $\ell = n$ state. But then, what happens if the excitation happens somewhere between two quanta?

For a potential rotating at an angular speed Ω_{rot}, it is useful to see what happens in the rotating frame. This can be computed by adding to the hamiltonian the term:

$$-\Omega_{\text{rot}} L_z = i\hbar\Omega_{\text{rot}} \frac{\mathrm{d}}{\mathrm{d}\phi}, \tag{4.6}$$

and we can then write it as:

$$\hat{\tilde{H}} = \frac{\hbar^2}{2Mr_0^2}\left(i\frac{\mathrm{d}}{\mathrm{d}\phi} + \frac{\Omega_{\text{rot}}}{\Omega_q}\right)^2 - \frac{1}{2}M\Omega_{\text{rot}}^2 r_0^2. \tag{4.7}$$

The eigenstates of this new hamiltonian are the same as in the non-rotating state (given by (4.2)), but their energies now write:

$$E_\ell(\Omega_{\text{rot}}) = \frac{\hbar^2}{2Mr_0^2}\left(\ell - \frac{\Omega_{\text{rot}}}{\Omega_q}\right)^2 - \frac{1}{2}M\Omega_{\text{rot}}^2 r_0^2 \tag{4.8}$$

$$= \frac{\hbar^2}{2Mr_0^2}\left(\ell^2 - 2\ell\frac{\Omega_{\text{rot}}}{\Omega_q}\right) = \frac{\hbar\Omega_q}{2}\left(\ell^2 - 2\ell\frac{\Omega_{\text{rot}}}{\Omega_q}\right). \tag{4.9}$$

These energies are shown on figure 4.1 (left). We see that the state with the lowest energy changes every Ω_q: for a potential rotating between $-\Omega_q/2$ and $\Omega_q/2$, the ground state will be $\ell = 0$, which is the state corresponding to the absence of rotation; for a rotation between $\Omega_q/2$ and $3\Omega_q/2$, it will be $\ell = 1$, rotating at Ω_q, etc. In other words, the ground state is the state n for which $n\Omega_q$ is the closest to Ω. Interestingly, it means that starting from a ring at rest, an excitation with angular velocity $|\Omega_{\text{rot}}| < \Omega_q/2$ will leave the atomic state into the non-rotating state, reminiscent of the critical velocity of a superfluid.

The last term in equation (4.7) corresponds to the centrifugal energy. It is uniform on the whole cloud and therefore doesn't depend on the state ℓ; we can thus remove it by an appropriate change in the energy reference. The energy of state ℓ then simply becomes:

$$E_\ell(\Omega_{\text{rot}}) = \frac{\hbar\Omega_q}{2}\left(\ell - \frac{\Omega_{\text{rot}}}{\Omega_q}\right)^2. \tag{4.10}$$

We then see that the relevant energy spectrum, plotted on figure 4.1 (right), is in fact periodic with respect to Ω_{rot}, with periodicity Ω_q: $E_{\ell+n}(\Omega_{\text{rot}} + n\Omega_q) = E_\ell(\Omega_{\text{rot}})$.

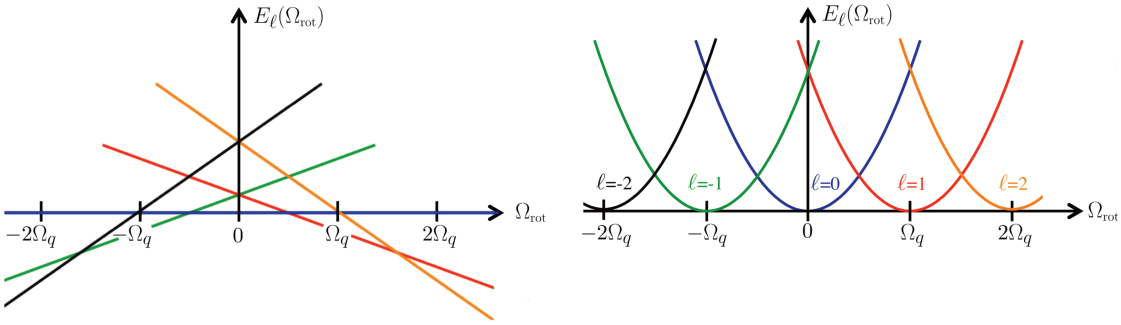

Figure 4.1 — Left: energy of the different states in the ring depending on the rotation frequency $\Omega_{\rm rot}$. The ground state changes every Ω_q. For $|\Omega_{\rm rot}| < \Omega_q/2$, the ground state is not rotating. Right: same energy spectrum when we discard the constant offset energy corresponding to the centrifugal term. We see that the relevant energy spectrum is in fact periodic. Figure adapted from [151].

4.1.2 Transition between states and persistent flow

The energy spectrum presented above is interesting as it shows the discrete circulation levels in the ring and gives their separation. However, it doesn't tell anything about the (meta)stability of the flow, because it doesn't describe what is probably the most interesting part of the physics in this system: the transition between states.

Indeed, changing the lowest-energy state doesn't mean that the system will follow: there is no simple way to continuously deform a phase winding ℓ_1 into a phase winding $\ell_2 \neq \ell_1$, and the states will have a "topological" protection that prevents change of state: a *phase slip* is required to allow transition between states. The mechanisms that allow such phase slips come with energetic barriers that can very significantly displace the threshold frequency for which the transition between states will happen. This makes the superfluid flow *metastable*, and leads to an hysteretic behavior [59, 152].

In all the experiments realized up to now, the system is not unidimensional but 2D or 3D, allowing the existence of vortices within the bulk; the role they play in the transition between states is crucial: a vortex crossing the annulus will generate a 2π phase jump in the ring (see figure 4.2). From the state of the art, we can typically distinguish two kinds of experiments and behaviors:

- The ring can be set into rotation by adding a *local* rotating potential, for example a blue-detuned beam piercing or reducing locally the atomic density [144, 145]. In this case, the local modification of the potential makes it favorable for something to happen there; especially in the case of a blue-detuned potential, the density is locally lowered and the mechanism for creating or dissipating flow seems to involve formation or breaking of a vortex-antivortex pair at this place [153, 154].

- The rotation can come from rotation of the *global* potential. This includes the interesting case of superfluid flow rotating in a static ring [58], as well as the case of a static annular gas evolving in a rotating potential, where the gas will be set into rotation due to potential rugosity. In this case, the dissipation will involve more global mechanisms like collective modes (the phase slip coming from an instability of such a mode). Dubessy

et al. [155] showed that the easiest modes to excite should be surface waves at the edges of the ring and showed good agreement with experiment [58] concerning the stability of the flow.

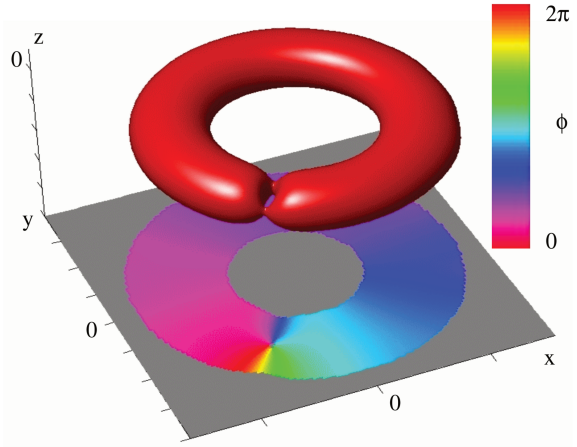

Figure 4.2 — Iso-density surface and phase profile of a ring-shaped BEC with a vortex present in the bulk. A loop along the ring enclosing the vortex ("outer" loop on the figure) shows a 2π phase winding, while a loop along the ring that doesn't enclose it ("inner" loop) has no overall phase winding. If the vortex crosses the annulus to reach the center, the final circulation will be $\ell = 1$, if it crosses it towards the outer edge, it will be $\ell = 0$. Vortices thus allow phase slips by creating a singularity within the gas. Figure taken from [156].

4.1.3 Measurement of superflow

Studying superfluid flow requires the ability to detect and measure it. The first observation of superflow was based on a "self-interference" method [57]: the ring potential is switched off and the atoms expand freely during a time-of-flight; it spreads and atoms coming from different places of the ring interfere together in the center. If the phase is uniform in the ring, these interferences are constructive and a peak is visible after TOF. If there is flow within the ring, there is also a $\ell \times 2\pi$ phase winding and these interferences are then destructive: a hole will remain in the center of the gas, and the size of the hole will provide a measurement of $|\ell|$.

This can be understood quite intuituitively from the 1D model described previously: the atomic density after a time-of-flight, if this one is long enough, corresponds to the momentum distribution of the atoms, i.e. to the square of the Fourier transform of the wavefunction. From equation (4.2), we can write the momentum-space wavefunction along an arbitrary axis $\mathbf{e}_x$ belonging to the ring plane:

$$\phi_\ell(\mathbf{p} = p\mathbf{e}_x) = \int \frac{dr\ rd\phi\ dz}{(2\pi\hbar)^{3/2}} \frac{1}{\sqrt{2\pi r_0}} e^{i(\ell\phi - \mathbf{r}\cdot\mathbf{p})} \delta(r = r_0, \phi, z) \tag{4.11}$$

$$\propto \frac{1}{2\pi} \int_{-\pi}^{\pi} d\phi e^{i(\ell\phi - r_0 p \sin\phi)} = J_\ell(r_0 p). \tag{4.12}$$

The momentum-space wavefunction corresponding to the state ℓ thus has the shape of a Bessel function of order ℓ, with a central peak for $\ell = 0$ and a central node for $\ell \neq 0$. The Bessel functions of order 0,1,2, as well as their squares (corresponding to the momentum distribution of the atoms) are plotted on figure 4.3. For $\ell \neq 0$, we see the presence of a node for $p = 0$, but also that the position of the maximum increases with ℓ.

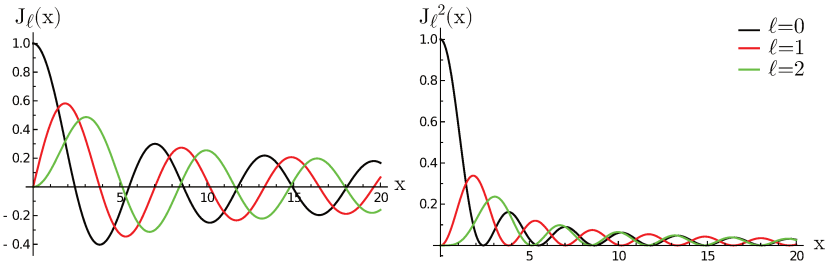

Figure 4.3 — Plot of the three first orders of the Bessel function (left) and their square (right)

Of course, in the three-dimensional case and in the presence of interactions things are not so simple, and in practice it is difficult to achieve time-of-flight expansions long enough to completely neglect the initial position distibution: a precise description of the density profile after time-of-flight requires Gross-Pitaevkii simulations [143], but this simple model already allows to get a good idea of what happens. This method has been the most used for superflow dectection and measurement; it was used for example by Moulder *et al.* to study the decay from a flow level to another, in a beautiful demonstration of both quantization and metastability of flow [58] (see figure 4.4).

Two other methods recently appeared: one also relies on interferences, this time between the ring and a phase reference, generating spiral patterns. This method allows one to detect the sign of the corcilation in addition to its absolute value [71, 146]. The second relies on the time evolution of sound standing waves in the ring, as the presence of a flow breaks the symmetry between waves propagating clockwise or counterclockwise along the ring [157].

4.2 Description of our trap

Let us now describe the principle we use to realize a ring trap for ultracold atoms. It was proposed soon after the first realization of a dressed trap [106]; a first experimental realization was achieved for thermal atoms two years later [107], but was never used to manipulate BECs. The idea is to confine the atoms at the intersection between a bubble, obtained through RF-dressing (as described in chapter 2), and a plane, obtained through a far-detuned laser beam generating vertical confinement (see figure 4.5). This confinement can in principle be obtained by either a vertical blue-detuned standing wave, as proposed initially [106] (the atoms are then confined between two intensity maxima; a beautiful realization of such a setup is presented in [158]), a red-detuned light sheet beam (never used for hybrid optical/RF traps but used for example in [58,146]), or a pair of blue-detuned light sheets (like in [71,107]). It is this last method that we use on our experimental setup.

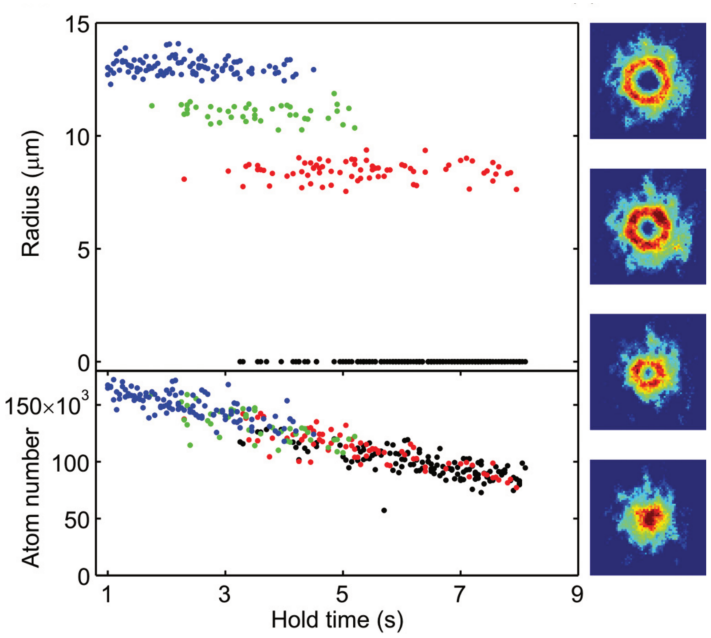

Figure 4.4 — Measurement of the evolution of superfluid flow in a ring with time, realized in the group of Z. Hadzibabic [58]. Left, top: size of the hole remaining in the gas after time-of-flight. Each point corresponds to one experiment: preparation of the ring and creation of $\ell = 3$ flow, wait for a given time, TOF and measurement of the atomic density profile. After time-of-flight, a hole remains in the gas (see text); three distinct radii of the hole or a bright central peak are measured, indicating four circulation levels ($\ell = 3, 2, 1, 0$). Initially prepared in $\ell = 3$, the flow in the ring decays with time, due to atomic losses. Since the trap is static, the ground state corresponds to $\ell = 0$, but the metastability of the states prevents the flow to decay; the reduction of atom number in the trap (Left, bottom) causes a reduction of the potential barrier associated to metastability, and the flow then slowly decays, following several random decay steps which are consistent with a decay through surface modes [155]. Right: profile of the ring after time-of-flight, showing discrete sizes of the central hole, or a peak in the center if no flow is present (top to bottom: $\ell = 3, 2, 1, 0$).

4.2.1 The light sheet setup

Let us begin by describing the way we realize this double light sheet (that I will simply call "the light sheet" in the following). It is obtained by placing a $0 - \pi$ phase plate on the path of a gaussian blue-detuned laser beam that is subsequently focused on the atoms. The phase plate applies a π phase shift to the vertical half of the beam with respect to the lower half (see figure 4.6): the applied phase difference creates a plane in which the light will interfere destructively, resulting in a local absence of light; the atoms can then be trapped there.

The computation of the light intensity on the atoms, i.e. in the focal plane, is simply done by computing light propagation. In our case, the beam propagates along the y axis and the phase plate is vertical. An incident field $E_i(x', z')$ with wavelength λ arrives on a lens with

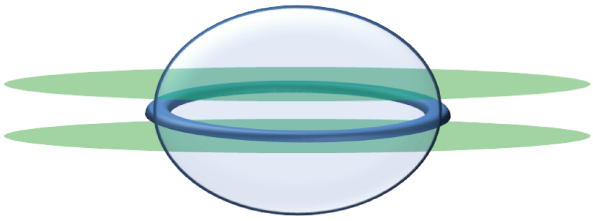

Figure 4.5 — General principle of our ring trap. The atoms are confined on the isomagnetic surface defined by RF dressing (blue ellipse) and within the plane defined by two blue-detuned light sheets (in green). The intersection of both traps creates a ring-shaped potential.

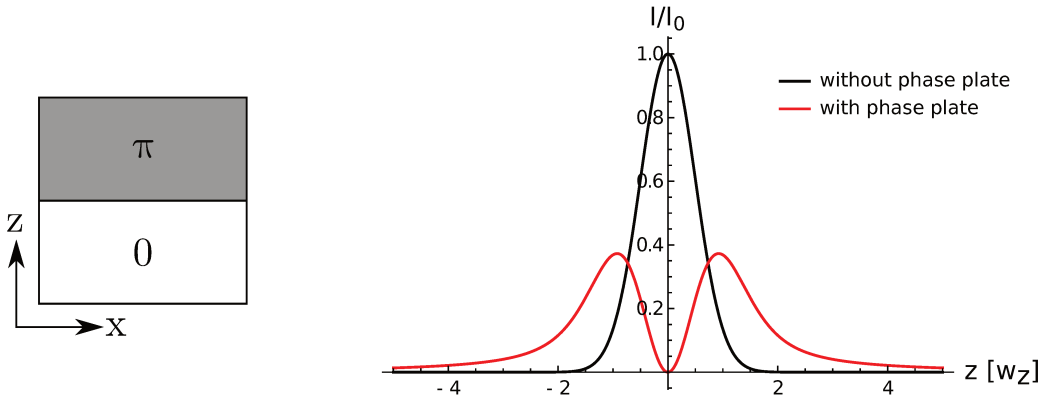

Figure 4.6 — Left: schematic representation of the phase plate. Right: Intensity profile (or equivalently light potential) of the light sheet beam (in red), normalized to the height of the gaussian profile corresponding to the absence of the phase plate (in black). The modulation by an error function creates a minimum of potential at the center of the light sheet. One may also note that the power decay for large z is also much slower [159].

focal length f, and we suppose that the phase plate is placed right in front of the lens[2]. The electric field in the focal plane then reads:

$$E_f(x,z) = \frac{1}{\lambda f}\int_{-\infty}^{\infty} dx \left(\int_0^{\infty} - \int_{-\infty}^{0}\right) E_i(x',z')e^{ik(x'x+z'z)/f}dz', \tag{4.13}$$

which can be rewritten as [160]:

$$E_f(x,z) = -i\sqrt{\frac{2P_{\mathrm{LS}}}{\pi w_x w_z}}\exp\left[-\left(\frac{x^2}{w_x^2}\right)-\left(\frac{z^2}{w_z^2}\right)\right]\mathrm{erf}\left(i\frac{z}{w_z}\right), \tag{4.14}$$

where w_x, w_z are the beam waists in the absence of the phase plate and P_{LS} is the total power in the light sheet beam. Supposing the incident beam was vertically collimated with waist $w_{i,z}$, the vertical waist on the atoms is then $w_z = \lambda f/\pi w_{i,z}$. The horizontal waist has no real constraint: if the incident beam's axis is the same as the axis of the phase plate, then horizontal and vertical axes are decoupled.

2. In our case the phase plate is placed approximately 30 cm before the lens, but since the beam is vertically collimated before the lens it doesn't change anything.

We see here that the vertical axis is simply "modulated" by the error function, and the electric field cancels as expected in the $z = 0$ plane. The corresponding intensity profile is shown on figure 4.6.

Outside the focal plane, the electric field can be written as [159]:

$$E(\mathbf{r}) = A_x(x)\frac{2i}{\sqrt{\pi w_z}}\int_0^\infty \sin\left(2u\frac{z}{w_z}\right) e^{i\frac{u^2 y}{z_R}} e^{-u^2} du, \tag{4.15}$$

where z_R is the vertical Rayleigh length, equal to $\pi w_z^2/\lambda$. Here, we exploited the independence of x and z axes: $A_x(x)$ is the field amplitude along the x direction. In our case, at the vertical focus point the beam is horizontally collimated[3], and A_x simply writes:

$$A_x(x) = \sqrt{\frac{2P_{\mathrm{LS}}}{\pi w_x}} e^{-\frac{x^2}{w_x^2}}. \tag{4.16}$$

The corresponding energy landscape for the atoms then simply writes: $U_{\mathrm{sheet}}(\mathbf{r}) = \eta_L |E(\mathbf{r})|^2$, where η_L gives the potential shift due to the presence of the dipole beam and depends on the detuning of the beam compared to the D_1 and D_2 lines[4]; in our case it is equal to $\eta_L = h \times 1.22 \times 10^9\,\mathrm{Hz}\cdot\mathrm{W}^{-1}\cdot\mu\mathrm{m}^2$ (computed taking into account non-RWA terms [161]).

4.2.2 Overall ring characteristics

Oscillation frequencies

Let us now describe the final ring potential. From previous section, we can deduce the vertical trapping frequency: close to $z = 0$, equation (4.14) can be approximated to:

$$E(0, 0, z \ll w_z) \approx \sqrt{\frac{2P_{\mathrm{LS}}}{\pi w_x w_z}} \frac{2z}{\sqrt{\pi} w_z}. \tag{4.17}$$

The resulting trapping frequency in between the two sheets is then:

$$\omega_{z,0} = \frac{4}{\pi}\sqrt{\frac{\eta_L P_{\mathrm{LS}}}{M w_z^3 w_x}}, \tag{4.18}$$

and if we slightly go off-center, the local vertical confinement varies as:

$$\omega_z(x, y) = \omega_{z,0} \times \exp\left(-\frac{x^2}{w_x^2}\right) \times \left[1 + \frac{y^2}{z_R^2}\right]^{-3/4}. \tag{4.19}$$

From a first-order development, we can then deduce a relation between w_x and z_R that minimizes the anisotropy of the trap close to the center: $z_R = \sqrt{3}/2 w_x$. From equation (4.14), we can also deduce that maximizing the vertical confinement at a distance r_0 in the x direction (for a given laser power) is achieved by choosing $w_x = 2r_0$.

The radial frequency in the ring is defined by the confinement on the isomagnetic surface, as described in (2.40). Having an azimuthally uniform confinement in the ring – to avoid

3. Strictly speaking, we have to replace w_x by $w_x\sqrt{1 + (y/x_R)^2}$, with x_R the horizontal Rayleigh length equal to $\pi w_x^2/\lambda$, but in our experiment x_R is more than 1000 times larger than all relevant dimensions.
4. Strictly speaking, it depends on all lines, but those are the two that have a non-negligible importance for the frequencies we consider here.

breaking rotational symmetry – supposes a circular RF polarization (cf 2.3.1), and the radial frequency, if the atoms are at the equator of the bubble, reads[5]:

$$\omega_{r,0} = \alpha\sqrt{\frac{2\hbar}{M\Omega_0}}. \tag{4.20}$$

If the atoms are not at the equator, it becomes:

$$\omega_r(z) = \omega_{r,0}\sqrt{1+\frac{2z}{r_b}}. \tag{4.21}$$

Finally, the critical temperature for condensation in the ring trap reads [124]:

$$k_{\mathrm{B}}T_c = \left(\frac{N\hbar^3\omega_z\omega_r}{\zeta(5/2)\sqrt{2\pi M}r_0}\right)^{2/5}, \tag{4.22}$$

where ζ is the Riemann zeta function. Note that this expression can also be recast under the form:

$$n_1\lambda_{\mathrm{dB}} = \zeta(5/2)\left(\frac{k_{\mathrm{B}}T}{\hbar\overline{\omega}}\right)^2, \tag{4.23}$$

with $n_1 = N/2\pi r_0$ being the one-dimensional density and $\overline{\omega} = \sqrt{\omega_r\omega_z}$ the geometrical average of the oscillation frequencies. It evidences the fact that the gas is harmonically trapped along two dimensions and uniform along the third one.

Chemical potential and lower dimensions

In a ring with radius r_0 and trapping frequencies ω_r, ω_z and azimuthally uniform confinement, the chemical potential for a 3D gas in the Thomas-Fermi regime reads [106]:

$$\mu_{3\mathrm{D}} = \hbar\overline{\omega}\sqrt{\frac{2Na}{\pi r_0}}. \tag{4.24}$$

If the chemical potential and the temperature are both lower than ω_z, (almost) all atoms are in the vertical ground state and we enter the two-dimensional regime. The chemical potential is then modified and is equal to:

$$\mu_{2\mathrm{D}} = \hbar\overline{\omega}\left(\frac{\omega_r}{\omega_z}\right)^{1/6}\left(\frac{3Na}{4\sqrt{\pi}r_0}\right)^{2/3}. \tag{4.25}$$

Our vertical trapping scheme allows reaching high trapping frequencies ($\omega_z \approx 2\pi \times 3\,\mathrm{kHz}$), and we can reasonnably expect to reach the quasi-2D regime with it. We can also, with only a few modifications, increase the radial trapping frequency around 1.5 kHz, which would allow to envision reaching $\mu_{2D} \leq \omega_r$ (see 5.4). In this last case, the atoms are almost all in the transverse ground state, entering the quasi-1D regime. The chemical potential then finally becomes:

$$\mu_{1\mathrm{D}} = \hbar\overline{\omega}\frac{Na}{\pi r_0}. \tag{4.26}$$

5. I remind here that Ω_0 is the Rabi frequency at the bottom of the bubble, and the coupling at the equator is $\Omega_0/2$.

Chapter 5

Experimental realization of the ring trap

The construction of the ring trap setup started with the previous PhD student who worked on the experiment, Camilla de Rossi [87]. The team succeeded in building the light sheet setup and realized ring-shaped traps; however the obtained annular gases were inhomogeneous or even disconnected when cold enough to be condensed, and could not be used for the studies we wanted to perform. The time spent trying to improve this initial setup led to a good understanding of some of the required tunings, but also to realize that the initial setup did not have the stability and the fine tuning possibilities required to achieve a "good enough" ring, and in the end most of the setup has been reconstructed.

The requirements our ring-shaped gas has to fulfill are the following:

- Ultracold temperature ($\sim 100\,\mathrm{nK}$), low enough to reach quantum degeneracy.
- A good regularity: we need the trap to be as smooth as possible to have rotational invariance; in other words we want the potential roughness to be much smaller than the chemical potential in the ring trap.
- A lifetime long enough to perform experiments within the ring trap (several seconds).

This chapter will give the experimental details about the ring setup implementation. It will be divided into three parts: in a first section I will start discussing the double light sheet setup, how we align the optical elements and how we load the resulting potential. The second section will be dedicated to a discussion about the required RF control, which happens to be much more critical than expected. The third section will present the work that was achieved on characterizing the finally obtained trap.

5.1 The double light sheet

5.1.1 Experimental system

Shaping the light sheet beam

The light sheet beam is shaped from a 532 nm, 5 W laser beam generated by a Coherent Verdi V5 monomode laser. The output beam is collimated, with a 1 mm waist. The beam is shaped

by the following elements (also presented on figure 5.1):

- A pair of cylindrical lenses (L_1, L_2) generates a vertical 3:1 telescope to expand the beam vertically to a 3 mm waist.
- A pair of lenses, one cylindrical and the second spherical (L_3, L_4) creates a horizontal telescope to give a horizontally collimated, 200 µm waist beam.
- The spherical lens also focuses the beam vertically, with a waist of 5.6 µm at the focal plane (where the atoms will be), with a Rayleigh length of 185 µm.
- A 0-π "step" phase plate is placed after lens L_3; it generates a plane with no laser power in which we can trap atoms vertically.

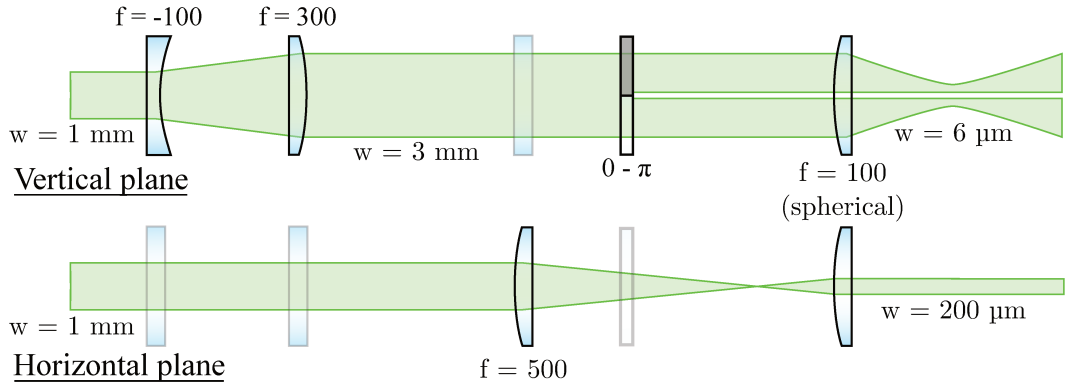

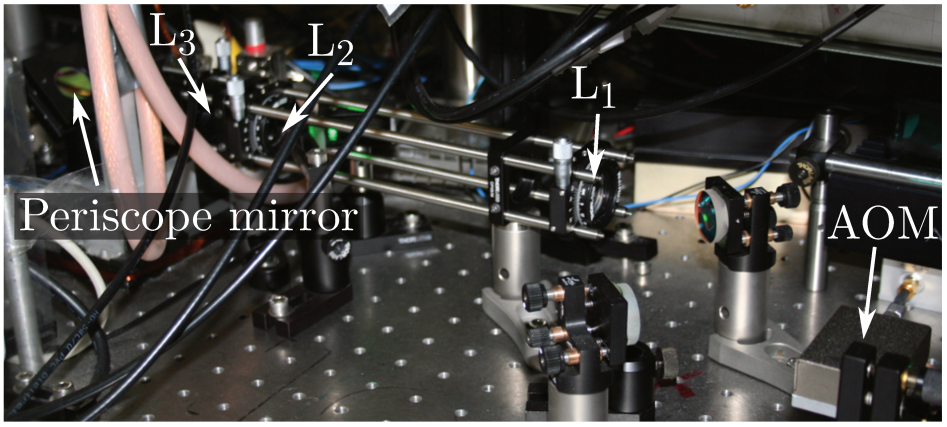

Figure 5.1 — Principle of the light sheet beam shaping (see text), and picture of the cage setup. L_1, L_2 and L_3 are cylindrical lenses; they are shown in transparency on the axes on which they do not act.

In practice, lenses L_1, L_2 and L_3 are mounted together on a cage system from Thorlabs (see fig. 5.1); it forces them to be parallel and aligned together. Each of them is placed in a rotation mount whose angle is controlled by a micrometric screw[1]: this enables fine tuning

1. CRM1P/M from Thorlabs.

of the lenses angles, and to *synchronously* rotate the lenses together (which is a precious possibility, since the relative angle of the cylindrical lenses is very critical – see section 5.1.4). This whole system will thereafter be called "the cage". It is placed on the main optical table, whereas the rest of the system is placed on a smaller breadboard placed at the height of the science cell; a periscope is placed right after the cage to lift the beam. The phase plate is located on this breadboard; it is mounted on a vertical translation stage[2] with a 1 µm resolution and a rotation mount. The final lens, L_4, is mounted on top of a micrometric translation stage along the beam propagation axis (longitudinal position) and its mount has translation screws[3] along both other axes (lateral and vertical position; the screws are not graduated and have a 250 µm per turn precision).

Turning on and off the light sheet

The control of the light sheet intensity is achieved by using a quartz acousto-optical modulator[4] (AOM): the 0^{th} order is sent to a beam blocker and the 1^{st} order goes to the experiment. The choice of a quartz AOM comes from the high power (5 W) that goes through: quartz AOMs are not very sensitive to high power (we haven't been able to see any thermal effect), whereas the previous AOM of the setup, with a TeO_2 crystal, had prohibitive thermal effects (large thermal lens effect and fluctuations of the beam position while switching from 0^{th} to 1^{st} order). This AOM works at fixed frequency and its angular separation is small (0.6°); the separation between both diffraction orders is done in the middle of the cage, almost 1 m away from the AOM. We also considered using a Pockels cell followed by a polarizing beamsplitter instead of an AOM, but we had problems of ringing when switching off the signal.

5.1.2 Installation of the light sheet

The light sheet setup is made of many elements, each of them having many degrees of freedom and needing careful setting and alignment. I will here describe the overall procedure and observables we used to install the system onto the experiment.

Aligning the (almost) naked beam on the atoms

The first step of alignment aims at ensuring that the beam reaches the atomic cloud (whose size is of the order of a few micrometers). This step is achieved with the "naked" beam, without the phase plate and without the cage. Before dismantling the previous light sheet setup (in which we were already able to load the atoms), we recorded its beam path using diaphragms; this allowed us to set back the beam at a position not too far away to the previous one. The spherical lens L_4 is then set in place.

The rough alignment is done using a thermal cloud as a probe: the naked beam is pointed onto an atomic cloud in the quadrupole trap for which we didn't evaporate until the end (in the absence of the plug beam). The cloud is then released from the trap in the presence of the beam: the repulsive effect of the laser can significantly modify the expansion of the thermal cloud, leading to "holes" in the profile after time of flight (see figure 5.2). The position of the beam with respect to the atoms can then be deduced from this profile; since the cloud is hot

2. M-461-7-M from Newport, with a SM-13 vernier micrometer.
3. Mount LM1XY/M from Thorlabs; it was mostly chosen for its compacity.
4. I-M110-2C10B6-3-GH26 from Gooch & Housego, with a A35110-S-1/50-P4K7U driver.

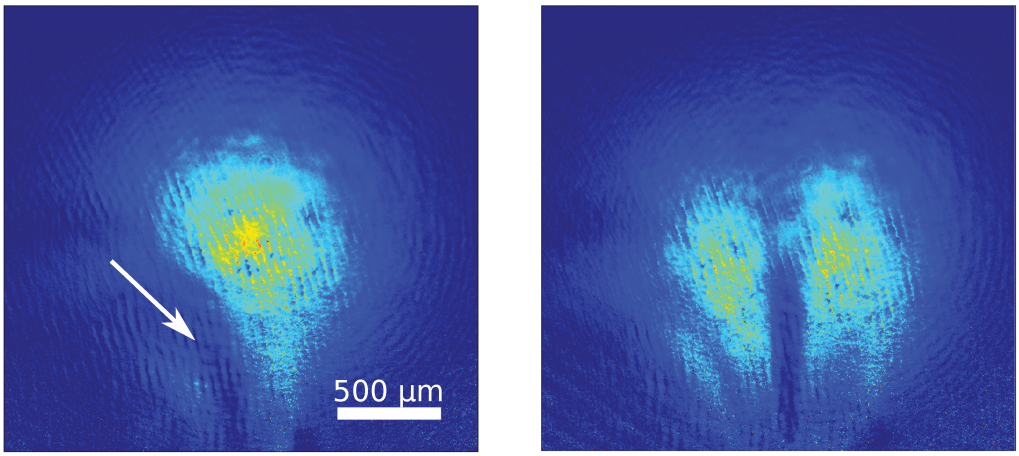

Figure 5.2 — Expansion of a hot thermal gas in the presence of the naked beam (only L_4 is present on the setup). The presence of the beam blocks the atoms and leads to regions where atoms do not spread (white arrow). Such pictures allow to deduce the position of the beam with respect to the cloud; on the right hand picture the depletion is centered, meaning that the beam is horizontally aligned with the atomic cloud.

and expands a lot is is possible to detect the laser on a broad zone. The beam position can then be adjusted by modifying the vertical and lateral position of L_4 to center it onto the atoms (i.e. on the center of the quadrupole). This method is adapted from the rough plug beam alignment procedure described in [86].

The fine alignment is done starting from a condensed cloud in the dressed trap; we shine the beam during a given time (typically 1 to 15 ms) while the BEC is released from the trap. A long pulse duration allows to deduce the relative position of the beam with respect to the cloud: if the beam is higher than the cloud, the cloud will fall without feeling its effect; if the beam is lower than the cloud the latter will be deviated or explode during its time of flight. The vertical position of the cloud can be adjusted using a vertical static magnetic bias field (see section 5.1.3); by playing on both its position and the vertical position of L_4 it is possible to align the beam at the desired vertical position (ideally, this position has to be slightly above the zero of the quadrupole trap, see section 5.1.3). We progressively reduce the pulse duration until we can precisely locate the beam and displace it as desired: if we know (from the long exposure) that the beam is placed below the atomic cloud but see no effect of the beam, it means that the cloud is too high and it doesn't have time to hit the laser before it is switched off. Figure 5.3 shows the typical time-of-flight pictures obtained in the different cases.

We note that these methods can also be useful with the final light sheet setup, to find the light sheet if it got misaligned and doesn't hit the atoms anymore.

The focus of lens L_4 (i.e. its longitudinal position) can also be achieved with a similar method: once the beam is aligned with the cloud (with the method mentioned above), shining onto the BEC a brief light pulse (0.1 ms at low power) while it is released from the trap will cause it to explode. We can then measure the "explosion width" (see figure 5.4) and use it as a criterion for tuning the focus of lens L_4, adjusting its longitudinal position to maximize

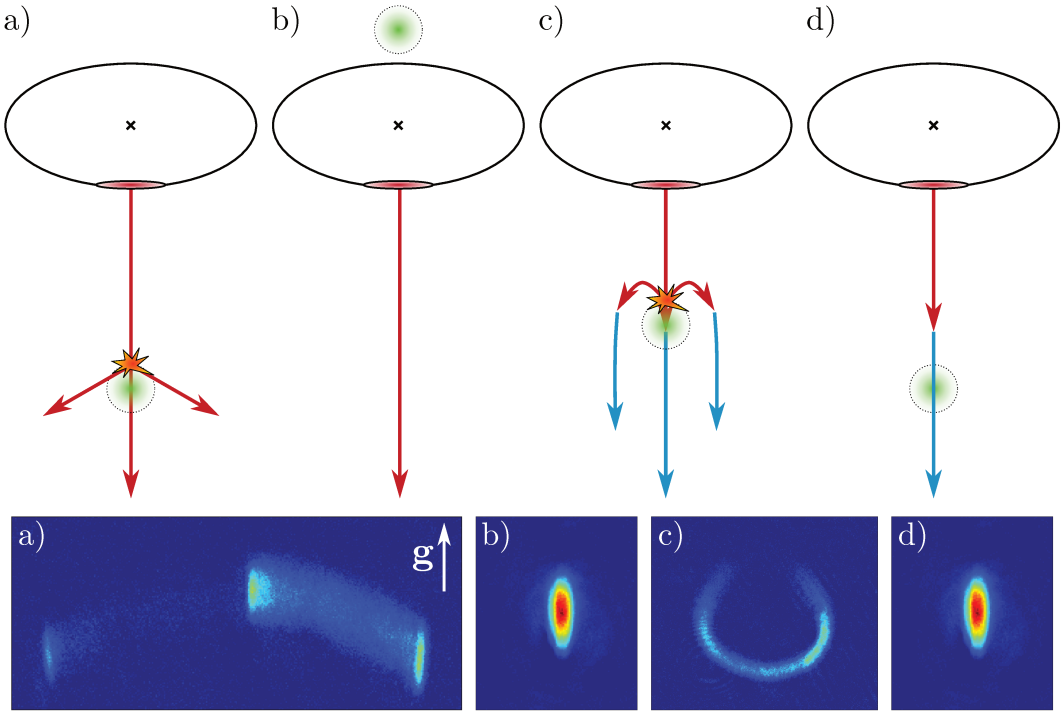

Figure 5.3 — Determination of the naked beam position using light pulses. The cloud is released from the bubble trap and the beam is turned on for a given duration at the same time. If the beam stays on for a long time (a,b), the cloud will burst if the beam is below the trap (a) or stay unharmed if the beam is above (b). If the beam stays on for a short time τ_{pulse} (c,d), two more cases exist: if the beam is closer than $g\tau_{pulse}^2/2$ from the atoms (c) the atoms will reach it while it is on, get deflected and then pursue their fall; if it is lower the beam will be off when the atoms reach its position. By adjusting the time during which the beam stays on while atoms fall, it is thus possible to measure the relative position of the trap and the beam.

the cloud explosion (see figure 5.4); we have in this way a precision of about 0.2 mm for a theoretical Rayleigh length of 1.7 mm (note that the Rayleigh length of the final beam will be 190 µm, due to the vertical expansion of the beam by the first telescope that is absent at this stage). A finer tuning of this focus will be achieved later by measuring the vertical oscillation frequency in the double sheet potential (cf section 5.3.3).

If the beam pitch is important, the vertical position of the cloud has to be adjusted significantly when the longitudinal position of L_4 is modified; this can be used to probe the horizontality of the beam and correct it (a mirror is placed before L_4; changing its vertical angle while shifting the vertical position of the lens allows to change the beam's angle without modifying its impact point). Using this observable, we were able to tune this angle within 1°.

Both these tunings are preliminary and can be achieved more precisely later using as a probe the behavior of the atoms within the light sheet; they aim at having an initial system sufficiently well aligned to load the atoms within the sheet.

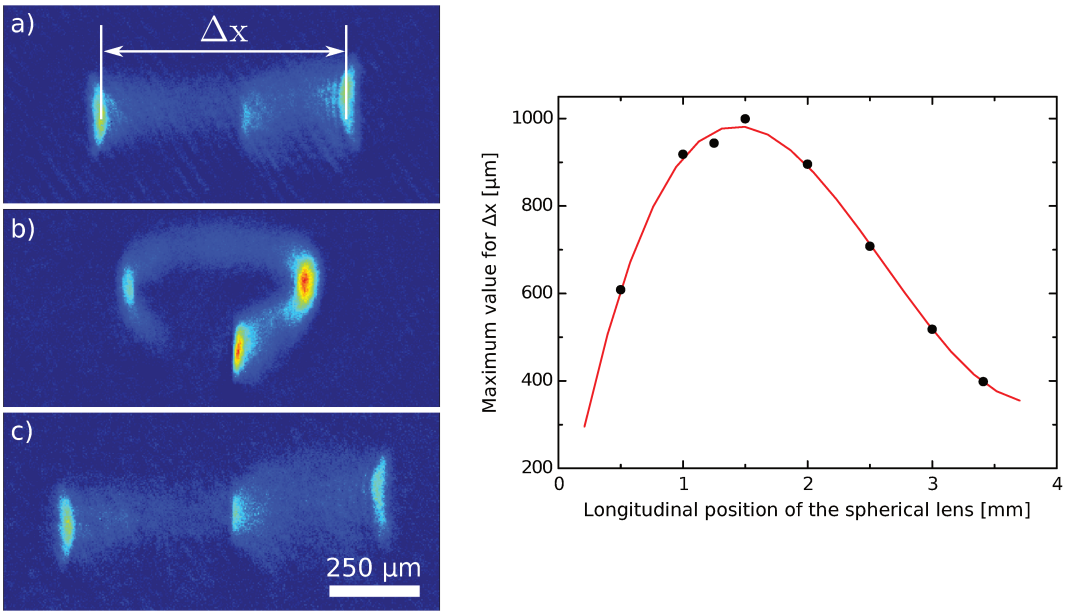

Figure 5.4 — Left: time-of-flight pictures of BECs after shining the Verdi beam directly onto it in the absence of the cage (only L_4 is present); the beam is shone during 0.1 ms at 10% of its maximal power as the trap is switched off. (a) is obtained for a beam well aligned on the cloud, (b) for a beam slightly above the cloud. (c) is also aligned with the cloud, but L_4 is better focused: the explosion of the cloud is more important. Right: "width" of explosion of the cloud Δx depending on the longitudinal position of L_4. Δx is measured only for a good alignment of the beam onto the atoms (situation a or c, not b). The red line is a polynomial fit shown as a guide to the eye.

Setting of the cage system and the phase plate

The relative angles of L_1, L_2 and L_3 are very critical (we need them to be aligned much better than 1°, cf section 5.1.4). The cage setup is prepared before being installed onto the experiment: it is easier to align L_1 and L_2 alone. L_1 is placed onto the cage and aligned to be close to vertical: the laser beam is sent onto a camera and we orient L_1 to measure a beam angle as close as possible to 90°). To position L_2, we have two degrees of freedom, the angle of the lens and the distance to L_1; the parallelism to L_1 is fixed by the cage. They are tuned by ensuring that the beam is collimated and doesn't rotate during its propagation (any small angle between both lenses causes a significant rotation of the beam's axis); we can tune the relative angle within 0.3° in this way. We tried to also tune the angle of L_3 before setting the cage using a camera, trying to get the same angle of the beam with L_3 than without; however the beam in the absence of L_3 is very large and its orientation is difficult to measure precisely (the beam is larger than the camera) and the obtained tuning turned out to be unsufficient (only 1° precision).

Once the alignment of the naked beam and L_4 were done, the cage has been installed on the experiment. Placing a camera to monitor the beam after the cell (around 3 cm after the focal point of the light sheet beam) allowed a better tuning of the angle of L_3: we measured the angle of the beam in the absence of L_3, then placed L_3 back and tuned its orientation such that the orientation of the final beam is unchanged. The beam profile at this position

in the presence of L_3 is not very anisotropic and its angle is not measured with a very good accuracy; we thus made a linear fit of the beam angle depending on the lens' orientation to compensate for the bad precision of the fit given by the beamprofiler on a single realization of the angle (fig. 5.5). We achieved in this way an accuracy better than 1° for tuning the angle of L_3. The longitudinal positioning of L_3 has been done by ensuring that the beam stays horizontally collimated after passing through the science cell.

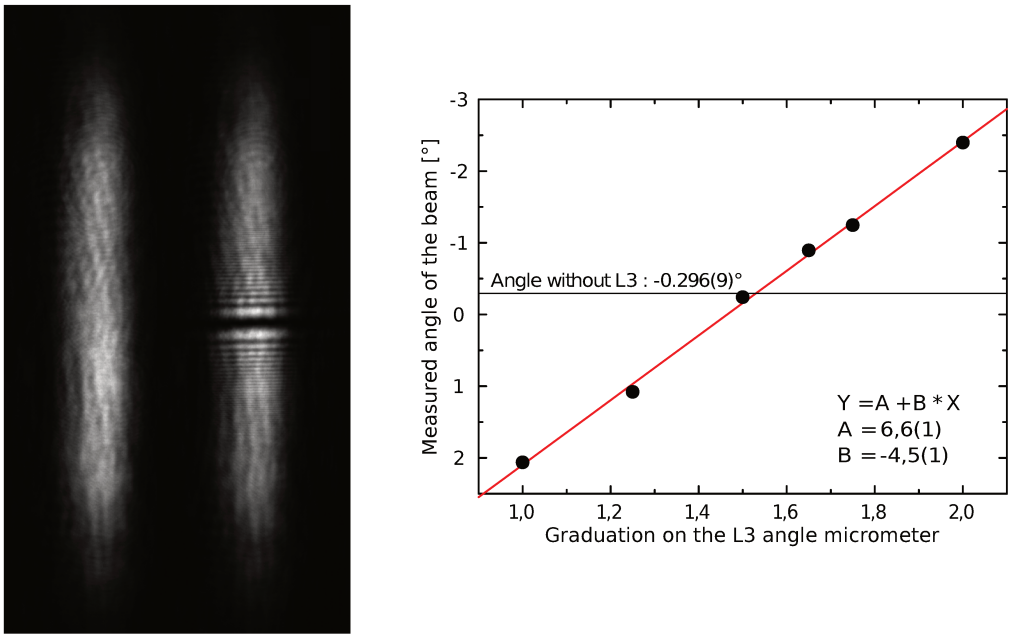

Figure 5.5 — Left: Profile of the light sheet measured with a beamprofiler camera placed approximately 3 cm away from its focal point, without (left) or with (right) the phase plate present on the beam path. Anisotropy is here reverted compared to the focal plane, due to the strong vertical focus (see figure 5.1). Before setting the phase plate, the beam's orientation is used to tune the angle of L_3; the phase plate is then placed in order to ensure that the slit created in the beam is orthogonal to its angle and that it is vertically centered. The fringes that are visible on both pictures (i.e. not the horizontal ones) come from interferences on the camera itself and are not present on the real beam. Right: Evolution of the orientation of the beam in the absence of the phase plate (corresponding to the left hand picture) with respect to the angle of L_3. The orientation of L_3 is tuned so that the orientation of the final beam (red line) is the same as the one measured in absence of L_3 (black horizontal line).

The phase plate is set into position using the same camera; its angle and height are tuned so that the slit created in the beam is aligned along the beam angle and centered. The angle of the phase plate isn't very critical and can stay at this value; its height requires more careful subsequent tuning.

Fine alignments of the light sheet

We want the dark region within the double sheet to be perfectly horizontal. The pitch angle, controlled through the vertical position of L_4 and the last deflector mirror, is tuned by loading atoms into the light sheet (cf section 5.1.3), then turning off the magnetic confinement: the atoms then spread into the sheet; if it is tilted we see on the vertical pictures that their center of mass drifts with time towards lower altitude regions. The roll angle is tuned by looking at the cloud after time-of-flight using our horizontal imaging: during TOF, the cloud expands perpendicularly to the light sheet, due to the strong vertical confinement. We thus align the light sheet's angle by synchronously rotating L_1, L_2 and L_3[5] to have the expansion of the cloud coincide with the angle of gravity (both angles being measured on our horizontal camera).

The angle of gravity with respect to the camera is measured through the free fall of the cloud: we let the atoms fall during different times t and record the position of their center-of-mass. It should follow the law:

$$z(t) = z_0 + v_{z,0}t + \frac{1}{2}g_z t^2, \tag{5.1}$$

$$x(t) = x_0 + v_{x,0}t + \frac{1}{2}g_x t^2, \tag{5.2}$$

where x and z are the position of the cloud's center of mass on the axes of the camera, $v_{j,0}$ the initial cloud velocity along these axes and g_j the projection of gravity along the same axes. The angle of gravity is then given by $\arctan(g_x/g_z)$, which we measure as being $0.7(5)^\circ$ (fig. 5.6). It is this measurement that limits the precision we achieve on the sheet's horizontality in the $x-y$ plane.

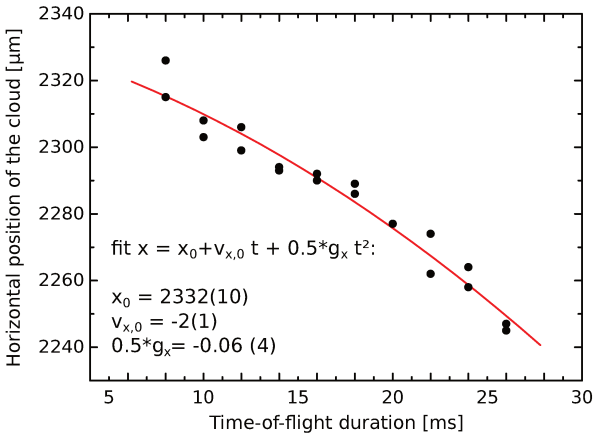

Figure 5.6 — Measurement of the projection of gravity g_x on the x axis of the horizontal imaging camera (see section 3.4). Combined to the corresponding projection on the z axis of the camera, this allows to measure the relative angle of the camera and gravity.

The expansion of a cloud loaded in the light sheet also allows to tune the lateral position of L_4: the atoms should be placed at the center of the light sheet, where the power and

5. In principle we should also tune the angle of the phase plate, but the effect of its angle on the resulting light sheet is very weak, and we thus do not have a very precise control on its angle: we cannot rotate it synchronously with the lenses when we correct for small angles.

vertical confinement are maximized; we thus try to maximize the vertical expansion of the cloud (i.e. its size after time-of-flight, measured on horizontal images) when released from the trap. Applying a static bias field along the x axis of the experiment allows to laterally displace the cloud in the light sheet and helps realizing the alignment (allowing to know in which direction to displace the sheet).

Finally, the focus of L_4 can also be improved by performing measurements on the trapped atoms, maximizing the vertical oscillation frequency measured in the double light sheet potential; this measurement is detailed in section 5.3.3.

5.1.3 Loading procedure

Basic principle

The loading scheme is, in its most basic principle, quite simple: we need to align the light sheet with the bottom of the bubble, so that the atoms get caught between the two intensity maxima of the sheet beam while it is turned on. In practice, it is simple to displace the bubble trap: a pair of vertical coils in Helmholtz configuration located above and below the cell generate a vertical bias magnetic field, which shifts the bubble trap vertically. However, the current in the coils cannot change sign: the bubble can be shifted only along one direction with respect to its position at zero bias. Details about its calibration are given in appendix A. On the contrary, displacing the light sheet vertically is quite difficult.

The simplest way to load the atoms into the light sheet and obtain an annular gas is then to first raise the bubble to a height z_{shift} while the laser is still off to align the bottom of the bubble with the position of the dipole trap minimum, turn on the sheet (we use a sine ramp), and then lower the bubble so that the atoms get displaced towards the equator of the bubble (see fig. 5.7). We do not necessarily have to bring them up to the equator; the height Δz from which the bubble is displaced in the second step allows to control the radius of the obtained ring.

We could also imagine instead lowering the bubble twice during this procedure[6], but this would lead to important currents in the bias coils in the final situation: ideally, we would like the magnetic bias field to be very small in the final configuration in order to minimize the position noise due to possible current noise in the power supply. For the same reason, the light sheet is aligned slightly above the center of the quadrupole trap[7], see figure 5.7 leftmost picture.

To check the good respective alignment of the cloud and the double light sheet after lifting the bubble, we turn off the magnetic confinement and shine briefly (0.1 ms pulse) the light sheet; the cloud then evolves during the usual time-of-flight procedure. The cloud doesn't have time to move during the light pulse, but it gets accelerated: its position and shape after the TOF then indicates what was its relative position with respect to the sheet (fig. 5.8). If the alignment is correct, the cloud's center of mass should not be displaced compared to its position in the absence of the light pulse, but it is broadened. On figure 5.8 we see that there are, in fact, three positions corresponding to an absence of average displacement; they can however easily be discriminated: two of them correspond to a maximum of light intensity at the position of the atoms while only one (the good one) corresponds to a minimum of

6. By having the bottom of the bubble above the light sheet before applying the vertical bias.
7. In principle, having the light sheet aligned right on the center of the would be better. However, the shift can be done only along one direction (to lift the bubble), which means that if the zero of the quadrupole is above the sheet the atoms will never be able to reach the equator. Since the light sheet position is subject to small drifts, we take a small safety margin to avoid having to displace the sheet.

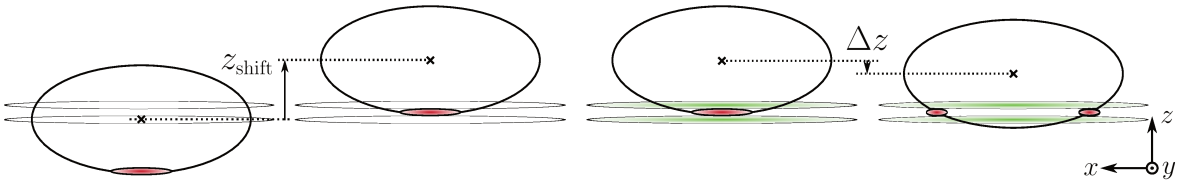

Figure 5.7 – Light sheet loading and ring formation scheme. In a first step, the bubble is lifted to align the atoms with the sheet, which is then turned on. The bubble is then lowered from a certain height to generate a ring-shaped trap.

intensity. If the atoms are aligned with the maximum of intensity, the final cloud will have a minimum of density at its center whereas it will have a maximum of atomic density at its center if it is aligned along the zero-intensity plane. Trying to load the atoms in the sheet also immediately discriminates between both situations. The light sheet position slightly drifts from day to day; this alignment therefore has to be done daily.

Compression with constant radius

The presence of residual defects in the light sheet that we couldn't remove led us to try compressing the ring, to increase the chemical potential of the gas (see section 5.1.4). Having a small ring also makes it easier to reach condensation, by increasing the atomic density. We thus needed a scheme to obtain a ring with a high magnetic gradient.

A first possibility consisted in compressing the cloud in the bubble before loading the sheet. However, compressing the cloud leads to significant heating: we need to apply a quite low RF knife during the compression to keep the cloud condensed, and this limits significantly the number of atoms we have in the trap after compression (around 1×10^5 atoms in a pure BEC). For reaching the 2D regime at the bottom of the bubble, this is not a problem, because we can work with the cloud right after that, but when we have to subsequenty load the ring, we end up with a too low number of atoms in the final trap. If we do not apply the knife during compression in order to keep many atoms, the cloud gets very hot and cannot be loaded into the light sheet properly anymore. We could also compress the cloud after loading the sheet but before making the ring; however in this situation the cloud is extremely sensitive to any fluctuation in the relative position between the sheet and the bubble, and the compression in this configuration leads to huge losses and heating.

Compressing the ring itself proved to be the best scheme. We tried to compress the ring while keeping its radius constant (i.e. increasing only ω_r), following two criteria:

- At the end of the ramp, the ring has to be at the equator of the final bubble.
- The radius of the ring has to remain constant during the whole ramp.

The first condition aims at minimizing the ring radius fluctuations (and the corresponding heating) that would come from fluctuations in the relative position of the sheet compared to the bubble (due to position noise in the sheet beam and current noise in the bias coils): at the equator, the derivative of the radius with respect to the position of the sheet cancels. The second condition aims at avoiding as much as possible changes in the cloud shape during the compression ramp, to minimize heating and losses: if we make a large ring at the equator of the bubble before the compression, the atoms will get dragged within the disorder created by

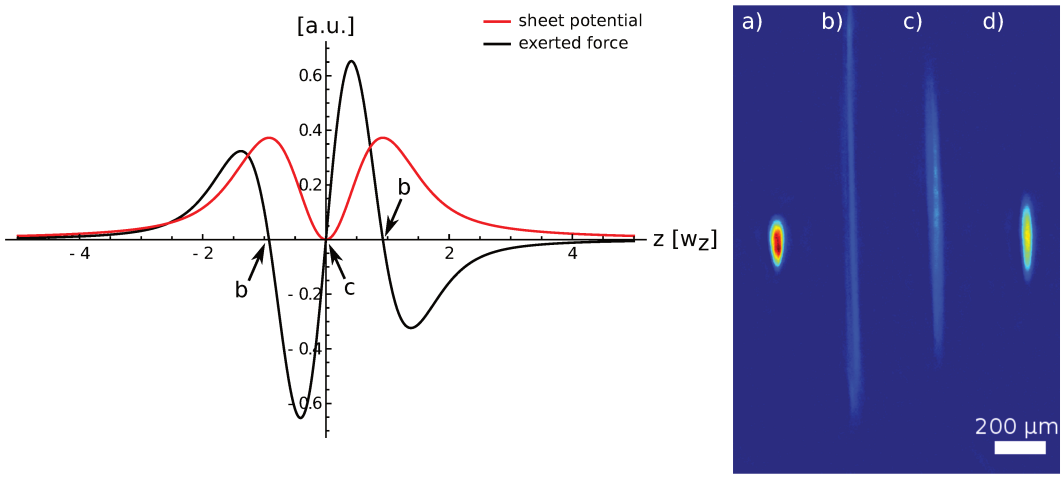

Figure 5.8 — Left: vertical potential profile of the light sheet (red) and its derivative (black), also corresponding to the opposite of the force exerted onto the atoms. There are three positions (b,c) for which the atoms are not displaced (zero force), but two of them correspond to potential maxima (b) and can be easily discriminated. The x-axis is graduated in units of the vertical waist in the absence of the phase plate (see fig. 4.6). Right: profile of the atomic cloud after time-of-flight expansion (23 ms). (a) corresponds to atoms in the dressed trap. (b) and (c) are taken after shining briefly a laser beam onto the atomic cloud in the dressed trap when the cloud is at positions indicated on the left plot. In both cases, we see no displacement of the cloud's center-of-mass, but for (b) the cloud expands a lot vertically and has a minimum of density in its center while in (c) it has a maximal density at the center, due to the different force profiles. If the cloud were at a position with respect to the sheet different from (b) or (c), the center-of-mass would be significantly displaced. The vertical position of the cloud is shifted by approximately 5.5 µm between (b) and (c), close to the expected value of w_z. Finally, (d) is taken after loading the light sheet. Since the vertical trapping frequency is significantly larger there than in the dressed trap, the vertical expansion is more important than in (a).

the light defects, and we would prefer to increase the magnetic gradient without displacing the atoms. It is possible to fullfill both conditions by loading the sheet from a bubble at low gradient and making a ring below the equator, with a small initial radius; we then adjust the vertical bias while compressing the bubble with a linear compression ramp (see figure 5.9). The details of the bias field ramp are given in appendix A.

5.1.4 Optical defects in the light sheet

To conclude this section, I will detail here the most notable issues we had that were due to the optical setup. They can be classified into two categories: the first ones are optical defects due to misalignments of the light sheet setup, and the second ones are optical defects due to bad optical quality of our glass cell.

The easiest way to diagnose the defects in the light sheet is to realize a "2D time-of-flight" (2D TOF): once the atoms are loaded within the light sheet, the magnetic confinement is switched off and the atoms freely evolve within the light sheet during typically 10 ms. They serve as a probe for measuring the potential landscape: if there are defects in the light sheet

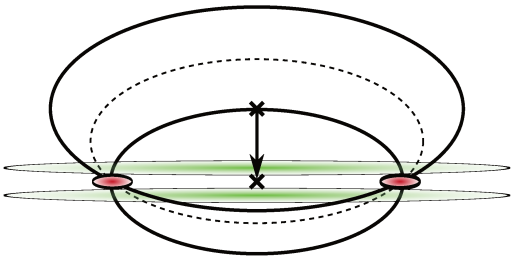

Figure 5.9 – Principle of the ring compression with constant radius: while the magnetic gradient increases, the size of the bubble decreases; the vertical bias is adjusted at the same time so that the ring radius stays constant. At the end of the compression, the ring is at the equator of the bubble, i.e. the vertical magnetic field cancels at the center of the light sheet. The ring position does not change, but the radial confinement increases significantly.

itself, instead of spreading isotropically the atoms will be trapped in optical defects and stay in the potential minima.

Most of our pictures taken to probe the light sheet were achieved in this way; however it is better to release the magnetic trapping after doing the "undressing" sequence we developed later (described in section 5.3.3): putting all atoms in only one Zeeman substate before switching off the RF avoids Stern-Gerlach effects due to residual magnetic fields (for example eddy currents when shutting down the quadrupole field) when the atoms spread between the two sheets.

Misalignments in the telescope

To help us understand the effect that the tuning of the different parameters could have on the final light sheet, we realized a complete modelisation of the light sheet setup[8] that allows us to numerically compute the resulting light sheet parameters. We have the possibility to tune all parameters (positions and angles) for each element in the setup, see the expected effect and compare it with the experiment (see figure 5.10).

In the end, we have two things that need to be aligned with specific care:

- The relative angles of the cylindrical telescope lenses: if their angles are not well parallel (or orthogonal), both axes "mix together" and instead of an absence of light within the sheet, there is no light only in the central *point* of the sheet; the beam still has the shape of a pair of sheets but there is also a lateral confinement. It is much weaker than the vertical confinement, but the lateral barriers can still be high enough (already 1 kHz for a 1° misalignment) to create a large "tube" within the sheet that prevents achieving a homogeneous sheet (fig. 5.10 a). This tuning is achieved by carefully preparing the telescope before setting it onto the experiment, as described in section 5.1.2.

- The vertical position of the phase plate: one could think that since the beam is very large at the position of the phase plate (3 mm waist vertically), the position of the plate is not very critical, while it is in fact extremely sensitive. For even a small misalignment of this position, the beam is not splitted into two equal parts anymore, and we see a

8. It is based on gaussian ABCD matrix propagation for describing the setup up to the phase plate, and direct light propagation computation beyond.

barrier appearing in the center of the sheet that can split the cloud in two parts (fig. 5.10 b). A vertical diplacement of 100 µm is already enough to create a barrier with more than 2 kHz height. In the end, we tune this parameter by minimizing the effect on the atoms after 2D TOF; we tune it within 10-20 µm.

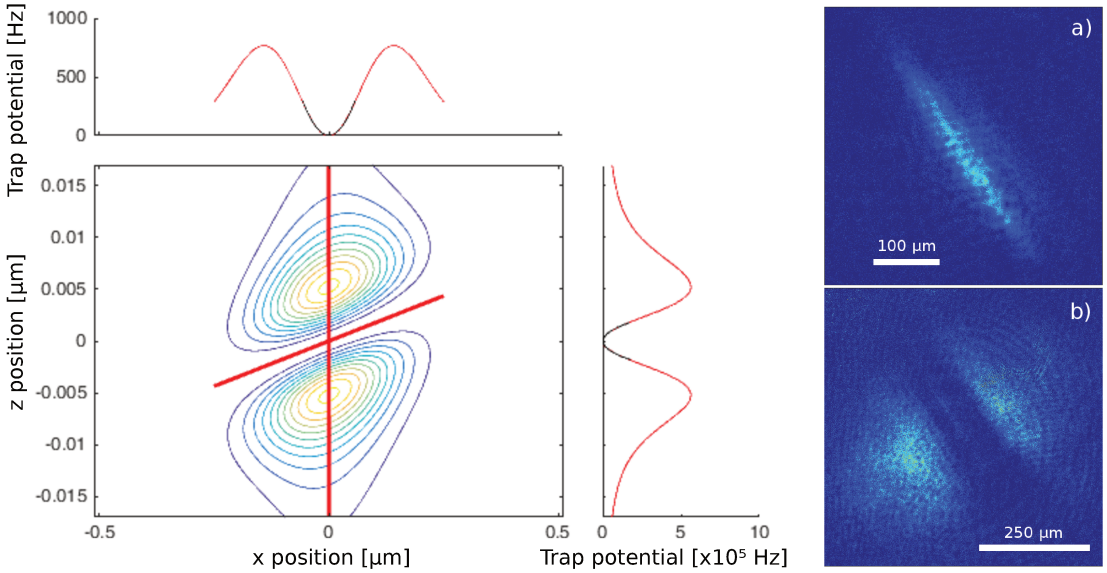

Figure 5.10 — Left: simulation of the effect of a 1° misalignment of the angle of L3. The central panel shows the light sheet profile, the top panel is a cut of the profile within the light sheet, and the right panel is a cut of the vertical profile of the light sheet. Right, a: effect of a misalignment in the telescope (L_3 has an angle of a few degrees compared to L_1 and L_2), seen after 24 ms spreading in the sheet (2D TOF). The atoms are confined within a lateral tube aligned with the axis of the light sheet, as seen on the left panel. b: effect of a misalignment of the phase plate height of around 300 µm, seen after 15 ms 2D TOF: a barrier appears in the center of the sheet, and the atoms are strongly expelled towards the sides.

Diffraction on the cell

In addition to the large-scale (i.e. comparable to the sheet dimensions) defects presented in the previous section, we saw also small-scale (a few micrometers) defects in the trapped gas. As previously, we can probe them by performing 2D TOF: we see small atomic "cigars" in which atoms stay trapped after expansion, whose orientation is similar to the axis of the light sheet (figure 5.11).

We interprete these defects as coming from diffraction and speckle on our optical cell, whose optical quality is not excellent: residual green light ending up inside the light sheet will create small barriers, preventing the atoms to reach the corresponding places. The small size of our cell also doesn't help, since the atoms are close (5 mm) from the diffracting surface. We haven't been able to average these defects by modulating the light sheet beam orientation (we can only marginally displace the sheet).

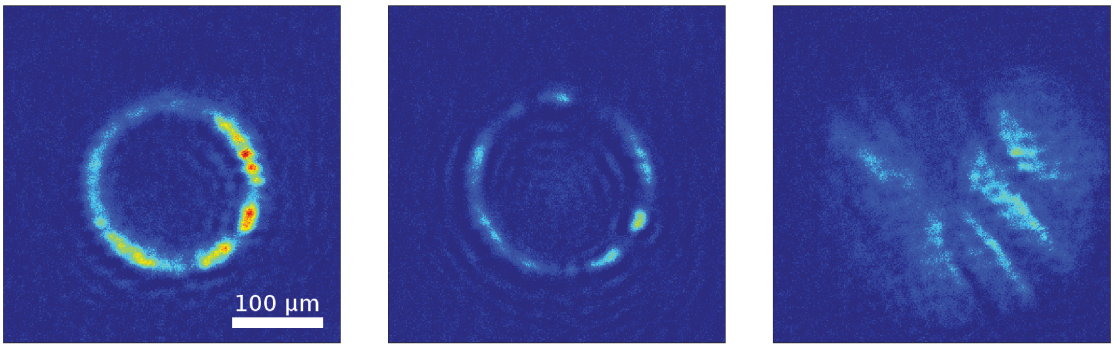

Figure 5.11 — Left: ring realized at low magnetic gradient (28.5 A / 56.5 G · cm^{-1} horizontally) and large RF frequency (1.2 MHz); the ring forms much below the equator: 7 µm above the bottom of the bubble for a 150 µm vertical radius. Center: same ring, with RF evaporation. For both rings, we see small defects all along the circumference. Right: expansion of a ring (2D time-of-flight) in the same sheet potential. All pictures correspond to the same region. We interprete theses small-scale defects as coming from green light diffracted by inhomogeneities of the glass cell.

It emerged from discussions with Thomas Bourdel, Martin Robert-de-Saint-Vincent, Jean-Loup Ville and Jérôme Beugnon (who also work or worked with 2D confinement) that they had similar problems; they solved it by either looking for regions free from defects (putting their cloud between two optical defects), using large vacuum chambers so that the atoms are far away from the windows, or having a chemical potential significantly larger than the height of the defects. The first solution isn't achievable for us since the size of our rings (typically 50 to 100 µm) is significantly larger than the distance between two defects, and the second one is even less (changing the cell would require a large amount of work to rebuild the system). We decided to try the second method by compressing the ring and using smaller radii, as described in section 5.1.3: this increases the chemical potential in the ring and we could hope to reduce in this way the relative density inhomogeneities coming from these incompressible optical defects; it indeed allowed us to achieve satisfying rings.

5.2 RF control improvement

Even though many careful alignments have to be done on the light sheet setup, the RF polarization happened to be another critical tuning. For a long time, we were confident in our control of the "dressed trap part" of the ring due to our experience of working with such traps [68, 102, 103]. However, all our previous experiments were realized at the bottom of the bubble: in these conditions, tuning the RF polarization corresponds to adjusting the oscillation frequencies and the trap's symmetry, for which the sensitivity to a good polarization circularity is quite weak (cf equation (2.85)). On the contrary, when making a ring at the equator of the bubble, the local RF coupling defines the value of the local (azimuthally) potential minimum [9]. Let us consider that the ring trap is achieved at the equator of the bubble; the corresponding potential in the $z = 0$ plane can then be expressed using polar

9. Stricly speaking, the Rabi coupling also strongly impacts the absolute value of the potential minimum at the bottom of the bubble, but it is almost uniform on the region explored by the atoms because the solid angle (considering the unflattened bubble) of this region is small.

coordinates (r, ϕ) as:

$$V(r,\phi) = \hbar\sqrt{\delta^2(r) + \Omega_1^2(\phi)}. \tag{5.3}$$

The potential energy along the ring (corresponding to $\delta(r) = 0$) is then equal to $\hbar\Omega_1(\phi)$. For a typical coupling of 50 kHz, even coupling variations at the level of a percent lead to 500 Hz variations in the trap potential undergone by the atoms, for a typical chemical potential between 1 and 5 kilohertz, leading to significant variations of the local atomic density.

5.2.1 Instability of the RF polarization

We became suspicious about RF misalignments after having implemented the ring compression, when we ended up with annular gases which had irregularities with a well-defined symmetry axis which could hardly be attributed to random optical defects and was not aligned with the sheet propagation axis (figure 5.12). We also saw instability in the orientation of this axis, and an attempt of measuring the Rabi coupling in the ring trap doing RF spectroscopy (as described in section 3.3.3) showed an extremely broad ($\gtrsim$ 10 kHz) resonance, indicating large coupling inhomogeneities.

The instability in the orientation of the inhomogeneities appeared to come from drifts in the relative phase of the antennas: the synthesizer generating the clock of the DDS was used for something else for a short period of time during the experimental sequence, leaving the DDS without a clock (before using the DDS, but after programming it). Its outputs were then randomly drifting in phase during that time – note for experimentalists wishing to use a DDS: *never* let it without its clock! The observed asymmetry thus comes from an elliptically polarized RF. We could easily solve the problem after having understood it but it led us to realize that we needed a more careful control of the RF polarization.

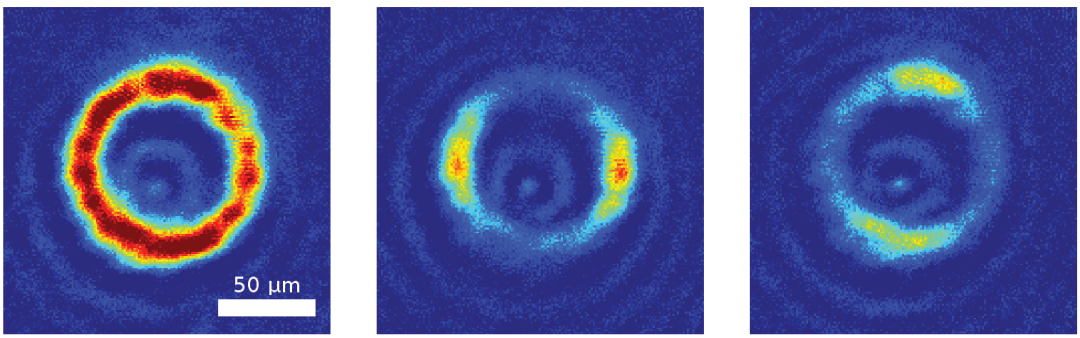

Figure 5.12 – Left: picture of a ring-shaped gas realized after implementing the compression scheme. We see no inhomogeneities that could be attributed to optical defects. The ring is at the equator, compressed at 100 A (198 G · cm^{-1} horizontally) and the dressing frequency is 0.6 MHz (the expected radius is then 44 µm). Center, right: same ring after performing RF evaporation to cool down the atoms; reducing the number of atoms and temperature allows to see inhomogeneities better. We end up with two ring pieces facing each other, signature of an elliptical polarization. Both rings are obtained within the same apparent conditions, indicating the instability of the DDS we had trouble with.

5.2.2 Implementation of a 3D polarization control

Need for a third antenna

With a careful tuning of the antenna's polarization, we were able to suppress the asymmetry leading to two "moon crescents" facing each other, but we ended up instead with a highly pronounced left-right asymmetry (figure 5.13). A spectroscopy measurement in the ring showed that the line was still extremely broad. This asymmetry looks like the effect of a lateral tilt in the light sheet's angle, but trying to rotate this angle showed no difference in the obtained ring (both in aspect and resonance width).

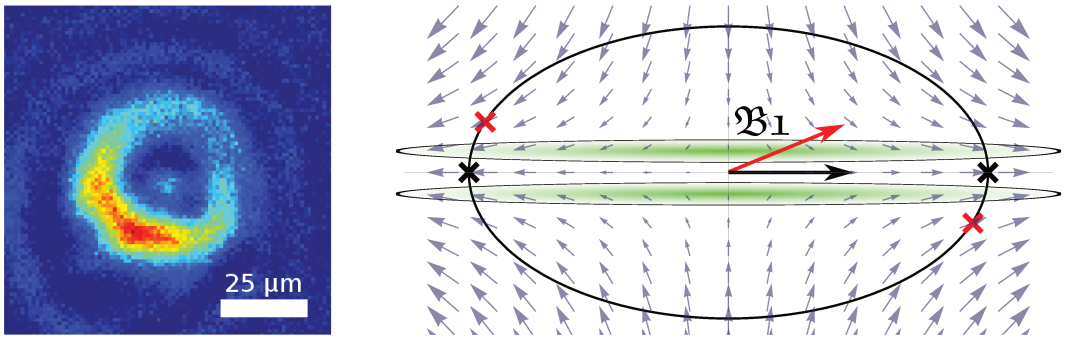

Figure 5.13 – Left: ring-shaped gas obtained for a tuning of the antennas leading to a rotationnaly invariant trap at the bottom of the bubble. We end up with a strong lateral imbalance, which is not due to an inclination of the potential caused by gravity. Ring realized for 110 A in the coils (218 $\mathrm{G \cdot cm^{-1}}$ horizontal gradient) and dressing at 0.3 MHz. Right: effect of a misalignment of the RF field with respect to the quadrupole axis. The local quadrupole field is represented by the blue arrows; the RF field (red or black arrow) is uniform over the whole system. I consider here only the contribution of a linearly polarized RF (in the plane of the drawing), as is the field created by a single antenna. The contribution of the RF field cancels where it is parallel to the local static field: if the RF field is horizontal (black arrow) it happens at the equator (black crosses), if it is tilted it happens both above and below the equator (red arrow and crosses). In this latter case, the contribution of this field to the coupling in the ring – i.e. at the equator – created by an antenna orthogonal to the plan of the drawing will be an increase of the coupling on one side of the ring and a decrease on the other side (this contribution has opposite projections on the local σ^+ polarization), resulting in a lateral imbalance of the ring.

After computing the effect that the tilt of a dressing antenna with respect to the horizontal plane would have (a tilt within the plane can be corrected by adjusting the relative phase between antennas), we realized that even a very small tilt could have an extremely large effect on the atoms : for a coupling at the bottom of the bubble around 100 kHz, an angle of 1° on one of the dressing fields leads to several kilohertz imbalance between both sides of the ring at the equator! (fig. 5.13).

However, the control we have on our antenna orientation is clearly below the precision that would therefore be necessary (the setup was not designed with this in mind), and changing the way the antennas are placed is now extremely difficult. We thus decided to, instead, install a *third* dressing antenna, that generates a vertical RF field: with three different antennas, it is

possible to generate any polarization in the 3D space, even if the antennas are not perfectly orthogonal with each other. We can then use it to correct the effects due to misalignments of the two main dressing antennas, similarly to [110].

Mathematical interlude

Let us consider an arbitrary polarized dressing RF field, with complex polarization $\boldsymbol{\epsilon} = \cos\Theta\cos\Theta_z\mathbf{e}_x + \sin\Theta\cos\Theta_z e^{i\Phi}\mathbf{e}_y + \sin\Theta_z e^{i\Phi_z}\mathbf{e}_z$. We want to compute the local coupling in the ring trap, that is, at the equator of the bubble. Defining the position with its azimuthal angle ϕ, the quadrupole field orientation writes: $\mathbf{u} = \cos\phi\ \mathbf{e}_x + \sin\phi\ \mathbf{e}_y$. From equation (2.47), the local coupling can be written as:

$$\Omega_1^2(\phi) = \frac{\Omega_{\mathrm{rf}}^2}{4}\left[\frac{3-\cos(2\Theta_z)}{2} - A_1\cos(\phi+\Phi_1) - A_2\cos(2\phi+\Phi_2)\right], \tag{5.4}$$

where A_1, Φ_1, A_2, Φ_2 are equal to:

$$A_1 = 2\sin(2\Theta_z)\sqrt{\sin^2\Theta\sin^2(\Phi-\Phi_z) + \cos^2\Theta\sin^2\Phi_z}, \tag{5.5}$$

$$\Phi_1 = -\arctan\left[\frac{\cos\Theta\sin\Phi_z}{\sin\Theta\sin(\Phi-\Phi_z)}\right], \tag{5.6}$$

$$A_2 = \cos^2\Theta_z\sqrt{\cos^2(2\Theta) + \sin^2(2\Theta)\cos^2\Phi}, \tag{5.7}$$

$$\Phi_2 = -\arctan\left[\cos\Phi\tan(2\Theta)\right]. \tag{5.8}$$

Even though these formulas are not very appealing, one can find here the two phenomena that are observed:

- A modulation with period π, corresponding to the "double-moon" asymmetry. It depends very weakly of the tilt Θ_z of the antennas with respect to the vertical axis, and appears if the polarization is elliptical.
- A modulation with period 2π, corresponding to the observed "lateral tilt", that depends strongly on Θ_z.

It can then be interesting to look at the limit described previously: a polarization that is circular, but slightly inclinated compared to the quadrupole axis due to a tilt of the antennas, that is: $\Theta = \pi/4$, $\Phi = \pi/2$, $\Theta_z \ll 1$. In this case, the local coupling simplifies to:

$$\Omega_1(\phi) = \frac{\Omega_{\mathrm{rf}}}{2}\sqrt{1 - \frac{4}{\sqrt{2}}\Theta_z\cos(\phi-\Phi_z)} \tag{5.9}$$

$$\approx \frac{\Omega_{\mathrm{rf}}}{2}(1 - \sqrt{2}\Theta_z\cos(\phi-\Phi_z)), \tag{5.10}$$

and we find a modulation of the Rabi coupling with an amplitude $\Omega_{\mathrm{rf}}\Theta_z$ whose orientation corresponds to the orientation of the z component of the polarization. Since we work with $\Omega_1 = 2\pi \times 100\,\mathrm{kHz}$, even a very small angle Θ_z can lead to a modulation whose amplitude will be on the order of a few kilohertz.

Choice of the antenna

The third antenna is necessarily very different from the two principal dressing antennas: the presence of the quadrupole coils prevents us to place it just next to the cell and close to the atoms like they are; it has to be placed above or below the coils.

To choose the antenna, we started by computing the expected coupling that a given antenna could create on the atoms (we tried at first to use old antennas that were already available). However, all antennas we tried had an effect on the atoms much smaller than expected, that we interpret as probably coming from a screening effect from the quadrupole coils. In the end, the protocol for choosing the third antenna turned out to be "try an antenna configuration and see whether it is satisfying". The criterion used to validate the antenna is the possibility to balance the atomic density in a ring (cf next section) realized with a high Rabi coupling ($> 50\,\mathrm{kHz}$ at the equator) for a dressing at low frequency ($0.3\,\mathrm{MHz}$) and to balance a ring at low coupling ($25\,\mathrm{kHz}$) and high frequency ($1.2\,\mathrm{MHz}$) – with the antenna geometries we have the possibility to install on the experiment, we systematically have a loss in admittance for increasing frequency. We finally use an antenna with 4 loops of copper wire, with dimensions $11 \times 6.5\,\mathrm{cm}$, placed below the quadrupole coils. Its admittance[10] is $Y = 128\,\mathrm{mS}$ when operated at $0.3\,\mathrm{MHz}$ and $Y = 32\,\mathrm{mS}$ at $1.2\,\mathrm{MHz}$.

Effect and tuning of the third antenna

Testing the third antenna on the "bare" dressed trap is difficult, because it has no effect at the bottom of the resonant ellipsoid (since the polarization of the RF it produces is aligned with the static field at this position). In particular, we cannot generate a dressed trap with this antenna alone and thus cannot calibrate it like we usually do; we haven't found a way to calibrate the antenna yet. We instead use the third antenna as a *correction* parameter and look for its effect on the ring itself, at the equator of the bubble. The antenna is simply turned on within a given configuration of phase and amplitude, together with both other antennas (tuned so that the trap at the bottom is as circular as possible). We load a ring with the usual protocol, and we see how the addition of the third RF field modifies the obtained ring configuration.

The addition of the third antenna allows us to modify the potential landscape and displace the atoms within the ring. The phase of the antenna controls the direction in which the atoms are attracted (compared to the situation in its absence), and the amplitude changes how much the atoms are displaced in this direction, see figure 5.14.

The tuning of the parameters of the antennas – three amplitudes and two relative phases – is eventually achieved by optimizing the density homogeneity of the ring. A π periodic asymmetry, as seen on figure 5.12 or the first ring of figure 5.14, is corrected by adjusting the relative phase and amplitude of the two main antennas; a 2π periodic asymmetry, as seen on figure 5.13, by adjusting the phase and amplitude of the third antenna. Applying a knife to reduce the chemical potential allows to be more sensitive to potential irregularities (if the cloud is condensed, which we are able to do – cf section 5.3.2) and achieve more precise tuning of the antennas.

We also realized a spectroscopic measurement of the coupling in the ring in the presence of the third antenna (figure 5.15); we saw as expected a strong reduction of the resonance width, confirming the "correction" of the coupling inhomogeneities by this new RF field.

10. measured with a vector network analyzer.

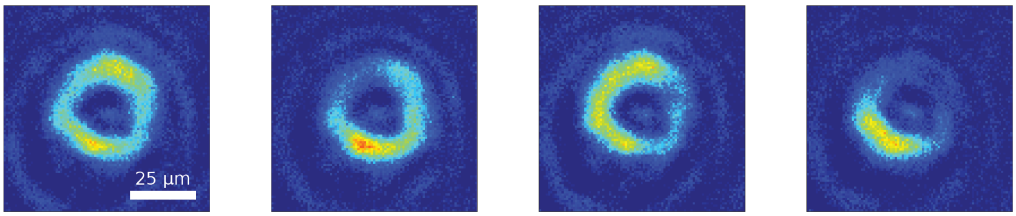

Figure 5.14 — Effect of the third antenna on the annular density. Left to right: annular gas obtained for a relative phase of the third antenna (within an arbitrary offset) of respectively 0, $-\pi/4$, $\pi/4$, π with identical amplitude. Changing the third antenna's phase allows to diplace the atoms within the ring. These rings are achieved with a dressing frequency of 0.3 MHz and 110 A in the quadrupole coils; the ring obtained in the absence of the third antenna is the one presented in figure 5.13. Here, there is a small residual imbalance between the main dressing antennas, that can be seen on the leftmost ring: when the third antenna is tuned properly, we have a residual "double moon" asymmetry like on figure 5.12.

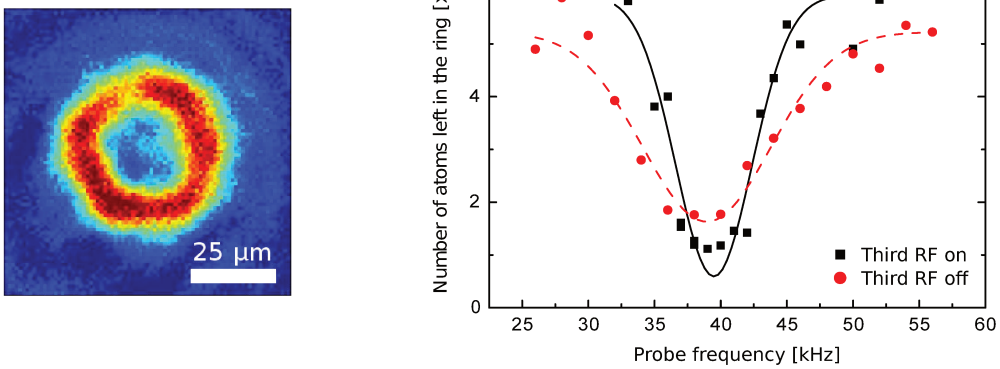

Figure 5.15 — Left: *in situ* picture of a ring balanced using the third antenna. The magnetic gradient is maximal (110 A/218 G · cm^{-1} horizontally) and the dressing frequency is 0.3 MHz. Right: spectroscopic line measured in the same ring, with and without turning on the third antenna. Without the third antenna, the line width is significantly broadened: a Gaussian fit gives a 4.8(6) kHz width, against 2.9(3) with the third antenna. Note that these data were taken in a ring which was not fully balanced yet (there is a small residual imbalance in the ring that was corrected later).

5.3 Characterization of the ring

Once we are able to generate a balanced ring-shaped gas, we need ways to characterize the trap and measure its oscillation frequencies (vertical and radial). We also need to characterize the number of atoms we are able to trap, as well as the temperature of the gas, its lifetime and its heating rate.

Up to now, we worked on characterizing only one realization of the ring: $I_{\text{quad}} = 90\,\text{A}$ in the quadrupole coils (178 G · cm^{-1} horizontally), dressing at $\omega_{\text{rf}} = 2\pi \times 0.3\,\text{MHz}$ with a

coupling $\Omega_0/2 = 2\pi \times 50\,\text{kHz}$ at the equator of the ring (shown on figure 5.16). However, the techniques described here should work for all ring parameters.

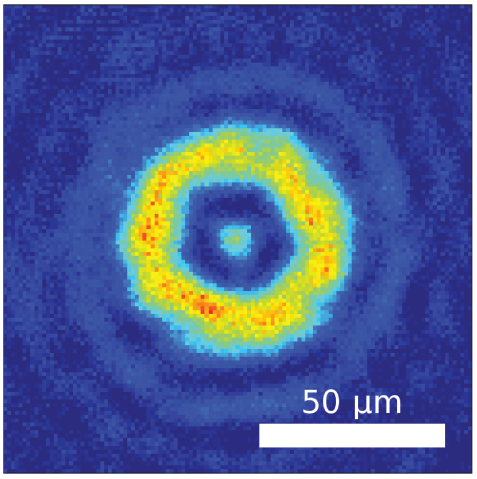

Figure 5.16 — Optimized ring that we characterized. The central dot and the outer concentric rings are due to diffraction in the imaging system and do not correspond to real atoms; we oriented the probe in order to align it in the center of the ring (to avoid overlap with the real ring profile).

5.3.1 Ring trap dimensions

Since the atomic cloud is placed on the surface of an ellipsoid, the evolution of the ring radius r_0 when the bubble is placed at a height z should follow the equation:

$$r_0^2 = r_b^2 - 4z_s^2 + 8zz_s - 4z^2, \tag{5.11}$$

where z_s is the position of the light sheet ($z = z_s$ corresponds to the ring being at the equator).

We can verify this relation by applying an additional vertical magnetic bias to the ring and measuring the radius of the obtained ring. Results of such a measurement are shown on figure 5.17. We find a good agreement with the expected behavior, however the measured maximum radius (22.3(1) µm) differs slightly from the radius expected with the parameters we use (24.6 µm, computed from equation (2.54)). We do not understand this discrepancy yet; we recalibrated the magnification of our vertical imaging setup but it did no improve the agreement. We also see a small offset in vertical position, meaning that the ramp we use for ring compression does not bring the cloud exactly at the equator. This offset had already been deduced from spectroscopy in the ring trap: the Rabi coupling measured in the ring trap was lower than half of the coupling at the bottom (for a circularly polarized RF, as discussed in section 2.3.1, the coupling at the equator is equal to half the coupling at the bottom). We can easily correct it by applying an offset to the final bias field used to displace the quadrupole trap and make the ring.

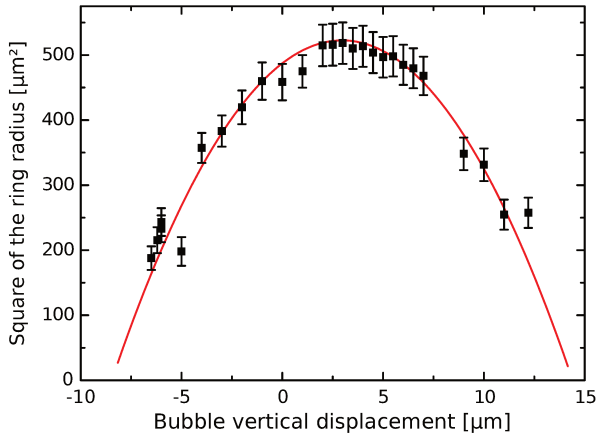

Figure 5.17 — Evolution of the square of the ring radius when the bubble is displaced. The red line shows a 2-parameter fit following equation (5.11). The fit shows a good agreement with the data; we find a maximal radius of 22.3(1) µm and a vertical offset of 3.0(1) µm compared to the ideal sheet position deduced from the light sheet loading procedure. The radius is computed by taking two cuts of the ring diameter along both axes of the camera; for each cut we make two Gaussian fits of the ring opposite positions and deduce the ring diameter (the radial profile is Gaussian because the Thomas-Fermi radius of the ring is significantly below our imaging resolution). The square of the radius is then computed by multiplying the radii obtained along both axes. Error bars correspond to the errors given by the Gaussian fit.

5.3.2 Cloud temperature and condensation of the annular gas

Loading procedure and evaporative cooling in the ring trap

Ideally, we would like to load as many atoms as possible in the ring, with a temperature as low as possible. However, the control of the gas temperature is achieved using a RF knife to cool down the atoms in the ring, at the price of atom losses. There is thus a tradeoff between both requirements. The loading procedure should also be as adiabatic as possible – even if in practice, we still have a large heating during the procedure: the temperature of the annular gas after loading can easily go beyond 600 nK in the absence of specific care.

We load the ring starting from a cloud that is condensed but not very cold and still contains many atoms ($\sim 4 \times 10^5$), and we maintain a RF knife during the whole loading procedure, high enough to avoid suffering too many losses during the transfer but also low enough to ensure that the temperature does not get too high and that we keep a configuration for which we can perform evaporative cooling efficiently. Once the ring is achieved, the knife is then slowly lowered to perform cooling in the ring and reach condensation again.

The knife was first optimized step after step during the ring loading procedure, trying to maximize the total number of atoms at each step. The most satisfying solution was eventually to keep the knife at a constant frequency, 455 kHz (i.e. initially 55 kHz above the trap bottom). The crucial part is probably the light sheet loading, because this value was found initially by maximizing the number of atoms loaded into the light sheet; trying to optimize the knife when making and compressing the ring leads to only minor improvements. In the end, we simply do the whole dressing procedure with a high knife and load and compress the ring without modifying the knife frequency. We load in this way around 3×10^5 atoms in the trap,

with a temperature of typically 230 nK.

Once the ring is loaded, we lower the knife and perform evaporative cooling in the ring in two steps. The knife is first strongly lowered quite fast (-65 kHz in 100 ms): during the compression, the Rabi coupling at the position of the atoms has been divided by two because the atoms went from the bottom to the equator of the bubble, and the knife is then very high; it can be lowered quickly without causing too much losses. A second ramp then lowers the knife more slowly, to evaporate atoms in the ring (-10 kHz in 200 ms). In the end, we can achieve a ring with typically 1 to 1.5 $\times$ 10^5 atoms and no detectable thermal fraction. A summary of the time evolution for the knife frequency can be seen on figure 5.18

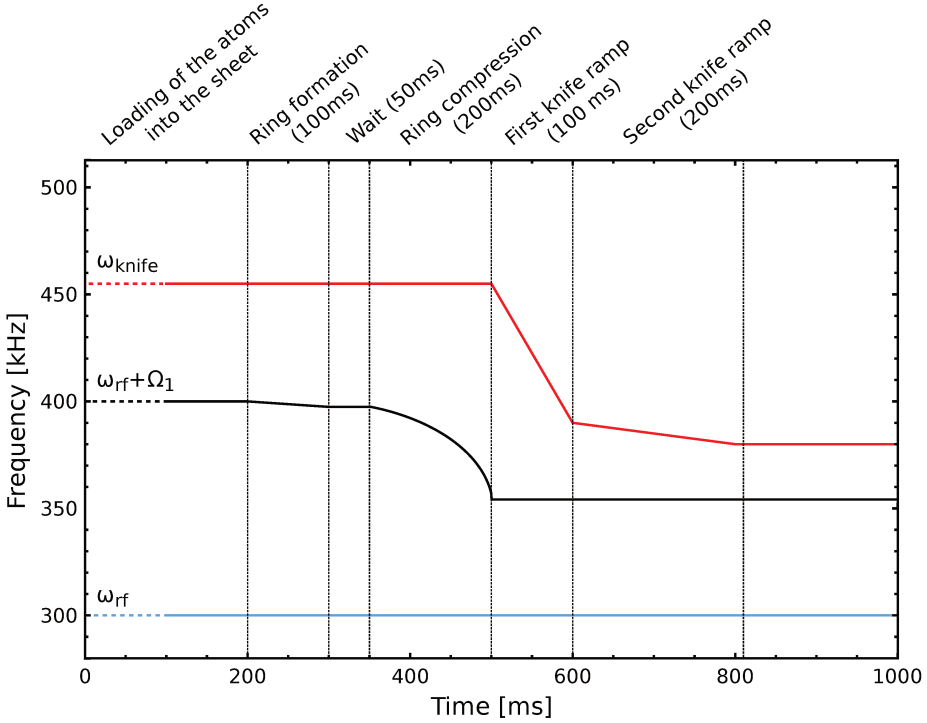

Figure 5.18 — Evolution of the knife frequency during the sequence, compared to the evolution of the Rabi coupling in the ring – plotted with an offset ω_{rf}. The depth of the trap is $\omega_{\mathrm{knife}} - \Omega_1 - \omega_{\mathrm{rf}}$ (see section 3.2.4). The different sequences to load and cool down the atoms in the ring are also indicated, with the corresponding timings.

Profile of the condensed annular gas

It would be useful to be able to measure properly the temperature and condensed fraction of the final gas, but we currently lack a proper model to analyze the profile of the ring measured after time of flight. Still, Murray *et al.* [143] computed the profile of a ring-shaped BEC after TOF seen from above using Gross-Pitaevskii equation, and we can already get expectations from it. In the absence of rotation, such a gas already has a bimodal profile (see figure 5.19): one part comes from the overall BEC expansion, and we also see an interference peak appearing in the center of the gas corresponding to constructive interferences between the

different parts of the ring, see section 4.1.3. In the presence of a thermal fraction, we would thus need a trimodal fit. Avinash Kumar and Romain Dubessy implemented Gross-Pitaevskii simulations of the atomic profile, which could help to discriminate and measure properly the different contributions, but this is still work in progress. For now, we can only say that we see no thermal fraction in the ring (both parts of the BEC expansion being anisotropic, unlike the thermal part, we can discriminate between them).

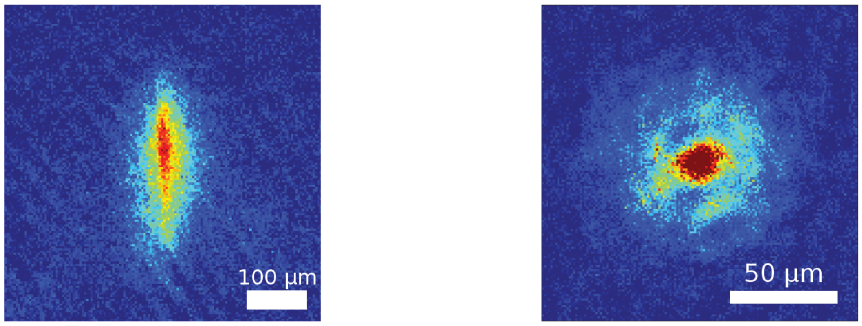

Figure 5.19 — Expansion of a ring-shaped BEC after time-of-flight, in the absence of rotation. Left: seen from the side after 23 ms TOF; right: seen from above, after 10 ms TOF. In both cases, we see a central interference peak.

5.3.3 Measurement of the oscillation frequencies

Vertical oscillation in the double light sheet

The vertical oscillation frequency in the light sheet is measured through the dipole motion of an atomic cloud evolving in the light sheet alone. To this aim, we load the atoms in the light sheet without making a ring, and then turn off the bubble trap. However, turning off the bubble trap abruptly would lead to *three* clouds evolving together within the light sheet (the atomic dressed state gets projected on $m = -1, 0$ and $+1$, cf section 3.4.3): we thus need to perform an "undressing" procedure before letting the cloud oscillate.

To do so, we increase the vertical bias field to shift the resonant surface far away above the light sheet, while the atoms remain confined by the dipole potential. In this way, we rotate the dressed state to align it with the static field (cf equation (2.35): we go from $|\delta| \ll \Omega$ to $|\delta| \approx \Omega$, thus θ goes from $\pi/2$ to 0), and we then bring all atoms in the same bare magnetic state ($|+1\rangle_\theta$ becomes $|+1\rangle_z$). We then switch off the RF field while keeping all atoms in the same Zeeman substate; the atoms get trapped in a combination of the double light sheet and the quadrupole trap (the sheets ensure vertical confinement and the quadrupole creates radial confinement), as shown on figure 5.20.

Since the quadrupole field still attracts the atoms to its center, the potential minimum in the vertical direction isn't exactly at the center of the light sheet at that time. To excite the vertical dipole motion, we then simply switch off the quadrupole field: the atoms oscillate around the minimum of the light potential. We let them evolve for some time, switch off the sheet too and measure the position of the atomic cloud after a fixed time-of-flight: this allows us to measure precisely (better than 1%) the vertical trapping frequency in the dipole trap alone (figure 5.21). We also measured the dependence of ω_z with respect to the light sheet

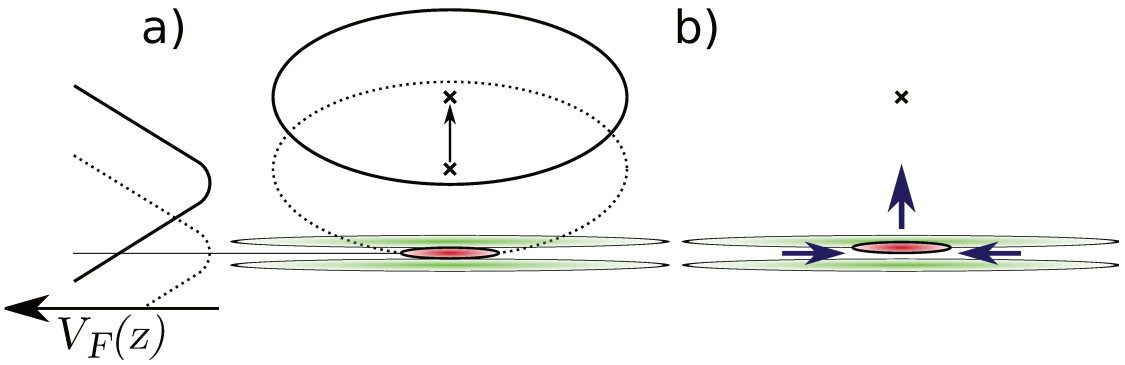

Figure 5.20 – Loading of the "sheet plus quadrupole" trap, starting from the double light sheet loaded from the bubble trap. In a first step (a), the bubble is lifted by applying a vertical bias field; the sheet confinement being much stronger than the quadrupole attraction the atoms stay trapped between the two sheets. The atoms thus get out of resonance, and the dressed state now coincides with the low-field seeker bare state. The RF field can then be turned off (b), and all atoms stay in the state attracted by the zero of the quadrupole (the corresponding forces are represented by the dark blue arrows). Vertically, the atoms stay trapped in the sheet, slighly off-centered due to the attraction of the quadrupole. When the latter is turned off, the atoms then ocillate vertically. Radially, the quadrupole attracts the atoms to the center of the light sheet, which creates a weak confinement (typically 10 Hz at low gradient).

power and verified that we had the expected $\sqrt{P_{\mathrm{LS}}}$ scaling. In the end, the maximal frequency we are able to achieve is 2.72(2) kHz.

The possibility to measure precisely ω_z also allows us to achieve a precise tuning of the focus of the last spherical lens, by maximizing the vertical trapping frequency (figure 5.22). The accuracy on the focus of L_4 is much better in this way (compared to the method described in section 5.1.2); we achieve a sensitivity around one tenth of the vertical Rayleigh length $z_{R,z}$ (expected around 150 µm). We could think about measuring $z_{R,z}$ in this way, but it would require additional data points.

Radial oscillation frequency

To measure the radial oscillation frequency, we slightly "shake" the ring radius: we slowly ramp up the dressing frequency by 8 kHz in 9.8 ms to increase the ring radius while keeping the atoms at rest, and the frequency is then ramped down to its initial value in 0.2 ms, too fast for the atoms to follow. The response time of the atoms is around $1/\omega_r \gtrsim 1$ ms but the ramp is still slow enough to fullfill the dressing adiabatic condition ($\dot{\delta}/\Omega_1^2 = 2.5 \times 10^{-3}$). The atoms are then in the ring we want to characterize but away from their equilibrium value, and start to oscillate. Choosing a frequency sweep much smaller than Ω_1 ensures that the oscillation happens in the harmonic part of the trap. We let them oscillate during a given time, and then take a picture from above; we expect to see the observed radius oscillate. As the in situ oscillation has a too small amplitude to be detected with a satisfying precision, we perform a small time-of-flight of 3 ms before taking the picture to increase the signal amplitude. Too long time-of-flight has to be avoided to ensure that the opposite sides of the ring never overlap. Typical results are shown on figure 5.23. We observe an oscillation of the

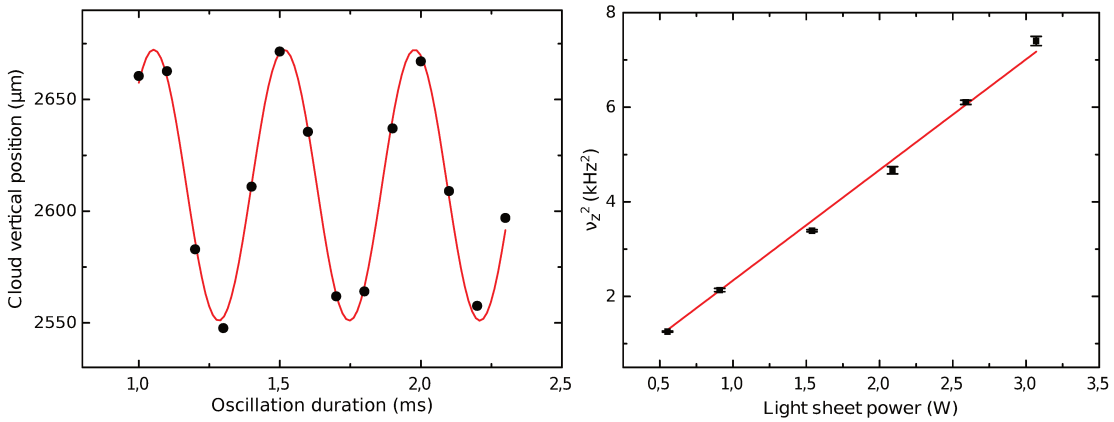

Figure 5.21 — Left: Oscillation of the cloud in the light sheet properly focused, for 20% of the maximal power, measured after 23 ms time-of-flight; the extracted frequency is 1.46(1) kHz. Right: Square of the measured frequency as a function of the power in the light sheet, measured after the phase plate. The real power on the atoms is probably slightly smaller due to losses on the next optical elements – the beam then passes through a lens, is reflected on a polarizing beamsplitter and goes through the first window of the science cell. We find the expected linearity.

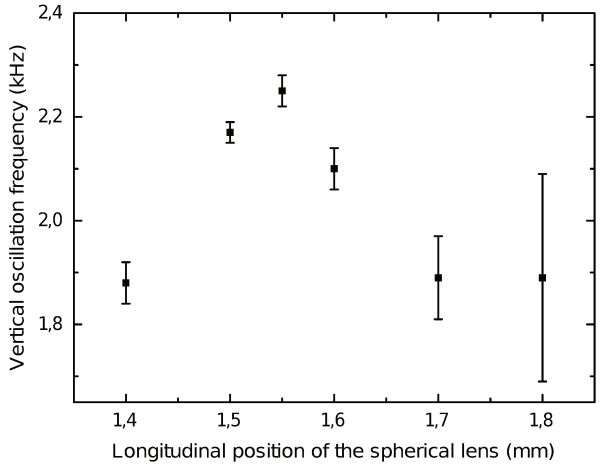

Figure 5.22 — Evolution of the measured vertical trapping frequency with the longitudinal position of L_4. The error bars are given by the fit of ω_z, similar to the one shown on figure 5.21 (left); these data were taken early after implementing the light sheet and we improved significantly our sensitivity in the determination of ν_z since then, explaining why the uncertainties are much larger here. The evolution of ω_z is supposed to follow expression (4.19), but we have too large error bars and/or not enough points to verify it accurately.

ring radius as expected, but we also see that the different parts of the ring are not in phase. To understand that in more details, we analysed the pictures by separating angular regions. We measure the oscillating frequency within each region, and we then compare the different results.

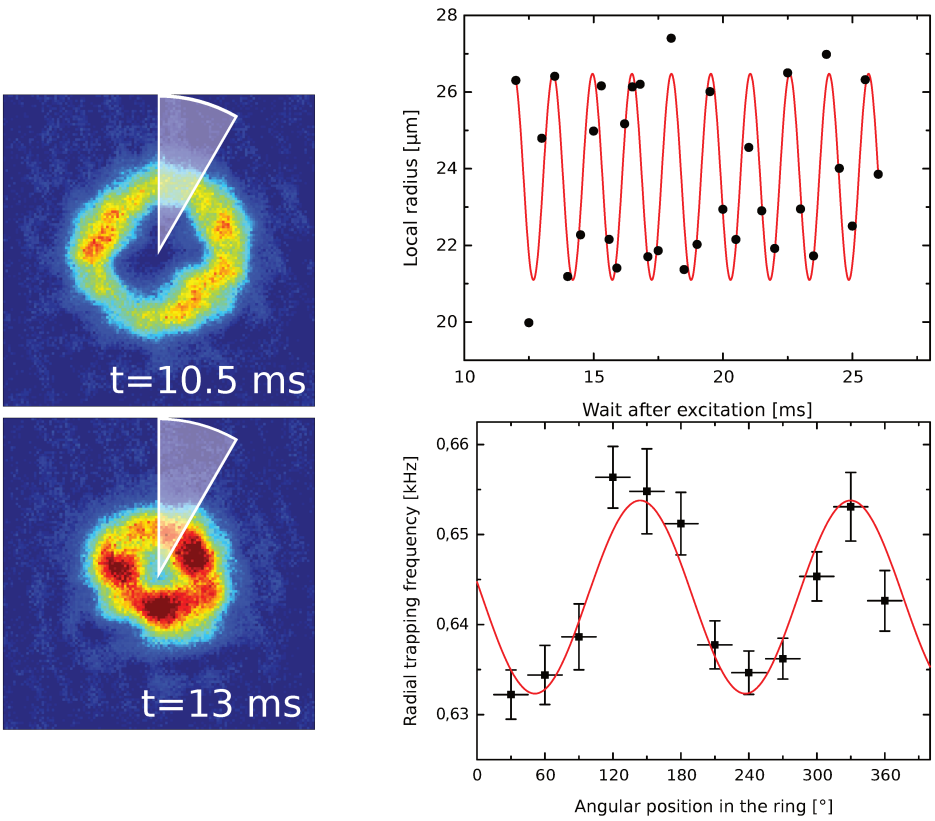

Figure 5.23 — Left: pictures of the oscillation of the ring, taken after a short 3 ms TOF. The radius of the ring oscillates, but it doesn't seem round anymore, indicating a dephasing between the different part of the rings. To look for this effect more in detail, we thus compute the *local* frequency, measured on small angular section of the ring (in white). Right, top: oscillation of the ring radius measured on a 30° wide region. The radius is measured by computing the distance between the center-of-mass of the whole ring and the center-of-mass of the atoms in the chosen region. We measure a 656(3) Hz frequency. Right, bottom: evolution of the measured frequency along the ring. On each angular region we measure the oscillation frequency as above. Horizontal lines indicates the angular domains over which the frequency was computed; vertical error bars are the errors given by the fits. The average radial frequency is 643(1) Hz for an expected frequency of 590 Hz. The red line is a sine fit to the data.

The average measured frequency, 643(1) Hz, is a bit larger than the frequency we would expect from equation (4.20), 590 Hz. We might note that this 10% discrepancy goes in the same direction that the 10% discrepancy on the expected radius (cf section 5.3.1). A possible explanation would be a drift in the quadrupole gradient or the control of the current in the coils since the corresponding calibration in 2011.

We also see an angular dependence of the frequency along the ring, with an identical frequency for places facing each other in the ring (a sine fit of the frequency evolution gives a 185(8)° period). The difference in frequency cannot be explained by inhomogeneities of the Rabi coupling in the ring: the coupling difference that would explain such inhomogeneities, around 6 kHz between points located at 90° from each other, would lead to large density inho-

mogeneities in the ring and would be seen directly on the ring profile at rest. Measurements of the radial frequency with a thermal cloud in the ring, without lowering the knife after the rinc compression ramp, lead to similar results. We intend in a near future to try measuring the radial frequency by exciting the parametric resonance of the ring (an oscillation of the ring radius at $2\omega_r$ should lead to large heating of the gas, even for small amplitude) to see if the results are identical.

5.3.4 Lifetime and heating rate

While working on the optimization of the ring, we realized that the lifetime and the heating rates in our trap were highly unsatisfactory, respectively less than 1 s and up to several microkelvin per second. This led to significant work in order to understand the phenomena leading to losses and heating in the ring.

Characterization of the noise and expected heating

To understand better the heating rate, we tried to separate the two parts contributing to the trap to see where the heating and losses come from:

- We observed the behavior of the "dressed part" of the trap by preparing dressed traps at the bottom of the bubble, with twice less current and Rabi coupling compared to the ring, to mimic the local magnetic gradient and coupling of the ring. In this trap, we observed very large lifetimes ($\sim 100\,\mathrm{s}$) and a heating rate around $10\,\mathrm{nK \cdot s^{-1}}$.

- We tried to isolate the behavior of the double sheet by measuring heating rates in the double sheet plus quadrupole trap (cf section 5.3.3). We measured initially a heating rate ranging between typically 10 and $100\,\mathrm{nK \cdot s^{-1}}$ depending on the laser power, that we were able to completely suppress by a careful mechanical isolation of the experiment (building a better isolation box around the experiment and displacing some fans, see below). The lifetime in this trap after working on heating prevention is around 5 to 10 s for maximal laser power, but it is probably unrelated to the lifetime in the ring trap as the radial confinement is extremly different.

To understand things better, we measured the noise spectrum of the trapping laser: both its power and beam-pointing fluctuations can cause heating of the trapped cloud, and the beam-pointing fluctuations can also lead to radial frequency and position fluctuations (see next section). The power noise can be easily measured using a photodiode; the beam-pointing noise is measured using a quadrant photodiode on which we image the focal point of the beam.

The measured values did not explain the high heating rate we observe in the light sheet and the ring: the heating rates that we deduce from these measurements are extremely low – the main source of noise seems to be the the position noise of the light sheet, leading to $2.2\,\mathrm{nK \cdot s^{-1}}$ at maximal light sheet power. However, we identified two fans that were placed on RF amplifiers to cool them down as a significant source of beam pointing noise[11] (see figure 5.24). We also tried to track other noise sources in the room by looking for modifications in the light sheet position noise power spectrum after turning off different devices but saw nothing significant.

11. Placing the RF amplifiers as close as possible to the experiment to avoid long cables and reduce leakage of RF photons is a good idea, but if they need fans to be cooled, they should not be placed on the optical table to avoid vibrations!

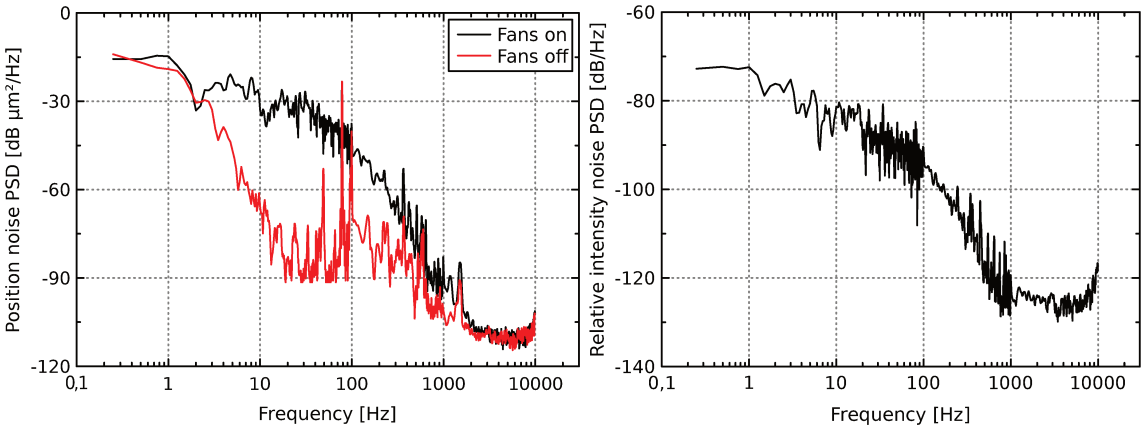

Figure 5.24 — Left: Measurement of the position noise power spectral density in the light sheet, performed with a quadrant photodiode. The black and red spectra are taken in the same conditions, except for two fans placed on the optical table that were turned off for the red spectrum. We see a drop of up to 60 dB in the position noise at low frequency. Right: Measurement of the relative intensity noise power spectral density of the light sheet beam. The beam is turned on at full power, and we measure the power fluctuations of a leakage of the beam through a mirror.

Detailed analysis of the noise sources

Let us discuss the (many) different possible heating sources on our experiment.

- **Photon scattering** from the light sheet can be a source of heating. In principle, the use of blue-detuned rather than red-detuned light sheet allows to reduce a lot this heating, because the atoms are placed in an intensity minimum. The scattering rate for atoms in the vertical ground state or for a thermal gas are respectively given by [106, 161]:

$$\Gamma_{\mathrm{sc},0} = \frac{\Gamma\omega_z}{4\delta_L}, \qquad \Gamma_{\mathrm{sc,th}} = \frac{\Gamma k_{\mathrm{B}} T}{2\hbar\delta_L}, \tag{5.12}$$

  where Γ is the natural linewidth of the D transition and δ_L the detuning between the light sheet and the transition. The corresponding increase in temperature is then $\langle\dot{T}\rangle = 2T_{\mathrm{rec}}\Gamma_{\mathrm{sc}}$ with T_{rec} the recoil temperature of the D transition, equal to 360 nK. For a thermal gas at a temperature $T = 100\,\mathrm{nK}$, the expected heating rate is $1\,\mathrm{nK}\cdot\mathrm{s}^{-1}$; in the vertical ground state and for the maximal vertical trapping frequency $\nu_z = 2.7\,\mathrm{kHz}$, we expect $0.6\,\mathrm{nK}\cdot\mathrm{s}^{-1}$. These expressions however suppose that the atoms are at the center of the light sheet; the presence of gravity could displace them towards regions with higher intensity and increase the scattering rate. For our typical parameters the corresponding shift $\delta z = -g/\omega_z^2$ is smaller but comparable to the size of the vertical harmonic oscillator (0.11 µm compared to 0.28 µm for $\nu_z = 1.5\,\mathrm{kHz}$), which should lead to a small increase of the heating rate, by a factor $1 + 2\delta z^2/d_z$ [124] (this corresponds typically to a 30% increase).

- **Intensity fluctuations** of the light sheet ("power noise") cause variations of the vertical oscillation frequency, leading to a parametric heating in the trap. The temperature increases exponentially, with a heating rate depending on the fluctuations at twice the

trapping frequency [162]. Writing $\epsilon(t)$ the relative fluctuations of ν_z^2: $\nu_z^2(t) = \nu_z^2(1+\epsilon(t))$, this heating rate reads:

$$\Gamma_I = \pi^2 \nu_z^2 S_\epsilon(2\nu_z), \tag{5.13}$$

where S_ϵ is the power spectral density of the stiffness relative noise (in Hz^{-1}), defined as:

$$S_\epsilon(\nu) = 4\int_0^{+\infty} d\tau \cos(2\pi\nu\tau)\langle\epsilon(t)\epsilon(t+\tau)\rangle; \tag{5.14}$$

in the case of light intensity, S_ϵ is equal to the relative intensity noise of the beam:

$$S_\epsilon(\nu) = \frac{4}{\langle I\rangle^2}\int_0^{+\infty} d\tau \cos(2\pi\nu\tau)\langle I(t)I(t+\tau)\rangle. \tag{5.15}$$

Using a photodiode, we measured the relative intensity noise PSD, which is equal to $-125\,\mathrm{dB}\cdot\mathrm{Hz}^{-1}$ in the 1 kHz–10 kHz range (see figure 5.24). If the light sheet is turned on at maximal power, leading to $\nu_z = 2.7\,\mathrm{kHz}$, the corresponding time constant is around $4\times10^4\,\mathrm{s}$: the effect of power noise should therefore be extremely weak.

- **Position fluctuations** of the light sheet ("position noise") also generate heating. This heating is linear and depends on the noise at the trap frequency [162]. The increase in energy reads:

$$\langle\dot{E}\rangle = \frac{1}{4}M\omega_z^4 S_z(\nu_z), \tag{5.16}$$

where S_z is the position noise power spectral density, in $\mathrm{m}^2\cdot\mathrm{Hz}^{-1}$; its measurement can be seen on figure 5.24. For a vertical trapping frequency of 2.7 kHz, this noise is approximately $-110\,\mathrm{dB}\cdot\mu\mathrm{m}^2\cdot\mathrm{Hz}^{-1}$, leading to an increase in energy of $k_\mathrm{B}\times2.2\,\mathrm{nK}\cdot\mathrm{s}^{-1}$. For a vertical trapping frequency of 1.2 kHz, corresponding to 20% of the maximal laser power, there is a peak on the noise PSD, which is approximately equal to $-90\,\mathrm{dB}$; the corresponding expected heating rate is $8\,\mathrm{nK}\cdot\mathrm{s}^{-1}$.

To the heating coming from the light sheet, we can add three "secondary" heating sources that specifically come from the way we achieve our ring:

- The position fluctuations of the light sheet cause fluctuations of the radial trapping frequency, as it changes the local Rabi coupling. From the same reasoning as [162], we can guess that it will generate parametric heating sensitive to the position noise at twice the radial frequency, with a heating rate:

$$\Gamma_z = \pi^2\nu_r^2\left(\frac{1}{\nu_r^2}\frac{\partial(\nu_r^2)}{\partial z}\right)^2 S_z(2\nu_r). \tag{5.17}$$

- The same position fluctuations also cause a variation of the ring radius, and thus generate a *radial* position noise. Again, reasoning like [162] suggests a linear heating depending on the sheet position noise at the radial frequency:

$$\langle\dot{E}\rangle_z = \frac{1}{4}M\omega_r^4\left(\frac{\partial r_0}{\partial z}\right)^2 S_z(\nu_r). \tag{5.18}$$

If the ring is at the equator, the derivative of r_0 is zero and this heating source then cancels. If the ring is above or below the light sheet ($z \neq 0$), we have to take into

account the evolution of both the ring radius and the radial frequency with z. We have $r_0 = \sqrt{r_b^2 - 4z^2}$, and its derivative with respect to z is then equal to $-4z/r_0$. The value of $\omega_r(z)$ is given by expression (4.21), and equation (5.18) becomes:

$$\langle \dot{E} \rangle_z = 4M\omega_r^4(z)\frac{z^2}{r_0^2} S_z(\nu_r(z)), \tag{5.19}$$

or equivalently:

$$\langle \dot{E} \rangle_z = 4M\omega_{r,0}^4 \frac{z^2}{r_b^2} \frac{1-\frac{2z}{r_b}}{1+\frac{2z}{r_b}} S_z(\nu_r(z)) \underset{z \ll r_b}{\simeq} 4M\omega_{r,0}^4 \frac{z^2}{r_b^2} S_z(\nu_r), \tag{5.20}$$

where $\omega_{r,0} = \omega_r(0)$ is the radial trapping frequency at the equator. Equation (5.17) also becomes:

$$\Gamma_z = \frac{\omega_r^2(z)}{4r_b^2} \frac{1}{\left(1+\frac{2z}{r_b}\right)^2} S_z(2\nu_r(z)) = \frac{\omega_{r,0}^2}{4r_b^2} \frac{1}{1+\frac{2z}{r_b}} S_z(2\nu_r(z)). \tag{5.21}$$

For our measured values, the corresponding heating rate and lifetime are respectively lower than $0.1\,\mathrm{nK \cdot s^{-1}}$ and on the order of $1 \times 10^6\,\mathrm{s}$, and these effects can therefore be completely neglected.

- The power fluctuations of the double light sheet will also lead to a position noise, as the vertical position of the atoms depends on the light sheet power due to the gravitational sag. The vertical position of the atoms in the double sheet compared to its center reads $\delta z = -g/\omega_z^2$. Following the same reasoning as previously, one can expect a linear heating:

$$\langle \dot{E} \rangle_z = \frac{1}{4} M g^2 S_\epsilon(\nu_r(z)). \tag{5.22}$$

The corresponding heating rate is on the order of $10^{-4}\,\mathrm{nK \cdot s^{-1}}$ and is therefore completely negligible. One could also think that if the atoms are not at the equator, the noise on the vertical position will also lead to radial position noise as well as fluctuations of the radial trapping frequency, but since the vertical position fluctuations are extremely weak these noise sources can probably be safely ignored.

Finally, the effect of fluctuations of the dressed trap part can be computed, using again the same principle:

- The **frequency noise** of the RF source will cause a fluctuation of the ring radius, and a position noise depending on the relative frequency noise of the RF source $S_{\nu_{\mathrm{rf}},\mathrm{rel}}$ at the radial frequency:

$$\langle \dot{E} \rangle_{\delta\nu_{\mathrm{rf}}} = \frac{1}{4} M\omega_r^4(z) \frac{r_b^4}{r_0^2} S_{\nu_{\mathrm{rf}},\mathrm{rel}}(\nu_r), \tag{5.23}$$

$$\langle \dot{E} \rangle_{\delta\nu_{\mathrm{rf}}} = \frac{1}{4} M\omega_{r,0}^4 r_b^2 \frac{1+\frac{2z}{r_b}}{1-\frac{2z}{r_b}} S_{\nu_{\mathrm{rf}},\mathrm{rel}}(\nu_r(z)) \underset{z \ll r_b}{\simeq} \frac{1}{4} M\omega_{r,0}^4 r_b^2 S_{\nu_{\mathrm{rf}},\mathrm{rel}}(\nu_r(z)). \tag{5.24}$$

To have a heating rate $\langle \dot{E} \rangle_{\delta\nu_{\mathrm{rf}}} < k_{\mathrm{B}} \times 1\,\mathrm{nK \cdot s^{-1}}$ with our trapping frequencies, the relative frequency noise of the RF source has to be lower than $-118\,\mathrm{dB \cdot Hz^{-1}}$. In

addition, if the ring is not at the equator, it will cause fluctuations of the radial trapping frequency, with a resulting parametric heating rate:

$$\Gamma_{\delta\nu_{\rm rf}} = \nu_r^2(z)\left(\frac{z}{r_b+2z}\right)^2 S_{\nu_{\rm rf},\rm rel}(2\nu_r), \tag{5.25}$$

$$\Gamma_{\delta\nu_{\rm rf}} = \omega_{r,0}^2\frac{z^2}{r_b^2}\frac{1}{1+\frac{2z}{r_b}}S_{\nu_{\rm rf},\rm rel}(2\nu_r(z)) \underset{z\ll r_b}{\simeq} \omega_{r,0}^2\frac{z^2}{r_b^2}S_{\nu_{\rm rf},\rm rel}(2\nu_r(z)). \tag{5.26}$$

If the initial temperature of the cloud is 100 nK and supposing a vertical offset of 1 µm, a heating rate lower than $1\,\mathrm{nK}\cdot\mathrm{s}^{-1}$ requires a relative frequency noise lower than $-65\,\mathrm{dB}\cdot\mathrm{Hz}^{-1}$ (note that this requirement is equivalent to having a time constant larger than 100 second).

- The **amplitude noise** of the RF source will cause fluctuations of Ω_1 and therefore of the radial frequency, and generate parametric heating with a time constant:

$$\Gamma_{\delta a} = \frac{\omega_r^2(z)}{4}S_{\rm a,rel}(2\nu_r) = \frac{\omega_{r,0}^2}{4}\left(1+\frac{2z}{r_b}\right)S_{\rm a,rel}(2\nu_r(z)) \tag{5.27}$$

where $S_{\rm a,rel}$ is the amplitude noise of the RF source. Supposing an initial temperature of 100 nK, the relative amplitude noise required to have a heating rate lower than $1\,\mathrm{nK}\cdot\mathrm{s}^{-1}$ is $-85\,\mathrm{dB}\cdot\mathrm{Hz}^{-1}$.

- The **fluctuations of the magnetic gradient** will cause both fluctuations of the ring radius and of the trapping frequency, leading to a linear heating:

$$\langle\dot{E}\rangle_{\delta\alpha} = \frac{1}{4}M\omega_r^4(z)\frac{r_b^4}{r_0^2}S_{\alpha,\rm rel}(\nu_r(z)), \tag{5.28}$$

$$\langle\dot{E}\rangle_{\delta\alpha} = \frac{1}{4}M\omega_{r,0}^4 r_b^2\frac{1+\frac{2z}{r_b}}{1-\frac{2z}{r_b}}S_{\delta\alpha}(\nu_r(z)) \underset{z\ll r_b}{\simeq} \frac{1}{4}M\omega_{r,0}^4 r_b^2 S_{\alpha,\rm rel}(\nu_r(z)). \tag{5.29}$$

and a parametric heating with a time constant:

$$\Gamma_{\delta\alpha} = \omega_r^2(z)\left(\frac{1+\frac{3z}{r_b}}{1+\frac{2z}{r_b}}\right)^2 S_{\alpha,\rm rel}(2\nu_r(z)), \tag{5.30}$$

$$\Gamma_{\delta\alpha} = \omega_{r,0}^2\frac{\left(1+\frac{3z}{r_b}\right)^2}{1+\frac{2z}{r_b}}S_{\alpha,\rm rel}(2\nu_r(z)) \underset{z\ll r_b}{\simeq} \omega_{r,0}^2 S_{\alpha,\rm rel}(2\nu_r(z)) \tag{5.31}$$

where $S_{\alpha,\rm rel}$ is the PSD of the relative noise on the gradient (which should correspond to the relative noise of the current supply). The formula giving the linear heating rate is the same than in the case of RF frequency fluctuations and the requirement on the relative fluctuations is therefore the same: it has to be lower than $-118\,\mathrm{dB}\cdot\mathrm{Hz}^{-1}$ for the linear heating to be lower than $1\,\mathrm{nK}\cdot\mathrm{s}^{-1}$. For the parametric heating, a time constant larger than 100 s requires a relative noise below $-95\,\mathrm{dB}\cdot\mathrm{Hz}^{-1}$.

Due to the low heating rate observed in the dressed trap, we however did not investigate these noise sources in detail for now.

Lifetime in the ring

After the heating sources, it is also useful to make the list of the possible origins for atom losses. There are six possible loss sources in our trap, among which two are susceptible to affect us:

- **Tunnelling through the light sheet** should not be a problem, as the barrier height is two orders of magnitude larger than any other energy in the system, and the barrier is also quite thick due to the slow intensity decay of the light sheet for large z.
- **Collisions with the background gas** set the ultimate lifetime of atoms in the trap; in ultra-high vacuum (10^{-11} mbar in the science cell) they are normally negligible – the corresponding lifetime is several minutes and is not limiting in our experiments.
- **Photon scattering** from the light sheet can lead, in addition to heating, to atom losses by a change in the atomic internal state. The scattering rate, given by equation (5.12), is however very small due to the choice of a blue-detuned double sheet, and this effect is negligible.
- **Landau-Zener losses** come from non-adiabatic following of the dressed atomic levels (see 2.1.3); a detailed theoretical description of their behavior can be found in [134]. They depend extremely strongly on the local Rabi coupling, almost creating a threshold effect: if Ω_1 is too low, the lifetime will be extremely small, if it is high enough the corresponding lifetime will be very large and the atomic lifetime will be set by other effects (a modification of Ω_1 by a few 10% can be enough to go from one regime to the other one). For a magnetic gradient $b' = 178\,\mathrm{G}\cdot\mathrm{cm}^{-1}$ horizontally, we usually work with $\Omega_1 = 2\pi \times 50\,\mathrm{kHz}$ (i.e. $\Omega_0 = 2\pi \times 100\,\mathrm{kHz}$ at the bottom of the bubble). At maximal gradient ($b' = 214\,\mathrm{G}\cdot\mathrm{cm}^{-1}$), while the lifetime is only 0.4 s for a 40 kHz coupling, it reaches several seconds for a coupling of 56 kHz; on the other hand, going from 56 kHz to 63 kHz had no aditional effect on the lifetime, which then appears to be limited by three-body losses. We might note that on our measurements the minimum value to have in the ring appears higher than the minimum value that would be required in an equivalent (i.e. same local gradient and local Rabi coupling) bubble trap. Additional work to understand this effect is planned in the near future
- **Three-body recombination** leads to the loss of the corresponding atoms from the trap. They depend only on the local atomic density, and set a definitive limit on the atom number we can expect with a given trapping frequency. The decay reads [163]:

$$\left.\frac{\mathrm{d}N}{\mathrm{d}t}\right|_{3b} = -K_3 \int dV n(t)^3, \tag{5.32}$$

where the coefficient K_3 has been measured by Burt *et al.* [163] to be around $6 \times 10^{-30}\,\mathrm{cm}^6\cdot\mathrm{s}^{-1}$ for a condensed gas of ^{87} Rb in the $F = 1,\ m = -1$ sublevel (for a thermal gas, it is 6 times larger due to bunching effects). In the ring trap and supposing that the gas is in the 3D regime, expression (5.32) can be rewritten:

$$\left.\frac{\mathrm{d}N}{\mathrm{d}t}\right|_{3b} = -K_3 \left(\frac{M\omega_r\omega_z}{4\pi^2 r_0 g}\right) N^2(t), \tag{5.33}$$

and in the absence of other loss sources, $N(t)$ therefore reads:

$$N(t) = \frac{1}{K_3 \left(\frac{M\omega_r\omega_z}{4\pi^2 r_0 g}\right) t + \frac{1}{N(0)}}. \tag{5.34}$$

- **The RF knife** could cause losses if the heating rate is large. This effect, however, has not been investigated for now.

For now, the lifetime in the ring seems to be limited by these three-body losses. A measurement of the lifetime in the ring trap is displayed on figure 5.25; an analysis of the data using formula (5.34) displays a very good agreement with the data. However, the corresponding lifetime is not very large, and suggests that increasing the chemical potential as much as possible through compression in order to overcome the light sheet defects can also be dangerous because it strongly increases the three-body losses, and we will have to search for the optimal tradeoff at some point. The observed lifetime of several seconds is however already large enough to perform experiments in the ring.

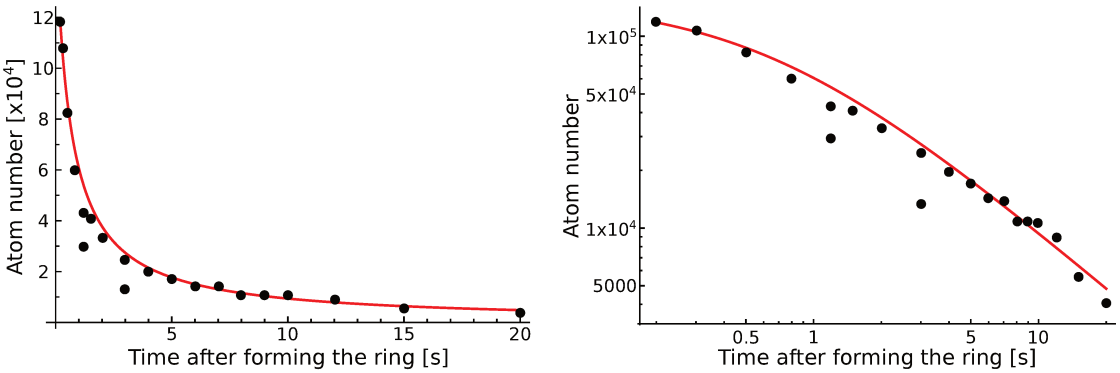

Figure 5.25 — Lifetime of the ring for $I_{\mathrm{quad}} = 110\,\mathrm{A}$, $\Omega_1 = 2\pi \times 56\,\mathrm{kHz}$ measured in the ring (100 kHz at the bottom) and low light sheet power (20% of the maximal power), plotted in linear scale (left) and logarithmic scale (right). The red line is deduced from equation (5.34) using the first datapoint as an initial parameter; no free parameter is used. Note that these data were taken with a higher gradient than what is described in most of section 5.3, $b' = 214\,\mathrm{G \cdot cm^{-1}}$ instead of $178\,\mathrm{G \cdot cm^{-1}}$. The ring radius was measured on the pictures to be equal to 17.7 µm, the vertical trapping frequency was measured later to be equal to 1.46 kHz, and the value for $K_3 = 5.8 \times 10^{-42}\,\mathrm{m^6 \cdot s^{-1}}$ is taken from [163] (note that the relative uncertainty on this last value is 33%). The radial trapping frequency has not been measured in these experimental conditions; I used as an input the frequency expected theoretically with a scaling factor 643/590 corresponding to the difference between the measured frequencies and the expected frequencies, see 5.3.3.

5.3.5 Conclusion

We still have some characterization work left to understand the behavior of the radial frequency and the exact ring dimensions, and we can probably find more optimal parameters to minimize the three-body losses in the ring while keeping a good regularity. However, we are now able to generate a ring trap good enough for performing experiments: the three requirements that were announced at the beginning (ultracold temperature, good regularity, decent lifetime) are now fullfilled. We also succeeded in generating a superflow in the trap; this point will be discussed in the next chapter.

5.4 Future developments: towards lower dimensions

I will conclude this chapter by a discussion about lower-dimensional regimes (2D and 1D ring). The possibility to access these regimes is one of the main interests of our method for realizing ring traps, and they now seem reasonably accessible; I will discuss here the conditions and methods to reach them.

5.4.1 Towards quasi-2D rings

The 2D regime we can expect to reach is the "saturnian ring" configuration (the "wrapped sheet" configuration would require a radial trapping frequency significantly larger than the vertical trapping frequency and would be much more difficult to reach). Reaching this quasi-2D regime requires a chemical potential and a temperature smaller than the vertical trapping frequency. The maximal vertical frequency we can achieve is 2.7 kHz. For the moment, we lack a proper measurement of the ring temperature: the ring profile measured after time-of-flight indicates that the temperature of the gas is below 280 nK as the gas stays condensed with 2×10^4 atoms (using formula (4.22) we estimate the critical temperature for this number of atoms to be around 280 nK), but this doesn't tell us whether the temperature is lower than the vertical trapping frequency (it corresponds to $k_B T/h \approx 5.8$ kHz). The chemical potential in the ring ranges between 1.5 and 4.5 kHz depending on the number of condensed atoms in the trap and the vertical trapping frequency[12], meaning that we should be very close to the two-dimensional regime. We can try to reduce it further by removing atoms from the trap or increasing the ring radius to lower the density. A difficulty can come from keeping a reasonable heating rate (a high power in the light sheet comes with more heating), and low enough three-body losses. We also have to ensure a good enough homogeneity of the potential: the lower the chemical potential, the better we need the potential to be homogeneous.

5.4.2 Towards quasi-1D rings

Reaching the quasi-1D regime requires the chemical potential and the temperature to be also smaller than the radial trapping frequency. The most favorable configuration to reach this regime corresponds to $\omega_z = \omega_r$. In this case, using equation (4.24), comparing the chemical potential to the trapping frequencies leads to the condition for reaching the quasi-1D regime:

$$\frac{2Na}{\pi r_0} \lesssim 1, \tag{5.35}$$

which appears to be independent from the trapping frequencies. It can even be simply expressed as a condition on the atomic linear density:

$$n_1 = \frac{N}{2\pi r_0} \lesssim \frac{1}{4a}, \tag{5.36}$$

equal to 47 atoms per micrometer. For a ring with radius 20 µm, it corresponds to approximately 6000 atoms, small but detectable. However, it might be useful to increase the chemical potential in order to reduce the relative effect of potential inhomogeneities, which would require to increase the trapping frequency ($\mu_{1D} = 2\hbar\overline{\omega} n_1$), by increasing the magnetic gradient. A stronger trapping would also make it easier to have a temperature lower than $\hbar\overline{\omega}/k_B$; it will however increase the three-body losses and there will probably be, again, a tradeoff to

12. $\mu_{3D} \propto \sqrt{N\omega_z\omega_r}$, see (4.24).

make. By increasing the magnetic gradient and keeping Ω_0^2/b' constant to avoid a too strong increase of the Landau-Zener losses, we can expect to achieve up to $\overline{\omega} = 2\pi \times 1.7\,\mathrm{kHz}$ with only minor modifications of the experimental system (by tripling the magnetic gradient, see later).

5.4.3 Coil heating tests

To increase b', we need to increase the current in the quadrupole coils. This requires a more powerful current supply, and also to be sure that the coils will be able to sustain the target current. We therefore made heating tests to estimate how much current we can put in the coils without risking to damage them.

Realizing heating tests on the real coils would be very dangerous, but we have a spare coil built on the same model than the ones we have on the experiment, on which we could perform tests. To try getting as close as possible to the real system, we did the tests with a pair of additional coils in series with the coil we wanted to test to have similar total electric resistance; all coils were water-cooled similarly to the real experiment, with a water flow adjusted to be identical ($0.9\,\mathrm{L}\cdot\mathrm{min}^{-1}$); the supply cables were also identical (same cable) to the ones we have on the experiment. We used the power supply of the magnetic transport coils[13] to realize the tests; it can deliver up to 400 A and 15 V. Temperature probes were installed on most elements: supply cables, coil, copper wire (downstream from the coil), junction between coil and supply wires.

In a first series of measurements, we measured the equilibrium temperature of the elements for a given current, once the system equilibrated. The first element to change will be the supply cable, which heats up a lot; to perform the experiments beyond 160 A we had to use two cables in parallel to avoid it heating too much. Finally, we were able to put 300 A in the system without suffering too much heating of the different elements: +40 °C in the bare wire, +30 °C in the wires and +25 °C in the coils, see figure 5.26. The limiting factor was then the junction between the two parallel supply cables, meaning that we will have to take care of the junction between the cable and the coil and the real experiment. Using a thermal camera could be useful to track local overheating points in the solderings.

A second set of experiments aimed at measuring the rising and lowering times of the elements' temperature. Indeed, in the real experiments we want to perform, the current in the coils will have to be very high only during a few seconds, with a duty cycle around one minute, meaning that the temporal behavior can be important. These measurements show two categories of behavior:

- For the elements made of hollow wire and water-cooled, the time constants are around 5 to 10 seconds, meaning that the steady state can be achieved during one experimental sequence. However, these elements do not suffer too much heating.

- for the larger, uncooled elements (cables and junctions), the time constants are around a few minutes, meaning that the steady state will never be reached during one experimental sequence. We thus expect that when cycling experiment, they will reach a steady state with a heating proportional to the duty cycle. We could confirm this behavior by applying current pulses lasting 10 s every two minutes and observed that the heating indeed stabilized around 10/120 of the value measured for continuous current.

13. SM15-400 from Delta Elektronika.

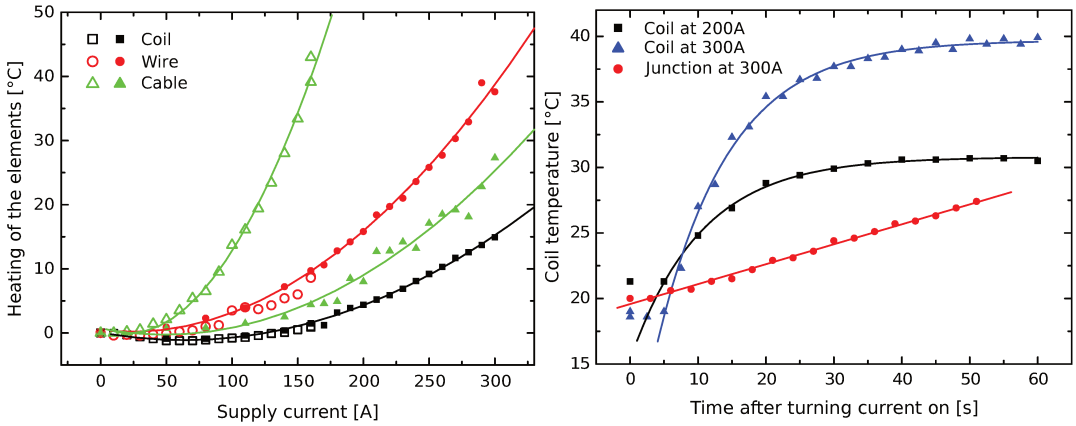

Figure 5.26 — Left: measurement of the steady-state heating (i.e. increase of temperature) of the different elements of the setup (supply cable, bare wire and coil) depending on the supply current. Hollow symbols correspond to data taken with one supply cable, full symbols after doubling it (see text). Solid lines are parabolic fits of the datasets. Right: measurement of the rise time for the current in the coils for 200 and 300 A (both measurements give the same time constant, 10.4(4) s and 10.4(6) s). I also show an equivalent curve for the junction between the cables: we see a linear increase, because the time constant is much larger: data taken for longer evolution, as well as combination of the slope and the steady-state measurement, give a rise time around four minutes.

Both cases suggest that we can go even beyond 300 A without suffering excessive heating. We tried to test that by pushing our supply up to 400 A for short amounts of time (a few seconds), but we were limited by the voltage the supply is able to deliver.

Looking for commercial power supplies, it seems that the final limitation will be the availability of a supply able to deliver enough power with a good enough stability at a reasonable price rather that heating problems; we still should be able to easily double or triple our gradient (provided that we change the supply cables). We will however take care to the evolutions of the magnetic gradient that could happen through possible thermal expansion of the coils for large current.

Chapter 6

Preparation of a persistent flow

Once a satisfying annular gas has been achieved in the ring trap, the next step to study superfluid flow is developing the ability to both generate and detect it. This has been done for our ring, and this chapter will describe it. Its first part will describe the three methods we implemented (or work at implementing) to generate rotation: the first one consists in putting into the ring a local defect that will then be displaced to stir it; the second one relies on imprinting directly onto the gas the phase we want the superfluid to acquire, and the third one consists in rotating the whole "dressed part" of the ring trap. The second part of this chapter will then describe the detection of the obtained flow.

6.1 Experimental tools for rotating the ring

6.1.1 The laser stirrer

A first method that allows to generate superfluid flow in a ring is to focus onto it a small blue-detuned laser beam whose position can be controlled, allowing in this way to displace an obstacle within the fluid [144,145,155]. Since the excitation is *local*, it is also a useful tool to probe the superfluid critical velocity and has been widely used in that purpose [47,67,164]. We have implemented and tested such a system on our experiment, that I will describe in the following.

Experimental system

The principle of the system is quite simple: a blue-detuned laser beam goes through a pair of successive crossed acousto-optical modulators[1] (AOMs), each of them deflecting the beam (we use the first order of both AOMs) from a certain angle that depends on its applied frequency, and the beam is subsequently focused onto the atomic gas. Adjusting the frequency of the AOMs allows to modify the impact position onto the atoms, and thus to displace the stirring beam within the gas (figure 6.1).

We want the final spot to be highly focused (around 5 µm waist), and the required power is rather weak (less than 10 mW); a leakage of the ALS laser beam used to generate the plug ($\lambda = 532\,\mathrm{nm}$) is then sufficient. For space reasons, there is 20 cm between the last lens of

1. DTSXY-250-532 from AA opto-electronic

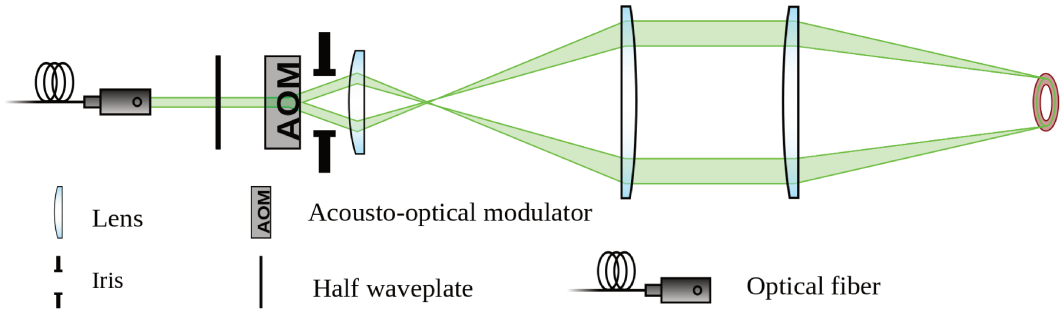

Figure 6.1 — Principle of the laser stirrer. A blue-detuned laser beam goes through a pair of AOMs and is then focused onto the atoms. Each AOM generates a diffracted beam whose position depends on the AOM frequency; we only use the doubly-diffracted beam (an iris filters the 0^{th} order of both AOMs). Adjusting the frequency of each AOM allows to displace the beam spot in the $x-y$ plane and to generate arbitrary time-varying position patterns. Mirrors are nor represented; in practice the setup is folded on itself for space reasons, and a dichroic mirror is placed between the last lens and the atoms to send the beam onto the atoms (the vertical probe beam passes through the same mirror). Only one axis is represented here (the other one is identical).

the setup and the atoms, making it difficult to focus the beam efficiently; we thus strongly defocus the beam after it gets deflected, before focusing it onto the atoms. At the output of the fiber, the beam has a 0.4 mm waist; after the AOMS a $f = 17.8$ mm achromatic doublet[2] expands it and it is then collimated by a $f = 250$ mm lens[3]. The beam waist is then around 5.6 mm; a $f = 200$ mm lens[3] then focuses the beam onto the atoms, with a final waist of 6 µm (the corresponding Rayleigh length is 212 µm). The final lens is placed in a threaded mount that can be rotated to adjust the beam focus[4].

Controlling the beam position

The RF signal sent to the AOM comes from a DDS chip[5] driven by a microcontroller[6], in a setup similar to the one described in section 3.3 ; the output signal then goes through two fixed gain amplifiers[7] before going to the AOMs. The setup has been built at the electronics workshop of the lab. Again, the choice of a digital synthesizer (rather than analog) gives a better frequency stability and therefore a lower position noise for the final beam. We compute and load in advance into the microcontroller the list of pairs of frequencies corresponding to the successive positions the beam will have to take, which are output at a given frequency that we set. After reaching the last position, the system comes back to the first in a closed loop. The frequency of the final motion is thus given by the output rate divided by the number of points in the list. The clock frequency of the microcontroller is 800 kHz, and we lock it on a 8 MHz quartz crystal clock; a trajectory containing 100 frequency couples can be operated up to 130 Hz. The AOMs operate at a central frequency of 80 MHz and have a

2. MAP052550-A from Thorlabs.
3. AC508-250-A and AC508-200-A from Thorlabs.
4. SM2V10 from Thorlabs.
5. AD9959 from Analog Devices, identical to the one used to generate the dressing RF field.
6. MSP430f169 from Texas Instruments.
7. AMPA-B-30 from AA opto-electonic.

50 MHz bandwidth; we calibrated the displacement of the spot as $10.23(8)\,\mu\text{m} \cdot \text{MHz}^{-1}$ and the displacement range of the spot is therefore 250 µm in each direction. Each frequency is encoded on 32 bits, and the precision on the AOM frequencies is below 1 Hz. Up to now, we mostly realized circular trajectories, but such a system can in principle produce arbitrary patterns and allow for optical painting (provided a change in the microcontroller to permit faster operation).

Power stabilization

Changing the AOM frequencies has the drawback of changing the diffraction efficiency; changing the frequency of the first AOM also changes the incidence angle on the second one (and thus, again, its diffraction efficiency), and the reflectivity of the mirrors also changes with the angle of incidence. Ensuring a constant power in the stirrer beam therefore requires a stabilization process.

Although a feedback loop adjusting the intensity in the beam sounds appealing, it would be very difficult to set up, as it requires a reliable error signal. Since the inclination of the beam constantly varies, a glass plate collecting a part of the stirrer beam would have a varying reflectivity and the intensity of the deflected beam would not directly match the intensity in the main beam.

Instead, we rely on the fact that the fluctuations to correct depend *only* of the beam's angle: we can thus expect to achieve a complete cartography of the system, measuring the obtained power in the beam for each possible position. We can thus adjust the power of the RF applied to the deflecting AOMs to ensure that the power in the final stirring beam is always the same. Using this method, we reduced the power fluctuations in the beam to 4% peak-to-peak with a standard deviation lower than 1% against respectively 20% and 6% in the absence of correction. The power spectral density with and without correction is shown on figure 6.2.

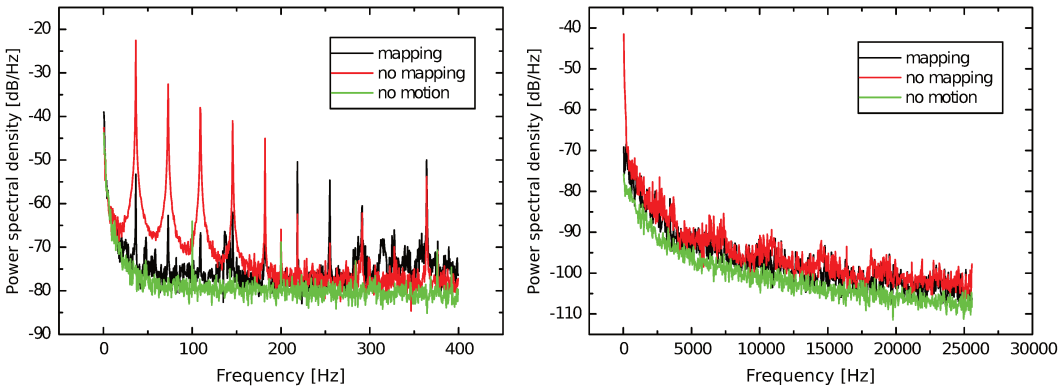

Figure 6.2 — Power spectral density of the relative intensity noise in the stirrer beam, measured with (black) and without (red) power stabilization process, between 10 and 400 Hz (left) and between 10 Hz and 25 kHz (right). The stirrer rotates at 37 Hz, and we see the peaks corresponding to its harmonics – the power stabilization doesn't suppress them, but we have a noise reduction up to 20 dB. The green line shows equivalent measurement achieved for a static beam, with constant orientation.

Alignments

Our vertical imaging setup allows us to monitor the profile of the stirrer beam at the position of the atoms (see fig. 6.3a). An interference filter can be placed onto the imaging axis to allow the 780 nm imaging light to pass while preventing the 532 nm light to reach the camera, or removed to allow taking pictures of the green light. In the first case, we can image the atoms in the presence of the stirrer beam, hoping for example to see a hole in the atomic cloud (6.3a). In the second case this is not possible: the stirrer beam is much more focused than the probe beam and saturates the camera if its dynamical range is chosen to image properly the probe. However, it allows to directly image the stirrer beam (figure 6.3b) and compare its position with the position of the atoms measured on pictures taken in the absence of the stirrer.

Aligning the stirrer onto the atoms can then be achieved by using this camera: we align the beam on the position where the atoms would be detected (without the filter). The stirrer beam is then roughly aligned, but still needs careful tuning: after this step, we usually still do not hit the atoms with the stirrer beam.

The fine alignment is then done taking in situ pictures of an atomic cloud at the bottom of the bubble in presence of the beam (with the filter). The first step is to detect the effect of the beam onto the atoms. If the stirrer is left static and turned on with a very high power (around 10 mW, which corresponds to a light shift on the atoms caused by the stirrer of approximately 100 kHz), the cloud is then usually slightly displaced, indicating the relative position of the stirrer compared to the atomic cloud (when the power is large, the beam has an effect even away from its central position, possibly due to the presence of a diffuse light pedestal around the "real" beam). It is also possible to describe circular trajectories at high frequency and look for the heating induced onto the atoms. Once we detect the effect of the stirrer, we try to pierce the cloud with it and adjust the beam position until we hit the center of the cloud (see figure 6.3b). This displacement can be done by changing the frequencies determining the impact point or the angle of the dichroïc mirror sending the beam onto the atoms. The former allows to be easily reproducible and more precise displacements, but the latter can be required to ensure that the cloud is in the center of the region accessible to the stirrer (limited by the AOM's bandwidth).

Beam focus and beam waist measurement

We can also try to use this vertical camera to focus the beam onto the atoms: it is possible to scan the vertical position of the camera to measure the beam profile, and compare the focal point obtained in this way with the camera position for which the imaging focus is correct. The longitudinal position of the last lens can then be adjusted to focus the stirrer properly[8]. These measurements seem to display a weak astigmatismn for the stirrer beam, as well as optical aberrations away from the focal point; the measured waist is around 8 µm. They have, however, to be taken with caution because the vertical camera was built initially to image 780 nm light, and the lenses were chosen with a coating (B coating from Thorlabs) that has a very weak reflectance for 780 nm light (0.2% announced by the manufacturer) but significant reflectance at 532 nm (around 9%), which limits the trust we can put into these images; we also noticed afterwards that some of the pictures used to perform the measurements were saturated, therefore increasing the measured waist. We can also note that due to the finite

8. However, when the screw blocking the lens translation is loosened there is some backlash on the lens lateral position, and the beam lateral alignment then has to be done again.

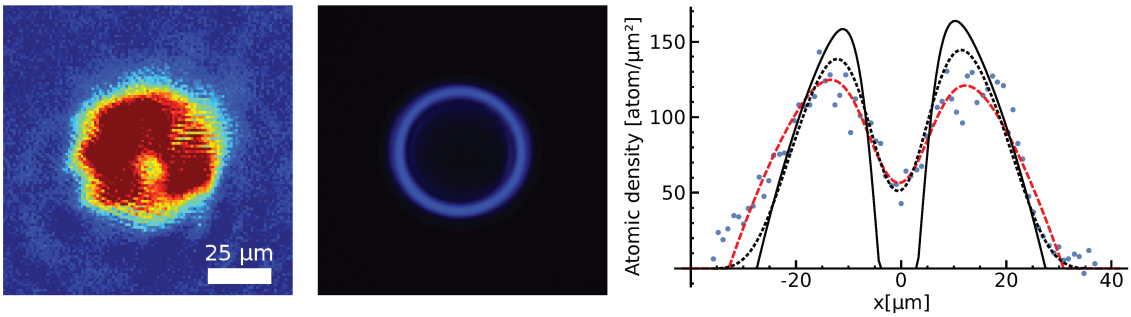

(a) (b) (c)

Figure 6.3 — (a) In situ picture of the atomic cloud in the presence of the stirrer beam, when the stirrer is aligned to hit the center of the cloud. (b) Circular trajectory of the stirrer beam imaged directly onto the vertical camera (in the absence of the filter). (c) Cut into the profile (a), fitted using different methods. The red, dashed line corresponds to a Thomas-Fermi fit of the addition of a parabolic profile to which is superimposed a gaussian profile, without constraint on the different parameters. The black dotted line is an attempt to match the same profile by computing the real atomic density using realistic parameters for the atom numbers, trap frequencies and beam power, and applying a gaussian blurring to take into account the finite optical resolution of the imaging system. The black solid line is the corresponding raw profile, before applying the blurring. While the real cloud is probably largely pierced by the stirrer beam, the hole observed on the pictures still doesn't seem very deep due to the limited optical resolution.

resolution of the imaging system, 4 µm, the lowest waist value we can measure on the camera is $\sqrt{6^2 + 4^2} = 7.2\,\mu\text{m}$.

Another method to achieve the beam focus and measure its waist would rely on the imaging of the condensate pierced by the stirrer: in the Thomas-Fermi regime, its profile should match the profile of the stirrer. Applying a vertical bias field allows to displace the cloud and therefore measure the evolution of the beam waist along its propagation axis. However, the waist measured using this method were significantly larger than expected (between 10 and 20 µm), and proportional to the stirrer beam power... We later realized that since the optical resolution of our imaging system is close to the beam waist, the atomic profile measured on the pictures is dramatically altered compared to the real profile (see figure 6.3c) and the fitted beam waist cannot be trusted. If we compute the expected atomic profiles and apply a gaussian blurring to take into account the imaging resolution, we are able to reproduce profiles that seem to match the measured ones, but the number of parameters that we have to adjust is too large to allow measuring the beam waist in this way with a good precision. These pictures also strongly suggest the presence of a diffuse light pedestal around the stirrer beam, as the Thomas-Fermi radii of the cloud increases way more in the presence of the stirrer beam than what the stirrer itself could cause. A light pedestal accompanying the beam could for example weaken the harmonic confinement, as it would be blue-detuned like the stirrer. These effects still require additional data to be properly understood.

Test of the stirrer: measuring a superfluid critical velocity

To ensure that the stirrer works properly, we used it to measure a critical velocity in the gas, similarly to [47]. We displace the stirrer beam within a very cold gas at the bottom of the bubble, following circular trajectories with 10 µm radius for different frequencies (the Thomas-Fermi radius of the gas is 22 µm). We expect to observe a threshold effect: if the linear velocity of the beam is below the critical velocity, nothing should happen, if it is above we expect to see heating in the cloud. These experiments were done in the presence of a RF knife, and the cloud heating instead translates into atom losses; the experiment was done in a compressed bubble ($b' = 198\,\mathrm{G}\cdot\mathrm{cm}^{-1}$) at 1 MHz dressing frequency; the trapping frequencies are approximately 37.5 Hz radially and 1600 Hz vertically.

The results are presented on figure 6.4: we see a clear threshold at a linear velocity of $0.37(12)\,\mathrm{mm}\cdot\mathrm{s}^{-1}$. The sound velocity is estimated around $2.6\,\mathrm{mm}\cdot\mathrm{s}^{-1}$. It is significantly larger, because our beam is intense enough to significantly lower the local density and then lower the *local* sound velocity; for obstacles whose size is significantly larger than the healing length ξ the dissipation mechanism involves nucleation of vortex-antivortex pairs [12, 165]. Critical velocity experiments performed with ultra-cold experiments typically give values for v_c/c between 0.1 and 0.5 [47,166], and our measurement is also within this range ($v_c/c \approx 0.14$). The critical velocity depends on many parameters (whether the cloud is completely pierced or not, hole size, density slope on the edge of the hole, ...) and there is yet no model that seem to predict the expected values properly.

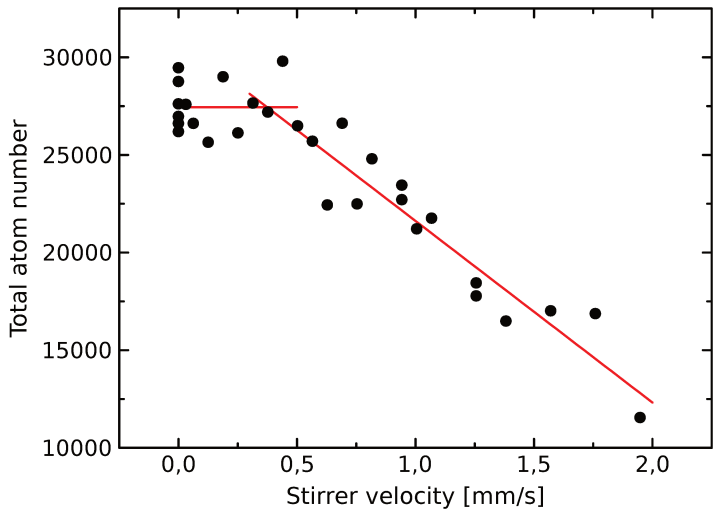

Figure 6.4 — Measurement of the critical velocity in a highly oblate gas. The stirrer is displaced within the gas at constant velocity, describing circular trajectories. At low velocities, nothing seems to happen; for higher velocities the atom number gets lowered: the stirrer creates excitations and heating, and the knife then removes atoms. We analyze the data by performing two linear fits on both regimes; the intersection corresponds to $v = 0.37(12)\,\mathrm{mm}\cdot\mathrm{s}^{-1}$.

6.1.2 Phase imprinting with a SLM

Another commonly used method to generate circulation in a ring trap relies on phase imprinting [57, 58]. It has the advantage of creating a deterministic flow into the ring with a good fidelity.

The current experimental implementations of such a scheme rely on Raman two-photon transition where one of the photons carries orbital angular momentum (coming from a Laguerre-Gauss beam) and the other one does not (coming from a gaussian beam). Such a method requires internal states between which the transition is driven, usually Zeeman substates: even though this method is very appealing, it is therefore very difficult to implement in a magnetic trap (and even more difficult in a RF-dressed trap, since the atoms are not in a single state but in a *mixture* of states).

We are currently trying to implement a setup that would allow us to similarly imprint a given phase onto the atoms, but relying on a beam with an *intensity* helix rather than a phase helix (i.e. a Laguerre-gaussian beam). The idea is to shine onto the atoms a laser beam with a position-dependent intensity $I(\mathbf{r})$ and corresponding position-dependent potential $U(\mathbf{r})$. If the beam is turned on during a short time τ, the atoms will locally acquire a phase proportional to the pulsed potential:

$$\psi(\mathbf{r}, \tau) = \psi(\mathbf{r}, 0) e^{-\frac{iU(\mathbf{r})\tau}{\hbar}}. \tag{6.1}$$

If we imprint in this way a $\ell \times 2\pi$ phase onto the atoms, we should be able to directly imprint the desired ℓ flow level.

In practice, the finite resolution of the optical system may however prevent from directly using such a scheme: the phase gradient is indeed applied on most of the ring, but instead of a local 2π phase jump, it will imprint a 2π phase *ramp* whose size will be the optical resolution. This ramp will then create a strong flow propagating against the one we want to create and cancel the effect of the prepared phase gradient (see figure 6.5 c). For this reason, we intend to use the stirrer beam described in previous section to deplete the region where the phase jump should happen while the intensity helix is applied. We have studied the dynamics of the flow after the barrier is removed and shown that the $\ell = 1 - 3$ states can be prepared efficiently [167].

The intensity helix will be generated by a Spatial Light Modulator (SLM) used in "mask mode": the SLM is placed between a pair of crossed polarizer analyzer, and locally rotates the beam polarization to determine the intensity that will go through the analyzer: the SLM imprints an arbitrary spatial polarization profile, which then becomes an arbitrary intensity profile after the analyzer. In the end, such a setup can in principle be used to generate arbitrary phase profiles. Beyond the idea of imprinting a given circulation, the possibility of imprinting any phase profile onto the atoms would be useful for example to generate and study solitons [168], or to study the recombination of phase domains and Kibble-Zurek mechanism (similarly to [149], but with controlled instead of random phases). The SLM has been tested in the lab and its use has been theoretically investigated during the last two years; it is now ready to be set up onto the experiment. Experimental details and numerical simulations can be found in [87, 167].

6.1.3 Rotating the bubble trap

A last method for setting the atoms into rotation consists in deforming and rotating the trap itself, similarly to a "rotating bucket" experiment. More precisely, we would like to rotate the radial part of the confinement, which happens to be the dressed trap.

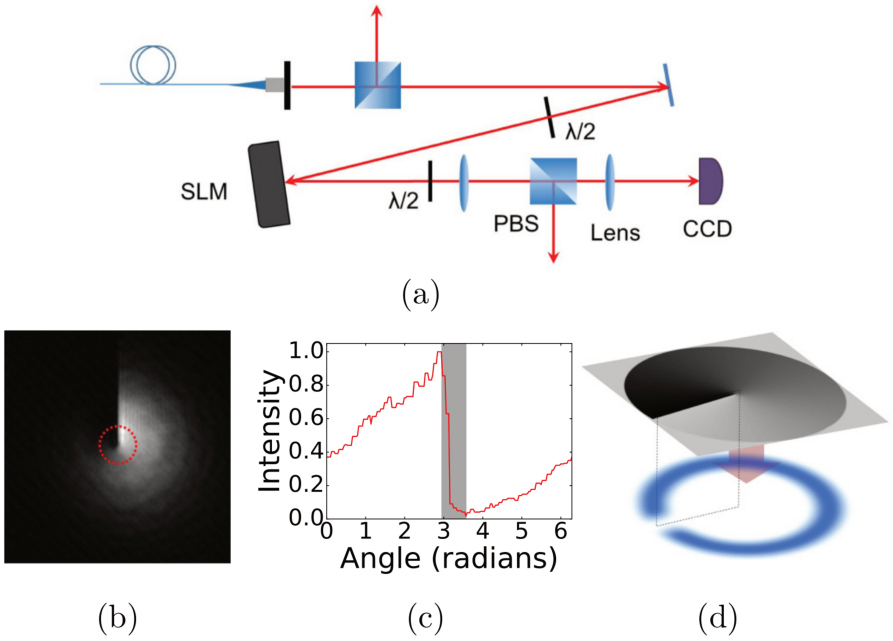

Figure 6.5 — Principle of our phase imprinting setup. (a) Optical setup used to generate the intensity helix (with a CCD camera to image the beam where the atoms will be). (b) Measured intensity pattern, showing the intensity helix. (c) Azimuthal intensity profile corresponding to the measurement shown in (b), along the red dotted circle. The gray region corresponds to the phase ramp that happens instead of the expected phase jump due to finite optical resolution (it will also happen on the real setup). (d) Principle of phase imprinting. The intensity helix is shone onto the ring-shaped gas, locally depleted where the $0 - 2\pi$ phase jump will be. Figure from [167].

Starting from a cylindrically symmetric trap (circular polarization), we deform it to make it slightly anisotropic. This is done by making the polarization slightly elliptic, increasing the amplitude of the current in one of the dressing antennas and decreasing it into the other one: we then end up in the "double-moon" configuration described in section 5.2.1 (see figure 6.6). We rotate in this way the axis of the polarization ellipse, which in turns rotates the atoms in the trap. The parametrization of such a rotation is described in 2.3.4, and the corresponding phase and amplitude applied to the antennas is shown on figure 6.6.

A limitation of this method is that it does not allow to rotate a deformation with a very small amplitude. Indeed, the resolution we have on the dressing field amplitudes corresponds to a 100 to 200 Hz precision on the Rabi coupling at the equator. Continuously deforming the trap therefore requires coupling variations of at least 1 kHz, and equivalent potential variations, meaning that they cannot be small as compared to the chemical potential of the gas (typically 1 to 5 kHz).

However, this method is very easy to apply and requires no alignment: we thus started with it to try generating superflow in the ring, which we did with success. This realization will be described in more detail in the next section.

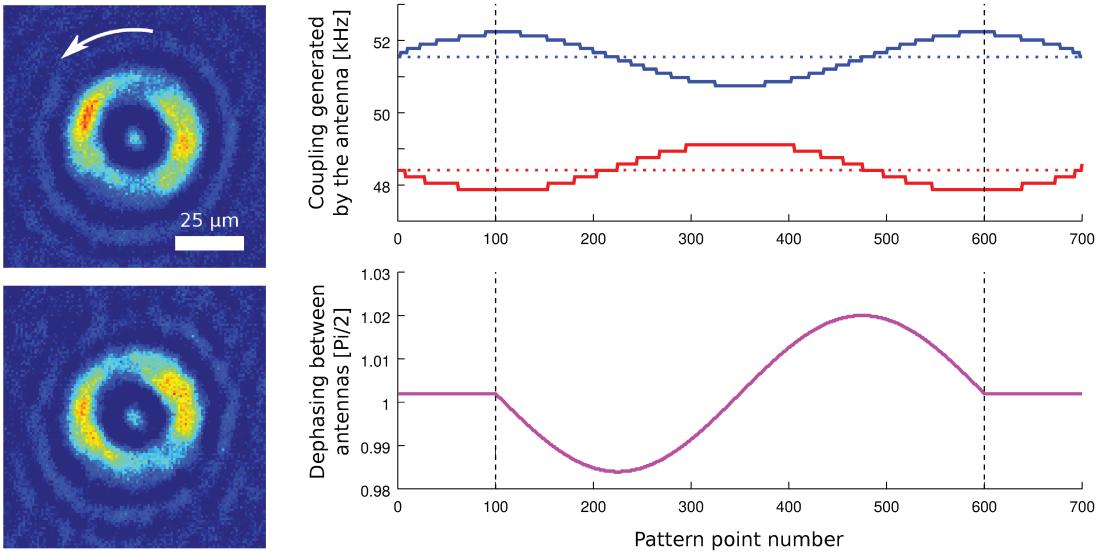

Figure 6.6 — Left: in situ pictures of a ring-shaped BEC during rotation for a ring configuration equivalent to the one described in 5.3, at different times of the rotation. An imbalance between antennas creates inhomogeneities within the ring whose axis can be controlled, allowing to set the ring into rotation. Right: parameters describing the successive states taken by the RF: amplitudes of the H1 (blue) and H2 (red) antennas, and relative phase between them (magenta). For the sake of comprehension, amplitudes are expressed as the corresponding coupling onto the atoms. In a first step (100 first points), an amplitude imbalance between the antennas is created (here, the peak-to-peak height of the deformation is around 1.2 kHz). The phase and amplitude then evolve following equations (2.89) and (2.91); due to the finite resolution of the DDS we see a discretization of the amplitudes (different for both antennas since they are not identical). This rotation pattern lasts 500 points; the refresh rate allows to control the rotation frequency and this step can be repeated to determine the number of turns. Finally, in a third step (100 last points), the antennas are brought back to the isotropic configuration. One may note that due to imperfect physical alignment of the antennas, the amplitudes of the antennas in the isotropic configuration (horizontal dotted lines) correspond to a small imbalance between antennas, and the relative phase is also slightly different from $\pi/2$.

6.2 Flow detection

Once we were able to obtain a ring-shaped gas that seemed able to withstand superfluid flow, as described in 5.3, we tried to generate and observe it. As a reminder, the corresponding ring has a 22.3(1) µm radius, vertical and radial frequencies around 2 kHz and 650 Hz, and typically 5×10^4 atoms; we do not know the cloud temperature but we see no discernable thermal fraction in a time-of-flight expansion.

As it is easier to set up, we chose to use the whole ring rotation to create a circulation (as described just above). We used various excitation amplitudes and rotation frequencies; these studies are for now preliminary and we do not have yet a specific and proven set of optimal parameters.

6.2.1 Time-of-flight detection

Presence of a hole after time-of-flight

For the detection of superfluid flow within the ring, we rely for now on the presence of a hole within the cloud after time-of-flight expansion, as described in 4.1.3. The first attempt of detection was done with a large excitation amplitude: the peak-to-peak height of the ring deformation was around 6 kHz (i.e. larger than the chemical potential), and the ring was rotated at 10 Hz (for a rotational quantum expected around 0.2 Hz).

We then turn off the confinement and let the cloud fall for 10 ms, and we applied a Stern-Gerlach procedure to get rid of the $+1$ and the -1 states (see section 3.4.3). Depending on whether we rotate the ring or not, we then see a hole or a peak in the center of the ring, as we could expect [143]. Looking at the cloud from the side in similar conditions, we either see one single peak at the center of the cloud, or a widened cloud that presents two maxima in the horizontal direction (figure 6.7). This gives us a very clear signature of the presence of a superflow in the ring.

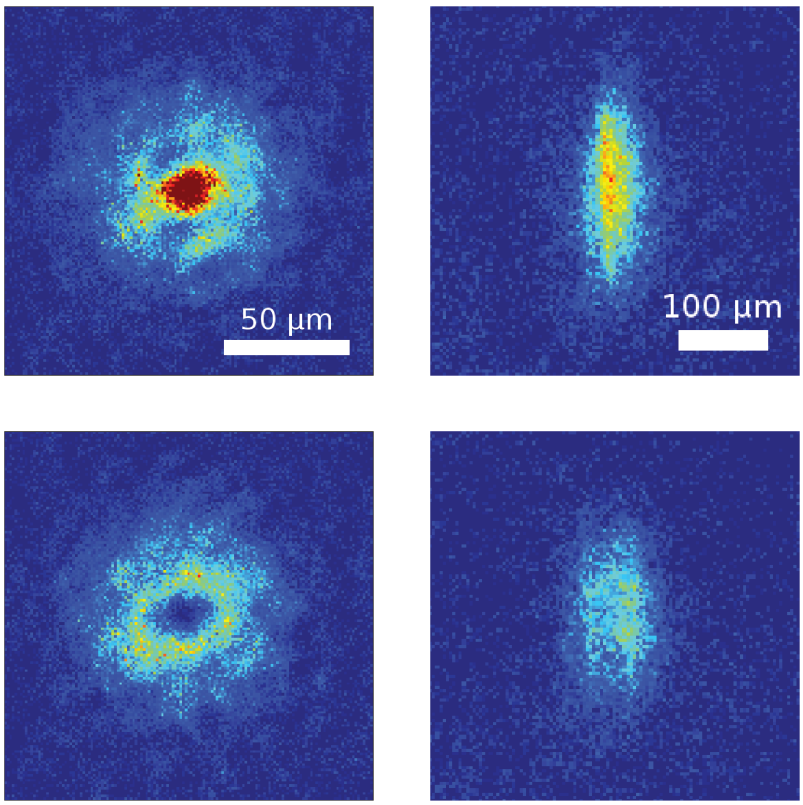

Figure 6.7 – Left: pictures of a ring without (top) and with (bottom) rotation, observed from above after 10 ms TOF and 0.7 ms Stern-Gerlach. Right: pictures of the same cloud observed from the side after 23 ms TOF and 0.5 ms Stern-Gerlach. The rotation is done at 10 Hz and lasts one turn; the cloud relaxes during 0.5 s before the imaging procedure.

Looking after a longer TOF to achieve a better resolution and trying various excitation parameters, we then end up with very different hole sizes (figure 6.8).

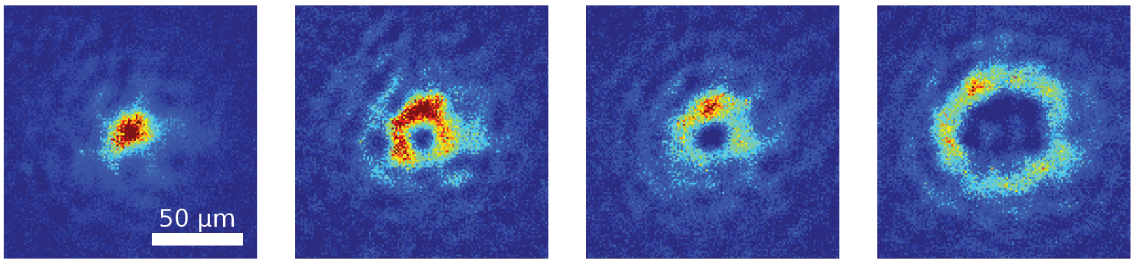

Figure 6.8 — Vertical pictures of the ring after rotation, 500 ms holding time and 23 ms time-of-flight. The excitation has a peak-to-peak height of around 1.2 kHz (the corresponding rotation pattern is the one displayed on figure 6.6) and we make 2.5 turns. The excitation frequencies are, from left to right, 8 Hz, 9 Hz, 9 Hz and 25 Hz. Repeating the sequence for an excitation frequency of 8 Hz, we never saw a hole in the cloud, suggesting that the critical rotation frequency lies between 8 and 9 Hz. Note that the size of all pictures is identical, but the color scale is different on the first picture (twice larger).

Hole size quantization and evolution

The observation of this hole within the cloud after time-of-flight with a variable diameter depending on the stirring parameters leaves no doubt about the presence of a superfluid flow within the ring. However, we would also like to observe the discrete character of the hole radius, and to be able to know which state was present in the ring from the TOF pictures. The method used by other teams to do so is the realization of a histogram of the obtained hole radii for various parameters. We expect to see well-separated peaks corresponding to the different ℓ states [58, 143]. This is the next thing we plan to achive for the work on the ring. Gross-Pitaevskii simulations of the cloud's expansion in the presence of a superfluid flow are also being performed in the team, and we hope to achieve quantitative comparison with our data.

After creating a large hole, we tried to look at the time evolution of the hole size, in order to ensure that the superfluid flow is indeed metastable. The results can be seen on figure 6.9. The hole size decreases slowly on a time scale comparable with the atom number evolution, probably due to atom losses as has been observed in [58]. We observe the presence of a hole in the gas up to 6 s after the initial excitation, however we do not have enough data yet to perform quantitative measurements.

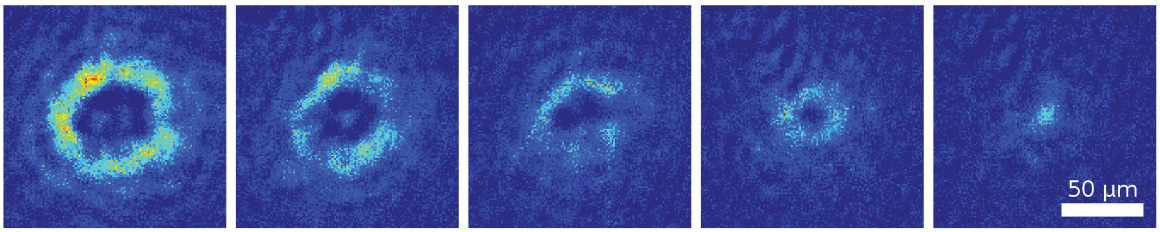

Figure 6.9 — Vertical pictures of the ring after rotation, various holding times and 23 ms time-of-flight. The excitation has a peak-to-peak height of around 1.2 kHz (the corresponding rotation pattern is the one displayed on figure 6.6) and we apply 2.5 turns at 25 Hz.

Part III

Fast rotating Bose gases in RF adiabatic potentials

Introduction

Superfluidity implies the irrotationality of the velocity field of a fluid. However, rotation is still possible if quantized vortices are introduced in the superfluid, creating density zeros around which the fluid is able to rotate [12, 13, 15, 92, 169]. When many of these vortices are present, they arrange into regular vortex arrays, allowing the superfluid to mimic a solid-body rotation velocity field, leading to the "coarse-grained" velocity regime [53].

Even though vortices are quantum objects, these effects can still be explained by a classical field description of the wavefunction of the fluid [170]. When the rotation gets even faster however, the quantum nature of the wavefunction cannot be neglected anymore, and the superfluid should enter exotic regimes like the Lowest Landau Level regime [54], analogue to the quantum Hall effect for a supraconductor. Strongly correlated states like Laughlin states can even be reached when the number of vortices becomes comparable to the number of particles in the fluid [171]. On the experimental side, the ability to produce and study increasingly fast rotating dilute superfluids was developed very rapidly after the realization of the first gaseous BECs [51–54, 172], but after 2005 the experimental efforts concentrated on other aspects of the vortex physics [173–178].

A promising method for reaching some of the fast rotating regimes is to use anharmonic trapping [179]. Indeed, one of the major experimental difficulties when entering fast rotating regimes is that in the usual case of harmonic traps, the centrifugal force compensates or overcomes the trapping force, leading to a divergence in the size of the gas when the rotation frequency approaches the trapping frequency, or even to the expulsion of all atoms if the rotation frequency exceeds the trapping frequency [170]. A stronger than harmonic confinement ensures to maintaining the atoms in the trap even if the rotation frequency is higher than the trapping frequency. The effective potential in the rotating frame then takes the shape of a Mexican hat and the gas becomes annular. If the rotation is large enough, all vortices then migrate within a central density hole and the gas becomes effectively 1D, leading to a stable, "giant" vortex [74–76, 79]. This regime has been approached in 2004 in the group of J. Dalibard [77], although without reaching a vanishing density in the center.

The experiments described in this part result from a proposition of Romain Dubessy, who suggested to stir a cloud at the bottom of the bubble in order to achieve a giant vortex: indeed, as the bubble trap is anharmonic, it could be a suitable system to explore these regimes. The initial attempts, described at the beginning of chapter 8, were unsuccessful, but the results were surprising enough to trig some studies in order to understand better our results, which finally led us to very interesting (and unexpected) results, among which the achievement of a

" dynamical" ring-shaped gas.

This part consists of two chapters: chapter 7 details the different rotation regimes of a superfluid and introduces from a theoretical point of view some of the techniques we used to study fast-rotating gases in bubble traps. Chapter 8 presents the experimental results, from the first attempts to the realization of fast-rotating dynamical rings, as well as the results we obtained on the characterization of such a system.

Chapter 7

Theory of rotating superfluids

This chapter aims at describing from a theoretical point of view the behavior of vortices in the case of fast rotating Bose gases, i.e. the case where many vortices are present in the gas, and to introduce in this way the basics on which the third part of my thesis relies. In a first section, I will describe the behavior of vortices in the case of small to moderate rotations ($\Omega_{\text{rot}} < \omega_\perp$); this regime has been studied a lot experimentally and theoretically and is now well understood. In a second section, I will describe the regime of fast rotations, when the rotation frequency gets very close to the trapping frequency. Despite the significant number of predicted phenomena that haven't been observed in this regime, no experimental work seems to have been carried on this topic during the last decade; it is this regime that we want to explore. Note that a more detailed review of these topics can be found in [170]. The third section will then describe the behavior of the quadrupole modes of rotating condensates, which gives useful tools to probe the properties of the superfluid. Finally, I will describe the theory that lies behind a few usual techniques for studying vortices: how we nucleate them and how we observe them.

All the experiments I will present in this part are performed at the bottom of our bubble trap: the trapping geometry there is highly oblate, with $\omega_z/\omega_\perp \sim 10$. For this reason, I will here consider only the case of 2D superfluidity, meaning that:

- All the rotations that will be considered are along the vertical axis.
- The quantized vortices are also aligned along this axis, and we neglect their possibility to tilt and/or bend.

In this case, the velocity field lies in the horizontal plane and does not depend on the z position. Note that this doesn't require the condensate to be 2D or quasi-2D: the restriction here applies only to the allowed behavior of the vortex lines [180].

7.1 Vortices in a rotating superfluid

7.1.1 A single vortex

Let us start by describing the behavior of a single vortex line in a superfluid. The most crucial relationship for describing the velocity field in a superfluid is the Feynman-Onsager relation

(1.34), that I recall here:

$$\oint_{\mathcal{C}} \mathbf{v}(\mathbf{r},t)\cdot \mathrm{d}\mathbf{l} = \frac{\hbar}{M}\Delta_{\mathcal{C}} S = \ell \times 2\pi\frac{\hbar}{M}, \ell \in \mathbb{Z}. \tag{7.1}$$

Computing this relation on a circle with radius r centered on the vortex leads to the velocity field it creates:

$$\mathbf{v} = \frac{\ell\hbar}{Mr}\mathbf{e}_\phi. \tag{7.2}$$

In principle, the "charge" of the vortex ℓ can take any integer value, but a vortex with $|\ell| > 1$ is unstable and spontaneously splits into several singly-charged vortices [56], and we will only consider $\ell = \pm 1$ in this chapter.

The Stokes' theorem then leads to a singular vorticity localized at the position of the vortex:

$$\boldsymbol{\nabla} \times \mathbf{v} = \frac{2\pi\hbar}{M}\delta(\mathbf{r})\mathbf{e}_z. \tag{7.3}$$

Since the velocity field diverges for $r \to 0$, the density has to vanish in this limit to keep a finite kinetic energy. Comparing the kinetic energy:

$$E_k = \frac{1}{2}M\mathbf{v}^2 = \frac{\hbar^2}{2Mr^2} \tag{7.4}$$

with the chemical potential μ allows to estimate the typical size over which the density will vanish, $r_v = \sqrt{\hbar^2/2\mu M}$, which happens to be the healing length ξ. We can note that ξ corresponds to the distance to the vortex below which the flow becomes supersonic (the sound velocity being given by (1.25)). More accurately, Gross-Pitaevskii simulations lead to a root-mean-square core radius around $r_v = 1.94\xi$ [54].

7.1.2 Many vortices: the coarse-grained vorticity approximation

Let us now consider the case of a rotating trapped gas in which a significant number of vortices are present. One can show [170] that for a given angular momentum L_z, the velocity configuration that minimizes the energy of a rotating fluid is the solid-body rotation $\mathbf{v}_{\mathrm{sb}} = \boldsymbol{\Omega} \times \mathbf{r}$, where Ω is given by the classical solid-body moment of intertia: $L_z = \Omega \times M\langle r^2\rangle$. This configuration, however, implies $\boldsymbol{\nabla} \times \mathbf{v} = 2\boldsymbol{\Omega}$ and is unachievable for a superfluid whose flow is irrotational.

Nevertheless, when several vortices are present in the superfluid, the way they distribute within the fluid allows many configurations for the velocity field, and the lowest energy configuration is the one that mimics the solid body rotation. For a sufficiently large amount of vortices, one can make the assuption of a "coarse-grained" vorticity, where the vortices are uniformly distributed within the condensate with a surface density [12]:

$$n_v = \frac{M\Omega_{\mathrm{eff}}}{\pi\hbar}, \tag{7.5}$$

where Ω_{eff} is defined from the mean angular momentum per atom L_z as:

$$\Omega_{\mathrm{eff}} = \frac{L_z}{M\langle r^2\rangle}. \tag{7.6}$$

As a useful formula, I recall here that for a harmonically trapped BEC, $\langle r^2 \rangle$ can be expressed from the Thomas-Fermi radii [181]:

$$\langle r^2 \rangle = \frac{R_x^2 + R_y^2}{7} \tag{7.7}$$

Each vortex having a singular vorticity h/M, the local vorticity is then $n_v h/M$, i.e. $\boldsymbol{\nabla} \times \mathbf{v} = 2\Omega_{\text{eff}} \mathbf{e}_z$, and we find the expected solid-body rotation. Note that Ω_{eff} can always be defined, even for a amount angular momentum per particle – however, for small numbers of vortices, the flow will of course significantly deviate from the solid-body rotation.

From the vortex density n_v one can then deduce the area per vortex $n_v^{-1} = \pi\hbar/M\Omega_{\text{eff}} \equiv \pi l^2$ and define the "magnetic length" (by analogy with the quantum Hall effect):

$$l = \sqrt{\frac{\hbar}{M\Omega_{\text{eff}}}}, \tag{7.8}$$

which would correspond to the radius of a circular cell: the intervortex separation is then approximately[1] $2l$.

The total number of vortices in the superfluid is then equal to:

$$N_v = \frac{R_\perp^2(\Omega_{\text{eff}})}{l^2}, \tag{7.9}$$

where $R_\perp$ increases with Ω_{eff} due to the centrifugal force.

Computing the ground state of the system is then relevant in the frame rotating at Ω_{eff}. In this referential, the total energy of the system in a configuration given by the wavefunction ψ writes [170]:

$$E[\psi] = \int dV \left[\left(\frac{1}{2} M \mathbf{v}^2 + V_{\text{ext}} \right) |\psi|^2 + \frac{1}{2} g_{\text{int}} |\psi|^4 \right] - \int dV M\Omega_{\text{eff}} \ \mathbf{e}_z \cdot \mathbf{r} \times \mathbf{v} |\psi|^2, \tag{7.10}$$

where we neglected the kinetic energy associated to the spatial variation of the condensate density, i.e. in the Thomas-Fermi approximation (not that this includes the kinetic energy associated to the density variation in the vortex core). Considering the hypotheses we made on 2D superfluidity and using the definition (7.6), this energy can be reexpressed as:

$$E[\psi] = \int dV \left[\left(\frac{1}{2} M \mathbf{v}^2 - M\Omega_{\text{eff}}^2 \mathbf{r}^2 + V_{\text{ext}} \right) |\psi|^2 + \frac{1}{2} g_{\text{int}} |\psi|^4 \right], \tag{7.11}$$

and one can finally split the energy functional into two parts, as:

$$E[\psi] = \int dV \left[\left(V_{\text{ext}} - \frac{1}{2} M\Omega_{\text{eff}}^2 \mathbf{r}^2 \right) |\psi|^2 + \frac{1}{2} g_{\text{int}} |\psi|^4 \right] + \int dV \frac{1}{2} M (\mathbf{v} - \mathbf{v}_{\text{sb}})^2 |\psi|^2. \tag{7.12}$$

The first term corresponds to the energy of the system in the solid-body configuration, and the second one to the additional kinetic energy of the deviation to this solid-body rotation (note that it is always positive, as the solid body rotation configuration is the one that minimizes the energy). The coarse-grained vorticity approximation (also called "diffuse vorticity") then

1. The exact distance between vortices depends on the vortex repartition geometry, for example in the triangular lattice configuration it is equal to $2l\sqrt{\pi/3}$.

consists in neglecting this second term; in this case we see that the rotation of the condensate simply leads to a weakening of the radial trapping.

In the case of a harmonically trapped condensate with radial frequency $\omega_\perp$, the radial trapping potential then simply becomes $\frac{1}{2}M(\omega_\perp^2 - \Omega_{\text{eff}}^2)r^2$; the Thomas-Fermi radii then vary due to the modification of the effective trapping frequencies as:

$$R_\perp(\Omega_{\text{eff}}) = R_\perp(0)\left(1 - \frac{\Omega_{\text{eff}}^2}{\omega_\perp^2}\right)^{-3/10}, \qquad R_z(\Omega_{\text{eff}}) = R_z(0)\left(1 - \frac{\Omega_{\text{eff}}^2}{\omega_\perp^2}\right)^{1/5}, \quad (7.13)$$

and the cloud's in-trap aspect ratio therefore reads:

$$\frac{R_\perp(\Omega_{\text{eff}})}{R_z(\Omega_{\text{eff}})} = \frac{\sqrt{\omega_\perp^2 - \Omega_{\text{eff}}^2}}{\omega_z}. \quad (7.14)$$

The subsequent modification of the cloud's in-trap aspect ratio can, for example, be used as an effective probe of the rotation frequency Ω_{eff} [54]. We can also notice that due to the weakening of the radial trapping frequency, the critical temperature decreases with the rotation frequency [182]:

$$\frac{T_c(\Omega)}{T_c(0)} = \left(1 - \frac{\Omega_{\text{eff}}^2}{\omega_\perp^2}\right)^{1/3}. \quad (7.15)$$

One has to note, however, that the vertical radius can become very small when Ω_{eff} becomes comparable with $\omega_\perp$; these formulas are only valid if we stay in the three-dimensional regime (i.e. if the vertical radius stays larger than d_z).

Finally, one may note that these considerations do not indicate anything about the arrangement of the vortices within the cloud. In most cases, however, the lowest-energy configuration corresponds to the triangular lattice, as initially predicted for vortices in type-II superconductors [183] or superfluid helium [184] (also called Abrikosov lattice). Pictures of such a vortex lattice observed in a dilute superfluid can be seen on figure 7.1. However, other lattices geometries might be obtained depending on the system; for example in a spinor consensate square lattices have been observed [185].

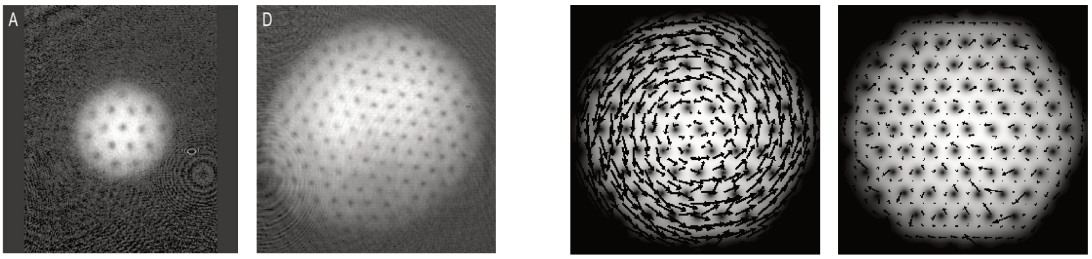

Figure 7.1 — Left: observation of vortex lattices in a rotating superfluid. One can see approximately 13 (left) and 130 (right) vortices, visible due to the depletion they create in the gas. Note that a time-of-flight expansion of the gas is necessary to see them. Figure from [53]. Right: Gross-Pitaevskii simulations of the density profile and velocity field (black arrows) of a rotating condensate, taken from [186]. The left plot corresponds to the velocity in the laboratory frame while the right one corresponds to the velocity in the frame rotating at Ω_{eff}, that is, the deviation to the solid-body rotation.

7.2 The fast-rotating regime

The coarse-grained vorticity description presented in section 7.1.2 works well for moderate rotation regimes ($\Omega_{\text{eff}} \lesssim \omega_\perp$), but fails in the fast rotating regime (for $\Omega_{\text{eff}} \to \omega_\perp$). We should even speak about fast-rotating regimes: as Ω_{eff} gets closer and closer to $\omega_\perp$, the quantum gas is predicted to undergo a series of quantum phase transitions and reach highly correlated states. Most of these regimes are yet completely unaccessible experimentally as they typically require a number of vortices comparable or even larger than the number of particles (for now, the lowest achieved values for $\nu = N/N_v$ are around 500 [54]), but even the regimes that are the easiest to achieve present a significant interest. They are the primary motivation for the work I will present in the next chapter, and I will here describe what is expected to happen in these rotation regimes and what has been experimentally achieved. Finally, I will describe what we can hope to achieve with our experiment on this topic.

7.2.1 Theoretical interest

The Lowest Landau Level

The coarse-grained vorticity is based on the mean-field Thomas-Fermi approximation: it neglects the kinetic energy associated to local density variations, that is, it considers the velocity field created by the vortices but not the modifications of the density in the vortex core. This is valid as long as the vortex core size is much smaller than the inter-vortex distance: $\xi \ll l$. However, as the effective rotation frequency Ω_{eff} grows closer to $\omega_\perp$, the radial trapping becomes extremely weak due to the centrifugal force and the chemical potential strongly drops: the healing length ξ then tends to diverge. On the other hand, the inter-vortex distance saturates to $l \approx d_\perp$ as Ω_{eff} approaches $\omega_\perp$: for large enough rotation rates, the previous approximations fall and another description of the system that fully takes into account its quantum nature becomes necessary.

To understand the physics in this system, it is useful to consider the quantum description of the trapped particles, using the creation and annihilation operators of the harmonic oscillator. The most convenient basis, more precisely, is the basis of circularly polarized states $\hat{a}_\pm = (\hat{a}_x \mp i\hat{a}_y)/\sqrt{2}$. In this basis, the hamiltonian of the harmonic oscillator reads:

$$H_0 = \hbar\omega_\perp(\hat{a}_+^\dagger \hat{a}_+ + \hat{a}_-^\dagger \hat{a}_- + 1), \tag{7.16}$$

and the angular momentum:

$$L_z = \hbar(\hat{a}_+^\dagger \hat{a}_+ - \hat{a}_-^\dagger \hat{a}_-). \tag{7.17}$$

Denoting $n_\pm$ the eigenvalues of the number operators $\hat{a}_\pm^\dagger \hat{a}_\pm$, the energy of the eigenstates in the rotating frame can then be written under the two equivalent forms:

$$E(n_+, n_-) = n_+\hbar(\omega_\perp - \Omega_{\text{eff}}) + n_-\hbar(\omega_\perp + \Omega_{\text{eff}}), \tag{7.18}$$

$$= n\hbar\omega_\perp - m\hbar\Omega_{\text{eff}}, \tag{7.19}$$

with $n = n_+ + n_-$ and $m = n_+ - n_-$. The corresponding energies are plotted on figure 7.2: we see that for $\Omega_{\text{eff}} \to \omega_\perp$ all states with $n = m$ become quasidegenerate, forming the so-called "Lowest Landau Level" (LLL).

Let us come back to our initial questioning. The condition $\xi \sim d_\perp$ can be reexpressed as $\mu \sim \hbar\omega_\perp$: in this case, supposing that the gas is quasi-2D (which is often the case since

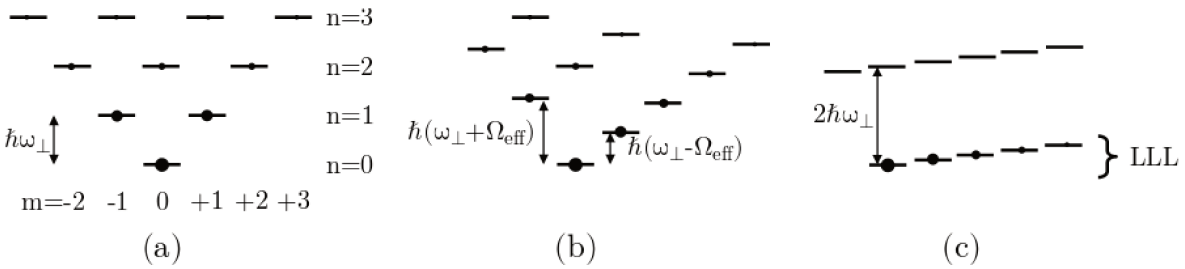

Figure 7.2 – Evolution of the energies given by (7.19) for (a) $\Omega_{\text{eff}} = 0$, (b) $\Omega_{\text{eff}} = 0.4\omega_\perp$ and (c) $\Omega_{\text{eff}} = 0.9\omega_\perp$. The splitting between opposite m levels increases with Ω_{eff}, and for $\Omega_{\text{eff}} =\!\!\rightarrow \omega_\perp$ all states with $n = m$ become quasidegenerate, forming the LLL. In this latter case, if $\mu < 2\omega_\perp$, the only significantly populated states are those of the LLL. Figure adapted from [187].

the chemical potential strongly drops for fast rotations), the single-particle states that are accessible are restricted to the LLL, i.e. $n = m$ (or equivalently $n_- = 0$). The condensate wavefunction can then be rewritten as [187]:

$$\psi(r) = \sum_m \alpha_m \varphi_m(r) \tag{7.20}$$

$$= \sum_m \alpha_m r^m e^{im\phi} e^{-r^2/2d_\perp^2}; \tag{7.21}$$

one can show that in this case, the gas keeps a parabolic shape but with a different radius than in the mean-field Thomas-Fermi regime (even though the kinetic energy term is now taken into account), and the size of the vortices saturates around $d_\perp$. One can also note that the number of vortices in the cloud then corresponds to the number of zeros in the wavefunction, given by the index of the highest populated state: $N_v = m_{\max}$. A more detailed review of the the gas properties in this state can be found in [170, 187].

Highly correlated states

As the rotation frequency gets closer to $\omega_\perp$, the number of states in the LLL that can get significantly populated grows. When this number becomes comparable to the number of particles ($N \sim m_{\max} = N_v$), the mean-field approach becomes irrelevant, and the system enters highly correlated many-body states. The first expected effect is the melting of the vortex lattice due to quantum fluctuations (for $N/N_v \lesssim 6$ [171]), and for even larger rotations the system enters Laughlin states. The system then loses its superfluid character. The physics of these states is far beyond the scope of what is described in this document, and reaching them experimentally with rotating superfluids appears for now as out of reach. A reader wishing more details about these regimes shoud direct towards [171].

Thermal melting of the vortex lattice

All the previous descriptions correspond to a zero-temperature behavior. We can note, however, that for large rotations in the quasi-2D regime a melting of the vortex lattice due to thermal fluctuations is expected. As discussed below, such a phenomenon can be described

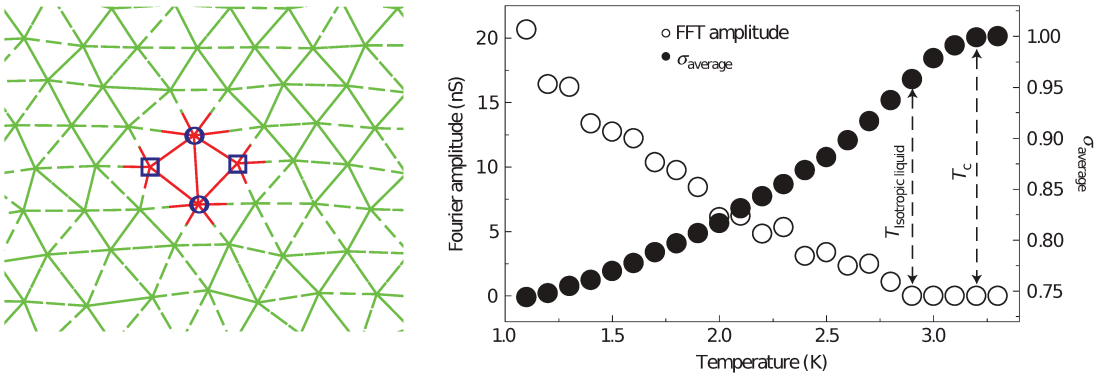

Figure 7.3 — Left: example of a local defect in a triangular lattice, with two sites having only 5 neighbours (marked with blue squares) and two sites with 7 neighbours (blue circles) close to each other. Such a defect can be seen as a dislocation pair (a dislocation corresponding to a site with 5 neighbours next to a site with 7 neighbours): as long as the pair stays tied, the orientational order can be preserved away from the defect, while if the thermal fluctuations are large enough to unbind such pairs, their proliferation will destroy long-range order, similarly to what happens in the BKT transition. Figure from [188,189]. Right: observation of melting in a 2D superconducting lattice by Guillamón *et al* [190]. Plotted are the amplitude of the peaks in the Fourier Transform of the vortex lattice pictures, and the parameter σ which indicates the Current-Voltage relationship in the superconductor ($\sigma = 1$ corresponds to a normal conductor and $\sigma < 1$ to a superconductor). They observe a range in temperature for which the studied sample is superconducting ($\sigma < 1$) but the absence of peaks in the Fourier transform indicates the absence of crystalline order, indicating a vortex liquid phase.

as a Kosterlitz-Thouless transition [62] due to the unbinding of thermal dislocations in a 2D lattice (see figure 7.3).

For a 2D vortex lattice in an incompressible superfluid (i.e. superfluid helium films), it has been predicted that the vortex lattice should melt above a temperature T_m lying below the BKT critical temperature T_{BKT}, $T_m = T_{\mathrm{BKT}}/4\pi\sqrt{3}$ [191] (i.e. $\approx 0.05 T_{\mathrm{BKT}}$). This result has been recently extended to the general case of superfluid vortex lattices by Gifford and Baym [192], based on the theory of 2D vortex melting for solids [193,194]. Again, a melting of the vortex lattice is predicted for $T_m < T < T_{\mathrm{BKT}}$. Matveenko and Shlyapnikov then computed the correlation function and phase coherence in such a system [195], and predicted that even when density fluctuations are strongly suppressed, the phase coherence can decay on a short lenghtscale and cause irregularities in the vortex lattice or even its melting if the temperature is not low enough.

Such a thermal melting has been observed in the case of a 2D superconducting vortex lattice [190] (see figure 7.3), but not in the case of a superfluid, and the physics of such a transition is still poorly understood.

Fast rotation in a harmonic plus quartic trap

The major difficulty for experimental achievement of harmonically trapped gases rotating close to $\Omega_{\mathrm{eff}} \approx \omega_\perp$ is the absence of radial confinement due to the centrigugal force. An interesting strategy that could enable reaching the fast-rotating regime lies in the addition of

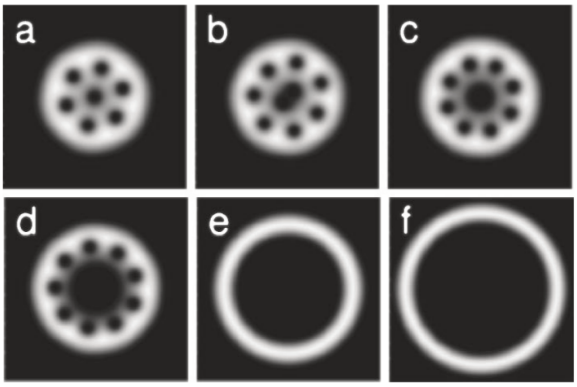

Figure 7.4 — Numerical simulations of the appearance of a giant vortex for a rotating gas confined in a harmonic plus quartic trap, taken from [76]. Starting from a regular vortex for low rotation frequencies (a), when the rotation increases a hole appears at the center of the cloud in which several vortices are present, while some other vortices stay in the bulk (c). Finally, for very large rotation frequencies, all the vortices merge into the hole (e), leading to formation of a "giant vortex".

a higher-order confinement, able to keep the atoms trapped for rotation frequencies equal or even larger than the trapping frequency. Most theoretical studies investigated the case of a harmonic plus quartic trap [76, 179, 196]:

$$V_{\text{ext}}(r) = \frac{1}{2} M \omega_\perp^2 \left(r^2 + \lambda \frac{r^4}{d_\perp^2} \right). \tag{7.22}$$

For such a trapping configuration, rotating faster than the harmonic trapping frequency leads to a mexican hat potential in the rotating frame, with a repulsive harmonic anticonfinement at the center of the trap and a quartic confinement at large distances.

Such a trap doesn't allow to explore exactly the same regimes than described previously in this section: for example, the LLL is now an approximation that holds only if the quartic term is weak compared to the harmonic confinement, and is not necessarily reached for increasing Ω_{eff} as the chemical potential doesn't drop arbitrarily low anymore. However, it also provides interesting regimes on its own. If the cloud rotates significantly faster than $\omega_\perp$, the repulsive barrier that appears at the center of the trap can become larger than the chemical potential, leading to the appearance of a central hole in the gas, which becomes annular (see figure 7.4). While some vortices remain in the bulk, others then locate within the hole present at the center of the cloud and become "phantom" vortices, leading to a multiply charged vortex in the center of the trap. For even larger rotations, all vortices are expected to migrate within this hole and leave the bulk vortex-free, forming in this way a "giant" multiply-quantized vortex with a pure irrotational flow within the bulk [74–76, 79]. In this limit, the annular gas reaches the one-dimensional regime.

7.2.2 Experimental achievements

Up to now, only two experiments tried to reach the fast-rotating regime:

- The first one, in the group of Eric Cornell, studied the Lowest Landau Level regime in a harmonically trapped gas [54]. Using an evaporative cooling technique to accelerate the

rotation of the gas followed by an optical increase of the rotation, they reached up to $\Omega_{\text{eff}} = 0.993\omega_\perp$ and started to enter the LLL regime. They observed the saturation of the vortex size (fig 7.5) and studied the oscillations of the vortex lattice, called "Tkachenko oscillations". We can also note that in his thesis, V. Schweikhard mentions that the observed vortex lattice became very fragile if the temperature was not kept very low, possibly due to thermal lattice melting effects [197].

- The second one, in the group of Jean Dalibard, tried to obtain fast-rotating gases in the harmonic plus quartic case [77]. When reaching $\Omega_{\text{eff}} \gtrsim \omega_\perp$, they observed a depletion of the density in the center of the cloud, but could not completely form the expected hole: trying to increase the cloud rotation further was unsuccessful (fig 7.5). In parallel to the density depletion, they also observed a blurring of the vortices in their condensate, whose origin remains unclear.

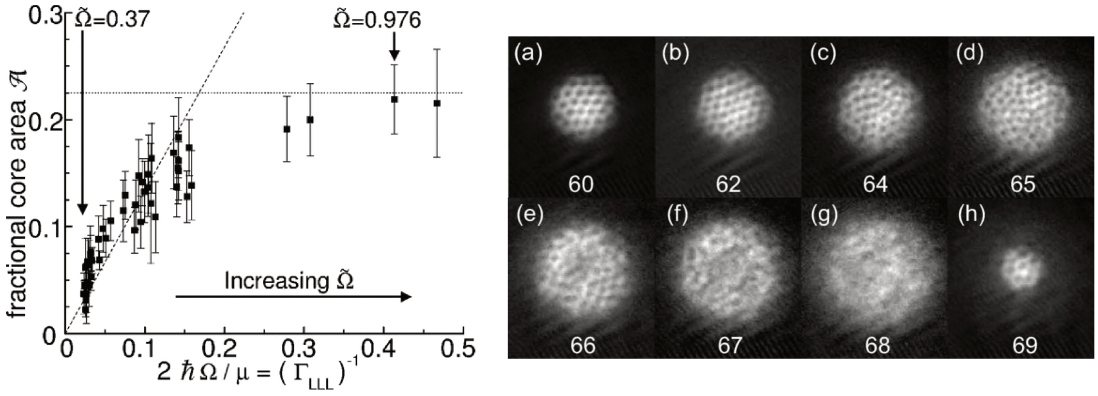

Figure 7.5 — Left: evolution of the fractional core area, i.e. the ratio between the surface of a vortex core πr_v^2 and the area per vortex in the lattice πl^2, as a function of the ratio between twice the rotation frequency and the chemical potential describing the entrance in the LLL regime. While for small rotation frequencies, the core size grows in proportion of the vortex lattice cell, it saturates for higher rotation frequencies (the dashed line is the prediction of the TF theory and the dotted horizontal line the one of the LLL theory). Figure from [54]. Right: pictures of the rotating gases in the experiment of Bretin *et al.* [77] after TOF expansion, for various excitation frequencies (written below the pictures). Above the trapping frequency ($\omega_\perp = 2\pi \times 64.8\,\text{Hz}$), a density minimum appears in the center of the cloud but the vortex lattice gets blurred. The attempt to reach faster rotation regimes was unsuccessful (picture h).

Even though these two experiments began entering the fast-rotating regime, they did not go further in their exploration, neither did any other.

7.2.3 Our strategy

General principle

Following the strategy of the addition of a higher order confinement described above, our bubble-shaped trap (described in chapter 2) has the advantage of being naturally anharmonic:

while the motion of the atoms is pendulum-like at the bottom of the bubble, when they get away from the center they have to climb the edges of the ellipsoid, leading to significantly stronger confinement. We can thus, without having to modify our experimental system, try to explore the regimes leading to the giant vortex. In this regard, our system has several advantages:

- We are able to achieve very smooth potentials with a good trapping lifetime, allowing to study the evolution of the system over long times.
- We have a good control of our trap's geometry and thus achieve a very good rotational invariance.
- This control of the geometry also allows to set the atoms into rotation easily.
- At the bottom of the bubble, we can easily reach the quasi-2D regime when rotating fast, as the vertical trapping frequency is quite high (above 300 Hz).

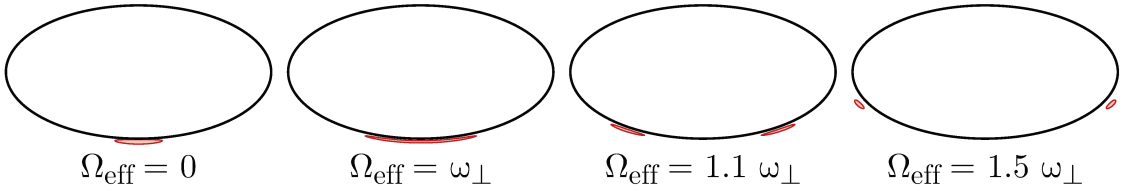

Figure 7.6 – Principle of the fast rotation in the bubble: for low rotation frequencies, the atoms stay at the bottom of the bubble; for rotation frequencies faster than the radial pendulum frequency they start to climb on the edges of the bubble. Here, the red lines are the numerically computed Thomas-Fermi surfaces of the cloud (i.e. the isopotential lines $V_{\text{ext}}(r,z) - M\Omega_{\text{eff}}^2/2 = \mu$) in the conditions of the experiments described in the next chapter, while the black lines correspond to the isomagnetic surface of the bubble trap, with a cut in the $x-z$ plane. Computations were done for the parameters we used in the experiments described in the next chapter: $\omega_{\text{rf}} = 2\pi \times 0.3\,\text{MHz}$ and 28.5 A in the quadrupole coils ($b' = 55.4\,\text{G}\cdot\text{cm}^{-1}$), corresponding to $r_b = 77.7\,\mu\text{m}$, $\Omega_0 = 2\pi \times 49.25\,\text{kHz}$ and 10^5 atoms in the cloud. Note that the Thomas-Fermi surfaces are here computed for a 3D cloud, but the cloud enters the quasi-2D regime during the process.

For those reasons, this system seems suitable to attempt further exploration of the fast-rotating regimes. We can however note a major drawback due to the "exotic" geometry of such a system, that is the absence of theory for this exact geometry and the difficulty to extend the existing theory (especially, for $\Omega_{\text{eff}} > \omega_\perp$, the cloud becomes tilted with respect to the rotation axis).

Technical details

Let us now describe more precisely the case of rotating gases in our bubble-shaped trap. For simplicity, I will suppose that the atoms stay on the resonant surface, which supposes the magnetic gradient to be significantly stronger than gravity: $\beta \ll 1$ and $\ell_b = r_b$, leading to

$z = -\sqrt{r_b^2 - r^2}/2$. We consider the case of a circularly polarized RF field, as described in section 2.3.1. In the rotating frame, the total potential can then be written as:

$$V(r,z) = F\hbar\Omega_1(r,z) + Mgz - \frac{1}{2}M\Omega_{\text{eff}}^2 r^2. \tag{7.23}$$

Using expression (2.60) for Ω_1, we can rewrite it as:

$$V_{\text{eff}}(r) = F\hbar\frac{\Omega_0}{2} - M\omega_\perp^2 r_b^2\sqrt{1-\frac{r^2}{r_b^2}} - \frac{1}{2}M\Omega_{\text{eff}}^2 r^2, \tag{7.24}$$

where $\omega_\perp$ is equal to:

$$\omega_\perp = \sqrt{\frac{g}{2r_b}}\left[1 - \frac{2F\hbar\Omega_0}{Mgr_b}\right]^{1/2}, \tag{7.25}$$

which coincides with expression (2.64) for $\beta \ll 1$. From equation (7.24), the equilibrium position can then be found, defining $\kappa \equiv \omega_\perp^2/\Omega_{\text{eff}}^2$, as:

$$r_{\text{eq}} = \begin{cases} 0 & \text{if } \Omega_{\text{eff}} \leq \omega_\perp, \\ r_b\sqrt{1-\kappa^2} & \text{if } \Omega_{\text{eff}} > \omega_\perp; \end{cases} \tag{7.26}$$

$$z_{\text{eq}} = \begin{cases} -\dfrac{r_b}{2} & \text{if } \Omega_{\text{eff}} \leq \omega_\perp, \\ -\kappa\dfrac{r_b}{2} & \text{if } \Omega_{\text{eff}} > \omega_\perp. \end{cases} \tag{7.27}$$

A hole will then appear at the center of the cloud if the chemical potential is lower than the centrifugal barrier height, which reads:

$$U_b = \frac{1}{2}M\Omega_{\text{eff}}^2 r_b^2\,(1-\kappa)^2\,. \tag{7.28}$$

Evaluating the chemical potential can get slightly tricky as the trapping frequencies change while the cloud climbs on the bubble's sides. In this case, the orientation of the local basis is determined by the angle $\theta_{\text{rot}} = \arctan(-r_{\text{eq}}/z_{\text{eq}})$, and the trapping frequencies become [125]:

$$\omega_{z'}^2 = \omega_z^2\left(\frac{1+3\kappa^2}{2(1+\kappa)} + \frac{\Omega_0^2}{\omega_{\text{rf}}^2}\frac{3\kappa(9\kappa^4-7\kappa^2-2)}{8(1+3\kappa^2)}\right) - \frac{1-\kappa^2}{1+3\kappa^2}\Omega_{\text{eff}}^2, \tag{7.29}$$

$$\omega_{\perp'}^2 = \omega_\perp^2\frac{4}{\kappa}\frac{1-\kappa^2}{1+3\kappa^2}. \tag{7.30}$$

Note that these equations are only valid for $\kappa < 1$. These trapping frequencies can then be used to compute the chemical potential using the same formulas than for the ring trap, (4.24) and (4.25).

It can also be useful to relate to the case of harmonic plus trapping; the corresponding predictions should be valid when the atoms stay close to the bottom of the bubble. The parameter λ describing the strength of the quartic confinement (see (7.22)) can be expressed easily from (7.24) as:

$$\lambda = \frac{d_\perp^2}{4r_b^2}. \tag{7.31}$$

In this case, the central hole is predicted to appear for an effective rotation frequency [76]:

$$\Omega_h = \omega_\perp \left[1 + 2\sqrt{\lambda}\left(\frac{3\sqrt{\lambda}\tilde{g}N}{2\pi}\right)^{1/3}\right]^{1/2}. \tag{7.32}$$

Note that this latter prediction relies on the quasi-2D character of the gas, $\tilde{g}$ being the dimensionless coupling constant (see 1.3); this hypothesis is fulfilled in the experiments that will be described in the next chapter: the chemical potential already dropped below $\hbar\omega_z$ due to the weakening of the radial confinement before the appearance of the hole.

Finally, one can note that the finite magnetic force that can be exerted onto the atoms sets an upper bound on the allowed rotation frequency: if the centrifugal force goes beyond the maximal magnetic force, the atoms are expelled from the trap. This condition can be estimated at the equator of the bubble as:

$$M\Omega_{\text{eff}}^2 r_b < F\hbar\alpha, \tag{7.33}$$

which gives an upper bound to the allowed rotation frequency:

$$\Omega_{\text{eff}} \sim \sqrt{\frac{F\hbar\alpha}{Mr_b}} \sim \omega_\perp\sqrt{2\beta}. \tag{7.34}$$

The maximal value for our magnetic gradient is currently $b' = 216\,\text{G}\cdot\text{cm}^{-1}$, the upper bound for the rotation frequencies we can achieve is therefore approximately $\Omega_{\text{eff}} \sim 3.5\omega_\perp$: we cannot hope to reach extremely fast rotations with this scheme, but it should still be sufficient to allow us performing interesting experiments.

7.3 Collective modes of a rotating condensate

The collective modes of a trapped atomic gas can give a significant insight about their behavior [50, 68, 103, 198]. Especially, in the case of rotating superfluids, the quadrupole mode can be used as a probe to measure the angular momentum of the gas, or equivalently its rotation frequency [199, 200]. Since we use this method to measure the rotation or our gases, I will here enter the details of the underlying theory.

7.3.1 Collective modes of a trapped condensate

Computing the low-energy collective modes of a trapped gas is achieved by following an approach similar to Bogoliubov's (see 1.2.1): the hydrodynamic equations are linearized by computing the effect of small variations $\delta n(\mathbf{r}, t)$ of the atomic density around the ground-state solutions $n(\mathbf{r})$. Since our system is highly oblate, we choose to look for transverse deformations, and exploiting the rotational invariance of our system, we look for δn solutions with the form:

$$\delta n(t) = e^{im_z\phi} r^{|m_z|} P(r^2) e^{-i\omega t}, \tag{7.35}$$

where P is a polynomial of degree p. Injecting these solutions within the hydrodynamic equations (and neglecting the quantum pressure terms – which correspond to the so-called hydrodynamic approximation) leads to the dispersion relation [201]:

$$\omega^2 = \omega_\perp^2\left(\frac{4}{3}p^2 + \frac{4}{3}pm_z + 2p + m_z\right). \tag{7.36}$$

The transverse modes are thus defined by two quantum numbers: p, which gives the number of radial nodes, and m_z, which corresponds to the symmetry of the mode with respect to the z-axis. A few examples of these modes are shown on figure 7.7.

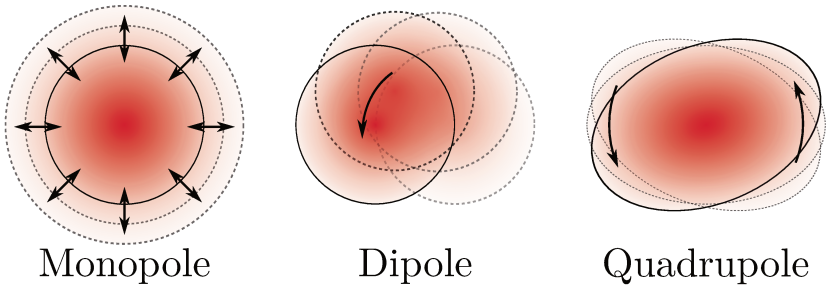

Figure 7.7 – Illustration of the simplest modes in a 2D condensate. From left to right: the monopole mode ($p = 1$, $m_z = 0$), the dipole mode ($p = 0$, $m_z = 1$) and the quadrupole mode ($p = 0$, $m_z = 2$).

One should note that the relation (7.36) is valid only in the oblate case. If the cloud is instead in the quasi-2D regime (i.e. if the Thomas-Fermi approximation is not valid in the vertical direction), the dispersion relation is different; the collective modes are similar but their frequencies are not the same anymore [103, 201]. On the contrary, if the cloud is not highly oblate, oscillations in the vertical direction are coupled to the transverse oscillations, which also leads to a different dispersion relation [89]. However, the modes with $p = 0$ keep the same frequency $\sqrt{m_z}\omega_\perp$ in all three cases. This is in particular the case of the quadrupole modes, in which we will be interested in the following.

7.3.2 The quadrupole modes in a rotating superfluid

The quadrupole modes are the modes corresponding to $p = 0$, $m_z = \pm 2$. The deformation then has the shape $\delta n = A_2 r^2 e^{-i\omega_\pm t + 2i\phi}$, with $\omega_\pm = \sqrt{2}\omega_\perp$. The cloud is elongated in one direction and compressed in the other one, and this deformation rotates at the frequency $\omega_\pm/2 = \omega_\perp/\sqrt{2}$ (with opposite direction of rotation for the $+2$ and the -2 modes). These modes are represented on figure 7.8.

If the cloud sustains angular momentum, the symmetry between the two modes gets broken, with a frequency splitting [199]:

$$\omega_+ - \omega_- = \frac{2L_z}{M\langle r^2\rangle} = 2\Omega_{\text{eff}}. \tag{7.37}$$

Their frequencies also follow the relation:

$$\omega_+^2 + \omega_-^2 = 4\omega_\perp^2, \tag{7.38}$$

which leads, combining both formulas, to the new frequency of both modes:

$$\omega_\pm = \sqrt{2\omega_\perp^2 - \Omega_{\text{eff}}^2} \pm \Omega_{\text{eff}}. \tag{7.39}$$

This splitting gives a useful tool for probing the angular momentum of a cloud; however in many cases it is easier to excite the superposition of both quadrupole modes rather than

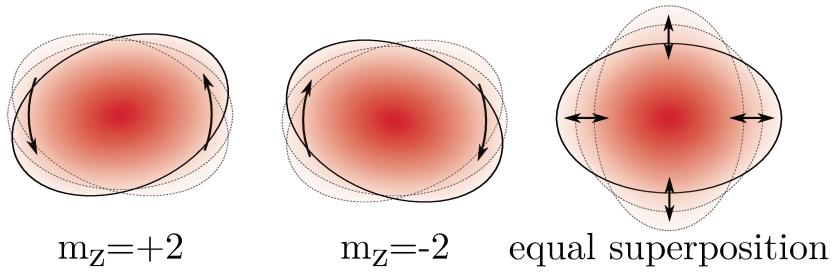

Figure 7.8 – Illustration of the two $m_z = \pm 2$ quadrupole modes of a flat (oblate or quasi-2D) gas, and their equal weight superposition, called "quadrupole oscillation". If the cloud carries angular momentum, the frequency of both modes are not identical anymore, and the axis of the quadrupole oscillation rotates at one fourth of the difference between the frequencies.

only one of them. In the absence of rotation of the cloud, this superposition corresponds to an oscillation of both cloud's radii in opposition of phase – which corresponds to the commonly called "quadrupolar oscillation". If the degeneracy of both $m_z = \pm 2$ modes is lifted by angular momentum present in the cloud, they do not rotate around the cloud at the same speed anymore: the axes of the quadrupolar oscillation then precesses at a frequency $\dot{\phi} = (\omega_+ - \omega_-)/4$ [200], providing in this way an observable to measure L_z.

7.3.3 Collective modes in the case of a harmonic plus quartic trapping

Finally, I will briefly discuss the case of the collective modes in the case of a harmonic plus quartic trapping. We have to distinguish two cases:

- If $\Omega_{\text{eff}} < \omega_\perp$, the condensate is still simply connected, and the modes are very similar to those in a harmonic trap, except for a shift in frequency. For example, while the frequency of the monopole mode is independent of the rotation frequency, it isn't the case anymore in the presence of the quartic trapping [202]. In the case of the quadrupole modes, their frequencies get shifted compared to the harmonic case (7.39) but the splitting between them remains equal to $2\Omega_{\text{eff}}$ [203]:

$$\omega_\pm = \sqrt{\left(2 + 3\lambda \frac{R_{\text{max}}^2}{d_\perp^2}\right)\omega_\perp^2 - \Omega_{\text{eff}}^2} \pm \Omega_{\text{eff}}, \tag{7.40}$$

  where R_{max} is the Thomas-Fermi radius of the cloud (taking into account the quartic confinement). Note that this formula is in fact valid as long as the cloud is simply connected, i.e. as long as $\Omega_{\text{eff}} < \Omega_h$ (in particular, it can be valid even for $\Omega_{\text{eff}} > \omega_\perp$).

- For faster rotations, once a hole appears at the center of the cloud, the frequencies of the modes are expected to significantly deviate. Two predictions, in particular, are remarkable: first, in the limit of large Ω_{eff} and/or small λ, there is an infinite family of modes with frequency $\sqrt{6\Omega_{\text{eff}}^2 - 2\omega_\perp^2}$, independent of both the polarity m_z and the quartic strength λ. Second, in the case of the quadrupole modes, once the hole formed there should be four quadrupole modes: two modes with $m_z = +2$ and two modes $m_z = -2$, with distinct frequencies (among which three should be possible to observe), see figure 7.9 [196, 203].

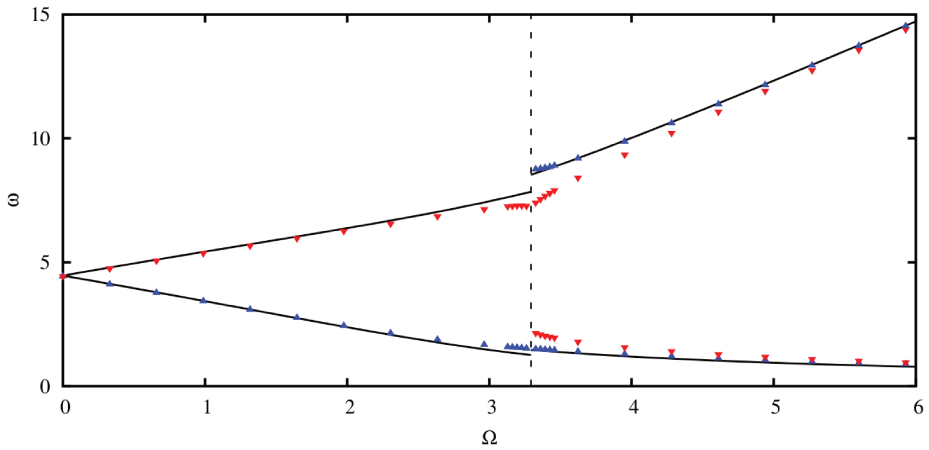

Figure 7.9 — Frequencies of the quadrupole modes in a harmonic plus quartic trap computed by M. Cozzini [203], plotted in units of $\omega_\perp$. The blue, upwards triangles correspond to the $m_z = +2$ modes and the red, downward triangles correspond to the $m_z = -2$ modes, obtained by numerically integrating the GP equation. The vertical dashed line indicates $\Omega_{\text{eff}} = \Omega_h$. It is much larger here than in our case ($\Omega_h \sim 1.05\omega_\perp$) because the chosen value for the quartic term is $\lambda = 0.5$ (while it is equal to 1.3×10^{-4} for our experiments): since the quartic term is much stronger, the hole formation requires a larger rotation frequency – see equation (7.32). Above this value, two additional modes appear, leading to two co-propagating and two counterpropagating modes. The solid lines correspond to sum rules predictions. For $\Omega_{\text{eff}} < \Omega_h$ the two lines correspond to the two solutions of equation (7.40). For $\Omega_{\text{eff}} \gg \Omega_h$, the upper frequencies tend towards $\sqrt{6\Omega_{\text{eff}}^2 - 2\omega_\perp^2}$.

In the case of the bubble trap, no calculations have been done and what should happen is unclear, but we can hope that for Ω_{eff} close to $\omega_\perp$ the system will stay close enough from the harmonic plus quartic trapping case for the predictions of this second case to be valid. Also, since the prediction of degenerate modes for larger Ω_{eff} is independent from λ, we can hope that it does not depend too much on the exact geometry of the cloud and will also stay valid.

7.4 Experimental techniques for studying vortices

I will finish this chapter by describing briefly the usual experimental methods that are used to study vortices in degenerate quantum gases; in particular I will discuss the case of vortex nucleation and vortex detection.

7.4.1 Nucleating vortices

There are principally two ways to introduce vortices within a superfluid. The first one relies on phase imprinting [51, 204]. It provides a very controllable way to create a given number of vortices or to generate multiply-charged vortices [56]. However, it is not efficient for generating very large number of vortices, and thus not suitable for the experiments we want to realize. The second way relies on the mechanical stirring of the cloud to inject large amounts of angular momentum, and it is the one we are interested in here.

The nucleation of vortices in a superfluid through stirring of the initially vortex-free cloud requires two main ingredients:

- The state containing vortices has to be energetically favorable compared to the vortex-free state, meaning that the cloud has to rotate fast and/or to carry angular momentum. In the harmonic case, the minimal rotation that the cloud has to achieve for the first vortex to be favored reads [170]:

$$\Omega_{\min} = \frac{5}{2}\frac{\hbar}{MR_\perp^2}\ln\left(\frac{R_\perp}{\xi}\right). \tag{7.41}$$

  This frequency is usually quite small, for example in the parameters of the experiments described in the next chapter it corresponds to approximately 5 Hz (while all the frequencies considered in the experiments are larger than 20 Hz).

- A surface instability: nucleating vortices requires to introduce a length scale ξ into the system, that is much smaller than the length scales of the system at rest. This requires surface instabilities, i.e. the flow at the nucleating surface has to become turbulent [205, 206].

These two ingredients can be obtained by different method: for example, one can displace a stirrer beam (or several stirrer beams) within the fluid faster than the critical velocity [166, 207], or rotate the cloud within an anisotropic trap [52, 90].

7.4.2 Driving the cloud through quadrupole resonance

I will detail more this latter case, as it is the one we use the most in our experiments. To generate rotation in the cloud, we make the trap anisotropic and rotate this anisotropy (see figure 7.10) at a frequency $\Omega_{\rm rot}$. The problem can then be expressed as: how can we couple angular momentum into the cloud through the rotation of the trap?

Let us express as ω_X and ω_Y the oscillation frequencies of the rotating trap; the trap's anisotropy is defined as $\varepsilon = (\omega_X^2 - \omega_Y^2)/(\omega_X^2 + \omega_Y^2)$. As we want to drag a superfluid initially at rest, its vorticity is necessarily zero as it has no vortices in it. We can look for the velocity field under the form of the quadrupolar flow (see fig. 7.10):

$$\mathbf{v} = \alpha_q \nabla(XY), \tag{7.42}$$

where $\mathbf{v}$ is the velocity in the laboratory frame and X, Y the coordinates in the frame rotating at $\Omega_{\rm rot}$. Injecting this formula into the hydrodynamic equations shows that in the rotating frame the cloud keeps the usual parabolic Thomas-Fermi shape, but with effective trapping frequencies [181]:

$$\tilde{\omega}_X^2 = (1+\varepsilon)\omega_\perp^2 + \alpha_q^2 - 2\alpha_q\Omega_{\rm rot}, \tag{7.43}$$

$$\tilde{\omega}_Y^2 = (1-\varepsilon)\omega_\perp^2 + \alpha_q^2 + 2\alpha_q\Omega_{\rm rot}, \tag{7.44}$$

and one can show that α_q verifies the equation:

$$\alpha_q^3 + \alpha_q(\omega_\perp^2 - 2\Omega_{\rm rot}^2) + \varepsilon\Omega_{\rm rot}\omega_\perp^2 = 0. \tag{7.45}$$

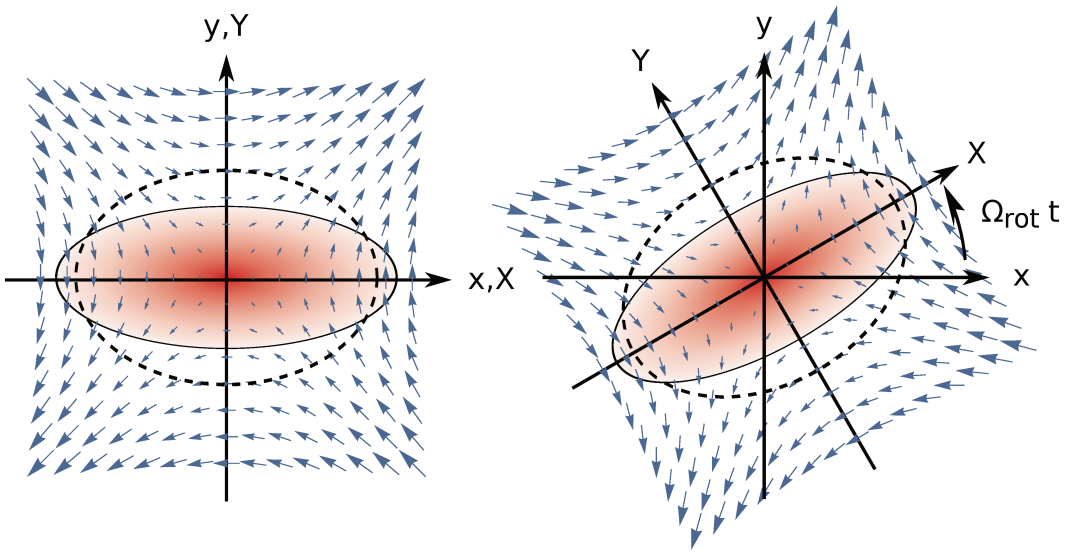

Figure 7.10 — Principle of the considered excitation: the trap is made anisotropic and rotates at a constant frequency Ω_{rot}. The cloud's anisotropy δ_c is not necessarily the same as the anisotropy ε of the trap and depends on both Ω_{rot} and ε; injecting angular momentum in the cloud requires to deform it significantly. In such a situation, the cloud's velocity is describes by the quadrupolar velocity field $\mathbf{v} = \alpha_q \nabla(XY)$ (blue arrays). It ensures $\boldsymbol{\nabla} \times \mathbf{v} = 0$ and is thus allowed in a superfluid; it allows the cloud to carry angular momentum even in the absence of vortices. Note that close to the large axis of the trap, the velocity field matches a solid-body rotation. The more the cloud is deformed the closer the cloud is to the solid-body rotation (and its angular momentum then also tends towards this limit).

α_q completely characterizes the velocity field and the shape of the condensate, and the solutions of this equation then give the possible behavior of the condensate. One can also show that α_q is linked to the deformation of the condensate $\delta_c \equiv (R_X^2 - R_Y^2)/(R_X^2 + R_Y^2)$:

$$\alpha_q = \Omega_{\text{rot}} \frac{\omega_X^2 - \omega_Y^2}{\omega_X^2 + \omega_Y^2} = \Omega_{\text{rot}} \delta_c. \tag{7.46}$$

The angular momentum per particle in the cloud then reads:

$$L_z = M \langle r^2 \rangle \delta_c^2 \Omega_{\text{rot}}. \tag{7.47}$$

We see that compared to the angular momentum of the classical flow $M\langle r^2 \rangle \Omega_{\text{rot}}$, there is a reduction of L_z by a factor δ_c^2. Injecting angular momentum in the cloud therefore requires to deform the condensate.

The solutions of equation (7.45) are plotted on the figure 7.11. Depending on the values of ϵ and Ω_{rot}, we see up to three possible solutions. They can be divided into two branches:

- The *normal* branch goes from $\Omega_{\text{rot}} = 0$ to ω_Y. For this branch, $\alpha_q < 0$, meaning that the long axis is oriented along the weak trapping direction. As Ω_{rot} increases, the deformation of the cloud increases, up to $\Omega_{\text{rot}} = \omega_Y$ where both the cloud's small radius and its angular momentum diverges.

- The *overcritical* branch, with $\alpha_q > 0$, corresponds to a cloud rotating with an orientation perpendicular to the trap's axes (i.e. with a big radius oriented along the *strong* trapping direction). It starts at $\Omega_{\rm rot} = +\infty$, comes to lower frequencies up to a back-bending point, and then ends up at $\Omega_{\rm rot} = \omega_X$. One can note that the upper part of this branch is dynamically unstable, while its lower part is stable and corresponds to a condensate rotating while keeping an almost round shape.

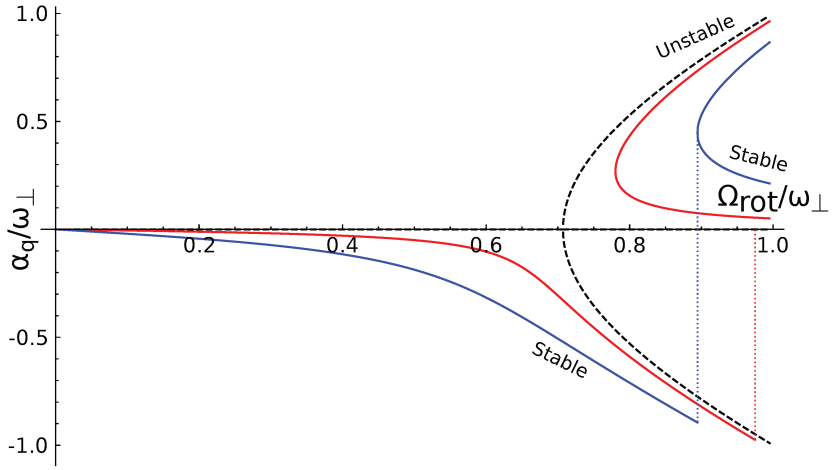

Figure 7.11 — Rescaled solutions of equation (7.45) depending on the rotation frequency of the trap $\Omega_{\rm rot}$ (plotted from 0 to $\omega_\perp$, for $\varepsilon = 0$ (black, dashed line), $\varepsilon = 0.05$ (red solid line) and $\varepsilon = 0.2$ (blue solid line). The vertical dotted lines correspond to $\Omega_{\rm rot} = \omega_Y$. For $\varepsilon = 0.2$, the limit of the normal branch coincides with the backbending point of the overcritical branch; for $\varepsilon > 0.2$ the normal branch ends before this point and there is a range of rotation frequencies for which no solution is allowed.

The backbending point happens at a frequency $\Omega_{\rm rot}$ which is the solution of [91]:

$$\varepsilon = \frac{2\omega_\perp}{\Omega_{\rm rot}} \left(\frac{2(\Omega_{\rm rot}/\omega_\perp)^2 - 1}{3} \right)^{3/2}. \tag{7.48}$$

Starting from a cloud at rest, turning on the rotating anisotropy with a rotation frequency above or below this point will lead to a strong change in the cloud's behavior, as the branch that gets the most easily excited is not the same anymore. In particular, as the deformation of the cloud is much weaker on the lower part of the overcritical branch, it allows the cloud to carry significantly less angular momentum than the normal branch.

7.4.3 Detecting vortices

In trapped atomic gases, ξ is usually very small, typically a few 0.1 µm: in most cases, it is well below the imaging resolution and cannot be detected directly. Imaging vortices in dilute superfluids thus requires to perform a time-of-flight expansion to allow the core size to expand: as the cloud expands freely, the density strongly drops and the healing length significantly increases and the size of the vortices can become large enough for them to be detected by conventional imaging techniques [52, 53].

The free expansion of a harmonically trapped BEC initially the Thomas-Fermi regime has been described by Castin and Dum [208]. The cloud keeps its parabolic shape, but the TF radii become rescaled by a factor λ_j: $R_j(t) = R_j(0)\lambda_j(t)$. Their results have been extended later to the case of a rotating cloud [209], and in this latter case the scaling factors follow the equations:

$$\ddot{\lambda}_\perp = \frac{\omega_\perp^2 - \Omega_{\text{eff}}^2}{\lambda_\perp^3 \lambda_z} + \frac{\Omega_{\text{eff}}^2}{\lambda_\perp^3}, \tag{7.49}$$

$$\ddot{\lambda}_z = \frac{\omega_z^2}{\lambda_\perp^2 \lambda_z^2}. \tag{7.50}$$

Depending on the shape of the trapped gas, we can then see two different limit behaviors for the expansion:

- In the case of a cigar-shaped gas, the expansion is essentially radial and $\lambda_z \sim 1$: the rotation then has only little effect on the expansion. The cloud's radial size becomes simply rescaled by a factor $\sqrt{1+\omega_\perp^2 t^2}$, and the vortex size evolves in the same proportion.
- In the case of a pancake-shaped gas, the vertical expansion of the cloud is much faster than the radial expansion. Therefore, the size of the vortices grows, in proportion, faster than the cloud's radius [210,211]. However, no simple analytical formulas are available in this limit.

Chapter 8

Fast rotating Boses gases in a RF-dressed trap

This chapter describes the experimental results that have been achieved on the topic of fast-rotating superfluids. All the experiments were realized at the bottom of the bubble trap, as described in the previous chapter (section 7.2.3). In particular, I will detail the achievement of a cloud rotating faster than the trapping frequency, which then takes a donut shape. To avoid confusion with the second part of this thesis, I will restrict the use of the terms "ring-shaped" and "annular" gases to the gas trapped with the blue-detuned double sheet, and rather speak of "donut-shaped gas" or "dynamical ring".

The first two sections of this chapter describe the achievement of such a donut-shaped gas, first using the stirrer beam, and then exciting the cloud with a quadrupole deformation. The two next sections then describe the study of this donut-shaped gas and the transition regimes from the connected gas. The third section presents how we probe the quadrupole modes in the gas, using both a percussive and a resonant method imported from the group of J. Dalibard [200, 212]. The fourth and last section discusses the vortex distribution in the dynamical ring – or rather, the absence of visible vortices in the dynamical ring and the progressive melting of the vortex lattice while we enter the fast-rotating regime.

8.1 First experiments with the laser stirrer: reaching the fast rotation regime

8.1.1 First attempt

The first attempts to achieve a fast rotating gas in the bubble trap were done with the stirrer beam (described in section 6.1.1). Starting from a gas at the bottom of the bubble, the stirrer was pointed onto it and described circular trajectories with various parameters (radius of typically 10 to 25 µm for a cloud size around 20 µm and frequencies around 35 to 50 Hz for a trapping frequency of 37.5 Hz). We initially tried to cool down the cloud during the stirring process: starting from a thermal cloud close to the BEC limit, the cloud was stirred during 500 ms while the RF knife was ramped down, and then allowed to relax in the presence of a low knife. In these conditions, we expect to prepare a cloud rotating at very large speed, and

even reach a situation where the central density is depleted due to the centrifugal force (see chapter 7).

As the stirring proceeds, we saw the gas expanding a lot in the horizontal plane. In addition, the cloud became very anisotropic, with the main axis almost always oriented in the same direction (in a few cases, it happened to be oriented approximately orthogonally to the most frequent orientation). This favored orientation appeared to depend on the amplitude balance between the dressing antennas. Looking for the time evolution of the cloud, the knife removed during the waiting time to ensure that it doesn't modify the behavior of the gas, we observed that for short times after excitation, the cloud displayed a lowered density at its center while being quite anisotropic, and equilibrated back to a round shape in approximately 1 s, passing through a highly anisotropic situation (see figure 8.1). Later tests also showed that the orientation of the cloud in the anisotropic phase depends on the rotation direction: the clouds obtained for clockwise or counterclockwise rotations were oriented orthogonally.

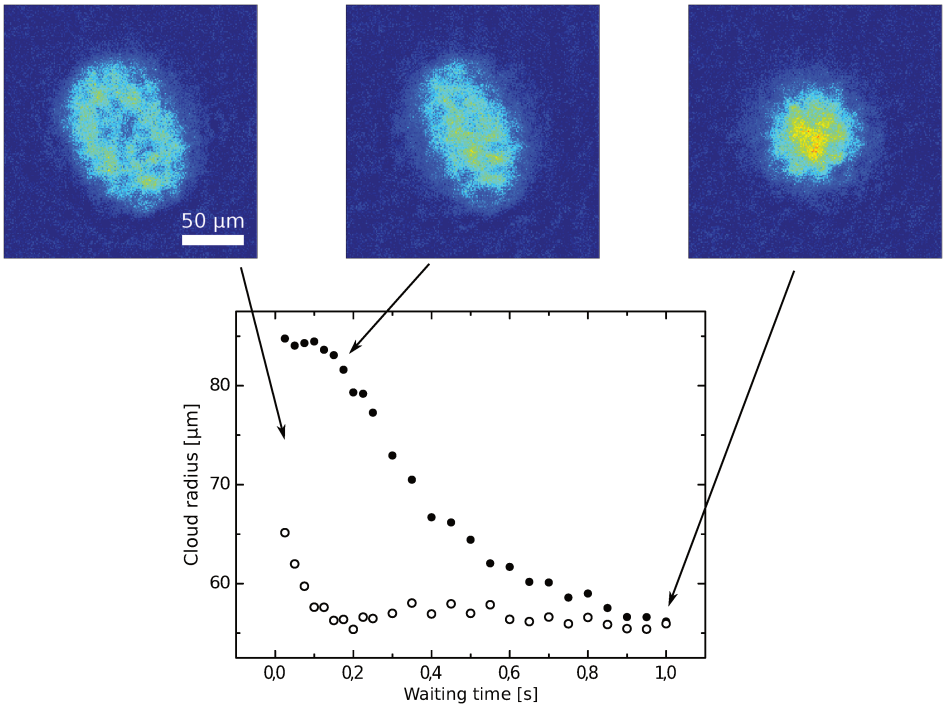

Figure 8.1 — Evolution of the anisotropy of a fast stirred cloud in a trap with residual asymmetry. The initial cloud has a lower density in its center which quickly fills while the short axis quickly reduces, leading to a rise of the anisotropy. The long axis then also reduces on a longer time scale, going back to a round gas.

8.1.2 Balance between antennas

The presence of a favored axis in a trap expected to be rotationnaly invariant appeared very surprising at first sight. However, previous works [172] reported that for very high rotation rates, even a small residual asymmetry of the trap can lead to large anisotropy of the final gas: indeed, as one of frequencies of the quadrupole mode becomes very close to zero when the

effective rotation frequency of the cloud gets closer to the trapping frequency (see equation (7.39)), this quadrupole mode will get resonantly driven by static asymmetries.

These experiments were performed before implementing the third dressing antenna, cf section 5.2.2: the small tilt of the dressing antennas could, for example, explain the origin of such a small asymmetry in the trapping potential. After implementing the third antenna, we repeated these experiments, looking for the effect it would have onto the atoms. When scanning the third antenna's parameters and looking for the cloud after a given time, we observed that the third antenna allows to reduce the anisotropy, corresponding to a slower relaxation dynamics and a larger depletion in the center at the beginning (figure 8.2).

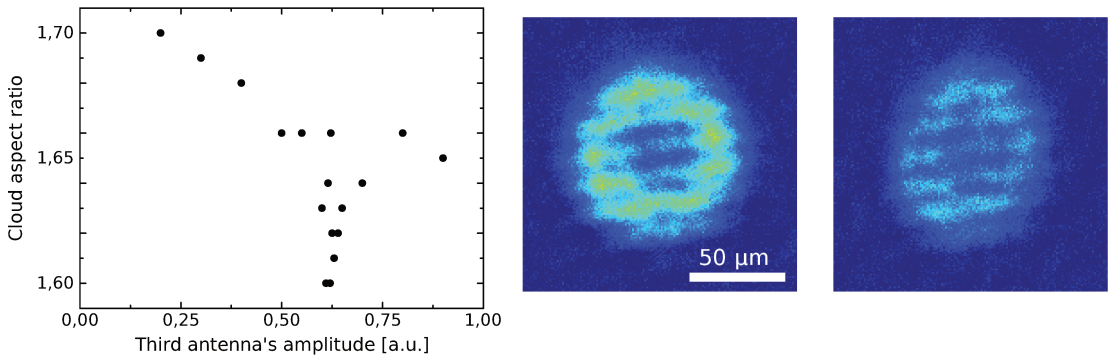

Figure 8.2 — Left: aspect ratio of the cloud measured in situ after fast stirring and 200 ms waiting time in the trap, as a function of the third antenna's amplitude (amplitude 1 corresponds to the maximum available power). We see a highly peaked resonance behavior, signature of the high criticity of the trap symmetry. Note that the two main dressing antennas were not very well balanced for these data, and the cloud's aspect ratio thus doesn't go down to 1. Right: in situ pictures of the cloud after respectively 200 ms and 4 s, for a careful tuning of all three antennas. The cloud has a clear depletion in its center and is much more round than previously; its relaxation dynamics is also much slower.

Finally, after a very careful tuning of the antennas, we were able to almost suppress the anisotropy, ending up with a "donut-shaped" gas for stirring frequencies exceeding the trapping frequency. This shape seemed to have a similar relaxation than previously, going through a very anisotropic phase, but on a much longer time scale (several seconds). For optimal tuning, we managed to reach a satisfying cylindrical symmetry with just the two main antennas (this will be discussed more in detail in section 8.2.5). It also appeared simpler use a low magnetic gradient (as it allows to keep more atoms in the trap) and to apply a constant knife during the whole experimental sequence.

8.2 The fast rotating bucket

The change of the DDS (cf 3.3) gave us the possibility to rotate the atomic gas using the bubble itself, and it to allows setting the atoms into rotation in a more controllable way than the stirrer, as it is insensitive to optical alignments. Since this is the method we used the most, I will now enter its details.

8.2.1 Rotation of the bubble itself

The overall idea of this rotation method is the "rotating bucket", already used since a long time to rotate superfluid helium [13] or dilute BECs [52]. The atoms are placed in a trap that is slightly anisotropic in the horizontal plane, and the anisotropy is then rotated at a given frequency. For dilute superfluids, the transfer of angular momentum from the container to the atoms has been studied in detail in the group of J. Dalibard [90, 213] and C.J. Foot [91].

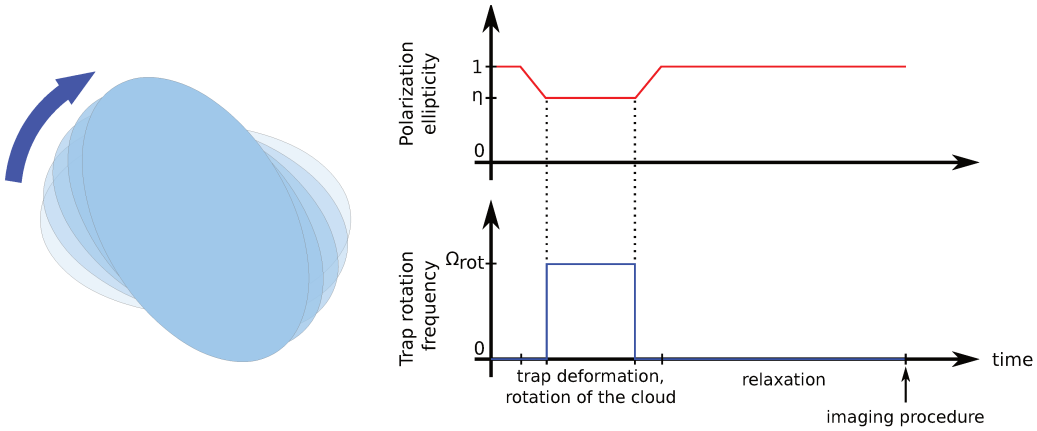

Figure 8.3 — Principle of the rotating bucket scheme. The polarization of the dressing RF (controlled by the parameter η, see 2.3.4) is made elliptical in a 0.8 ms ramp, and the polarization axis is then rotated for a given time; the polarization is then made circular again. This allows to make the trap anisotropic and rotate it at the desired frequency. After a given waiting time in the rotationnaly invariant trap, the resulting cloud is imaged (in situ or after a time-of-flight procedure). Note that this scheme can be repeated at the end of the waiting time to excite the cloud again, for example to excite quadrupole modes in the rotating cloud (see 8.3).

In our case, the control of the RF polarization allows us to easily perform such an experiment: the degree of ellipticity of the RF polarization sets the anisotropy of the trap, and the axis of the polarization ellipse determines the orientation of the trap; corresponding theoretical details are given in sections 2.3.3 and 2.3.4.

In the absence of additional precision, all the experiments described below follow the experimental sequence shown on figure 8.3: starting from a condensate at rest at the bottom of a bubble in circular polarization, we ramp up the anisotropy in a short time (0.8 ms), rotate it at a constant anisotropy and frequency for a certain number of turns[1], and the anisotropy is then ramped down in a short time, again 0.8 ms, while the trap doesn't rotate anymore. The cloud then evolves in a rotationally invariant potential; the radial and vertical frequencies have respectively been measured as 34.2(2) Hz and 357.9(5) Hz. The parameters of the trap used for all these experiments are $b' = 55.4\,\mathrm{G}\cdot\mathrm{cm}^{-1}$ (the quadrupole current was 28.5 A), $\omega_{\mathrm{rf}} = 2\pi \times 0.3\,\mathrm{MHz}$ and $\Omega_0 = 2\pi \times 49.3\,\mathrm{kHz}$; the expected bubble radius is then $r_b = 78\,\mu\mathrm{m}$.

1. For practical reasons, this number is integer or half-integer

8.2.2 Resonance at $\omega_\perp/\sqrt{2}$

Setting the cloud into rotation with this method was demonstrated to occur through the resonance of the quadrupolar modes [90, 91], expected around $\omega_\perp/\sqrt{2}$. A good way to ensure that the rotation process works as expected is to look for this resonance. For that, we rotate a very small anisotropy ($\varepsilon = (\omega_x^2 - \omega_y^2)/(\omega_x^2 + \omega_y^2) = 0.03$). After a relaxation time of 15 s, we let the cloud expand to observe possible vortices and count them. The corresponding measurements are shown on figure 8.4. We find the expected resonance, centered as predicted.

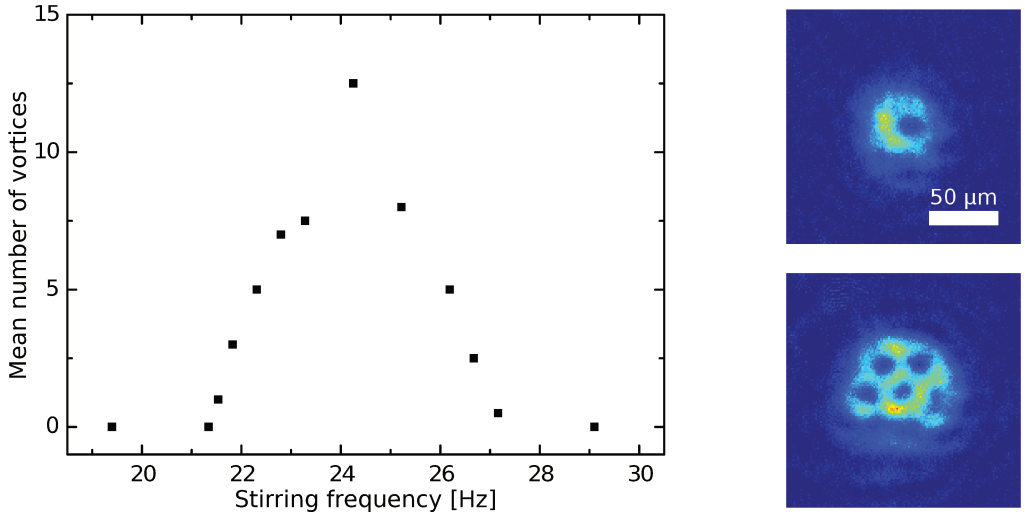

Figure 8.4 — Left: Mean number of vortices depending on the stirring frequency. The resonance of the quadrupole mode is expected to happen at $\omega_\perp/\sqrt{2} = 24.1$ Hz. Each point is the average of two or three measurements. Right: example pictures of vortices, with respectively 1 and 7 vortices. The imaging of vortices is discussed in section 8.4.

8.2.3 Effect of a large excitation on the atoms

In order to reach faster rotation regimes, we tried to use large anisotropies, and working with large anisotropies for the excitation broadens the quadrupole resonance (see section 7.4.2). We first tried to see how much rotation we were able to generate into the cloud for a given anisotropy and rotation frequency. We excited the cloud during a long time (40 or 50 turns), let it relax during 1 s and used as an observable the transverse radius after time-of-flight expansion: due to the centrifugal force, the more the cloud rotates the larger the radius after expansion. The measurement results are shown on figure 8.5.

We see that for large anisotropies, the resonance becomes highly asymmetric. Increasing the excitation frequency leads to an increase of the rotation of the cloud, until a very clear threshold frequency. Below their respective thresholds, all points seem to gather on the same curve. This threshold can be interpreted as coming from the existence of the overcritical branch in the excitation spectrum of the quadrupole (see 7.4.2). This branch is expected to appear above a frequency given by (7.48); solving this equation shows a quite good agreement with the thresholds observed on figure 8.5, even though the measured threshold is always slightly higher than the expected one by a few percent.

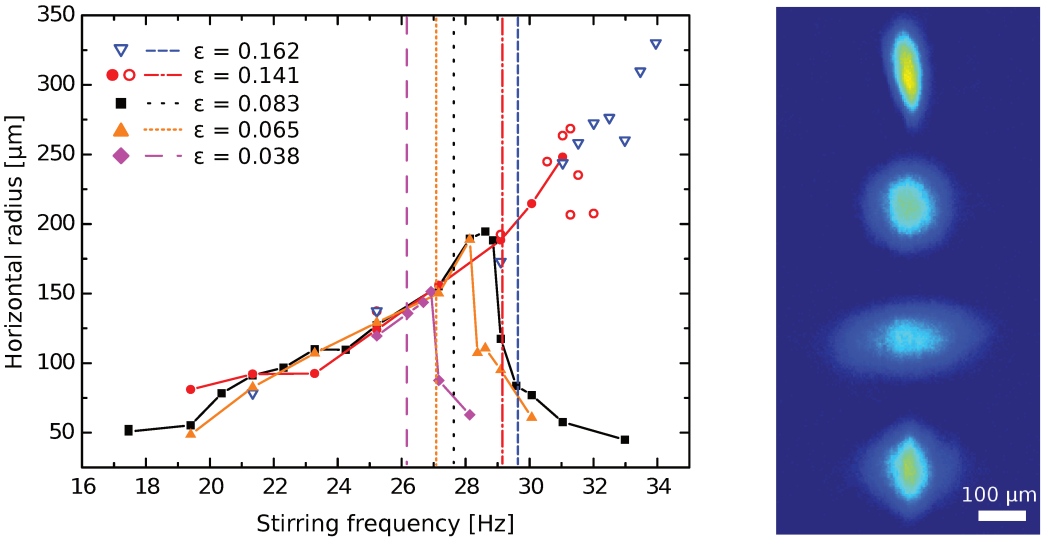

Figure 8.5 — Left: Horizontal radius of the cloud depending on the rotation frequency, measured for various anisotropies. Full symbols are taken for 40.5 turns and hollow for 50.5 turns. The vertical dashed lines correspond to the maximal rotation frequency calculated from (7.48). Note that the cloud relaxed 1 s each time, and ulterior experiments showed that this was not always enough for the cloud to reach equilibrium, however this should not change the conclusions we deduce from these measurements. Right: pictures of the cloud excited with an anisotropy 0.093 and respective frequencies (top to bottom) 20.4, 23.3, 28.1 and 29.1 Hz. For increasing rotation frequencies, the horizontal radius increases while the vertical radius slightly shrinks. Above a certain threshold (last picture), the horizontal radius is smaller again.

8.2.4 Dynamical ring formation

Using this excitation technique with large anisotropies ($\varepsilon = 0.14$) and large rotation frequencies ($\Omega_{\text{rot}} \geq 30\,\text{Hz}$), we saw, again, a donut-shaped cloud appearing, but this time on a very long time scale: right after stirring, the cloud still has a maximum in its center, which progressively depletes over approximately 20 s. The resulting cloud then lasts extremely long: several tens of seconds (see figure 8.6). Surprisingly, the donut appears even for excitation frequencies lower than $\omega_\perp$; this point will be discussed in section 8.3.

8.2.5 (Very) fine tuning of the antennas

The donut-shaped cloud appears to be extremely long-lived, possibly due to the very good smoothness of our trap. However, it also requires an extremely fine tuning of the trap's anisotropy. The tuning precision we achieve on the amplitude of the antennas is around 0.2% (we are limited by the resolution of the DDS) and the precision on their relative phase is 0.3°. From these numbers we estimate that the residual anisotropy of our trap is $\varepsilon \lesssim 0.001$; we obtain a dynamical ring if the residual anisotropy is lower than 0.3%.

The tuning of the antenna's parameters is achieved by limiting as much as possible the dissipation of rotation within the trap:

- The rough tuning is achieved by rotating the cloud at a moderate frequency ($\sim 20\,\text{Hz}$)

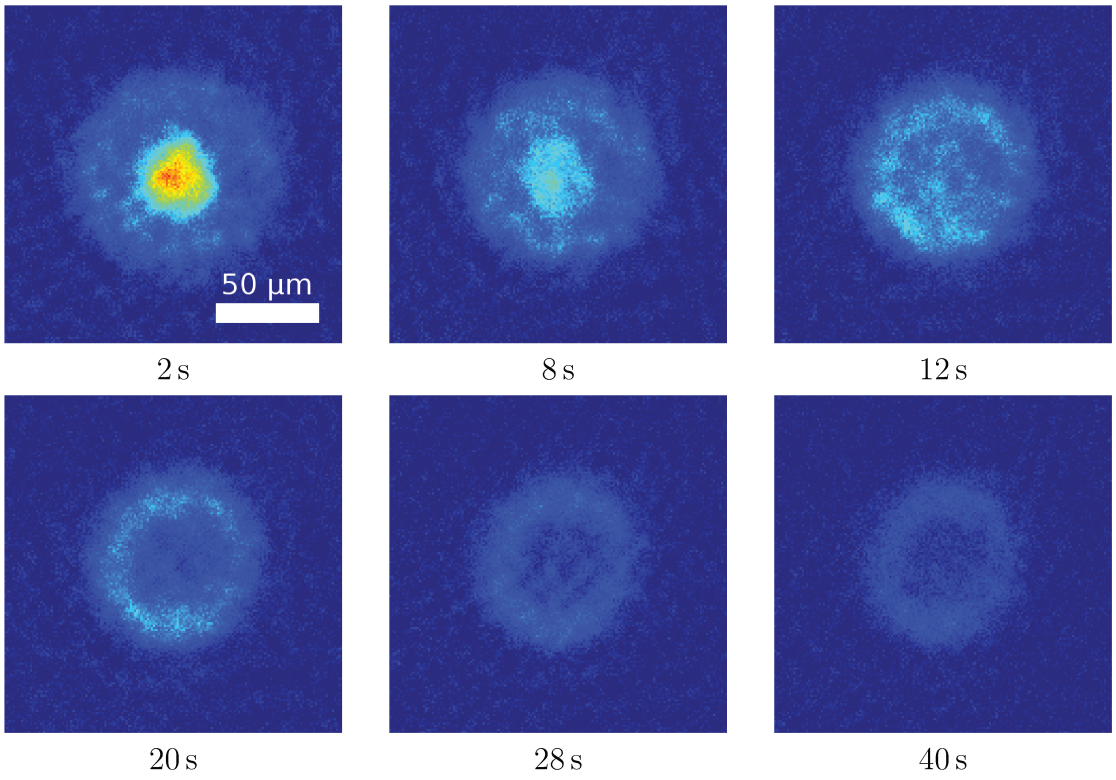

Figure 8.6 — Time evolution of a fast-stirred cloud excited with the rotating bucket scheme. The excitation anisotropy was $\varepsilon = 0.14$ and the cloud was rotated at 31.1 Hz for 5.5 turns. All pictures are taken in situ.

and moderate anisotropy. The phase and amplitude of the antennas are then adjusted to maximize the horizontal size of the cloud, similarly to 8.2.3. We achieve in this way an anisotropy at the level of a few percent. The corresponding curves are shown on figure 8.7.

- The fine tuning is achieved by performing fast rotation with large anisotropy (31.1 Hz and $\varepsilon = 0.14$) and looking at the cloud after a long waiting time (several seconds). We then minimize the observed anisotropy and ensure that the donut survives: if the anisotropy is too large, the cloud will have came back to a simply connected situation. We first take pictures after 5 s, adjust the antennas to have an isotropic and large cloud, then look after 10 s and repeat the procedure... Taking pictures after increasing waiting times ensures that we always have a signal to optimize.

We can, however, wonder why we are able to achieve such a round trap without using the third antenna to correct for the antenna's angle if the circularity of the trap is so critical. A possible answer would be that at a given place, it is always possible to adjust the RF polarization so that its projection onto the local σ^+ polarization is equal to the one of the circular polarization. We can then locally compensate the tilt of the antennas by adjusting the relative amplitude applied to each other. This would explain why, to achieve a very round trap, we need to apply amplitudes to both antennas that are not identical (the coupling they would create at the bottom of the bubble, if they were used alone in linear polarization, would differ by a few percent – see section 3.3.3). This would mean that we optimize the

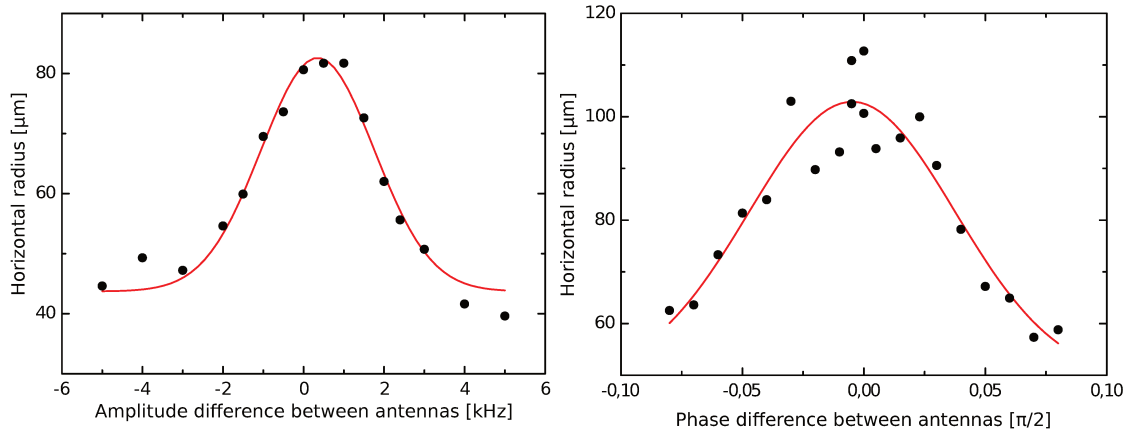

Figure 8.7 — Tuning of the difference of amplitude between antennas (left) and their relative phase (right). We rotate the cloud at 20 Hz during 3.5 turns with an anisotropy 0.12, and let it relax during 1 s. We then perform a 23 ms time-of-flight, take a picture from the side, and measure the cloud's horizontal radius. In both cases, we end up with a bell-shaped curve centered on the parameters corresponding to an isotropic trap (red lines correspond to Gaussian fits). Note that the left curve was measured first and the right curve second, after choosing parameters deduces from the first one, explaining why it has a higher maximum.

trap's isotropy at the bottom of the bubble trap, but if the atoms get too far away from it we can guess that the trap will not be rotationally invariant anymore.

8.2.6 Is it condensed?

One crucial question we need to anwer is: is this donut-shaped cloud phase coherent? Indeed, as our stirring process is extremely violent, we could fear that it would cause heating. Also, once the gas acquired its donut shape its density has strongly dropped, and the phase-space density could have become too low for the gas to stay condensed.

To get insight on the possible condensation of our gas, we performed time-of-flight experiments. We simply release the gas from its trap, let it expand in free fall during various durations, and image it from the side after that. This gives us the atomic density integrated along the imaging axis (y), such as presented on figure 8.8. In order to avoid making hypotheses on its radial profile, we also integrate the data along the cloud's large axis (after expansion). The resulting profile appears to be nicely Gaussian, with a width that evolves linearly with a coefficient $1.51(2) \times 10^{-3}\,\mathrm{m \cdot s^{-1}}$.

Based on this measurement, we can exclude the possibility for the gas to be thermal using a proof by contradiction. Indeed, if we suppose that the gas is thermal, its temperature can be deduced from its vertical expansion (supposing that the initial size of the cloud can be neglected):

$$\sigma(t) = \sqrt{\frac{k_\mathrm{B}T}{M}}t. \tag{8.1}$$

From the measured vertical expansion, we deduce a temperature $T = 23.8(6)\,\mathrm{nK}$. Using the in situ pictures of the dynamical ring, we can also deduce the expected value for Ω_eff from the ratio between the radius of the donut-shaped cloud and the radius of the bubble at the

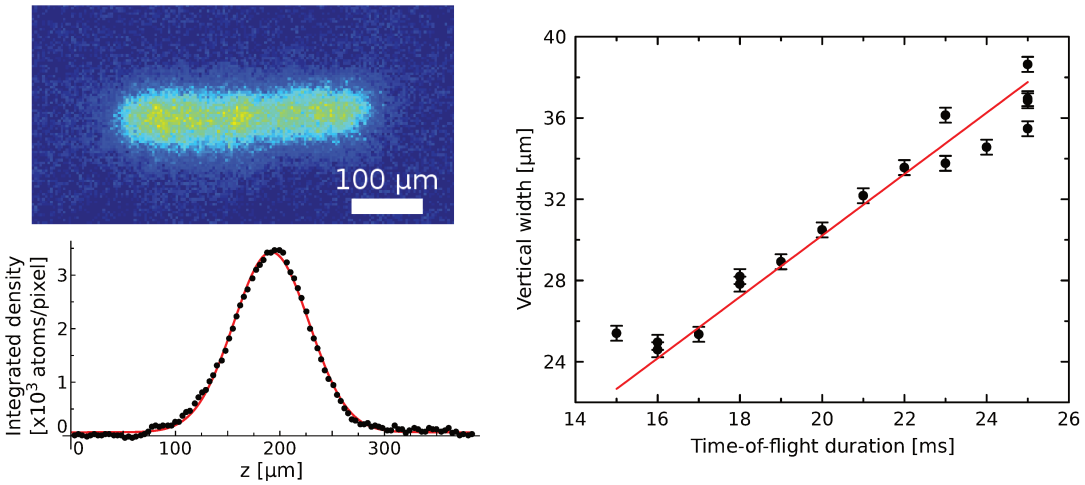

Figure 8.8 — Left, top: picture of the dynamical ring after a 23 ms expansion, taken from the side. Left, bottom: density profile of the upper picture, integrated along the cloud's large axis. A Gaussian fit (red solid line) gives a width of 36.1(3) µm. The angle used to integrate the upper picture is chosen in order to minimize the fitted width. Right: evolution of the cloud width with the time-of-flight duration. A linear fit of the data (red solid line) gives a slope of $1.51(2)\,\mu\mathrm{m}\cdot\mathrm{ms}^{-1}$.

equator using the relation (7.26). This then allows us to estimate the trapping frequencies at the position of the atoms, and therefore the peak atomic density. The radius of the dynamical rings we observe is typically 35 µm, corresponding to $\Omega_{\mathrm{eff}} \approx 1.05\times\omega_\perp$; in this case the trapping frequencies, given by equations (7.30) and (7.29), are approximately $\omega_{\perp'} = 2\pi \times 11\,\mathrm{Hz}$ and $\omega_{z'} = 2\pi \times 345\,\mathrm{Hz}$ (in the mexican hat potential). With both the trap parameters and the temperature, we can compute the corresponding phase-space density. If the 10^5 atoms of the donut-shaped cloud were thermal at 24 nK we would obtain a phase-space density around 13, which in turns contradicts our assumption of a thermal gas.

One could still object that if the density is low enough, the gas would hardly thermalize and could have different vertical and radial temperature (with a low vertical temperature and very large radial temperature). However, in such a case the radial width of the cloud would express as $\sqrt{k_{\mathrm{B}}T/M\omega_{\perp'}^2}$: a radial temperature higher than 120 nK would imply a radial width larger than 35 µm and can therefore be excluded, as we would see no central hole in such a case. Allowing a radial temperature of 100 nK and a vertical temperature of 24 nK, an estimation of the collision rate as $\overline{n}\overline{v}\sigma_0$ ($\overline{n}$ being the average density, $\overline{v}$ the average velocity and σ_0 the collisional cross-section) [214] leads to approximately 3 collisions per second: the cloud would therefore have thermalized after 20 s, and this case is then also irrelevant.

The other hypothesis is that we observe a purely condensed cloud, and we should ensure that this hypothesis is relevant. The Gaussian vertical profile after expansion suggests that the cloud is in the two-dimensional regime: we can compare the measured expansion to the free expansion of the ground state of the vertical harmonic oscillator. The corresponding density profile would also be Gaussian, with an asymptotical expansion given by [215]:

$$\sigma(t) = \sqrt{\frac{\hbar\omega_{z'}}{2M}} \times t. \tag{8.2}$$

The corresponding increase in the Gaussian width would be $0.89 \times 10^{-3}\,\mathrm{m \cdot s^{-1}}$, comparable to our measured expansion even though quite smaller. If we compute the expected 3D chemical potential using formula (4.24) (which should be valid for a condensed dynamical ring) with the aformentioned values for the trapping frequencies and atom number, the result is approximately $h \times 230\,\mathrm{Hz}$, lower than the vertical trapping frequency, which confirms that the hypothesis of a quasi-2D condensate is relevant.

From this discussion, we believe that the observed cloud is quantum degenerate, and we will make this supposition during the rest of the chapter.

8.2.7 Effect of the RF knife

One element of the experiments has been neglected up to now in our analysis of the system: the RF knife, which is required to suppress the cloud heating during the experiments, in particular at long times. Indeed, as it causes atomic losses, it can have an impact on the rotation of the cloud, and as it is selective in position due to coupling inhomogeneities (see section 3.2.4) this effect might not be simple.

The effect of the knife can be seen by looking for the time evolution of a cloud rotating at the bottom of the bubble for different knife heights. In a series of experiments, we set a gas into rotation at the bottom of the bubble following the procedure described previously, with a quite smooth excitation: $\Omega_{\mathrm{rot}} = 2\pi \times 24.3\,\mathrm{Hz}$, $\eta = 0.995/\varepsilon = 0.039$ and 5.5 turns. During the formation of the cloud and the rotation process, the knife is left at a frequency $\omega_{\mathrm{knife}} = 2\pi \times 0.37\,\mathrm{MHz}$ (i.e. 20.7 kHz above the bottom of the trap[2]); 250 ms after the end of the excitation the knife is then ramped down to another value in 100 ms. The 250 ms waiting time before ramping down the knife allow the cloud to go back to its round shape. We then let the cloud evolve during various waiting times and image it from the side after a 23 ms time-of-flight. Depending on the final knife value, the cloud shows strikingly different profiles, with an aspect ratio varying from a factor up to three (see figure 8.9).

The aspect ratio of the cloud after time-of-flight is an interesting observable to measure the rotation, as it depends only on the trap's parameters (which can be precisely measured) and the rotation frequency. Its evolution with the rotation frequency can be computed from equations (7.49) and (7.50) (assuming a harmonic trapping), and we can hope to access in this way the rotation frequency of the cloud. It is plotted on figure 8.9: sadly, we have no analytic formula that could allow us to convert the aspect ratio into the rotation frequency, but we also see that very conveniently the aspect ratio evolves almost linearly with Ω_{eff} over a very wide range of frequencies. A linear fit of the central part of the data allows to recover the correct result within 1% for rotation frequencies between 7.2 and 32.1 Hz and gives an easy and convenient way to measure the rotation frequency of the gas. The fact that this linear relation does not work for very low or very high frequencies is not really a problem: for low frequencies, the coarse-grained vorticity approximation is not valid anymore and Ω_{eff} does not describe the system accurately, while for high frequencies the trapping is not harmonic anymore and the computed expansion is wrong anyway.

Using this linear dependence of the effective rotation frequency, we can come back to the data by looking, now, to the evolution of Ω_{eff} as a function of the knife (plotted on figure 8.10). We observe a slow increase of the rotation frequency with time after the initial excitation, which depends on the final knife height: for a high knife, this increase is negligible, while as we lower the knife value this increase gets more and more important. For long waiting times,

2. I recall here that the relative height of the knife compared to the bottom of the trap is $F\hbar(\omega_{\mathrm{knife}} - \omega_{\mathrm{rf}} - \Omega_0)$, and the atoms are in $F = 1$.

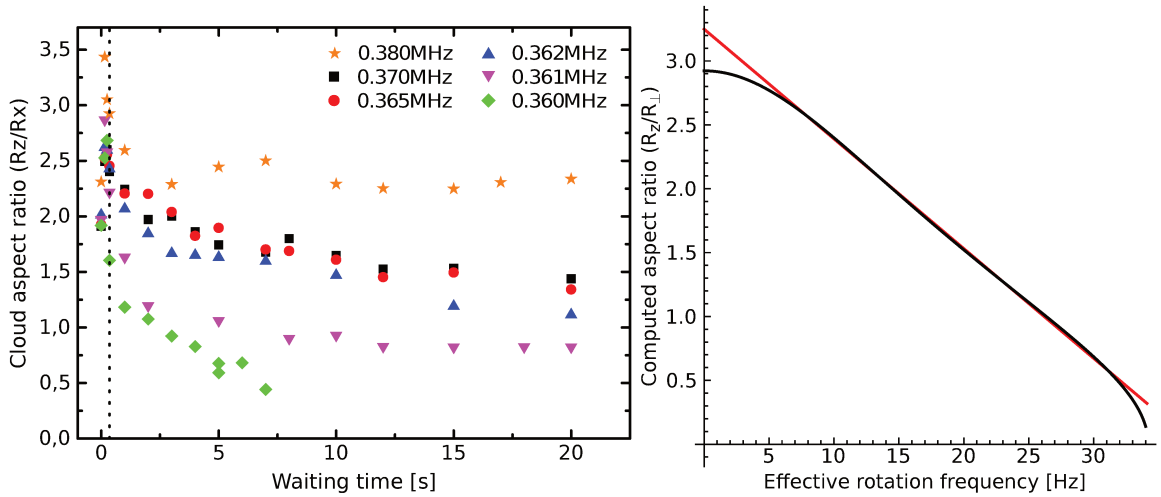

Figure 8.9 — Left: evolution of the cloud's aspect ratio with time, measured after a 23 ms time-of-flight, for different values of the knife during the waiting time (the vertical dotted line indicates the end of the knife ramp). $t = 0$ corresponds to the end of the rotating bucket excitation. Right: expected aspect ratio of the cloud after 23 ms TOF, depending on the cloud's effective rotation frequency. The red line is a fit of the computed values for $7\,\mathrm{Hz} < \Omega_{\mathrm{eff}}/2\pi < 33\,\mathrm{Hz}$; the deviation to the exact value is less than 1% for rotation frequencies between 7.2 and 32.1 Hz. The corresponding relation is $\Omega_{\mathrm{eff}}/2\pi = 37.82 - 11.64 \times R_\perp/R_z$.

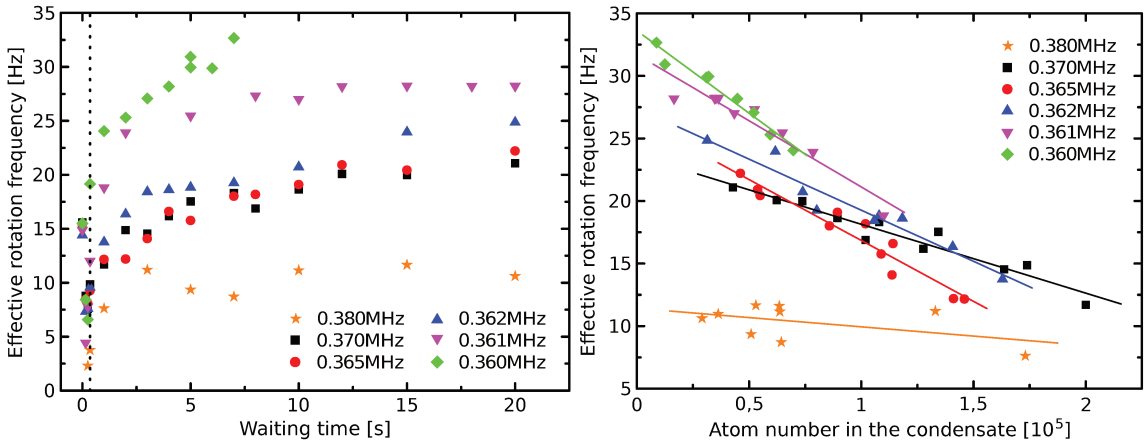

Figure 8.10 — Left: evolution of the cloud's effective rotation frequency with time for various knife frequencies, deduced from the data of figure 8.9. $t = 0$ corresponds to the end of the rotating bucket process. The vertical dotted line indicates the end of the knife ramp. Right: effective rotation frequency of the cloud as a function of the number of atoms left in the cloud, for the same dataset as presented on the left. Solid lines are linear fits to the data. Note that the points corresponding to waiting times below 1 s are not plotted on this figure.

the rotation frequency seems to saturate. We can also look for the variations of Ω_{eff} with respect to the number of atoms left in the BEC; we see that the rotation frequency seems to increase linearly with atom losses, and the lower the knife, the stronger the dependency (the slope of the linear relationship increases).

We interprete this effect as a "spin-up evaporation" similar to the one used in the Cornell group [172]. Indeed, as the local Rabi coupling decreases while the atoms get further away from the trap center, the knife will remove more efficiently the atoms that are close to the axis of rotation and have a lower angular momentum, and spin up the cloud in this way. This effect is far from being negligible: depending on the knife, the achieved rotation frequencies can vary from more than a factor of two. Adjusting the knife therefore gives us an additional tool to control the rotation frequency of the cloud. This gives, for example, a possible explanation to the fact that we are able to generate a dynamical ring with excitation frequencies lower than $\omega_\perp$: while the initial amount of angular momentum would lead to a cloud rotating slower than $\omega_\perp$, during the relaxation the rotation is also slowly accelerated by the knife, up to $\Omega_{\text{eff}} > \omega_\perp$. A confirmation of this possibility was obtained by starting from a cloud set into rotation with parameters that appeared to lead to a simply connected rotating gas: lowering the knife more than usual allowed to transform it into a donut-shaped cloud (even though the atom number in the final cloud was lower than what we are able obtain with a more violent initial stirring).

Note that all the experiments described in this chapter, unless specific precision, were performed with the same knife as the one used for the first experiments, at 0.365 kHz.

8.3 Quadrupole modes in the dynamical ring

We have demonstrated the production of these "dynamical ring" gases, the next step is then to characterize their behavior and properties: especially, we would like to have a direct proof of superfluidity and to measure their rotation frequency. A study of the quadrupole modes in such a gas would therefore be extremely interesting: indeed, as described in section 7.3, their frequencies can allow to access the effective rotation frequency of the cloud, as well as give a tool to discriminate a superfluid from a thermal cloud. We have no theory that could describe properly the case of these modes for a dynamical ring in the bubble trap, but we know what to expect when the cloud is still simply connected and it is interesting to see how the quadrupole modes behavior evolves when going from a regime to the other one.

8.3.1 Percussive excitation of the quadrupole modes

A first method to probe these modes consists in applying to the cloud a strong static anisotropy for a short time: η is ramped from 1 to typically 0.65-0.85 (corresponding to $\varepsilon \sim 0.2$) in 0.3 ms, stays constant during 4.4 ms and is then ramped back to 1 in 0.3 ms. The complete scheme lasts 5 ms while we have $2\pi/\omega_\perp = 29$ ms: the atoms do not have the time to significantly move, but they feel the force exerted by the anisotropic potential. We then observe the subsequent evolution of the cloud in the rotationally invariant potential. We excite in this way the superposition of both +2 and -2 modes: we therefore look for the out-of-phase oscillation of both radii of the cloud (see figure 8.11). In the presence of rotation, due to the lifted degeneracy between +2 and -2 modes, the axes of this ocillation will then precess at $(\omega_+ - \omega_-)/4$. Repeating the experiment and taking in situ pictures for different durations of the waiting time in the trap after excitation, we can then track the orientation of the axis of the oscillation and deduce the corresponding effective oscillation frequency. Note that the

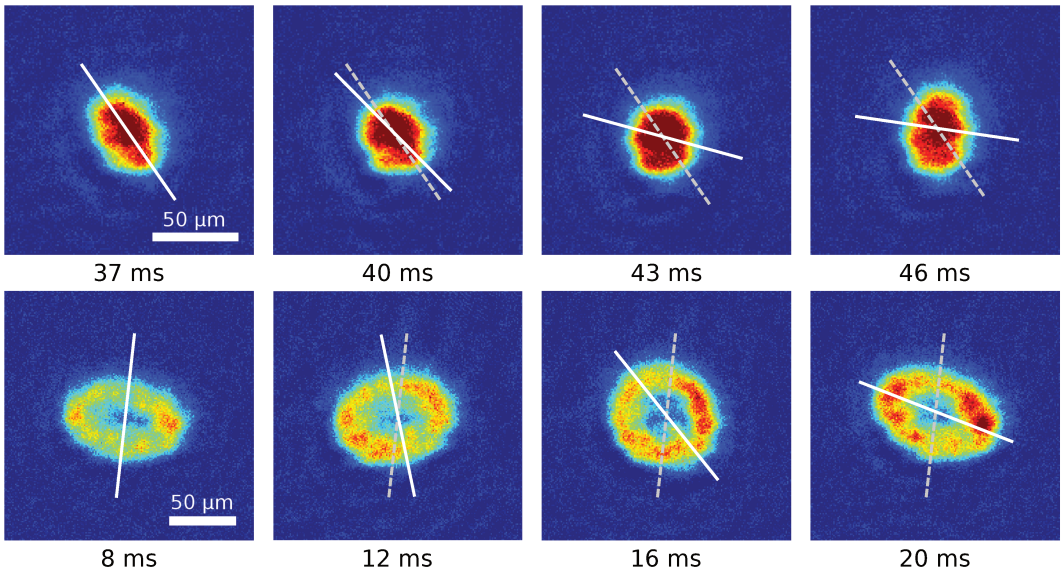

Figure 8.11 — In situ pictures of a rotating gas for different times after percussive excitation of the quadrupole modes (top: excitation at 24.3 Hz, bottom: 31.1 Hz). We observe an out-of-phase oscillation of the cloud radii as well as a precession of the axis of the cloud. In both cases, the cloud was allowed to relax during 20 s after the initial rotation before excitation of the quadrupole.

oscillation of the radii happens at a different frequency than the precession of the axes; it also depends on the cloud's rotation frequency but less directly and we did not try to analyze this part of the data in detail.

A test of the method on simply connected rotating BECs (i.e. not rotating faster than the trapping frequency) showed the expected behavior (see figure 8.11). Applying this scheme to the dynamical ring, we saw the same kind of behavior, while the hole in the center stays present. Analysis of the data to sort the fitted angle leads to an almost linear evolution of the angle and allows to extract the effective rotation frequency of the cloud (see figure 8.12).

The measured effective frequency appears to be significantly different from the excitation frequency; especially for a stirring at large frequency we see that the final cloud rotates *faster* than the excitation. This probably comes from the effect of the RF knife, which spins up the cloud as described in section 8.2.7. This is also comforting us about the interpretation of the donut shape as due to a gas rotating faster than the trapping frequency. Since they were obtained for stirring frequencies lower than $\omega_\perp$, observing them was somehow puzzling; these data confirm that the cloud indeed rotates faster than the trapping frequency. Indeed, the points for which a hole is present in the gas (stirring at 32 Hz) seem to display an effective rotation frequency above $\omega_\perp$. It is also above the value for which the hole is expected to appear, $\Omega_h = 2\pi \times 35.3\,\mathrm{Hz}$, that we can compute from the harmonic plus quartic approximation of the trap, see equation (7.32). It depends on the number of atoms, but very weakly; a 50% variation in the number of atoms leads to a variation of approximately 0.5% of Ω_h – the value here corresponds to 10^5 atoms, typical from the atom number we have in the dynamical rings. We still have to take care that the theory allowing to get Ω_{eff} from the quadrupole modes is in principle not valid anymore once the hole in the gas is formed, and the rotation frequency of the corresponding point has to be taken with caution.

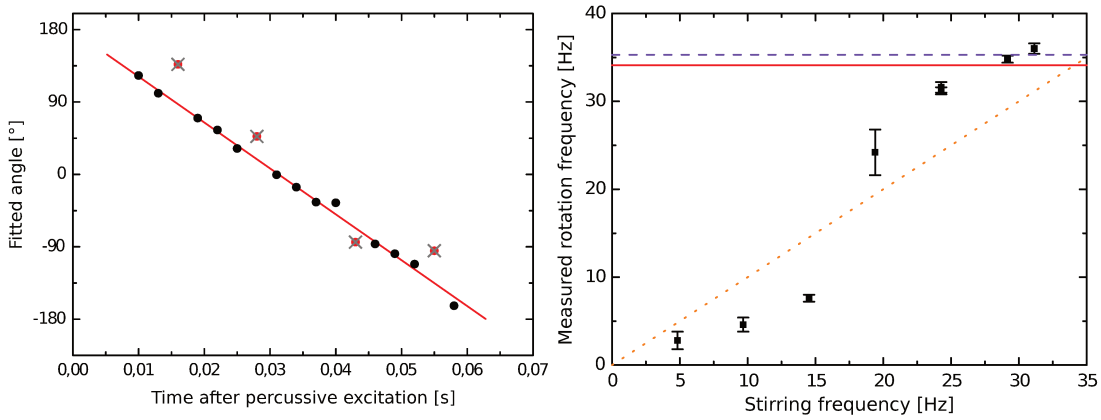

Figure 8.12 — Left: fitted angle of the cloud for different times after percussive excitation of the quadrupole modes (the dataset is the one corresponding to the top row of fig. 8.11, for an excitation at 25 Hz). The angles were sorted by hand to have a monotonous evolution of the angle. Crossed, red points correspond to the inversion of ellipticity of the cloud; they are ignored in the fit as they have a too small anisotropy to allow a precise determination of their orientation. The red line is a linear fit of the data; we find a -5705(118) $^\circ \cdot \mathrm{s}^{-1}$ slope, corresponding to 15.8(3) Hz precession frequency. The corresponding effective rotation frequency of the cloud is therefore $\Omega_{\mathrm{eff}} = 2\pi \times 31.6(6)$ Hz. Right: Evolution of the effective rotation frequency of the obtained cloud, measured by this method, as a function depending on the excitation frequency. The anisotropy used to set the cloud into rotation was $\varepsilon = 0.14$, and the cloud relaxed in the rotationally invariant trap during 20 s before probing the quadrupole modes. The orange dotted line corresponds to $\Omega_{\mathrm{eff}} = \Omega_{\mathrm{rot}}$, the red solid line to $\Omega_{\mathrm{eff}} = \omega_\perp$ and the violet dashed line to $\Omega_{\mathrm{eff}} = \Omega_h$. The last point, which displays an effective frequency above Ω_h, corresponds to a dynamical ring (see figure 8.11): its value for Ω_{eff} is therefore an extrapolation of the theory that applies in the absence of a hole.

Even if this method gives interesting results, the analyis of the precession of the axes relies on sorting the points by hand, following the expected rotation of the cloud. We also tried to fit the measured evolution of the anisotropy and orientation of the cloud using a model based on the decomposition of the condensate wavefunction on the Bogoliubov modes basis (described in [209, 212]). However, the fit is quite difficult (it is a dual fit of angle and ellipticity with 6 common parameters) and doesn't give very precise results. We finally prefered to use another method, based on the resonant excitation of quadrupole modes.

8.3.2 Resonant excitation of the quadrupole modes

The second method to probe the quadrupole mode frequencies relies on a resonant excitation of the modes: this time, we make the trap only slightly anisotropic (typically $\eta = 0.97/\varepsilon = 0.065$) and rotate the trap at a frequency Ω_{probe}. If the corresponding excitation is resonant with one of the quadrupole modes, this mode will become highly populated and the cloud will become significantly anisotropic. As the modes $m_z = \pm 2$ rotate at the frequency $\omega_\pm/2$, this resonance should happen for $\Omega_{\mathrm{probe}} = \omega_\pm/2$, and can provide in this way a measurement of $\omega_\pm$ – and a measurement of Ω_{eff} by comparing ω_+ and ω_-.

Starting from the cloud we want to study, we ramp up η in 0.8 ms and set the cloud into

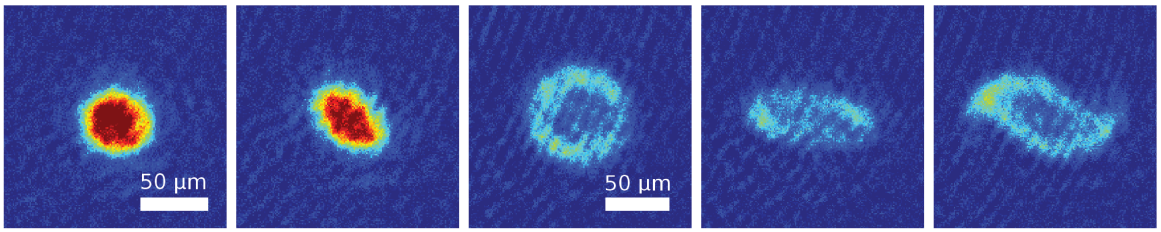

(a) (b) (c) (d) (e)

Figure 8.13 — In situ pictures of rotating clouds after application of a rotating anisotropy to probe the quadrupole modes. From left to right: cloud set into rotation with $\Omega_{\text{rot}}/2\pi = 26.2\,\text{Hz}$ and probed at respectively $\Omega_{\text{probe}}/2\pi = 40.1\,\text{Hz}$ (a) and 37 Hz (b) after 10 s relaxation, cloud set into rotation at 31.1 Hz and probed at respectively 11.6 (c), 1.0 (d) and 37.0 Hz (e) after 20 s wait (i.e. in the dynamical ring). Out of resonance (first and third picture), the cloud doesn't react to the probe excitation, while on resonance it becomes very anisotropic. In the dynamical ring, the low-frequency and high-frequency modes seem to react differently to the probe excitation.

rotation again, similarly to 8.2.1. We then take in situ pictures of the cloud 25 ms after the beginning of the rotation, while the trap is still rotating, and measure the cloud's aspect ratio. Typical pictures are shown on figure 8.13: as expected, we see that depending on the frequency of the "probe excitation", the cloud can stay round or become very anisotropic. We fit the evolution of its aspect ratio with respect to the frequency of the probe excitation using a model based again on the Bogoliubov description (see [209, 212]). The aspect ratio $\zeta = R_{\text{large}}/R_{\text{small}}$ after an excitation of duration δt is expected to read:

$$\zeta(\Omega_{\text{probe}}) = 1 + \sum_{m=\pm 2} \zeta_{m,0} \sqrt{\frac{1 + e^{-2\Gamma_m \delta t} - 2e^{-2\Gamma_m \delta t}\cos[(\omega_m - 2\Omega_{\text{probe}})\delta t]}{(\omega_m - 2\Omega_{\text{probe}})^2 + \Gamma_m^2}}, \tag{8.3}$$

where ω_m and γ_m are the frequencies and damping rates of the modes m and $\zeta_{m,0}$ are amplitudes used for the fit. The results of the fit are shown on figure 8.14. For each cloud, we clearly see two resonances corresponding to the two quadrupole modes $m_z = \pm 2$. The frequency splitting between them being equal to $2\Omega_{\text{eff}}$, we can measure very precisely the rotation of the cloud in this way. The results are very similar to the ones obtained with percussive excitation, but with a significantly better precision. All the data presented on figure 8.14 are taken 10 s after stirring: in this case, even for a stirring at 32 Hz, the hole still did not appear in the cloud (see figure 8.6). For this point, the value of the effective rotation frequency, 34.8(4) Hz, is still valid because the cloud is still connected [203]: we have $\omega_\perp < \Omega_{\text{eff}} < \Omega_h$. When Ω_{eff} reaches $\omega_\perp$, the curvature at the center of the trap becomes negative, but the centrifugal barrier that appears in the center of the trap still needs to become higher than the chemical potential for the hole to appear. The absence of a hole 10 s after the end of the rotating bucket is therefore not surprising, and suggests that the very slow appearance of the hole in the center of the cloud comes from the slow acceleration of the rotation generated by the RF knife: 10 s after rotation, the cloud rotates faster than the trapping frequency and the center of the cloud exhibits a local minimum of density, and the hole slowly appears during the next 10 s.

Finally, we also apply this method to the dynamical ring (see figure 8.13). Again, we see

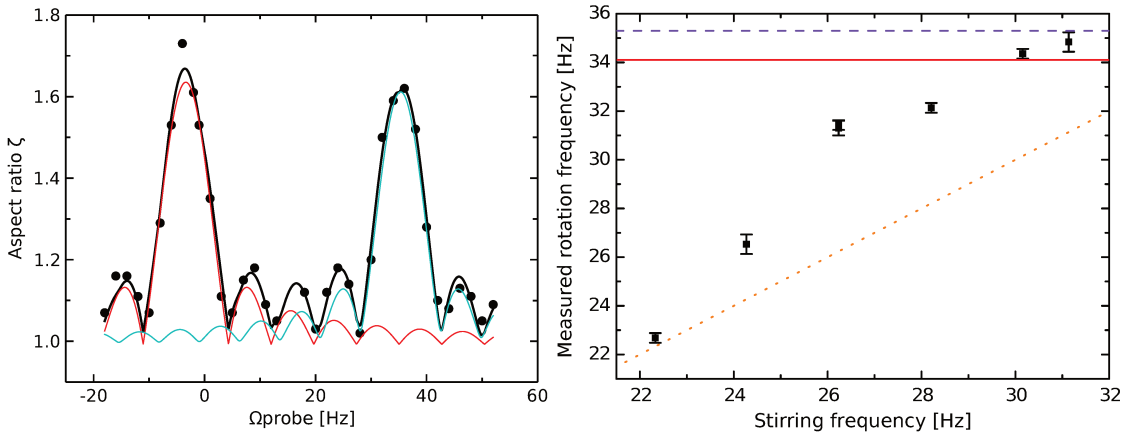

Figure 8.14 — Left: Evolution of the cloud's aspect ratio in situ with the probe excitation frequency. We see two clear resonance peaks, corresponding to the $m = \pm 2$ modes. The black line is a fit of the data using equation (8.3); the blue and red lines are the two components of the model corresponding to the two separate modes. The cloud was initially set into rotation with a stirring frequency 27 Hz and anisotropy $\varepsilon = 0.14$ for 5.5 turns and allowed to relax during 10 s (the dataset is the one shown on figure 8.13). The frequencies of the two resonance peaks are 70.7(2) Hz and −6.8(2) Hz; the effective rotation frequency of the cloud is then 31.9(2) Hz. Note that the negative frequencies correspond to counterclockwise rotations: we use them because we need to take into account the overlap of both resonances, but the splitting has to be calculated using the absolute values in the laboratory frame. Right: evolution of the effective frequency with the stirring frequency, measured after a 10 s relaxation. The orange dotted line corresponds to $\Omega_{\text{eff}} = \Omega_{\text{rot}}$, the red solid line to $\Omega_{\text{eff}} = \omega_\perp$ and the violet dashed line to $\Omega_{\text{eff}} = \Omega_h$. We see an evolution very similar to fig. 8.12, but with slightly lower frequencies. This is probably due to the effect of the rotation acceleration by the knife (see section 8.2.7): these data were taken after a 10 s waiting time while data from figure 8.12 were taken after a 20 s waiting time.

two resonances for the quadrupole modes and the evolution of the anisotropy can be very well fitted by the same two-mode model than previously. We can note that this time, the pictures of the cloud show different shapes for the upper and the lower quadrupole mode. The frequencies of the two modes are respectively $\omega_- = 2\pi \times 0.79(38)$ Hz, $\omega_+ = 2\pi \times 74.41(59)$ Hz. Surprisingly, the lower resonance seems to correspond to a rotation *in the same direction* than the upper one; this suggests that both modes would correspond to $m_z = +2$ modes (as the sign of m_z indicates the direction in which the mode propagates). This could perhaps be a signature of the appearance of the second $m_z = +2$ mode predicted to appear once the hole is formed [196, 203] (see section 7.3.3), but the $m_z = -2$ is however not predicted to disappear. A proper understanding of this observation will require additional data.

8.3.3 Shift of the quadrupole frequencies in the presence of a quartic confinement

The resonant excitation of the quadrupole modes, in addition to be more precise than the percussive excitation, has also the interest of giving us both quadrupole frequencies, and not only their difference. We can therefore try to measure the evolution of the mode frequencies

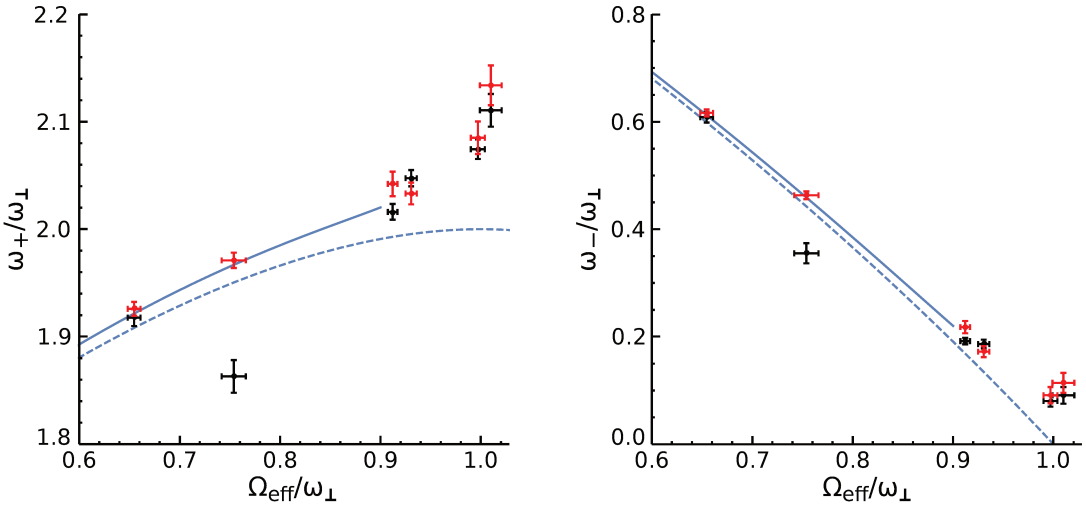

Figure 8.15 — Frequencies of the $m_z = +2$ (left) and $m_z = -2$ (right) modes, plotted with respect to the effective rotation rotation frequency of the cloud (deduced from the difference between both modes), in dimensionless units. The black points correspond to the experimental points, measured using the resonant excitation of the quadrupole modes; the red points correspond to the values predicted by equation (7.40), using as an input the measured Thomas-Fermi radii of the cloud and the value. The blue dashed line corresponds to the quadrupole frequencies predicted for the harmonic case, the blue solid line to the frequencies predicted by (7.40) using the TF radius predicted from equation (7.13), i.e. considering the shift due to the quartic confinement while neglecting the contribution of this confinement to the density profile (which should be very small in the plotted region) – it is plotted here to display the kind of expected behavior rather than for quantitative comparison.

with the effective rotation of the cloud and compare it with the predictions (7.39)(7.40). In fact, to do so, we compare the absolute values of the frequencies of the modes to their splitting. The results are plotted on figure 8.15: we see a small but significant deviation compared to the harmonic prediction (7.39), which depends only on Ω_{eff}. We can then try to compare the mode frequencies with the deviation predicted due to the presence of the quartic term, injecting the Thomas-Fermi radii measured on the in-trap cloud (using a harmonic plus quartic fit of the profiles) and the value for the quartic term λ predicted from (7.31): the predicted deviation agrees very well with the observed frequencies, suggesting that the observed frequency shift is indeed due to this confinement. It also confirms the very good precision that can be achieved through the method of resonant excitation, as the corresponding effect is very small.

8.4 Time-of-flight analysis of the rotating clouds

One of the most useful tools for studying rotating quantum gases is the time-of-flight detection of vortices, and it would be especially interesting to observe the vortex distribution in the dynamical ring. We can note, in particular, that the other experiment that tried to enter the faster-than-harmonic rotation regime in a harmonic plus quartic trap [77] had observed a disappearance of the vortices while entering this regime, which is still not fully explained. We therefore tried to develop the ability to image the vortices in our gases.

8.4.1 Detection of vortices

The first attempts to observe the vortices in the cloud were done with simply connected gases rotating at the bottom of the bubble trap. They were set into rotation using the rotating bucket method, with an important excitation (typically $\varepsilon = 0.14$ and a rotation frequency around 25 Hz) to ensure there should be many vortices in the cloud, and a long relaxation time (typically 10 or 20 s) to ensure that the cloud reaches equilibrium before imaging. The expected signature for the presence of vortices is the triangular lattice distribution of the holes after expansion of the cloud (if we saw holes but not the array, we could for example interprete them as coming from imaging defects due to fringes or a bad camera focus).

To image the vortices, the simplest method appeared to be the best: we remove the trapping potential, perform a time-of-flight and take a vertical absorption picture of the atoms. For a time-of-flight longer than 20 ms, we begin to guess the presence of vortices in the cloud due to local density reduction, and after 30 ms, the observed holes significantly pierce the cloud (see figure 8.16). For time-of-flight durations longer than 30 ms, the cloud crashes on the lower window of the science cell. The vertical camera has to be translated every time we change the time-of-flight duration to adjust the focus on the atoms (the whole imaging setup – camera and lenses – is mounted on a micrometric translation stage).

We realized later that a Stern-Gerlach procedure (see section 3.4.3) considerably increases the visibility of the vortices: in the absence of the Stern-Gerlach procedure, when we perform a time-of-flight even at low magnetic gradient, the shutdown of the magnetic fields is not instantaneous and the three Zeeman substates get very slightly separated; this results in a blurring of the final pictures (and looking at the Fourier transform of the pictures shows a favored axis in the distribution identical on all pictures, indicating the direction of splitting of the clouds).

Once we were able to see the vortices, we then performed weak excitations around the quadrupole resonance to ensure that we were able to observe the expected behavior and to detect unique vortices – this was discussed in section 8.2.2.

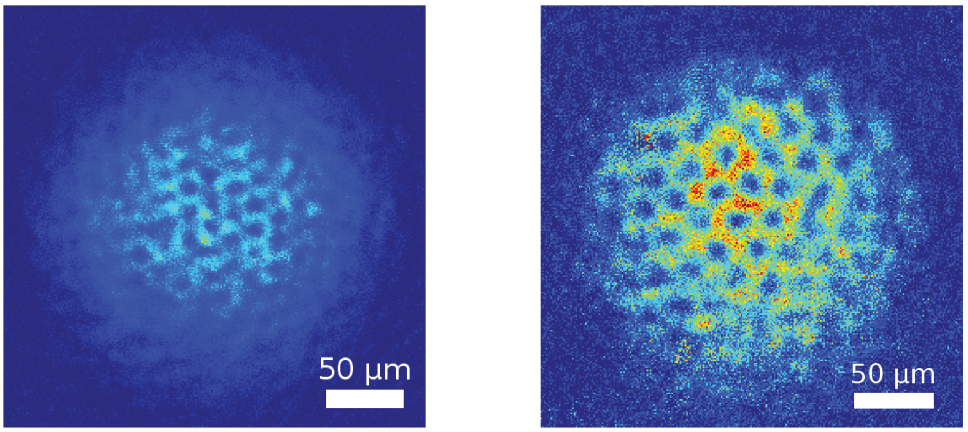

Figure 8.16 — Example of vortex lattice pictures. Left: rotation at 25.3 Hz and $\varepsilon = 0.14$ during 5.5 turns, 20 s waiting time after rotation and 20 ms time-of-flight; it is the first picture where we clearly saw vortices. Right: rotation at 24.3 Hz and $\varepsilon = 0.08$ during 5.5 turns, 15 s waiting time after rotation and 30 ms time-of-flight.

8.4.2 (Absence of) vortices in the dynamical rings

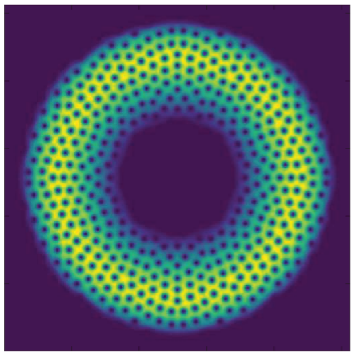

Figure 8.17 — Gross-Pitaevskii simulation of the vortex density distribution for a gas rotating at 35 Hz at the bottom of the bubble trap, realized by Romain Dubessy.

Now confident in our ability to generate and detect vortices, we then tried to apply the same time-of-flight procedure to the dynamical rings, after and during formation, to compare it with the vortex distribution expected from Gross-Pitaevskii computations (see figure 8.17). However, the observed profile did not match with the expected distribution: we do not really see individual vortices in the cloud – we possibly see some vortices, but the contrast is not good enough to allow claiming it with certainty (figure 8.18). We however see large-scale fluctuations in the atomic density after time-of-flight, with a size significantly larger that the one of vortices. Similarly to pictures taken in situ (figure 8.6), the cloud seems bimodal during the formation of the dynamical ring, with the inner cloud seeming to slowly transfer into the outer donut-shaped cloud. Whether the cloud is or not at rest during these steps is unclear yet: we could think that the gas is still highly excited and turbulent (which is suggested by the

observed profiles), or that the cloud follows the equilibrium state corresponding to the slow acceleration caused by the knife (considering the dynamics is extremely slow and expecting that the cloud should have time to equilibrate).

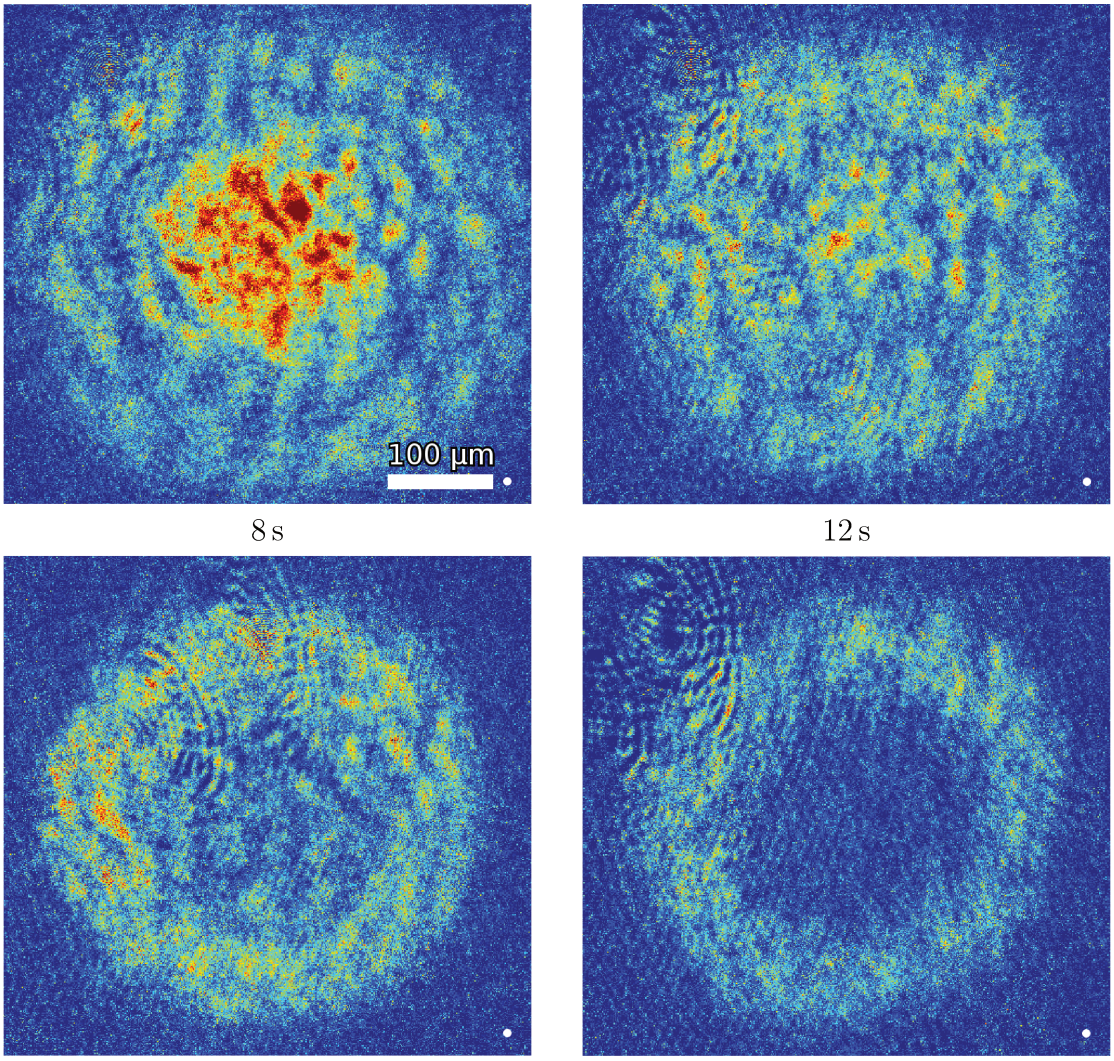

Figure 8.18 — Pictures of the dynamical ring formation, taken after a 23 ms time-of-flight expansion (note that no Stern-Gerlach procedure is used here). We see large density fluctuations, with a size much larger than the one of vortices – the small white circles in the bottom right corner of the pictures correspond to the size of vortices observed in a simply connected gas for similar imaging conditions. Note that the large blurrings in the top left corner come from defects on the imaging camera (we usually try to take pictures of clouds outside this region but here the imaged cloud is so large that we cannot completely avoid it). The corresponding in situ pictures can be seen on figure 8.6.

We have to note, however, that measuring the density of these clouds after time-of-flight is quite difficult: during the expansion, due to the strong centrifugal forces the cloud becomes

very large (after 23 ms TOF its radius is typically beyond 150 µm) and the density drops significantly, causing a high sensitivity to residual imaging noise and fringes. It also prevents us from using the parameters that are optimal for imaging "normal" vortex lattices: for these parameters (30 ms TOF and Stern-Gerlach procedure) the density is simply too low for taking pictures, with optical densities significantly smaller than one.

8.4.3 Loss of contrast of the vortex lattices in the fast-rotating regime

Observing a loss of contrast in the vortices was not necessarily surprising, as the earlier attempts to enter this regime also displayed this effect [77]. In order to understand better the loss of contrast of vortices in the donut-shaped cloud, we tried to vary the excitation procedure used to generate it, trying for example to achieve it using two excitations. The goal was to first realize a nice and large vortex array, and subsequently enter the dynamical ring regime with only a weak excitation, in order to avoid the apparently strongly excited step we see on figure 8.18. However, all the realizations of clouds with many vortices showed a lot of disorder in the vortex lattice, even after very long relaxation times (more than 10 s).

At first, this was quite surprising, because the early works on vortex lattices [53] sytematically displayed higly ordered lattices, and even claimed that obtaining the lattice was *easier* than initially expected; they also used very strong excitations to nucleate the vortices and still saw quick relaxation (in less than 1 s) towards very regular arrays. However, we then realized that these experiments were realized in cigar-shaped traps, while ours are performed in pancake-shaped traps; other experiments realized in similar pancake-shaped traps seem to also display less-ordered lattices [216].

We think that these effects could come from thermal fluctuations: when our cloud rotates fast we get close from the two-dimensional regime (and even finally enter it), in which the coherence length is expected to decrease with the rotation frequency [195]. The vortex lattice could then melt while the cloud stays superfluid, for example through thermal activation of dislocation pairs, as described in section 7.2.1. We can try to use the estimations of Gifford and Baym for the melting temperature [192], neglecting the quartic contribution to our trap: for our trap frequencies with typically 1.5×10^5 atoms, this temperature ranges typically between 0.1 and $0.2T_c$; for a cloud rotating at 26 Hz the corresponding temperature should be around 20 nK while for a cloud rotating at 32 Hz it drops to approximately 10 nK; while we do not know our temperatures precisely the hypothesis of thermal melting therefore seems relevant. Note that the approximation of harmonic trapping is relevant if $1-(\Omega_{\text{eff}}/\omega_\perp)^2 \gg \lambda(R_\perp/d_\perp)^2$; for a cloud rotating at $\Omega_{\text{eff}}/2\pi = 32$ Hz we still have a factor of 5 between these terms.

In order to investigate this effect, we took time-of-flight pictures of gases rotating at various frequencies. We simply excite the gas using the rotating bucket method at a given frequency (the number of turns, 5.5, is kept constant for all pictures), and let the cloud relax for 10 s; the conditions for stirring and waiting are identical to the conditions in which the data of figure 8.12 were taken, which allows us to know the effective rotation frequencies of the clouds. We then perform a 30 ms time-of-flight with a Stern-Gerlach procedure and image the cloud. Typical results are shown on figure 8.19. For moderate rotation frequencies, we observe well-ordered vortex lattices, but when Ω_{eff} gets closer to the trapping frequencies the cloud gets more and more disordered and even seems to completely lose the lattice structure.

Even though some theoretical work has been achieved about thermal fluctuations in 2D vortex lattices, there is yet no model that could be used to quantitatively analyze these pictures. We however tried to quantify the loss of the vortex lattice visibility, computing the

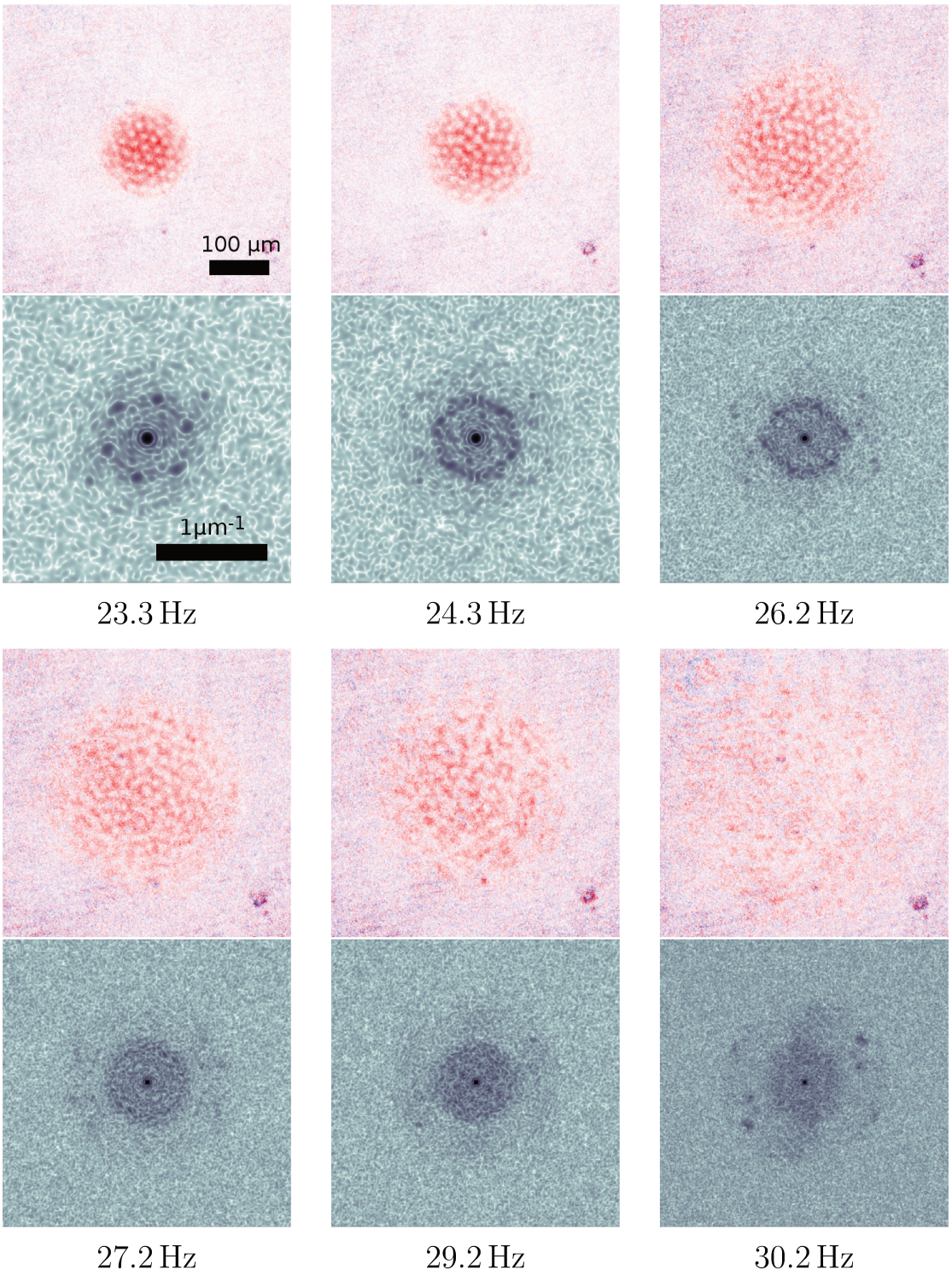

Figure 8.19 — Upper pictures: Time-of-flight pictures of gases stirred for various frequencies. The corresponding effective rotation frequencies of the gas are displayed on figure 8.12. The cloud is rotated during 5.5 turns and relaxes during 10 s; it is then imaged after a Stern-Gerlach procedure and 30 ms TOF. The color scale is here different from the one used in other pictures as the treatment of data is here slightly different to allow a better correction of imaging fringes (blue shades indicate "negative" densities). Lower pictures: 2D discrete Fourier transform of the upper pictures, plotted in log scale.

2D Fourier transform of the pictures:

$$\tilde{n}(k_x, k_y) = \int dxdy \exp(-ik_x x) \exp(-ik_y y)\bar{n}(x, y), \tag{8.4}$$

where $\bar{n}$ is the vertically integrated density profile of the atoms, measured on the experimental pictures. The computed $\tilde{n}(k_x, k_y)$ are displayed on figure 8.19. For low frequencies, we clearly see the six peaks corresponding to the triangular lattice; for higher frequencies the visibility of the peaks decreases and they get blurred along the azimuthal direction and the Fourier distribution now displays a ring, indicating the presence of a typical distance between vortices but a loss of the global lattice orientation. Finally, at high frequency this ring disappears, leaving only a disc at small momenta.

To go further in the analysis, we then compute the radial average of the Fourier Transform:

$$\rho(k) = \int k d\theta \tilde{n}(k, \theta) \tag{8.5}$$

with $k = \sqrt{k_x k_y}$ and $\theta = \arctan(k_y/k_x)$; the corresponding results are shown on figure 8.20. The lattice now appears through a peak in the Fourier distribution. The height of this peak decreases with the rotation frequency, indicating that the distance between vortices gets more loose, and the peak completely disappears for excitation frequencies larger than 29 Hz (which corresponds to the cloud rotating around 33 Hz, see figure 8.14). We also see that the peak's position drifts towards lower momenta. This can be associated with the evolution of the magnetic length $l = \sqrt{\hbar/M\Omega_{\text{eff}}}$, which gives the intervortex spacing (see section 7.1.2): a lower momenta in the Fourier transform after time-of-flight corresponds to a smaller distance in situ. It is however difficult to quantitatively describe it, as the relation between the in situ distance and the distance after time-of-flight is not exactly a Fourier transform: our time-of-flight is not long enough to allow being in the far field regime.

These data suggest that we should be able to perform interesting measurements about what seems to be the thermal melting of the vortex lattice. However, we lack for now a proper theoretical model with which to compare: first, to adapt the theoretical work achieved on finite-temperature, fast-rotating gases [195] to the finite-size case we achieve experimentally. Second, to translate the effect of phase fluctuations within the trapped gas into a measurable quantity, taking into account the time-of-flight expansion of the gas.

In this latter dataset, the contrast of the pictures decreases dramatically when Ω_{eff} gets too close to $\omega_\perp$. It would also be interesting to observe the vortex distribution at the edge between both regimes, once we seem to be completely outside the regime of the vortex lattice but before the appearance of the hole in the system, i.e. right when the harmonic trapping cancels. We achieved that by exciting the cloud the same way we would do as to realize a dynamical ring (5.5 turns at 31.1 Hz and $\varepsilon = 0.14$), but performing the sequence with a higher knife frequency: 0.369 Hz instead of 0.365 Hz; the spin-up effect due to the knife is therefore weaker. After various waiting times we then perform a 23 ms time-of-flight and image the cloud from above. The corresponding pictures are shown on figure 8.21. The observed density profile is quite spectacular, and we see that the atoms seem to gather into small "blobs", without looking in any way like a vortex lattice. While one could think about turbulent behavior, the corresponding behavior shows no sign of relaxation; even after a 60 s waiting time the atomic cloud, while much smaller, still displays these small blobs. If we are, as we expect, in the presence of a melted vortex lattice, this possibly corresponds to phase

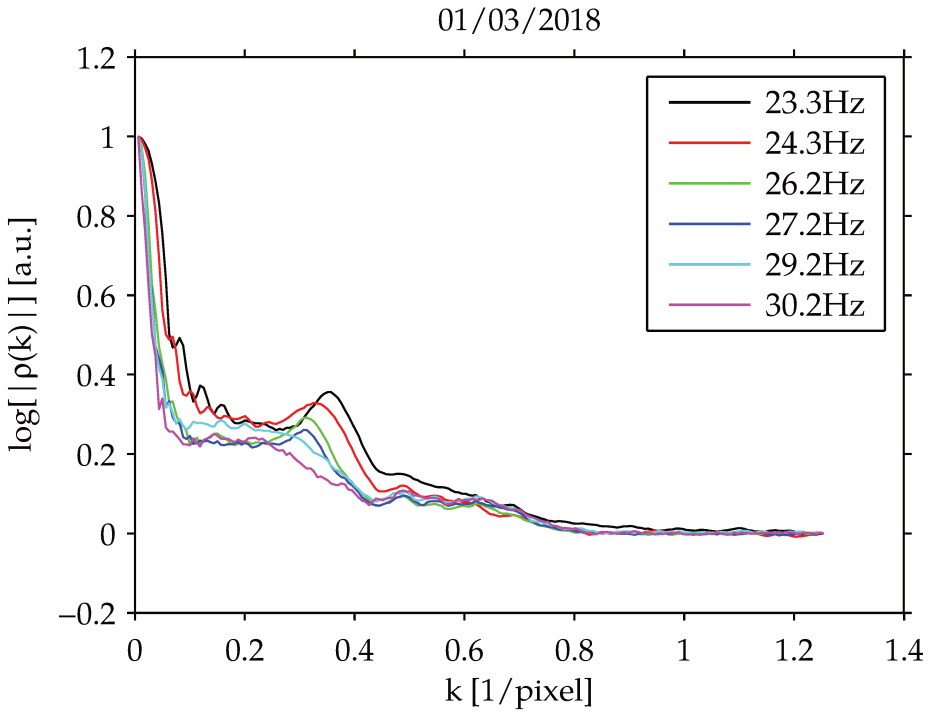

Figure 8.20 — Radial average of the Fourier Transform of the time-of-flight pictures presented on figure 8.19, for different stirring frequencies. Each curve is the average of 10 different pictures. Note that the vertical axis is in logarithmic scale; the horizontal axis is plotted in pixel units but our magnification is such that 1 pixel corresponds to 1.03 µm.

domains defined by the phase flucuations within the cloud; their size could then allow to estimate the correlation length within the cloud. We can also try to compare with the second picture of figure 8.18 (at 12 s). In both cases, the cloud rotates at $\Omega_{\text{eff}} \approx \omega_\perp$ and we see large fluctuations over the cloud but the size of the fluctuations is smaller here than on figure 8.18. A possible explanation would be that the knife is higher here: the temperature is thus probably higher, and the correlation length smaller due to more important phase fluctuations. However, on figure 8.18, the situation was not stationnary and the cloud continued to evolve further, it is therefore not sure that the situations can be relevantly compared (even though the very slow evolution suggests that we could be in a quasi-stationnary regime, that slowly adapts to the increase of rotation due to the knife).

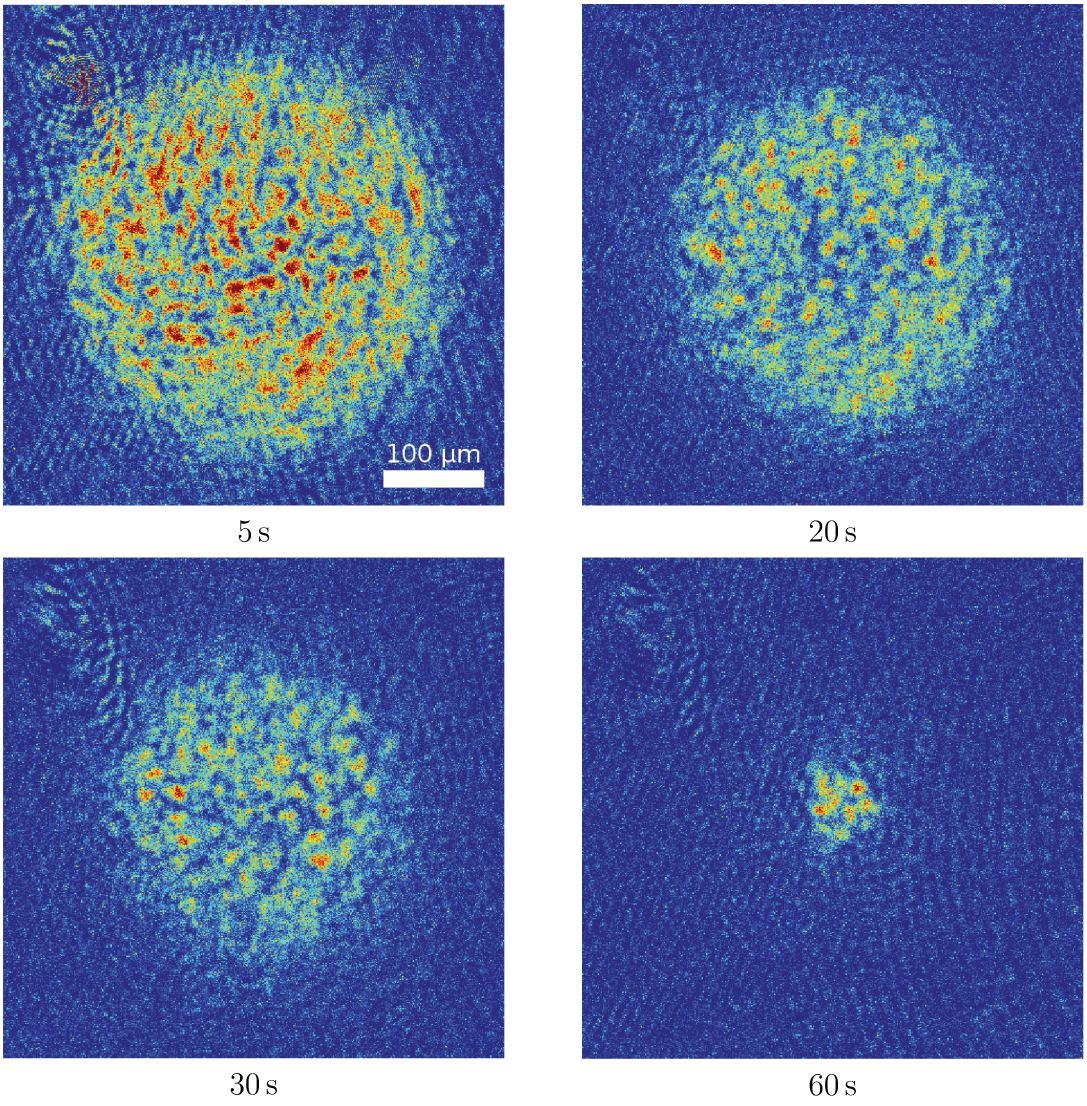

Figure 8.21 — Density profile of a cloud rotating at $\Omega_{\text{eff}} \approx \omega_{\perp}$ obtained by the same fast stirring procedure allowing to create a dynamical ring but with a higher knife, measured after a 23 ms TOF, respectively 5, 20 and 60 s after stirring.

Conclusion

The annular geometry is ideally suited to study superfluidity thanks to its ability to withstand persistent flow [57]. In such a system the continuity of the superfluid wavefunction, that has to be single-valued, also implies that the circulation of the velocity field along the waveguide has to be quantized [58]; the combination of the flow metastability with the circulation quantization leads to an hysteretic behavior [59]. Many experimental and theoretical efforts are currently being dedicated to exploit the remarkable properties of ring-shaped quantum gases to achieve "atomtronic" circuits [72, 73, 146] or to perform quantum simulation [149, 150].

During my PhD, I demonstrated the possibility to achieve a connected, condensed gas in a ring trap realized by combining a radiofrequency-dressed trap and a blue-detuned double light sheet. RF dressing is a trapping technique that combines RF photons and a static magnetic field. It allows to trap atoms on the isomagnetic surface where the RF is resonant with the splitting between the different Zeeman substates of the static field: in our case, we trap in this way the atoms on a surface of an ellipsoid, leading to a bubble-shaped trap. The double light sheet then confines the atoms within a thin slice of this bubble, leading to a ring-shaped trap. This achievement requires a very good precision on the optical alignments in the system generating the light sheet, a very fine control over the polarization of the dressing RF wave, as well as a great care in the control of potential heating sources. We then demonstrated the ability of the ring-shaped condensate to sustain a superfluid flow.

The technique used to generate the ring presents the advantage of enabling, in principle, to reach the quasi-2D or even quasi-1D regimes, and the experimental results presented in this manuscript suggest that we could be close to these regimes. The quasi-1D regime, in particular, presents a high theoretical interest as it can be seen as a uniform 1D system with periodic boundary conditions: the experimental availability of such a system would therefore open up interesting possibilities to perform quantum simulation. There are three main difficulties that could make it hard to enter this regime. First, the trapping frequencies we can currently achieve set strong limits on the temperature we can accept to enter the quasi-1D regime, which should stay lower or comparable to 30 nK. Second, lowering the chemical potential will increase the sensitivity to residual optical defects and potential inhomogeneities. One can note that even if this difficulty appears too hard to overcome, it could also be turned into an advantage for studying annular 1D gases in the presence of disorder, which also presents a real interest due to localization effects [217, 218]. Third, the very low atom number required for the gas to be quasi-1D could cause difficulties to obtain accurate images of the cloud and require improvements of the optical system.

Now that our ring trap is operational (in the 3D case), we can start developing an experimental toolbox around it. We are, for example, planning to implement a phase imprinting system, for which a significant preparatory work has already been achieved [167]. While its first purpose is to generate a superfluid flow, it will also provide the ability to imprint arbitrary potential landscapes. This could open considerable opportunities in the perspective of quantum simulation, allowing for example to generate arbitrary phase domains and study their recombination (using the laser stirrer to generate barriers between the domains), or to imprint solitons [168]. A digital micromirror device could also bring many possibilities that are complementary to the ones offered by the phase imprinting setup, built around a SLM: while an SLM allows to imprint continuous spatial patterns but cannot be dynamically configured, a DMD imprints only discrete spatial patterns (light or no light) with a very fast operation rate – however in this second case a quasi-continuous pattern can be recovered by binning pixels and taking advantage of the finite optical resolution.

The improved control over the dressing RF field developed in order to improve the homogeneity of the ring-shaped gas also allowed us to achieve "dynamical rings" at the bottom of the bubble trap, i.e. gases rotating faster than the trapping frequency and maintained trapped by the anharmonicity of the bubble [76]. Deforming and rotating the trap allows to set the atoms into very fast rotation, and the high smoothness of the trapping potential allows us to keep the atoms in rotation during tens of seconds. Careful checks give evidence that the corresponding donut-shaped cloud is still quantum degenerate.

We then adapted to our experiment some of the tools that have been previously developed to study rotating superfluids.

One of these tools is the ability to probe the quadrupole modes of the gas, by a percussive or a resonant excitation. The collective modes of trapped gases provide a way to probe their behavior, and the frequency modification of these modes in the presence of rotation is especially interesting. We achieved a very good accuracy on the measurement of the quadrupole mode frequencies and demonstrated our ability to probe fine effects like the shift of these frequencies in the presence of anharmonicities. The experimental availability of the dynamical ring, combined with the many possibilities to excite the cloud offered by the versatility of the RF-dressed trap, now opens the possibility to observe the predicted behavior of collective modes in such a system, for instance for the monopole and quadrupole modes [196, 203] or in the more exotic case of Rossby waves [78].

The second tool is the ability to image quantized vortices inside the rotating gas through time-of-flight expansion. While we can observe regular vortex lattices for moderate frequencies, these lattices seem to melt for fast rotations, getting more and more disordered as the rotation frequency increases; and the dynamical ring displays no vortices but large-scale density fluctuations. We interprete this effect as a thermal melting of the lattice: indeed, a vortex lattice can be considered as a 2D crystal. It is therefore sensitive to phase fluctuations and can undergo a BKT-type melting towards a liquid phase at finite temperature, even while the gas is still condensed [191–193]. This effect has only be sparsely explored with quantum gases and lets us hope for fascinating developments. For example, by combining the mechanical stirring of the gas and the spin-up evaporation by the RF knife, it should be possible to produce gases rotating at identical frequencies but various temperatures and observe the subsequent effect on the atoms. The possibility to adjust the vertical frequency of our trap could also allow us to observe the interplay between this effect and the (conventional) BKT physics when the gas itself becomes quasi-2D. The main requirement to perform these studies would be the ability to relate the density fluctuations observed after time-of-flight to the in-trap phase

fluctuations [219], that will probably soon be numerically investigated in our team.

To conclude, the high versatility and potential regularity of RF-dressed quadrupole traps allows to achieve novel kinds of ring-shaped superfluids. The first kind, using a ring-shaped potential, suggests the possibility to achieve unidimensional quantum gases with periodic boundary positions, which would provide new possibilities to study the fascinating 1D physics. The second kind, exploiting the centrifugal force, allows to enter the fast-rotating regimes of superfluidity deeper than ever. While we are still far away from reaching the "giant vortex" configuration, this achievement could open the way to a better understanding of these regimes, in which our preliminary experiments suggest that there is still a lot to explore.

Appendices

Appendix A

Compression of the ring with constant radius

A.1 Calibration of the vertical bias

A good calibration of the vertical magnetic bias field is necessary to control properly the sheet loading and the ring formation. It is achieved by simply measuring the position of the cloud after a fixed time of flight for different values of the magnetic bias field. The bias coils create a constant magnetic field offset and the quadrupole field is linear; the subsequent displacement should then increase linearly with the magnetic bias or with the current in the bias coils. A linear fit of the position of the cloud position then gives the slope of the position versus current function. This slope depends on the quadrupolar gradient, and thus on the current in the quadrupole coils. The most interesting value is, in fact, the product of the slope by the quadrupole current, that I will call α_{zs}, which is fixed for our coil geometry. If we denote $B_b = B_{b,0} \times I_{\mathrm{bias}}$ the static field created by the vertical bias field, the total vertical magnetic field reads $B_{\mathrm{bias}} - 2b'z$ (I recall here that b' is the horizontal magnetic gradient generated by the quadrupole coils). The equilibrium position therefore writes:

$$z_{eq} = \frac{B_b}{2b'} = \frac{B_{b,0}}{2b'} \times I_{\mathrm{bias}}. \tag{A.1}$$

We also have $b' = b'_0 I_{\mathrm{quad}}$ ($b'_0 = 1.98\,\mathrm{G}\cdot\mathrm{cm}^{-1}\cdot\mathrm{A}^{-1}$ on our experiment), and multiplying the slope by the current in the quadrupole coils I_{quad} for which it was measured gives the constant coefficient α_{zs}:

$$\alpha_{\mathrm{zs}} = \frac{B_{b,0}}{2b'_0} \tag{A.2}$$

In general, applying a current Z_{shift} in the bias coils leads to a displacement z_{shift} of the bubble that depends on the current in the quadrupole coils I_{quad}:

$$z_{\mathrm{shift}} = Z_{\mathrm{shift}} \times \frac{\alpha_{\mathrm{zs}}}{I_{\mathrm{quad}}}. \tag{A.3}$$

This equation allows one to convert any vertical distance in microns into the corresponding amount of current in the bias coils (given the quadrupole current I_{quad}). I will, as a convention,

denote z (lowercase) the "real distances", in micrometers, and Z (uppercase) the corresponding "current distances", in amperes; such distinction will be useful later.

Measurements of α_{zs} are showed on figure A.1. We did the measurement at low and high gradient to ensure that it is independent from the quadrupole current as expected; the coefficient can be measured within 1%.

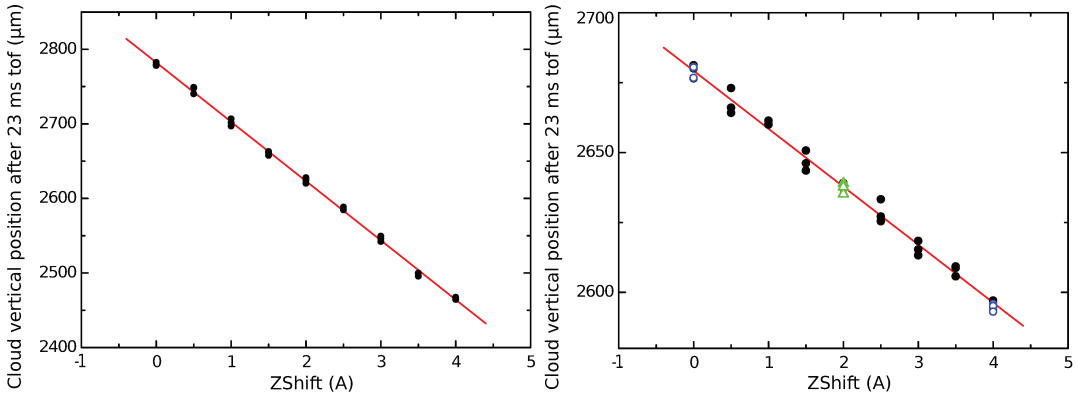

Figure A.1 — Calibration of the coefficient α_{zs}. Left: data taken for a quadrupole current $I_{quad} = 28.5\,\mathrm{A}$. A linear fit gives a coefficient $-79.5(6)\,\mu\mathrm{m}\cdot\mathrm{A}^{-1}$, corresponding to $\alpha_{zs} = -79.5 \times 28.5 = 2266(17)\,\mu\mathrm{m}$. Right: data taken at 110 A; the linear fit gives $-20.7(4)\,\mu\mathrm{m}\cdot\mathrm{A}^{-1}$, corresponding to $\alpha_{zs} = 2277(44)\,\mu\mathrm{m}$. The combination of both measurements gives $\alpha_{zs} = 2267(16)\,\mu\mathrm{m}$. To ensure that the cloud is at rest and that no residual motion perturbs the measurement, a few points were taken 2 s (blue open circles) and 5 s (green open triangles) after loading.

A.2 Details about the ring compression procedure

I will here describe the vertical bias field ramp that allows us to compress the ring while keeping its radius constant as described in chapter 5, section 5.1.3. Note that gravity will be neglected in the following calculations, which could lead to deviations if the magnetic gradient is very low at the beginning of the procedure.

We need to compress the ring while keeping its radius constant (i.e. increasing only ω_r), following two criteria:

- At the end of the ramp, the ring has to be at the equator of the final bubble.
- The radius of the ring has to remain constant during the whole ramp.

Figure A.2 describes the geometrical parametrization of the problem.

The two conditions mentioned above imply, at any time:

$$r_{fin}^2 + 4z_{cs}(I_{quad})^2 = r_b^2(I_{quad}), \tag{A.4}$$

where r_b is the radius of the bubble at the equator, r_{fin} the final value of this radius, and z_{cs} the desired distance between the center of the bubble and the light sheet. From equation

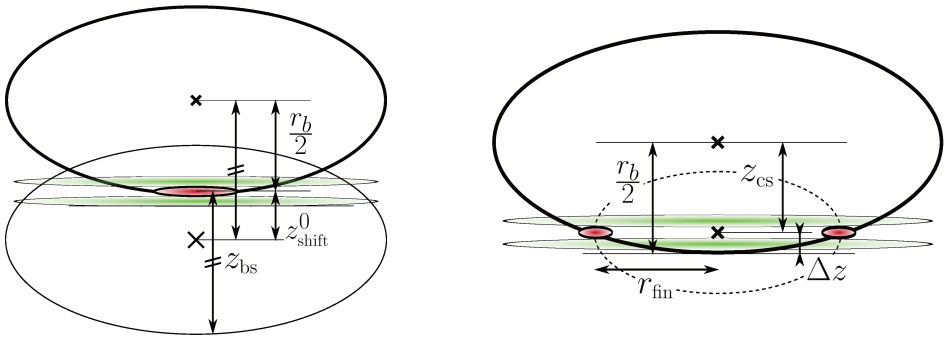

Figure A.2 – Sketch of the lengths defined in this appendix. Left: alignment of the bubble with the sheet. Thin line: bubble in the absence of bias. Thick line: in presence of a bias superimposing the bottom with the light sheet). Right: compression of the bubble. Dashed line: bubble in the desired final situation. Thick line: bubble for an arbitrary current in the coils.

(2.54), one can deduce the expression of the bubble radius $r_b(I_{\text{quad}})$:

$$r_b(I_{\text{quad}}) = \frac{\omega_{\text{rf}}}{\alpha} = \frac{\hbar\omega_{\text{rf}}}{|g_F|\mu_{\text{B}} b'_0\ I_{\text{quad}}}, \tag{A.5}$$

where $b'_0 \times I_{\text{quad}} = b'$ is the horizontal gradient of the quadrupole (b'_0=1.98 G · cm^{-1} · A^{-1}).

Keeping the dressing frequency constant thus implies conservation of the product $r_b \times I_{\text{quad}}$, and then:

$$r_b(I_{\text{quad}}) = r_{\text{fin}} \times \frac{I_{\text{fin}}}{I_{\text{quad}}}, \tag{A.6}$$

where $I_{\text{fin}} = \hbar\omega_{\text{rf}}/|g_F|\mu_{\text{B}} b'_0\ r_{\text{fin}}$ is the desired current in the coils at the end of the compression procedure. z_{cs} thus reads:

$$z_{\text{cs}}(I_{\text{quad}}) = \frac{r_{\text{fin}}}{2}\sqrt{\left(\frac{I_{\text{fin}}}{I_{\text{quad}}(t)}\right)^2 - 1}. \tag{A.7}$$

Starting from the situation where the bottom of the bubble is aligned with the light sheet, the displacement to apply to the bubble to create a ring with radius r_{fin} is then:

$$\Delta z(I_{\text{quad}}) = \frac{r_b(I_{\text{quad}})}{2} - z_{\text{cs}}(I_{\text{quad}}) \tag{A.8}$$

$$= \frac{r_{\text{fin}}}{2}\left[\frac{I_{\text{fin}}}{I_{\text{quad}}(t)} - \sqrt{\left(\frac{I_{\text{fin}}}{I_{\text{quad}}(t)}\right)^2 - 1}\right], \tag{A.9}$$

and the corresponding current reads:

$$\Delta Z(I_{\text{quad}}) = \frac{I_{\text{quad}}}{\alpha_{\text{zs}}} \times \Delta z(I_{\text{quad}}) = \frac{r_{\text{fin}}}{2\alpha_{\text{zs}}}\left(I_{\text{fin}} - \sqrt{I_{\text{fin}}^2 - I_{\text{quad}}^2}\right). \tag{A.10}$$

The total current in the bias coils then has to be :

$$I_{\text{biasZ}} = Z_{\text{bs}}(I_{\text{quad}}) - \Delta Z(I_{\text{quad}}), \tag{A.11}$$

where $Z_{\mathrm{bs}}(I_{\mathrm{quad}})$ is the current that has to be applied to align the bottom of the bubble with the light sheet. It is relevant to separate it into two parts, one corresponding to the distance between the center of the light sheet and the center of the quadrupole trap denoted z^0_{shift}, and the other to the radius of the bubble r_b:

$$Z_{\mathrm{bs}}(I_{\mathrm{quad}}) = \left[z^0_{\mathrm{shift}} + \frac{r_b(I_{\mathrm{quad}})}{2} \right] \times \frac{I_{\mathrm{quad}}}{\alpha_{\mathrm{zs}}} \tag{A.12}$$

$$= z^0_{\mathrm{shift}} \times \frac{I_{\mathrm{quad}}}{\alpha_{\mathrm{zs}}} + \frac{\hbar\omega_{\mathrm{rf}}}{2|g_F|\mu_{\mathrm{B}} b'_0 \alpha_{\mathrm{zs}}}. \tag{A.13}$$

We can then write $Z_b = \hbar\omega_{\mathrm{rf}}/|g_F|\mu_{\mathrm{B}} b'_0 \alpha_{\mathrm{zs}}$ the bias current corresponding to a vertical displacement equal to the vertical size of the bubble, which doesn't depend on I_{quad}. z^0_{shift} can be deduced from the value $Z_{\mathrm{shift}} = Z_{\mathrm{bs}}(I_{\mathrm{ini}})$, which is the current put in the coils to load the light sheet described in section 5.1.3, as:

$$z^0_{\mathrm{shift}} = \left(Z_{\mathrm{shift}} - \frac{Z_b}{2} \right) \times \frac{\alpha_{\mathrm{zs}}}{I_{\mathrm{ini}}}. \tag{A.14}$$

Combining everything, the current to apply in the bias coils finally reads:

$$I_{\mathrm{biasZ}} = \left(Z_{\mathrm{shift}} - \frac{Z_b}{2} \right) \frac{I_{\mathrm{quad}}}{I_{\mathrm{ini}}} + \frac{Z_b}{2} - \Delta Z(I_{\mathrm{quad}}) \tag{A.15}$$

$$= Z_{\mathrm{shift}} + \left(Z_{\mathrm{shift}} - \frac{Z_b}{2} \right) \left(\frac{I_{\mathrm{quad}}}{I_{\mathrm{ini}}} - 1 \right) - \frac{r_{\mathrm{fin}}}{2\alpha_{\mathrm{zs}}} \left(I_{\mathrm{fin}} - \sqrt{I^2_{\mathrm{fin}} - I^2_{\mathrm{quad}}} \right). \tag{A.16}$$

Appendix B

Additional details about high intensity absorption imaging

The last tunings and calibrations of our high intensity imaging setup were performed as I was a master student in the team, between March and July 2015, and represented a significant amount of the work I performed at that time. I include here the translated chapters of the corresponding report that relate to how we implemented this technique.

When we installed the laser stirrer on the experiment, we had to place a dichroic mirror on the probe beam path: this implied a recalibration of the parameter α^* that we use to compute the optical density in the case of high-intensity absorption imaging. However, this work on the imaging system led us to observe a phenomenon that we did not take into account until then, leading to an artificial diminution of the measured atom number. Taking care about this effect led to a reduction of the signal-to-noise ratio (SNR) of our imaging, and I finally worked on the optimization of the imaging accuracy, in order to compensate this SNR reduction.

B.1 High-intensity imaging of dense clouds

B.1.1 Two-level system modelization and corresponding notations

Let us begin by properly defining the studied system. At the end of the cooling process, we obtain a cloud of ultracold atoms that we want image as accurate as possible in order to deduce its characteristics (temperature, excitations, collective modes, etc.). All these informations are deduced from the atomic density profile measured on the pictures and the precision of this density measurement is therefore highly critical.

In practice, studying the imaging process corresponds to studying the interaction of an atomic ensemble with a laser beam – in this case tuned on the D_2 transition (see figure 3.2). The number of atomic levels that can have an impact on the system in this process is considerable: 4 principal levels ($F = 1$, $F = 2$, $F' = 2$, $F' = 3$) can be populated in a

non-negligible proportion, 20 if we take into account all Zeeman sublevels. It is unrealistic to try taking everything into account; considering that two atomic levels will concentrate most of the atomic population we will simplify the system by modelling it as a two-level system, where $F = 2$ will play the role of the ground state g and $F' = 3$ will be the excited state (figure B.1). Levels $F = 1$ and $F' = 2$ are only sparsely populated – they only intervene in the case of a non-resonant depumping effect – and the Zeeman sublevels have no importance in the case of non-polarized light. Their effects will not be taken into account at first, and I will precise the situations where they need to appear: in the absence of specific indication, all equations will correspond to this two-level system.

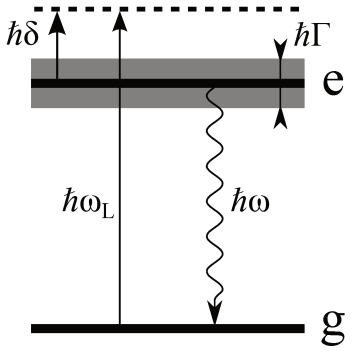

Figure B.1 – Modelization of the rubidium atoms by a two-level system. The transition between these levels corresponds to the $5S_{1/2}$, $F = 2 \rightarrow 5P_{3/2}$, $F' = 3$ transition (see figure 3.2).

The useful notations are indicated on figure B.1: ω is the transition frequency and λ the corresponding wavelength, Γ its linewidth. The frequency of the probe laser is denoted ω_L and its detuning $\delta = \omega_L - \omega$.

In this case, one can also give the value of the resonant cross-section of the transition, as well as the resonant saturation intensity:

$$\sigma_0 = \frac{3\lambda^2}{2\pi} \text{ et } I_{\text{sat}} = \frac{\hbar\omega^3\Gamma}{12\pi c^2}. \tag{B.1}$$

We will also denote I_i and I_f the intensities of the probe beam before and after absorption by the atoms. Both are measured by taking a picture of the probe beam on a CCD camera, to which a picture of the background noise is substracted.

B.1.2 Imaging dense clouds

Low-intensity absorption imaging works very well to image sparse clouds. However, when one wants to image very dense clouds – which is the case when taking in situ pictures of the clouds – things become much more complex. Indeed, if the incident beam is not intense enough, it will be completely absorbed by the cloud and the density profile will be clipped; in addition, collective effects (for example multiple diffusion) become non-negligible. It is therefore necessary to work with very high probe intensities, larger than the saturation intensity of the atoms: if the atomic transitions are saturated, all photons cannot be absorbed anymore by the first atoms encountered by the probe beam, and multiple scattering is suppressed. In

this case, the effective cross-section depends on the ratio between the probe intensity and the saturation intensity and can be written:

$$\sigma = \frac{\sigma_0}{1 + I/I_{\text{sat}}}. \tag{B.2}$$

In practice, the situation is more complex because we have more than two levels, and it depends on the polarization configurations and the real atomic structure. One therefore introduces heuristically the α^* parameter, trying to keep the two-level atom model but replacing the parameters that intervene in the process by their *effective* values [139]: α^* is defined so that the effective saturation intensity is equal to $\alpha^* I_{\text{sat}}$. In this case, the absorption cross-section writes:

$$\sigma = \frac{\sigma_0}{\alpha^* + I/I_{\text{sat}}}. \tag{B.3}$$

From this expression, one can deduce the formula allowing to compute the optical density from the incident and transmitted intensities:

$$\sigma_0 n(x,y) = -\alpha^* \ln\left[\frac{I_f(x,y)}{I_i(x,y)}\right] + \frac{I_i(x,y) - I_f(x,y)}{I_{\text{sat}}} \equiv d_O(x,y), \tag{B.4}$$

where $n(x,y)$ is the integrated density in the 3D case. $d_O(x,y)$ is called the *generalized optical density*. These results were introduced in [139] in the 3D case, then extended to the 2D case in [220].

B.1.3 Calibration of the α^* parameter

The α^* parameter, that thus allows to compute the optical density, cannot be obtained theoretically; it depends on the imaging system and has to be calibrated. To do so, we choose an atomic cloud (in our case, with an optical density of 3 or 4) from which we take a set of pictures while varying the probe intensity: as the cloud is identical on all pictures, if α^* is calibrated correctly all the optical densities computed from the different pictures should also be identical. The optical density on each picture is computed using different values for α^*; the correct value should be the one for which the deviation between the optical densities of the different pictures is minimized. In practice, we try to minimize the standard deviation between the curves describing the evolution of the optical density with the radius, taken from a cloud whose density is rotationally invariant (see figure B.2).

Note that this method requires to constantly work with a very high intensity (typically $I \geq 10 I_{\text{sat}}$) in order to eliminate multiple scattering phenomena: otherwise, we systematically underestimate the number of atoms present in regions where the atomic density is high, factor α^* or not [220].

B.1.4 Alternative method for computing α^*

The above method, initiated by G. Reinaudi in 2007 [139], has recently been improved and developed in more detail by L. Chomaz, who describes in his thesis an alternative method for measuring the factor α^* [140] based on the decomposition of the right-hand member of the equation (B.4) in two terms, which we will later call $d_{\log}$ and d_{diff}:

$$\begin{cases} d_{\log}(x,y) \equiv -\ln\left[\dfrac{I_f(x,y)}{I_i(x,y)}\right], \\ d_{\text{diff}}(x,y) \equiv \dfrac{I_i(x,y) - I_f(x,y)}{I_{\text{sat}}}. \end{cases} \tag{B.5}$$

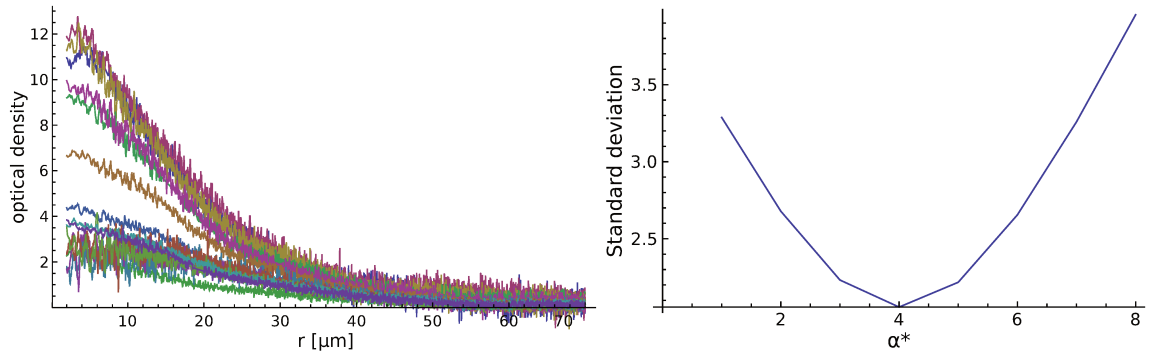

Figure B.2 – Left: Evolution of d_O with the distance to the cloud's center, computed for $\alpha^* = 1$. The different curves correspond to measurements of the *same* cloud, but realized with various intensities; they are obtained by azimuthally averaging the optical density. If the value for α^* was correct, all curves should overlap (we here deliberately show curves cumputed using a bad value for α^* to explain the principle of the method). Right: Evolution of the standard deviation of the amplitudes (obtained through a gaussian fit) of the curves presented on the left with the value of α^* used to compute them. Here, the optimal value for α^* is 4.

These two terms can be measured directly from the images produced, and allow to calculate α^* via the relationship:

$$d_{\text{diff}}(x, y) = \alpha^* d_{\log}(x, y) + d_O(x, y). \tag{B.6}$$

Thus, if we have a set of measurements of the same optical density taken using different intensity values, the points $\{d_{\log}, d_{\text{diff}}\}$ should be aligned along a line, and we can calculate α^* from a linear regression: the slope of the curve gives direct access to α^*, and its ordinate at the origin corresponds to the optical density.

In practice, these measurements are made from a set of images of the same cloud taken at different intensities (as in B.1.3), for which the points will be grouped by distance from the center of the cloud (we take images of round clouds, and therefore assume that the points located at equal distance from the center have the same optical density). For each group of points, corresponding therefore to a constant optical density, a linear regression can be performed as described above (figure B.3).

This method has the advantage of directly associating α^* and optical density; we can therefore quite naturally be interested in a possible evolution of α^* with respect to this last one. We tried to make these measurements to compare their results with those obtained by the previous method (used until then in the team); for this purpose, we compared the curves of α^* as a function of d_O made for three different clouds (hot and dense, hot and not very dense, cold and dense). The data we took showed, rather than a constant α^*, a linear evolution of α^* with the atomic density (figure B.3):

$$\alpha^*(d_O) = \alpha_0 + \alpha_s \times d_O. \tag{B.7}$$

It can be noted that in his thesis [140], L. Chomaz had observed on his evolution curves of α^* a plateau for low densities followed by a linear evolution of α^*; here we do not observe a plateau. The calibration of the α^* factor therefore becomes a calibration of the origin and the

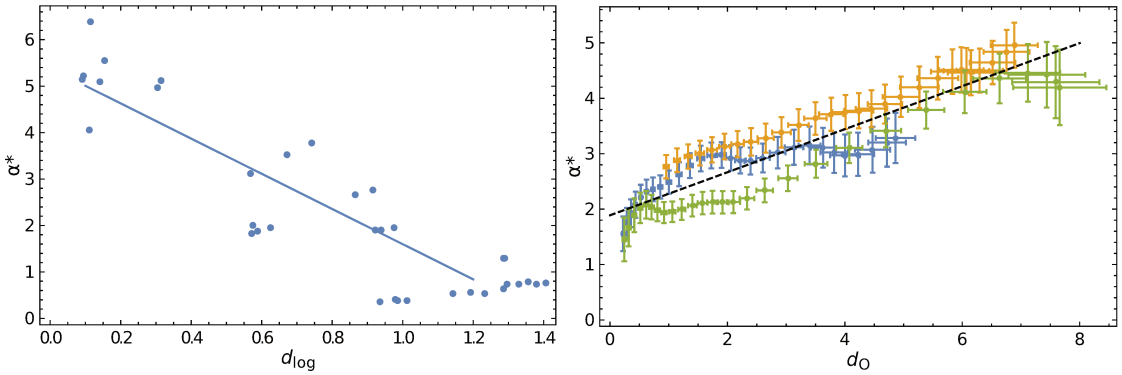

Figure B.3 — Left: Example of a linear regression allowing to determine α^*. Each point corresponds to the average value of the couples $\{d_{\log}, d_{\text{diff}}\}$ measured on the pixels corresponding to a distance of 12 to 14 μm from the cloud center (one point = one image). The line corresponds to the fit of the points obtained for a series of images of the same cloud – here, the points correspond to $d_O = 5.38$, $\alpha^* = 3.78$. Right: Evolution of the value of α^* as a function of the optical density. Three series of points are displayed, corresponding to the values measured for three different clouds of atoms (in blue/middle, a warm and lightly dense cloud; in yellow/upwards, a warm and dense cloud; in green/down, a cold and dense cloud). A regression as depicted in a) corresponds to a point on the curve; the error bars correspond to the uncertainties on the determination of the parameters during the fit (which is performed without error bars). The black dotted line corresponds to the fit of the data set – used for the rest of the experiments; we measure $\alpha_0 = 1.89 \pm 0.05$ and $\alpha_s = 0.39 \pm 0.02$

.

slope α_0 and α_s (in our case, we find $\alpha_0 = 1.89 \pm 0.05$ and $\alpha_s = 0.39 \pm 0.02$), and by replacing α^* by its value deduced from (B.7) in the calculation of the generalized optical density (B.4), we obtain a new expression:

$$\sigma_0 n = \frac{\alpha_0 d_{\log} + d_{\text{diff}}}{1 - \alpha_s d_{\log}}, \tag{B.8}$$

where $d_{\log}$ and d_{diff} are directly calculated from the images taken. The increase of α^* with optical density is interpreted as collective effects becoming more and more important as atomic density increases, which result in a decrease in absorption: the increase of α^* amounts to a decrease in the effective effective section (equation (B.3)).

It should also be noted that the use of this new expression assumes $d_{\log} < 1/\alpha_s$: if the probe is too weak and almost totally absorbed, the expression will no longer be valid. This provides a criterion for discriminating between situations where the probe is too weak and situations where the probe is intense enough.

B.2 Restrictions due to the Doppler effect and to depumping

During measurements to calibrate the α^* factor, I realized that the number of atoms measured decreased when the duration τ_{pulse} of the imaging pulses increased, in significant proportions (up to 50% of the atoms missing during the measurement). It turned out that two factors had not yet been taken into account when setting up the imaging:

- the Doppler effect induced by the acceleration of atoms: indeed, when atoms scatter the photons of the probe, they are generally accelerated in the direction of the probe beam, and this increase in velocity makes them come out of resonance: the photons arriving at the end of the image taking are therefore less likely to be absorbed. If the number of photons scattered during imaging is large (typically a few hundred, which are reached very quickly when working at high intensity), artificial losses are created.
- an effect of depumping atoms towards $F = 1$, through the level $F' = 2$ (absorption towards $F' = 2$ followed by a spontaneous emission towards $F = 1$). When we are very far from resonance, which is the case[1] for the transition $F = 2 \to F' = 2$, the probability of absorption increases linearly with the light intensity[2]. If the pulses that are used are very intense, the probability of depumping is no longer negligible (exponential decay whose time constant is in the order of a few tens of microseconds).

It is recalled that for a two-level atom (cf. B.1.1), the photon absorption rate is proportional to $\frac{s}{1+s}$, where s is the atom saturation parameter, defined by:

$$s = \frac{I}{I_{\text{sat}}} \times \frac{\Gamma^2/4}{\delta^2 + \Gamma^2/4}. \tag{B.9}$$

In both cases, we end up with an excess of photons arriving on the camera at the end of the image capture, which distorts the measurement of the number of atoms. These effects are summarized in Figure B.4.

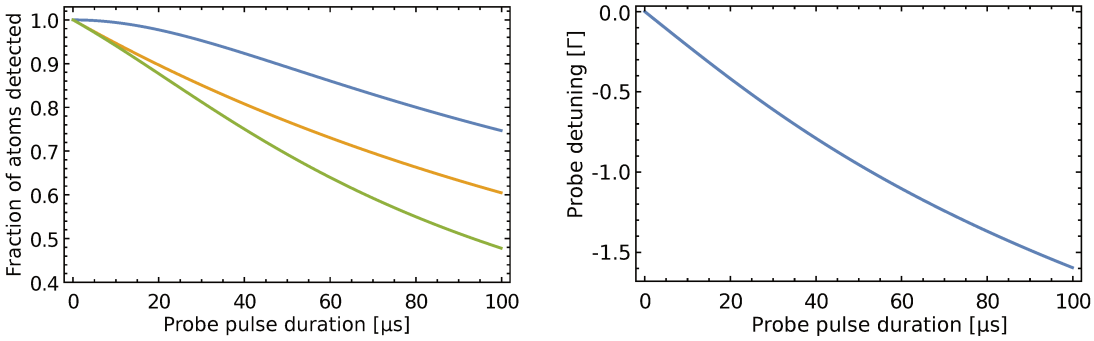

Figure B.4 — Left: Simulated evolution of the fraction of atoms detected (number of atoms detected divided by the number of atoms actually present) as a function of the duration of the cloud illumination: in blue/high, if only the Doppler effect is taken into account; in yellow/middle, if only the depumping is taken into account; in green/low, by combining both effects. Right: Evolution of the detuning δ of the probe with time due to the Doppler effect (depumping has no effect on this parameter). The two graphs are simulated for a probe intensity of $9I_{\text{sat}}$; the details of the simulation are given in Appendix B.4.

One consequence of this problem is that the calibrations of the α^* factor performed so far[3] were distorted: being performed with variable conditions of intensity and duration of the

1. 267 MHz detuning, for a linewidth of 6 MHz.
2. For a two-level atom: I assume here that the two transitions $F = 2 \to F' = 2$ and $F = 2 \to F' = 3$ can be described independently by two two-level systems
3. This is not the case for the curves presented in section B.1.2, redone taking this effect into account.

probe beam, the bias caused by these systematic effects varies from one point to another in significant proportions.

B.2.1 Effect of the probe beam intensity

The first factor that can be considered to understand better these effects is the intensity of the probe beam. Let us start by looking at the case where only the Doppler effect comes into play: when we tend towards high intensities in front of I_{sat}, we see that the fraction of atoms measured goes through a minimum around $2I_{\text{sat}}$, then increases with intensity (figure B.5). This effect can be explained by two limit cases:

- If the intensity is very low compared to I_{sat}, the number of scattered photons per atom remains very low, and the atoms are only slightly accelerated: the Doppler effect is negligible; the atom remains resonant for the entire duration of the pulse.
- If, on the other hand, the intensity is very high compared to I_{sat}, the detuning between the probe and the atom quickly becomes important, but the intensity is sufficient for the resonance to be very wide and the saturation parameter to remain high in front of 1: the atom remains saturated throughout the whole duration of the pulse.

The Doppler effect alone is not enough to explain all the missing atoms; it is also necessary to take into account the depumping to $F = 1$ through the level $F' = 2$. The saturation parameter associated with the transition $F = 2 \rightarrow F' = 2$ is much lower than 1 because the probe detuning is very large (about 267 MHz, since we are tuned to resonance with the transition $F = 2 \rightarrow F' = 3$). The absorption to $F' = 2$ – and therefore the depumping rate – thus increases linearly with the intensity of the probe. When we add depumping to the calculation of artificial losses caused by the Doppler effect, the minimum is no longer a minimum: beyond this point, the fraction of detected atoms continues to decrease, even if it does so less sharply.

Nevertheless, calculating the depumping from the sole calculation of the saturation parameter is insufficient; it is also necessary to take into account the polarization of the probe beam: if the incident photons have a circular polarization, the conservation of the angular momentum forbids the transition $|F = 2, m_F = +2\rangle \rightarrow |F' = 2, m_F = +2\rangle$ (figure B.6). In the case of our vertical imaging system, we dispose of a fine tuning of the polarization, so the depumping should be very low; on the other hand this tuning is not present in the case of our horizontal imaging and the depumping should be much more present there.

To take into account the impact of polarization, we multiply the depumping rate calculated from the saturation parameter by a coefficient γ_{dep} between 0 and 1. This coefficient is determined by measuring the curve of the number of atoms detected as a function of the probe duration, and by making an adjustment[4] of these data by our decrease model (figure B.6). We find a coefficient $\gamma_{\text{dep}} = 0.97 \pm 0.01$ on the horizontal axis and $\gamma_{\text{dep}} = 0.18 \pm 0.01$ on the vertical axis; this corresponds well to what we expected and confirms the relevance of the model used.

B.2.2 Effect of the probe pulse duration

Although its impact is interesting to study in order to understand the phenomenon, the intensity of the probe beam is not a factor that can really be exploited to take images:

4. By a least square method.

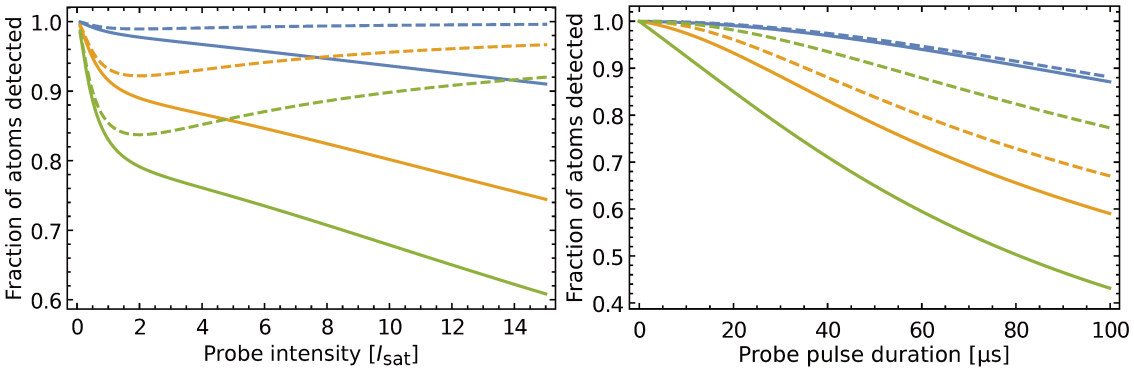

Figure B.5 — Left: Evolution of the fraction of atoms detected as a function of the probe intensity, for $\tau_{\text{pulse}} = 10\mu s$ (blue/high), 30 μs (yellow/middle) and 50 μs (green/low). The dotted curves correspond to the case where the depumping is not taken into account, the continuous curves to the case of maximum depumping ($\gamma_{\text{dep}} = 1$). Right: Evolution of the fraction of atoms detected as a function of the cloud illumination time, for a probe intensity of 0.2 I_{sat} (blue), 2.5 I_{sat} (yellow) and 12 I_{sat} (green). The dotted/continuous curves also correspond to the cases of no depumping/ maximal depumping. It should be noted that in the absence of the depumping effect, atoms are detected better for 12 I_{sat} than for 2.5 I_{sat}, whereas the opposite is true once the depumping is taken into account.

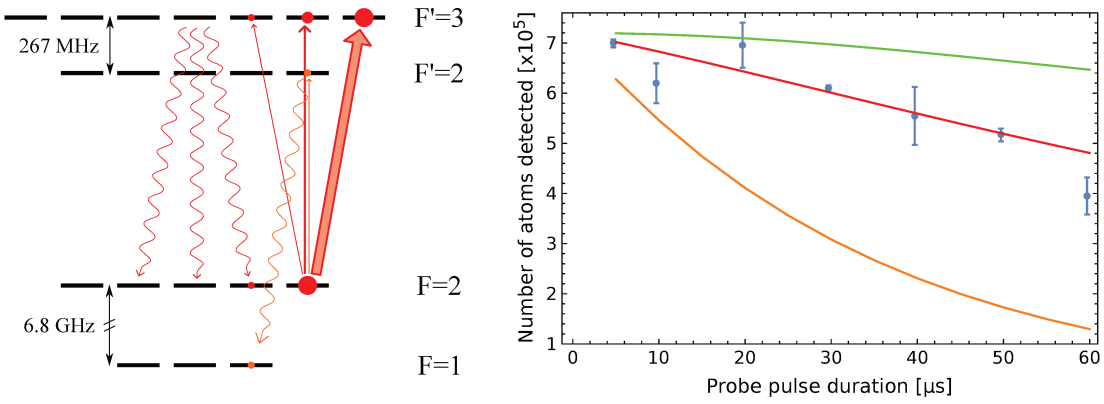

Figure B.6 — Left: Diagram of the levels involved in the depumping process. If the probe beam is σ^+ polarized, the absorption is preferably from m_F to $m_{F'} = m_F + 1$ while the decay is from $m_{F'}$ to $m_{F'} - 1$, $m_{F'}$ or $m_{F'} + 1$, and the atoms are pumped into the $m_F = F$ sublevels. The depumping (in orange) then requires either the absorption of $F = 2, m_F = +2$ to $F' = 2, m_F = +2$ (unfavorable because of the polarization σ^+), or the absorption of $F = 2, m_F = +1$ to $F' = 2, m_F = +2$ (unfavorable because the initial level is sparsely populated). Right: Calibration of the coefficient γ_{dep}: the red/middle curve corresponds to the adjustment of the data by our decay model (described in detail in B.4). The green and orange curves (up/down) correspond to the cases of zero depumping ($\gamma_{\text{dep}} = 0$) and maximal depumping ($\gamma_{\text{dep}} = 1$) .

imaging dense clouds requires a high probe intensity anyway (see B.1.2). The only factor that we can actually control is the pulse duration. This time, the impact of this parameter is

one-sided: its increase systematically causes an (artificial) decrease of the fraction of atoms detected. However, it can be noted that the behaviour of the two effects, for short pulses, is very different: while the Doppler effect has a zero slope at the origin and takes some time to cause problems, depumping leads to an exponential decay. For short duration pulses, it is therefore the depumping that will be the most constraining (figure B.5).

To measure the actual number of trapped atoms, there are then two solutions: either add a corrective factor to the number of atoms after the measurement, or work with shorter probe pulses to limit both the number of atoms depumped and the number of scattered photons (thus the velocity transferred to atoms). Adding a corrective factor being much riskier (exposing oneself to more systematic effects that are not necessarily very well controlled), the choice was made to reduce the duration of the probe pulses. We therefore wish to define a tolerance threshold, i.e. the maximum acceptable pulse duration (for a given intensity) so that the losses per depompage/Doppler effect are low (for example 1 or 2%). Once the coefficient γ_{dep} has been measured, numerical simulations can easily determine this threshold.

Effect of the initial probe detuning

Since the Doppler effect results in a red shift of the laser frequency perceived by the atoms, it seems legitimate to assume that slightly detuning the initial laser frequency towards blue will (partially) compensate for this effect. This is indeed what emerges from the numerical simulations: for a given pair of values $\{\tau_p, I\}$, there is an optimal value of the initial detuning, slightly blue-detuned, which partially compensates for the signal defect (figure B.7). On the other hand, this does not in any case make it possible to correct the depumping effect, because in we will anyway remain very far from the resonance of the phenomenon and the evolution of the detuning will not affect its impact in a significant way.

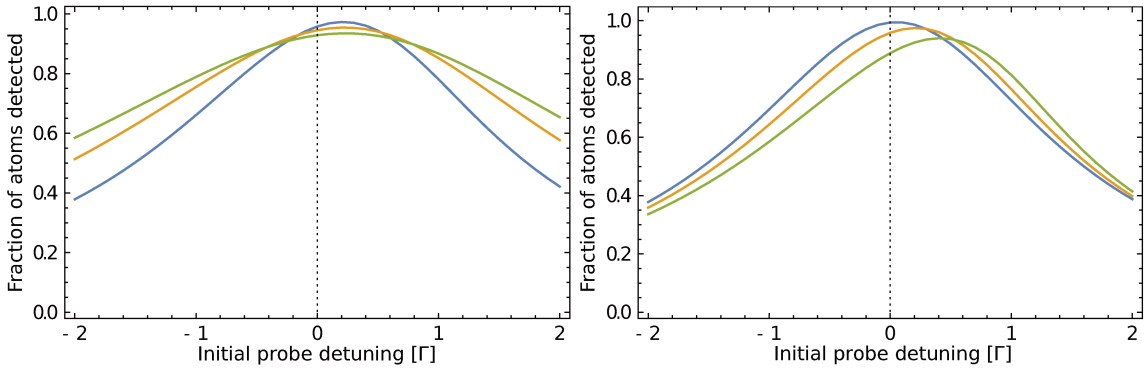

Figure B.7 – Evolution of the fraction of atoms detected as a function of the initial detuning of the probe, for (left) $\tau_{\text{pulse}} = 20\,\mu\text{s}$ and $I = 10,\ 20,\ 30\ I_{\text{sat}}$ (blue lines, yellow, green/green/broader) and (right) $I = 9\ I_{\text{sat}}$ and $\tau_{\text{pulse}} = 5,\ 20,\ 40\,\mu\text{s}$ (blue, yellow, green/left to right curves). One can see that the increase in intensity causes the resonance to broaden (and slightly collapse), while the increase in pulse duration shifts and deforms it.

Two scenarios are then to be taken into account:

- Either the depumping is important, and the pulses must absolutely be chosen very short. The Doppler effect will not be sufficiently present in this case for an initial frequency offset to be useful (optimal disagreement very close to 0).
- Or the depumping is very low: in this case we can consider using longer pulses. The Doppler effect is important in this case, and one can consider shifting the initial frequency to optimize the detected atom fraction.

However the value of γ_{dep}, even for the vertical axis, is quite constraining, and the change in the frequency of the probe is quite painful (the frequency is not difficult to change, but it would require to measure the resonance curve every time to be certain of the optimal value).

The shift in the probe resonance implies that the calibrations performed so far were distorted: indeed, until then, the probe frequency was tuned by measuring such resonance curves but the corresponding measurements were probably distorted due to the Doppler effect. Resonance measurements repeated with shorter probe pulses displayed a probe resonance that is actually closer to the atomic resonance. One can also note that the Doppler effect causes a deformation of the resonance curve of the probe (which is no longer Lorentzian). This effect is quite delicate to observe, and its measurement should not bring much information; I did therefore not focus onto it in particular.

B.3 Signal to noise ratio and optimization of the imaging parameters

This (necessary) reduction in the signal-to-noise ratio during the imaging process has led me to work on optimizing the imaging parameters: what are the parameters that allow images to be taken with the best sensitivity, while limiting the systematic effects? We also considered activating the EMCCD gain[5] (electron multiplication) of the CCD cameras used on the experiment.

I therefore calculated the detailed evolution of the signal-to-noise ratio as a function of the imaging parameters (intensity and duration of the probe, EMCCD gain value, and number of imaged atoms) – which is not linear, because the number of photons received depends non-linearly on the number of atoms: see B.1.2.

B.3.1 Analysis of the different noise sources

The factors that influence the signal-to-noise ratio are the following:

- the shot noise: it corresponds to the fluctuations of the number of photons in the probe; it is poissonian, with a variance N_{ph}. It is a fundamental noise, independent of the properties of our cameras. Once converted into the number of counts on the camera, it is equal to $\sigma_{\text{phot}} = \sqrt{C/\epsilon}$, where C is the number of counts measured by the camera and ϵ the number of electrons created on the sensor needed to obtain a measured count on the camera (1.2 electrons for the horizontal camera, 1.8 for the vertical camera).
- the probability of detection of photons by the camera (depending on its quantum efficiency and on losses on the different windows/mirrors/etc...), which can be modelled by a coefficient η: a photon passed through the cloud has a probability η of generating an electron on the camera.

5. "Electron Multiplying Charged Coupled Device ".

- the readout noise: error on the number of electrons detected when reading a pixel. It is equal to $\sigma_{ro} = 17.2$ electrons – either 9.6 counts or 60 photons – for the vertical camera (Andor Luca-R) and $\sigma_{ro} = 5.5$ electrons – either 4.6 counts or 60 photons – for the horizontal camera (Andor iXon DV885)[6].

- the digitization noise: error related to the discretization of the output signal, it corresponds to 1 count (13.1 photons for the iXon, 6.26 for the Luca). It is negligible compared to the readout noise.

- the dark current, corresponding to the parasitic electrons created on the camera sensor by something other than incident photons – by thermal effects or during charge transfer. In our case, it is systematically negligible: the images are taken too quickly for these phenomena to have an impact[7]

- the use or not of electron multiplication (and if so, its value G). The use of EMCCD allows to reduce very significantly the impact of reading noise, which does not depend on the amplitude of the measured signal, but increases shot noise by a factor of $\sqrt{2G}$ due to the principle of electron multiplication by avalanche effect.

- The noise added to the pictures when subtracting the background image (systematic effects are corrected, but at the cost of adding noise). The shot noise being very low on this image, we consider that the additional noise is equal to the reading noise σ_{ro}. In all the following, I will consider that the subtraction of the background noise is taken into account by adding this noise, and I will reason as if we were working with only two images.

The variance of the signal measured on one image is thus:

$$\begin{cases} \mathrm{Var}(C) = \frac{\langle C \rangle}{\epsilon} + 2\sigma_{ro}^2 & \text{if the EMCCD gain is disabled} \\ \mathrm{Var}(C) = 2G\frac{\langle C \rangle}{\epsilon} + 2\sigma_{ro}^2 & \text{if a gain } G \text{ is used,} \end{cases} \tag{B.10}$$

where C is the random variable describing the number of counts measured.

B.3.2 Relative error on the measured atom number

This variance corresponds to the noise measured on *one* image; in practice, two pictures (with and without atoms) are measured and the density of atoms in the cloud is calculated from these two images (equation (B.8)): it is the uncertainty on this density that we are interested in.

We can estimate via a numerical calculation the error we will have on the measurement of an optical density. This calculation is done in three steps:

- calculation of the number of photons N_f passing through the cloud (by numerically inverting the equation (B.8)).

- calculation of the noises associated with the measurements of C_i and C_f (number of counts measured for the images with and without atoms) by the CCD camera.

6. We measured 13.1 photon per count and 1.2 electrons per count – either one electron for 11 photons – for the iXon, and 6.26 photons per count and 1.8 electron per count – or one electron for 3.5 photons – for the Luca.
7. It can be noted that it increases in proportion to the square of the EMCCD gain, but the envisioned values for the gain are not large enough to make it important.

- estimation of the total error on the atomic density measurement σ_{d_O} from the errors on the measured parameters: $C_i, C_f, \alpha_0, \alpha_s$. It should be remembered that the error on the measurement of a quantity $A(X_1, ..., X_n)$ is, if the measurements of X_i are independent:

$$\sigma_A = \sqrt{\sum \left(\frac{\partial A}{\partial X_i}\right)^2 \times \sigma_{X_i}^2}, \tag{B.11}$$

  where σ_{X_i} is the standard uncertainty on the measurement of X_i.

Details about this calculation can be found in B.5.

B.3.3 Combination of all the studied effects

Preliminary calculations quickly showed that the optimization of the relative accuracy on the optical density was far from obvious and depended a lot on the optical densities to be measured. These calculations also showed that the increasing the duration of the probe pulses systematically results in more accurate measurements: while the risk of systematic errors requires short pulses, the accuracy of our measurements requires long pulses. For a given probe intensity, there is an optimal value of τ_{pulse} resulting from the compromise between these two effects – chosen as follows: I consider that a couple of parameters $\{\tau_{\text{pulse}}, I\}$ is acceptable if the systematic error caused by the Doppler effect and the depumping is hidden within the measurement error, i.e. less than twice the standard error on the measurement (the factor of two is chosen arbitrarily).

Once this criterion has been defined, the accuracies obtained for different imaging parameters can be compared, as shown in figure B.8. These comparisons show that there is no optimal parameter pair, but that the optimal pair is to be chosen according to what we are trying to observe (i.e. the density of the cloud we are interested in). Even if there are generic parameters that can be used to make fairly accurate measurements over all possible clouds, it may still be interesting to look for parameters that optimize the accuracy over the desired area (for example, our cloud temperature measurements are based on a Hartree-Fock fit of the cloud wings, and in this case high density areas are not of interest to us).

It should also be noted that these calculations can also give us directly the error bars to be used during our measurements.

On the other hand, while at first glance attractive, the EMCCD gain finally proved to be uninteresting in our case: as soon as we work with intensities or exposure times that are a little high, the shot noise becomes very important (see B.3.1) and so does the error on the optical density; the only use we could find would be to improve very low intensity images for the α_0 and α_s calibration – that is, not interesting enough for us to take the time to make the necessary calibrations to use this functionality.

B.3.4 Conclusions about the imaging process

These studies allowed us to correct systematic effects that were present until then on our imaging system, and to improve its accuracy; we can say with certainty that we now have a more reliable system than before. The calculations of the accuracy that we performed should allow us to knowingly choose the best imaging parameters for each measurement.

The first measurements performed after this work, aiming to measure the temperature of atomic clouds in the dressed trap from a Hartree-Fock fit of the wings of the in-trap cloud, were much more satisfactory than those performed so far. In particular, the two

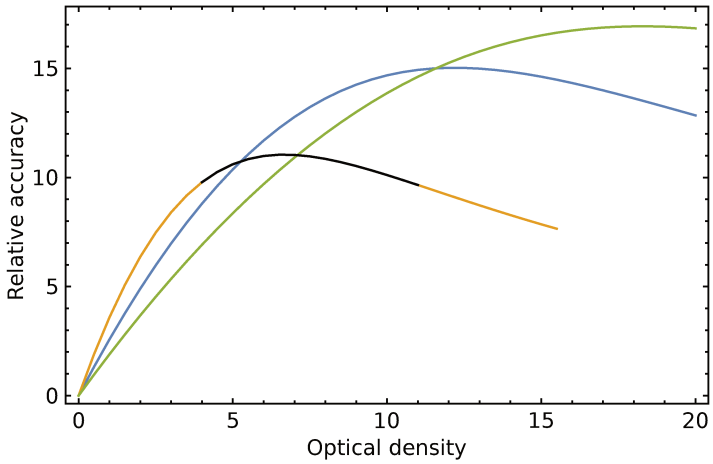

Figure B.8 – Relative accuracy (mean value divided by standard error) on the measurement of d_O as a function of the optical density measured for different imaging parameters: in yellow/high, $\{\tau_{\text{pulse}} = 23\,\mu\text{s},\ I = 5\ I_{\text{sat}}\}$ (parameters suitable for measuring low-density clouds); in blue/middle, $\{\tau_{\text{pulse}} = 160\,\mu\text{s},\ I = 12\ I_{\text{sat}}\}$ (parameters suitable for measuring dense clouds while optimizing accuracy over low density areas); green/low, $\{\tau_{\text{pulse}} = 12\,\mu\text{s},\ I = 20\ I_{\text{sat}}\}$ (parameters adapted for measuring dense clouds, optimizing accuracy over high density areas). The areas drawn in black correspond to situations that do not meet the low systematic error criteria.

imaging systems (horizontal and vertical) give much more consistent results between them than what we previously had. These results are encouraging with regard to the quality of future measurrements.

B.4 Computing the depumping and Doppler effects

This section[8] is intended to detail the model and calculations used in the previous section to simulate the artificial losses caused by the Doppler effect and depumping during the imaging process.

B.4.1 Modelization

Our calculation of the Doppler effect and the depumping is based on the optical Bloch equations, from which the population of the excited state and the number of photons scattered over time are calculated. The calculation does not take into account collective effects and considers the atoms to be all independent[9].

For a two-level atom as presented in the section B.1.1, the atomic saturation parameter is written as a function of Γ (natural linewidth, equal to $2\pi \times 6.07\,\text{MHz}$) and δ (beam detuning):

$$s = \frac{I}{I_{\text{sat}}} \times \frac{\Gamma^2/4}{\delta^2 + \Gamma^2/4}. \tag{B.12}$$

8. Translator's comment: note that this section, as well as the next one, was initially an appendix to the internship report, and they contain the technical details about what is described in the previous sections.
9. This is not very true for dense clouds, but it is difficult to do the calculation otherwise; the agreement of the obtained results with our observations validates the model a posteriori.

If we assume the system to be constantly in its stationary state (i.e. if we look at the system at long durations compared to $1/\Gamma$ or if we look at the average state of the system[10], the average population in the excited state reads:

$$\sigma_{ee} = \frac{1}{2} \times \frac{s}{1+s}. \tag{B.13}$$

The number of photons scattered by one atom between t and $t+dt$ is thus:

$$N_{\text{diff}}(t) = \Gamma_{\text{diff}}(t)\ dt = \Gamma\sigma_{ee}\ dt = \frac{\Gamma}{2} \times \frac{s(t)}{1+s(t)}\ dt, \tag{B.14}$$

where s varies with time through δ.

Calculation of the Doppler effect

To take into account the Doppler effect, one has to replace δ by $\delta(t)$, computed from the recoil velocity of the atoms and $\Gamma_{\text{diff}}(t)$. The recoil velocity of the atoms (velocity acquired through the absorption of a photon) reads:

$$v_{\text{rec}} = \frac{\hbar k}{m}. \tag{B.15}$$

An absorption-emission cycle[11] therefore leads to an evolution of detuning equal to:

$$\delta_{\text{phot}} = k \cdot v_{\text{rec}} = \frac{\hbar k^2}{m} = \frac{2\pi h}{m\lambda^2} = 2\omega_{\text{rec}}, \tag{B.16}$$

where $2\pi\omega_{\text{rec}}$ is the recoil frequency. $\delta(t)$ then reads:

$$\delta(t) = \delta_{\text{phot}} \times \int_0^t \Gamma_{\text{diff}}(t)\ dt. \tag{B.17}$$

Calculation of depumping

Depumping has no effect on the atomic detuning (as the previous calculation does not depend on the number of atoms), but it leads to a diminution over time of the number of atoms remaining in the system. To take it into account, one has to calculate the transition rate from $F=2$ to $F'=2$. This rate can be calculated from the optical Bloch equations as above, this time taking into account the two-level system corresponding to the $F=2 \rightarrow F'=2$ transition (there is no coupling between $F'=2$ and $F'=3$, and the two transitions are thus assumed to be independent) – this leads to the same calculation by replacing δ by $\delta' = \delta + \Delta_{22}$, where Δ_{22} is the detuning between the $F=2 \rightarrow F'=2$ and $F=2 \rightarrow F'=3$ transitions (equal to $2\pi \times 267\,\text{MHz}$). This gives the value of $\sigma_{ee,22}$, that is the proportion of excited atoms in the state $F'=2$.

Between t and $t+dt$, the number of atoms decreases by $N(t) \times \Gamma\sigma_{ee,22} \times dt \times \eta_{\text{dep},22}$ where $N(t)$ is the number of atoms and $\eta_{\text{dep},22}$ is the branching factor (probability of falling from one state to another) from $F=1$ to $F'=2$ (equal to 0.5).

In fact, this rate depends on the light polarization (cf. B.2.1), and we use a coefficient γ_{dep} experimentally determined to take this into account; the decrease in the number of atoms thus becomes:

$$N_{\text{at}}(t+dt) \ = \ N_{\text{at}}(t) - N_{\text{at}}(t) \times \Gamma\ \sigma_{ee,22}\ \eta_{\text{dep},22}\ \gamma_{\text{dep}}\ dt. \tag{B.18}$$

10. Which is the case for imaging since we are interested in the atomic ensemble rather than individual atoms.
11. As we are interested in the ensemble behaviour, we consider that spontaneous emission has no effect because its averages to zero.

B.4.2 Principle of computations

Solving this system analytically promises to be quite unpleasant[12]. However a numerical calculation with discrete steps of dt seems appropriate and much easier. Let us replace the values $X(t)$ by their value at $t = i \times dt$, denoted X_i. To follow the evolution of the system with time, one simply has to follow the loop:

- We know $\Gamma_{\text{diff},i}, s_i, \delta_i, v_i, N_{\text{at},i}$.
- Calculation of s:
$$s_{i+1} = \frac{I}{I_{\text{sat}}} \frac{\Gamma^2/4}{\delta_i^2 + \Gamma^2/4}$$
- Calculation of the number of photons scattered between t and $t + dt$:
$$\Gamma_{\text{diff},i+1} = \frac{\Gamma}{2} \times \frac{s_{i+1}}{1 + s_{i+1}}$$
- Inclusion of the Doppler effect:
$$\delta_{i+1} = \delta_i + \Gamma_{\text{diff},i+1} \times \delta_{\text{phot}} \times dt$$
- Calculation of the depumping and diminution of the atom number (après computing $\sigma_{ee,22,i}$):
$$N_{\text{at},i+1} = N_{\text{at},i} - N_{\text{at},i} \times \Gamma \sigma_{ee,22,i}\ \eta_{\text{dep},22}\ \gamma_{\text{dep}}\ dt$$
- ... And back to step 1.

By having the system evolve in this way and adding the values of $N_{\text{at},i}\Gamma_{\text{diff},i}$ at each step, the total measured signal (i.e. the number of photons absorbed by the cloud) can be calculated and compared to what we would expect without the two parasitic effects.

B.5 Calculation of the relative error on the optical density

This section is intended to detail the calculations used in section B to calculate the relative accuracy on the measured optical density (B.3).

B.5.1 Influence of shot noise on the measured images

This calculation is strongly inspired from what is described in Appendix A of [221], adapted to our system.

Detection of the light signal

We can model the detection of N_{ph} photons (poissonian signal[13]) by the camera as a beam-splitter with a transmission coefficient η (taking into account the camera's quantum efficiency, losses, etc.): an incident photon gives an electron with a probability η.

12. It is feasible "almost" simply if we assume a constant $\sigma_{ee,22}$, i.e. that the detuning caused by the Doppler effect is negligible compared to Δ_{22}.
13. This concerns both the partially absorbed signal and the signal without absorption, because the absorption by the atoms retains the poissonian character of the light signal.

The number of created electrons is then:

$$N_{\text{ei}} = \sum_{i=1}^{N_{\text{ph}}} X_i,$$

where N_{ph} is the number of incident photons and X_i the number of electrons obtained for one photon ($X_i = 0$ ou 1, with probability $1-\eta$ and η):

$$\begin{cases} \langle N_{\text{ph}} \rangle & = N, \\ \text{Var}(N_{\text{ph}}) & = N. \end{cases} \qquad \begin{cases} \langle X_i \rangle & = \eta, \\ \text{Var}(X_i) & = \eta(1-\eta). \end{cases}$$

The average value and variance of N_{ei} therefore read:

$$\begin{cases} \langle N_{ei} \rangle & = \eta N, \\ \text{Var}(N_{\text{ei}}) & = \langle N_{\text{ph}} \rangle \text{Var}(X_i) + \text{Var}(N_{\text{ph}}) \langle X_i \rangle^2 = N\eta(1-\eta) + N\eta^2 = \langle N_{ei} \rangle . \end{cases} \tag{B.19}$$

One can note that the signal stays poissonian.

Amplification of the light signal

The amplification of the initial electronic signal is based on a probabilistic cascade process: it is therefore inseparable from shot noise. For more details on the EMCCD gain (principle and equation of noise), the reader is invited to go towards [221].

The final electronic signal can be written as:

$$S = \sum_{i=1}^{N_{ei}} X_i,$$

where N_{ei} is the number of electrons generated on the CCD sensor during image capture and X_i is the number of electrons obtained after cascade for one initial electron:

$$\begin{cases} \langle N_{ei} \rangle & = \eta N, \\ Var(N_{ei}) & = \eta N. \end{cases} \qquad \begin{cases} \langle X_i \rangle & = G, \\ \text{Var}(X_i) & = G^2. \end{cases}$$

The average value and variance of S therefore read:

$$\begin{cases} \langle S \rangle & = \eta N G, \\ \text{Var}(S) & = \langle N_{\text{ei}} \rangle \text{Var}(X_i) + \text{Var}(N_{\text{ei}}) \langle X_i \rangle^2 = 2\eta N G^2 = 2SG. \end{cases} \tag{B.20}$$

Mesurement of the light signal

Finally, the camera counts the electrons collected on each pixel (ϵ electrons give one measured count). The finally measured signal is therefore:

$$\begin{cases} \langle C \rangle & = \frac{\eta N G}{\epsilon}, \\ \text{Var}(C) & = \text{Var}(S) \times 1/\epsilon^2 = 2\frac{\eta N G^2}{\epsilon^2} = \frac{2CG}{\epsilon} + 1 \end{cases} \tag{B.21}$$

if the signal is amplified, and:

$$\begin{cases} \langle C \rangle & = \frac{\eta N}{\epsilon}, \\ \text{Var}(C) & = \text{Var}(S) \times 1/\epsilon^2 = \frac{\eta N}{\epsilon^2} = \frac{C}{\epsilon} + 1 \end{cases} \tag{B.22}$$

if no amplification is used.

The addition of a square count to the variance corresponds to the error related to discretization; in practice it is negligible.

B.5.2 Error on the measured optical density

The optical density reads (section B.1.4):

$$\sigma_0 n \equiv d_O = \frac{\alpha_0 d_{\log} + d_{\text{diff}}}{1 - \alpha_s d_{\log}}, \tag{B.23}$$

with:

$$\begin{cases} d_{\log} = -ln\left[\dfrac{I_f}{I_i}\right] = -ln\left[\dfrac{C_f}{C_i}\right] \\ d_{\text{diff}} = \dfrac{I_i - I_f}{I_{\text{sat}}} = \dfrac{C_i - C_f}{C_{\text{sat}}} \end{cases}, \tag{B.24}$$

where C_{sat} is the number of counts corresponding to I_{sat}, that is:

$$C_{\text{sat}} = I_{\text{sat}} \times \frac{\lambda\ \tau_{\text{pulse}}\ a_{\text{pix}}^2}{\epsilon\ hc\ G^2},$$

with a_{pix} the pixel size (8 µm for both our cameras) and G the magnification of the imaging system (8.3 for the vertical axis, 2.17 for the horizonal one).

There are 4 independent sources of error: errors related to measurements of C_i and C_f, and those related to calibrations[14] of α_s and α_0.

I recall here that the error on the measurement of a quantity $A(X_1, ..., X_n)$ is, if the measurements of the X_i are independent:

$$\sigma_A = \sqrt{\sum \left(\frac{\partial A}{\partial X_i}\right)^2 \times \sigma_{X_i}^2}, \tag{B.25}$$

where σ_{X_i} is the standard uncertainty on the measurement of X_i.

One has:

$$\begin{cases} \dfrac{\partial d_O}{\partial \alpha_0} = \dfrac{d_{\log}}{1 - \alpha_s d_{\log}}, \\ \dfrac{\partial d_O}{\partial \alpha_s} = \dfrac{d_{\log}}{1 - \alpha_s d_{\log}} \times d_O, \\ \dfrac{\partial d_O}{\partial d_{\log}} = \dfrac{\alpha_0 + \alpha_s d_O}{1 - \alpha_s d_{\log}}, \\ \dfrac{\partial d_O}{\partial d_{\text{diff}}} = \dfrac{1}{1 - \alpha_s d_{\log}}, \end{cases} \qquad \begin{cases} \dfrac{\partial d_{\log}}{\partial C_i} = \dfrac{1}{C_i}, \\ \dfrac{\partial d_{\log}}{\partial C_f} = -\dfrac{1}{C_f}, \\ \dfrac{\partial d_{\text{diff}}}{\partial C_i} = \dfrac{1}{C_{\text{sat}}}, \\ \dfrac{\partial d_{\text{diff}}}{\partial C_f} = -\dfrac{1}{C_{\text{sat}}}. \end{cases} \tag{B.26}$$

The uncertainty on the measured optical density therefore reads:

$$\sigma_{d_{opt}} = \frac{1}{|1 - \alpha_s d_{\log}|} \left[(d_{\log})^2\ \sigma_{\alpha_0}^2 + (d_{\log} d_O)^2\ \sigma_{\alpha_0}^2 + \left(\frac{\alpha_0 + \alpha_s d_O}{C_i} + \frac{1}{C_{\text{sat}}}\right)^2 \sigma_{C_i}^2 + \left(\frac{\alpha_0 + \alpha_s d_O}{C_f} + \frac{1}{C_{\text{sat}}}\right)^2 \sigma_{C_f}^2 \right]^{1/2}. \tag{B.27}$$

14. These calibrations being performed together, we may have doubts about the independence of errors on α_s and α_0, but it is unlikely that this will significantly affect the final result.

Appendix C

Table of notations and symbols

The experiments described in this document extend to a quite wide range of topics, leading to a large number of notations between which it is easy to get lost (especially, studying rotating gases in RF-dressed traps leads to a very large number of "omega-something" notations). I include here as a reminder a list of the main notations, with the pages where they are introduced or defined.

General notations

Constants:

Symbol	Description	Value
h ($\hbar$)	(reduced) Planck constant	$6.626 \times 10^{-34}\,\mathrm{J \cdot s^{-1}}$ ($1.054 \times 10^{-34}\,\mathrm{J \cdot s^{-1}}$)
c	Speed of light	$2.998 \times 10^{8}\,\mathrm{m \cdot s^{-1}}$
k_B	Boltzmann constant	$1.381 \times 10^{-23}\,\mathrm{J \cdot K^{-1}}$
μ_B	Bohr magneton	$9.274 \times 10^{-24}\,\mathrm{J \cdot T^{-1}}$ ($h \times 1.399\,\mathrm{MHz \cdot G^{-1}}$)
M	Atomic mass of the ^{87}Rb	$1.443 \times 10^{-25}\,\mathrm{kg}$
g	Gravitational acceleration	$9.81\,\mathrm{m \cdot s^{-2}}$

Coordinates systems and axes:

Symbol	Description
x, y, z	Cartesian coordinates
$\mathbf{e}_x, \mathbf{e}_y, \mathbf{e}_z$	Corresponding basis
$\mathbf{e}_+, \mathbf{e}_-, \mathbf{u}$	Spherical basis defined by the orientation of the static magnetic field $\mathbf{u}(\mathbf{r})$
r, ϕ, z	Cylindrical coordinates
$\mathbf{e}_r, \mathbf{e}_\phi, \mathbf{e}_z$	Corresponding basis

Description of the trap and the trapped gas:

Symbol	Description	Page
ω_j/ν_j	Trapping frequency in the direction j, in rad $\cdot$ s^{-1}/Hz	16
d_j	Length of the harmonic oscillator associated to the trapping in direction j	19
R_j	Thomas-Fermi radius in the direction j	19
$V_{\text{ext}}(\mathbf{r})$	External trapping potential	19
T	Temperature of the gas	15
T_c	Critical temperature for Bose condensation	16, 75
λ_{dB}	de Broglie wavelength	9
N	Number of particles	15
μ	Chemical potential	15, 19
g_{int}	Coupling constant	18
$\tilde{g}$	Dimensionless coupling constant (in the 2D case)	26
$\psi(\mathbf{r},t)$	Atomic wavefunction	18
$n(\mathbf{r},t)$	Atomic density	19
ξ	Healing length	20
$S(\mathbf{r},t)$	Local phase of the wavefunction	23
$\mathbf{v}(\mathbf{r},t), v(\mathbf{r},t)$	Superfluid velocity	23

Magnetic trapping and RF dressing:

Symbol	Description	Page
$\mathbf{B}_0(\mathbf{r})$	Static magnetic field	30
$\mathbf{B}_1(t)$	Oscillating RF magnetic field	32
F	Total angular momentum of a single atom	30
g_F	Corresponding Landé factor	30
m	Atomic magnetic state	34
$\omega_0(\mathbf{r})$	Larmor frequency	34
ω_{rf}	RF frequency	31
$\Omega_1(\mathbf{r})$	Local Rabi coupling	32
$\delta(\mathbf{r})$	Detuning between the RF frequency and the local Larmor frequency	32
$\boldsymbol{\epsilon}$	RF polarization	34
η	Anisotropy of the RF coupling	44
α	Magnetic gradient (in units of frequency)	37, 38
b'	Horizontal gradient of the quadrupole static field	38
r_b	Horizontal radius of the bubble trap	38
Ω_0	Rabi coupling at the bottom of the bubble	40
Ω_{rf}	Maximal achievable Rabi coupling	37
β	Ratio between the magnetic gradient and gravity	40
R	Distance between the atoms and the center of the quadrupole	41
ω_{knife}	Frequency of the RF knife	53

Part II: Utracold atoms in a ring-shaped trap

Symbol	Description	Page
ℓ	Winding number	67
r_0	Radius of the ring trap	67
ω_r	Radial trapping frequency (in the ring-shaped trap)	75
ω_z	Vertical trapping frequency	74
L_1,L_2,L_3,L_4	Designation of the successive lenses of the light sheet setup	78

Part III: Fast-rotating Bose gases in RF adiabatic potentials

Symbol	Description	Page
ω_z	Vertical trapping frequency	41
$\omega_\perp$	Radial trapping frequency (in the isotropic case)	41
ε	Horizontal trap anisotropy	44
Ω_{rot}	Angular velocity of the trap (if it is rotating)	144
L_z	Average angular momentum of the gas (along the z axis)	130
N_v	Number of vortices in the gas	131
n_v	Vortex surface density	130
Ω_{eff}	Effective rotation frequency of the gas	130
λ	Relative strength of the quartic trapping term compared to the harmonic trapping	136
Ω_h	Rotation frequency of the gas required for the appearance of a central hole	140
l	Magnetic length of the rotating gas	131
$\omega_\pm$	Frequency of the $m_z = \pm 2$ quadrupole modes	141

Bibliography

[1] P. Kapitza, "Viscosity of Liquid Helium below the λ-Point". *Nature* **141**, 74 (1938).

[2] J.F. Allen and A.D. Misener, "Flow of Liquid Helium II". *Nature* **141**, 75 (1938).

[3] A. Einstein, "Quantentheorie des einatomigen idealen Gases". *Sitzungsber. Kgl. Preuss. Akad. Wiss.*, 261–267 (1924).

[4] A. Einstein, "Quantentheorie des einatomigen idealen Gases. Zweite Abhandlung". *Sitzungsber. Kgl. Preuss. Akad. Wiss.*, 3–14 (1925).

[5] F. London, "On the Bose-Einstein Condensation". *Phys. Rev.* **54**, 947–954 (Dec 1938).

[6] T W B Kibble, "Topology of cosmic domains and strings". *Journal of Physics A: Mathematical and General* **9** (8), 1387 (1976).

[7] J. Palfreyman, J. M. Dickey, A. Hotan, S Ellingsen and Willem van Straten, "Alteration of the magnetosphere of the Vela pulsar during a glitch". *Journal of Physics A: Mathematical and General* **556**, 219 (2018).

[8] A. J. Leggett, "Superfluidity". *Rev. Mod. Phys.* **71**, S318 (1999).

[9] D.R. Allum, P.V.E. McClintock, A. Phillips and R.M. Bowley, "The breakdown of superfluidity in liquid ^{4}He: an experimental test of Landau's theory". *Philosophical Transactions of the Royal Society of London A: Mathematical, Physical and Engineering Sciences* **284** (1320), 179–224 (1977).

[10] H.E. Hall, "The angular acceleration of liquid helium II". *Philosophical Transactions of the Royal Society of London A: Mathematical, Physical and Engineering Sciences* **250** (980), 359–385 (1957).

[11] S. C. Whitmore and W. Zimmermann, "Observation of Quantized Circulation in Superfluid Helium". *Phys. Rev.* **166** (1), 181–196 (Feb 1968).

[12] R.P. Feynman, "Chapter II Application of Quantum Mechanics to Liquid Helium". volume 1 of *Progress in Low Temperature Physics* pages 17 – 53, Elsevier (1955).

[13] V.F. Vinen, "The detection of single quanta of circulation in liquid helium II". *Proceedings of the Royal Society of London A: Mathematical, Physical and Engineering Sciences* **260** (1301), 218–236 (1961).

[14] G. B. Hess and W. M. Fairbank, "Measurements of Angular Momentum in Superfluid Helium". *Phys. Rev. Lett.* **19**, 216–218 (Jul 1967).

[15] E. J. Yarmchuk, M. J. V. Gordon and R. E. Packard, "Observation of Stationary Vortex Arrays in Rotating Superfluid Helium". *Phys. Rev. Lett.* **43**, 214–217 (Jul 1979).

[16] D. J. Wineland, R. E. Drullinger and F. L. Walls, "Radiation-Pressure Cooling of Bound Resonant Absorbers". *Phys. Rev. Lett.* **40**, 1639–1642 (1978).

[17] W. Neuhauser, M. Hohenstatt, P. Toschek and H. Dehmelt, "Optical-Sideband Cooling of Visible Atom Cloud Confined in Parabolic Well". *Phys. Rev. Lett.* **41**, 233–236 (1978).

[18] S. Chu, L. Hollberg, J. E. Bjorkholm, A. Cable and A. Ashkin, "Three-dimensional viscous confinement and cooling of atoms by resonance radiation pressure". *Phys. Rev. Lett.* **55**, 48–51 (1985).

[19] S. Chu, J.E. Bjorkholm, A. Ashkin and A. Cable, "Experimental observation of optically trapped atoms". *Phys. Rev. Lett.* **57** (3), 314–317 (1986).

[20] Alan L. Migdall, John V. Prodan, William D. Phillips, Thomas H. Bergeman and Harold J. Metcalf, "First Observation of Magnetically Trapped Neutral Atoms". *Phys. Rev. Lett.* **54**, 2596–2599 (Jun 1985).

[21] E.L. Raab, M. Prentiss, A. Cable, S. Chu and D.E. Pritchard, "Trapping of neutral sodium atoms with radiation pressure". *Phys. Rev. Lett.* **59** (23), 2631–2634 (1987).

[22] M.H. Anderson, J.R. Ensher, M.R. Matthews, C.E. Wieman and E.A. Cornell, "Observation of Bose-Einstein condensation in a dilute atomic vapor". *Science* **269**, 198–201 (1995).

[23] K.B. Davis, M.-O. Mewes, M.R. Andrews, N.J. van Druten, D.S. Durfee, D.M. Kurn and W. Ketterle, "Bose-Einstein condensation in a gas of sodium atoms". *Phys. Rev. Lett.* **75** (22), 3969–3973 (1995).

[24] C. Cohen-Tannoudji, "Nobel Lecture: Manipulating atoms with photons". *Rev. Mod. Phys.* **70**, 707 (1998).

[25] S. Chu, "Nobel Lecture: The manipulation of neutral particles". *Rev. Mod. Phys.* **70**, 685 (1998).

[26] W. D. Phillips, "Nobel Lecture: Laser cooling and trapping of neutral atoms". *Rev. Mod. Phys.* **70**, 721 (1998).

[27] E. A. Cornell and C. E. Wieman, "Nobel Lecture: Bose-Einstein condensation in a dilute gas, the first 70 years and some recent experiments". *Rev. Mod. Phys.* **74**, 875 (2002).

[28] W. Ketterle, "When atoms behave as waves: Bose-Einstein condensation and the atom laser". *Rev. Mod. Phys.* **74**, 1131 (2002).

[29] M. Greiner, O. Mandel, T. Esslinger, T.W. Hänsch and I. Bloch, "Quantum Phase Transition from a Superfluid to a Mott Insulator in a Gas of Ultracold Atoms". *Nature* **415**, 39 (2002).

[30] W. S. Bakr, J. I. Gillen, A. Peng, S. Fölling and M. Greiner, "A quantum gas microscope for detecting single atoms in a Hubbard-regime optical lattice". *Nature* **462**, 74 (2009).

[31] J. F. Sherson, C. Weitenberg, M. Endres, M. Cheneau, I. Bloch and S. Kuhr, "Single-atom-resolved fluorescence imaging of an atomic Mott insulator". *Nature* **467**, 68 (2010).

[32] Manuel Endres, Hannes Bernien, Alexander Keesling, Harry Levine, Eric R. Anschuetz, Alexandre Krajenbrink, Crystal Senko, Vladan Vuletic, Markus Greiner and Mikhail D. Lukin, "Atom-by-atom assembly of defect-free one-dimensional cold atom arrays". *Science* **354** (6315), 1024–1027 (2016).

[33] H. Kadau, M. Schmitt, M. Wenzel, C. Wink, T. Maier, I. Ferrier-Barbut and T. Pfau, "Observing the Rosensweig instability of a quantum ferrofluid". *Nature* **530**, 194 (Feb 2016).

[34] M. Schmitt, M. Wenzel, F. Böttcher, I. Ferrier-Barbut and T. Pfau, "Self-bound droplets of a dilute magnetic quantum liquid". *Nature* **539**, 259 (Nov 2016).

[35] C. R. Cabrera, L. Tanzi, J. Sanz, B. Naylor, P. Thomas, P. Cheiney and L. Tarruell, "Quantum liquid droplets in a mixture of Bose-Einstein condensates". *Science* **359** (6373), 301–304 (2018).

[36] Y.-J. Lin, R. L. Compton, K. Jiménez-García, J. V. Porto and I. B. Spielman, "Synthetic magnetic fields for ultracold neutral atoms". *Nature* **462**, 628 (2009).

[37] Jean Dalibard, Fabrice Gerbier, Gediminas Juzeliūnas and Patrik Öhberg, "*Colloquium*: Artificial gauge potentials for neutral atoms". *Rev. Mod. Phys.* **83**, 1523–1543 (Nov 2011).

[38] B. K. Stuhl, H.-I. Lu, L. M. Aycock, D. Genkina and I. B. Spielman, "Visualizing edge states with an atomic Bose gas in the quantum Hall regime". *Science* **349** (6255), 1514–1518 (2015).

[39] R. Landig, L. Hruby, N. Dogra, M. Landini, R. Mottl, T. Donner and T. Esslinger, "Quantum phases from competing short- and long-range interactions in an optical lattice". *Nature* **532**, 476 (Apr 2016).

[40] J. Léonard, A. Morales, P. Zupancic, T. Esslinger and T. Donner, "Supersolid formation in a quantum gas breaking a continuous translational symmetry". *Nature* **543**, 87 (Mar 2017).

[41] B. J. Bloom, T. L. Nicholson, J. R. Williams, S. L. Campbell, M. Bishof, X. Zhang, W. Zhang, S. L. Bromley and J. Ye, "An optical lattice clock with accuracy and stability at the 10^{-18} level". *Nature* **506**, 71 (Jan 2014).

[42] C. W. Chou, D. B. Hume, T. Rosenband and D. J. Wineland, "Optical Clocks and Relativity". *Science* **329** (5999), 1630–1633 (2010).

[43] T. van Zoest, N. Gaaloul, Y. Singh, H. Ahlers, W. Herr, S. T. Seidel, W. Ertmer, E. Rasel, M. Eckart, E. Kajari, S. Arnold, G. Nandi, W. P. Schleich, R. Walser, A. Vogel, K. Sengstock, K. Bongs, W. Lewoczko-Adamczyk, M. Schiemangk, T. Schuldt, A. Peters, T. Könemann, H. Müntinga, C. Lämmerzahl, H. Dittus, T. Steinmetz, T. W. Hänsch and J. Reichel, "Bose-Einstein Condensation in Microgravity". *Science* **328** (5985), 1540–1543 (2010).

[44] M. Schellekens, R. Hoppeler, A. Perrin, J. Viana Gomes, D. Boiron, A. Aspect and C. I. Westbrook, "Hanbury Brown Twiss Effect for Ultracold Quantum Gases". *Science* **310** (5748), 648–651 (2005).

[45] Raphael Lopes, Almazbek Imanaliev, Alain Aspect, Marc Cheneau, Denis Boiron and Christoph I Westbrook, "Atomic Hong–Ou–Mandel experiment". *Nature* **520**, 66–68 (2015).

[46] R. Islam, R. Ma, P. M. Preiss, M. Eric Tai, A. Lukin, M. Rispoli and M. Greiner, "Measuring entanglement entropy in a quantum many-body system". *Nature* **528**, 77 (Dec 2015).

[47] C. Raman, M. Köhl, R. Onofrio, D. S. Durfee, C. E. Kuklewicz, Z. Hadzibabic and W. Ketterle, "Evidence for a Critical Velocity in a Bose-Einstein Condensed Gas". *Phys. Rev. Lett.* **83**, 2502–2505 (Sep 1999).

[48] M.-O. Mewes, M.R. Andrews, N.J. van Druten, D.M. Kurn, D.S. Durfee, C.G. Townsend and W. Ketterle, "Collective excitations of a Bose-Einstein condensate in a magnetic trap". *Phys. Rev. Lett.* **77** (6), 988–991 (1996).

[49] D. S. Jin, J. R. Ensher, M. R. Matthews, C. E. Wieman and E. A. Cornell, "Collective Excitations of a Bose-Einstein Condensate in a Dilute Gas". *Phys. Rev. Lett.* **77**, 420–423 (Jul 1996).

[50] O. M. Maragò, S. A. Hopkins, J. Arlt, E. Hodby, G. Hechenblaikner and C. J. Foot, "Observation of the Scissors Mode and Evidence for Superfluidity of a Trapped Bose-Einstein Condensed Gas". *Phys. Rev. Lett.* **84**, 2056–2059 (Mar 2000).

[51] M. R. Matthews, B. P. Anderson, P. C. Haljan, D. S. Hall, C. E. Wieman and E. A. Cornell, "Vortices in a Bose–Einstein Condensate". *Phys. Rev. Lett.* **83** (13), 2498–2501 (Sep 1999).

[52] K. W. Madison, F. Chevy, W. Wohlleben and J. Dalibard, "Vortex formation in a stirred Bose-Einstein condensate". *Phys. Rev. Lett.* **84**, 806 (2000).

[53] J. R. Abo-Shaeer, C. Raman, J. M. Vogels and W. Ketterle, "Observation of Vortex Lattices in Bose-Einstein Condensates". *Science* **292**, 476 (2001).

[54] V. Schweikhard, I. Coddington, P. Engels, V.P. Mogendorff and E.A. Cornell, "Rapidly rotating Bose-Einstein condensates in and near the lowest Landau level". *Phys. Rev. Lett.* **92** (4), 040 404, 1–4 (2004).

[55] N. R. Cooper, N. K. Wilkin and J. M. F. Gunn, "Quantum Phases of Vortices in Rotating Bose–Einstein Condensates". *Phys. Rev. Lett.* **87** (12), 120 405 (Aug 2001).

[56] Y. Shin, M. Saba, M. Vengalattore, T. A. Pasquini, C. Sanner, A. E. Leanhardt, M. Prentiss, D. E. Pritchard and W. Ketterle, "Dynamical Instability of a Doubly Quantized Vortex in a Bose-Einstein Condensate". *Phys. Rev. Lett.* **93**, 160 406 (Oct 2004).

[57] C. Ryu, M. F. Andersen, P. Cladé, V. Natarajan, K. Helmerson and W. D. Phillips, "Observation of Persistent Flow of a Bose-Einstein Condensate in a Toroidal Trap". *Phys. Rev. Lett.* **99**, 260 401 (2007).

[58] Stuart Moulder, Scott Beattie, Robert P. Smith, Naaman Tammuz and Zoran Hadzibabic, "Quantized supercurrent decay in an annular Bose-Einstein condensate". *Phys. Rev. A* **86**, 013 629 (Jul 2012).

[59] Stephen Eckel, Jeffrey G. Lee, Fred Jendrzejewski, Noel Murray, Charles W. Clark, Christopher J. Lobb, William D. Phillips, Mark Edwards and Gretchen K. Campbell, "Hysteresis in a quantized superfluid 'atomtronic' circuit". *Nature* **506** (7487), 200–203 (02 2014).

[60] L. Pricoupenko, H. Perrin and M. Olshanii (editors), *Quantum Gases in Low Dimensions*, J. Phys. IV France (2004).

[61] V. Berezinskii, "Destruction of long-range order in one-dimensional and 2-dimensional systems having a continuous symmetry group, 2 - quantum systems". *Sov. Phys. JETP-USSR* **34**, 610 (1972).

[62] J.M. Kosterlitz and D.J. Thouless, "Ordering, metastability and phase transitions in two-dimensional systems". *J. Phys. C : Solid State Phys.* **6**, 1181–1203 (1973).

[63] Z. Hadzibabic and J. Dalibard, "Two-dimensional Bose fluids: An atomic physics perspective". *Rivista del Nuovo Cimento* **34**, 389 (2011).

[64] Richard J. Fletcher, Martin Robert-de Saint-Vincent, Jay Man, Nir Navon, Robert P. Smith, Konrad G. H. Viebahn and Zoran Hadzibabic, "Connecting Berezinskii-Kosterlitz-Thouless and BEC Phase Transitions by Tuning Interactions in a Trapped Gas". *Phys. Rev. Lett.* **114**, 255 302 (Jun 2015).

[65] D.S. Petrov, G.V. Shlyapnikov and J.T.M. Walraven, "Regimes of quantum degeneracy in trapped 1D gases". *Phys. Rev. Lett.* **85** (18), 3745–3749 (2000).

[66] T. Kinoshita, T. R. Wenger and D. S. Weiss, "Observation of a one-dimensional Tonks-Girardeau gas". *Science* **305**, 1125 (2004).

[67] R. Desbuquois, L. Chomaz, T. Yefsah, J. Leonard, J. Beugnon, C. Weitenberg and J. Dalibard, "Superfluid behaviour of a two-dimensional Bose gas". *Nature Physics* **8**, 645 (2012).

[68] Camilla De Rossi, Romain Dubessy, Karina Merloti, Mathieu de Goër de Herve, Thomas Badr, Aurélien Perrin, Laurent Longchambon and Hélène Perrin, "Probing superfluidity in a quasi two-dimensional Bose gas through its local dynamics". *New Journal of Physics* **18** (6), 062 001 (2016).

[69] J.L. Ville, R. Saint-Jalm, É. Le Cerf, M. Aidelsburger, S. Nascimbène, J. Dalibard and J. Beugnon, "Sound propagation in a uniform superfluid two-dimensional Bose gas". *preprint* (2018). ArXiv:1804.04037.

[70] W.H. Zurek, "Cosmological experiments in superfluid helium?" *Nature* **317**, 505–508 (1985).

[71] L. Corman, L. Chomaz, T. Bienaimé, R. Desbuquoi<s, C. Weitenberg, S. Nascimbène, J. Dalibard and J. Beugnon, "Quench-Induced Supercurrents in an Annular Bose Gas". *Phys. Rev. Lett.* **113**, 135 302 (Sep 2014).

[72] C. Ryu, P. W. Blackburn, A. A. Blinova and M. G. Boshier, "Experimental Realization of Josephson Junctions for an Atom SQUID". *Phys. Rev. Lett.* **111**, 205 301 (Nov 2013).

[73] Luigi Amico, Gerhard Birkl, Malcolm Boshier and Leong-Chuan Kwek, "Focus on atomtronics-enabled quantum technologies". *New Journal of Physics* **19** (2), 020 201 (2017).

[74] Kenichi Kasamatsu, Makoto Tsubota and Masahito Ueda, "Giant hole and circular superflow in a fast rotating Bose-Einstein condensate". *Phys. Rev. A* **66**, 053 606 (Nov 2002).

[75] G M Kavoulakis and Gordon Baym, "Rapidly rotating Bose-Einstein condensates in anharmonic potentials". *New Journal of Physics* **5** (1), 51 (2003).

[76] Alexander L. Fetter, B. Jackson and S. Stringari, "Rapid rotation of a Bose-Einstein condensate in a harmonic plus quartic trap". *Phys. Rev. A* **71**, 013 605 (Jan 2005).

[77] V. Bretin, S. Stock, Y. Seurin and J. Dalibard, "Fast rotation of a Bose-Einstein condensate". *Phys. Rev. Lett.* **92** (5), 050 403, 1–4 (2004).

[78] H Terças, J P A Martins and J T Mendonça, "Rossby waves in rapidly rotating Bose–Einstein condensates". *New Journal of Physics* **12** (9), 093 001 (2010).

[79] M. Correggi, F. Pinsker, N. Rougerie and J. Yngvason, "Giant vortex phase transition in rapidly rotating trapped Bose-Einstein condensates". *Eur. Phys. J. Special Topics* **217**, 183 (Mar 2013).

[80] Jieli Qin, Guangjiong Dong and Boris A. Malomed, "Stable giant vortex annuli in microwave-coupled atomic condensates". *Phys. Rev. A* **94**, 053 611 (Nov 2016).

[81] F. Dalfovo, S. Giorgini, L.P. Pitaevskii and S. Stringari, "Theory of Bose-Einstein condensation in trapped gases". *Rev. Mod. Phys.* **71** (3), 463–512 (1999).

[82] L. Pitaevskii and S. Stringari, *Bose-Einstein condensation*. Oxford University Press (2003).

[83] Oliver Penrose and Lars Onsager, "Bose-Einstein Condensation and Liquid Helium". *Phys. Rev.* **104**, 576–584 (Nov 1956).

[84] Lene Vestergaard Hau, B. D. Busch, Chien Liu, Zachary Dutton, Michael M. Burns and J. A. Golovchenko, "Near-resonant spatial images of confined Bose-Einstein condensates in a 4-Dee magnetic bottle". *Phys. Rev. A* **58**, R54–R57 (Jul 1998).

[85] J.T.M. Walraven, *Quantum Gases* (2017). Lecture notes, course given at the university of Amsterdam.

[86] Karina Merloti, *Condensat de Bose–Einstein dans un piège habillé: modes collectifs d'un superfluide en dimension deux*. PhD thesis, Université Paris 13 (2013).

[87] Camilla de Rossi, *Gaz de Bose en dimension deux : modes collectifs, superfluidité et piège annulaire*. PhD thesis, Université Paris 13 (2016).

[88] L.D. Landau, "The theory of syperfluidity of helium II". *J.Phys. USSR* **5**, 71 (1941).

[89] S. Stringari, "Collective excitations of a trapped Bose-condensed gas". *Phys. Rev. Lett.* **77** (12), 2360–2363 (1996).

[90] K. W. Madison, F. Chevy, V. Bretin and J. Dalibard, "Stationary states of a rotating Bose–Einstein condensate: Routes to vortex nucleation". *Phys. Rev. Lett.* **86**, 4443 (2001).

[91] E. Hodby, G. Hechenblaikner, S. A. Hopkins, O. M. Marago and C. J. Foot, "Vortex Nucleation in Bose–Einstein Condensates in an Oblate, Purely Magnetic Potential". *Phys. Rev. Lett.* **88**, 010 405 (2001).

[92] L. Onsager, "Statistical hydrodynamics". *Il Nuovo Cimento Series 9* **6** (2), 279–287 (1949).

[93] Y. Castin and R. Dum, "Bose-Einstein condensates with vortices in rotating traps". *The European Physical Journal D - Atomic, Molecular, Optical and Plasma Physics* **7** (3), 399–412 (Oct 1999).

[94] Nikolay Prokof'ev, Oliver Ruebenacker and Boris Svistunov, "Critical Point of a Weakly Interacting Two-Dimensional Bose Gas". *Phys. Rev. Lett.* **87**, 270 402 (Dec 2001).

[95] D.S. Petrov, D.M. Gangardt and G.V. Shlyapnikov, "Low-dimensional trapped gases". In *Proceedings of the Euroschool on quantum gases in low dimensions, Les Houches 2003*, volume 116, edited by L. Pricoupenko, H. Perrin and M. Olshanii 5, J. Phys. IV (2004).

[96] V. Bagnato and D. Kleppner, "Bose-Einstein condensation in low-dimensional traps". *Phys. Rev. A* **44** (11), 7439–7441 (1991).

[97] Markus Holzmann, Maguelonne Chevallier and Werner Krauth, "Universal correlations and coherence in quasi-two-dimensional trapped Bose gases". *Phys. Rev. A* **81**, 043 622 (Apr 2010).

[98] O. Zobay and B.M. Garraway, "Two-dimensional atom trapping in field-induced adiabatic potentials". *Phys. Rev. Lett.* **86** (7), 1195–1198 (2001).

[99] Y. Colombe, E. Knyazchyan, O. Morizot, B. Mercier, V. Lorent and H. Perrin, "Ultracold atoms confined in rf-induced two-dimensional trapping potentials". *Europhys. Lett.* **67** (4), 593–599 (2004).

[100] Hélène Perrin and Barry M. Garraway, "Chapter Four - Trapping Atoms With Radio Frequency Adiabatic Potentials". volume 66 of *Advances In Atomic, Molecular, and Optical Physics* pages 181 – 262, Academic Press (2017).

[101] Y. Colombe, B. Mercier, H. Perrin and V. Lorent, "Loading a dressed Zeeman trap with cold atoms". In *Proceedings of the Euroschool on quantum gases in low dimensions, Les Houches 2003*, volume 116, edited by L. Pricoupenko, H. Perrin and M. Olshanii 247, J. Phys. IV (2004).

[102] K. Merloti, R. Dubessy, L. Longchambon, A. Perrin, P.-E. Pottie, V. Lorent and H. Perrin, "A two-dimensional quantum gas in a magnetic trap". *New Journal of Physics* **15** (3), 033 007 (2013).

[103] Karina Merloti, Romain Dubessy, Laurent Longchambon, Maxim Olshanii and Hélène Perrin, "Breakdown of scale invariance in a quasi-two-dimensional Bose gas due to the presence of the third dimension". *Phys. Rev. A* **88**, 061 603 (Dec 2013).

[104] R. Dubessy, C. De Rossi, T. Badr, L. Longchambon and H. Perrin, "Imaging the collective excitations of an ultracold gas using statistical correlations". *New Journal of Physics* **16** (12), 122 001 (2014).

[105] T. Schumm, S. Hofferberth, L.M. Andersson, S. Wildermuth, S. Groth, I. Bar-Joseph, J. Schmiedmayer and P. Krüger, "Matter wave interferometry in a double well on an atom chip". *Nature Phys.* **1**, 57 (2005).

[106] O. Morizot, Y. Colombe, V. Lorent, H. Perrin and B.M. Garraway, "Ring trap for ultracold atoms". *Phys. Rev. A* **74**, 023 617 (2006).

[107] W. H. Heathcote, E. Nugent, B. T. Sheard and C. J. Foot, "A ring trap for ultracold atoms in an RF-dressed state". *New Journal of Physics* **10** (4), 043 012 (2008).

[108] N. Lundblad, P. J. Lee, I. B. Spielman, B. L. Brown, W. D. Phillips and J. V. Porto, "Atoms in a Radio-Frequency-Dressed Optical Lattice". *Phys. Rev. Lett.* **100**, 150 401 (Apr 2008).

[109] Igor Lesanovsky and Wolf von Klitzing, "Time-Averaged Adiabatic Potentials: Versatile Matter-Wave Guides and Atom Traps". *Phys. Rev. Lett.* **99** (8), 083 001 (Aug 2007).

[110] B. E. Sherlock, M. Gildemeister, E. Owen, E. Nugent and C. J. Foot, "Time-averaged adiabatic ring potential for ultracold atoms". *Phys. Rev. A* **83**, 043 408 (Apr 2011).

[111] P Navez, S Pandey, H Mas, K Poulios, T Fernholz and W von Klitzing, "Matter-wave interferometers using TAAP rings". *New Journal of Physics* **18** (7), 075 014 (2016).

[112] Nathan Lundblad, Thomas Jarvis, Daniel Paseltiner and Lannert Courtney, "Progress toward studies of bubble-geometry Bose-Einstein condensates in microgravity with a ground-based prototype of NASA CAL". poster presented in DAMOP2016 (2016). http://meetings.aps.org/link/BAPS.2016.DAMOP.K1.119 .

[113] Barry M Garraway and Hélène Perrin, "Recent developments in trapping and manipulation of atoms with adiabatic potentials". *Journal of Physics B: Atomic, Molecular and Optical Physics* **49** (17), 172 001 (2016).

[114] C. Cohen-Tannoudji, *Atomes ultra-froids – Piégeage non dissipatif et refroidissement évaporatif*. Cours de physique atomique et moléculaire, Collège de France, année 1996-1997.

[115] E. Majorana, "Atomi orientati in campo magnetico variabile". *Nuovo Cimento* **9**, 43–50 (1932).

[116] I. I. Rabi, J. R. Zacharias, S. Millman and P. Kusch, "A New Method of Measuring Nuclear Magnetic Moment". *Phys. Rev.* **53**, 318–318 (Feb 1938).

[117] A. Messiah, *Quantum Mechanics*. North Holland, John Wiley & Sons (1966).

[118] L. Landau, "Zur Theorie der Energieübertragung - II". *Phys. Z. Sowjetunion* **2**, 46–51 (1932).

[119] C. Zener, "Non-adiabatic crossing of energy levels". *Proc. R. Soc. London Ser. A* **137**, 696–702 (1932).

[120] D.T. Pegg and G.W. Series, "Semi-classical theory of the Hanle effect with transverse static and oscillating magnetic fields". *J. Phys. B: Atom. Mol. Phys.* **3**, L33 (1970).

[121] D T Pegg, "Misalignment effects in magnetic resonance". *Journal of Physics B: Atomic and Molecular Physics* **6** (2), 241 (1973).

[122] A.J. Moerdijk, B.J. Verhaar and T.M. Nagtegaal, "Collisions of dressed ground-state atoms". *Phys. Rev. A* **53** (6), 4343–4351 (1996).

[123] O. Morizot, C.L. Garrido Alzar, P.-E. Pottie, V. Lorent and H. Perrin, "Trapping and cooling of rf-dressed atoms in a quadrupole magnetic field". *J. Phys. B: At. Mol. Opt. Phys.* **40**, 4013–4022 (2007).

[124] Hélène Perrin. private communication.

[125] Romain Dubessy. private communication.

[126] Thomas Liennard, *Construction d'un montage de condensation de Bose–Einstein de rubidium et étude théorique d'un superfluide en rotation dans un anneau*. PhD thesis, Université Paris-Nord - Paris XIII (2011).

[127] R. Dubessy, K. Merloti, L. Longchambon, P.-E. Pottie, T. Liennard, A. Perrin, V. Lorent and H. Perrin, "Rubidium-87 Bose-Einstein condensate in an optically plugged quadrupole trap". *Phys. Rev. A* **85**, 013 643 (Jan 2012).

[128] O. Morizot, *Pièges radiofréquence très anisotropes pour un condensat de Bose–Einstein*. PhD thesis, Université Paris 13 (2007).

[129] Wolfgang Petrich, Michael H. Anderson, Jason R. Ensher and Eric A. Cornell, "Stable, Tightly Confining Magnetic Trap for Evaporative Cooling of Neutral Atoms". *Phys. Rev. Lett.* **74**, 3352–3355 (Apr 1995).

[130] D. S. Naik and C. Raman, "Optically Plugged Quadrupole Trap for Bose-Einstein Condensates". *Phys. Rev. A* **71**, 033 617 (2005).

[131] Y.-J. Lin, A. R. Perry, R. L. Compton, I. B. Spielman and J. V. Porto, "Rapid production of ^{87}Rb Bose-Einstein condensates in a combined magnetic and optical potential". *Phys. Rev. A* **79** (6), 063 631 (Jun 2009).

[132] O. Morizot, L. Longchambon, R. Kollengode Easwaran, R. Dubessy, E. Knyazchyan, P.-E. Pottie, V. Lorent and H. Perrin, "Influence of the Radio-Frequency source properties on RF-based atom traps". *Eur. Phys. J. D* **47**, 209 (2008).

[133] A. Benabdesadok, *Construction, Caractérisation et Mise en Place d'Antennes Radiofréquence*. L3 internship report, Université de Cergy Pontoise (2003).

[134] Kathryn A. Burrows, Hélène Perrin and Barry M. Garraway, "Nonadiabatic losses from radio-frequency-dressed cold-atom traps: Beyond the Landau-Zener model". *Phys. Rev. A* **96**, 023 429 (Aug 2017).

[135] C.L. Garrido Alzar, H. Perrin, B.M. Garraway and V. Lorent, "Evaporative cooling in a radio-frequency trap". *Phys. Rev. A* **74**, 053 413 (2006).

[136] Romain Dubessy, "The RFBOX manual". Internal report of the team (2017).

[137] Marcus Gildemeister, *Trapping ultracold atoms in time-averaged adiabatic potentials*. PhD thesis, St John's College, Oxford University (2010).

[138] C. F. Ockeloen, A. F. Tauschinsky, R. J. C. Spreeuw and S. Whitlock, "Detection of small atom numbers through image processing". *Phys. Rev. A* **82**, 061 606 (Dec 2010).

[139] G. Reinaudi, T. Lahaye, Z. Wang and D. Guéry-Odelin, "Strong saturation absorption imaging of dense clouds of ultracold atoms". *Opt. Lett.* **32** (21), 3143–3145 (Nov 2007).

[140] Lauriane Chomaz, *Coherence and superfluidity of Bose gases in reduced dimensions: from harmonic traps to uniform fluids*. PhD thesis, Ecole Normale Supérieure (novembre 2014).

[141] S. Gupta, K. W. Murch, K. L. Moore, T. P. Purdy and D. M. Stamper-Kurn, "Bose-Einstein Condensation in a Circular Waveguide". *Phys. Rev. Lett.* **95**, 143 201 (2005).

[142] A. S. Arnold, C. S. Garvie and E. Riis, "Large magnetic storage ring for Bose-Einstein condensates". *Phys. Rev. A* **73**, 041 606 (2006).

[143] Noel Murray, Michael Krygier, Mark Edwards, K. C. Wright, G. K. Campbell and Charles W. Clark, "Probing the circulation of ring-shaped Bose–Einstein condensates". *Phys. Rev. A* **88**, 053 615 (Nov 2013).

[144] K. C. Wright, R. B. Blakestad, C. J. Lobb, W. D. Phillips and G. K. Campbell, "Driving Phase Slips in a Superfluid Atom Circuit with a Rotating Weak Link". *Phys. Rev. Lett.* **110**, 025 302 (Jan 2013).

[145] K. C. Wright, R. B. Blakestad, C. J. Lobb, W. D. Phillips and G. K. Campbell, "Threshold for creating excitations in a stirred superfluid ring". *Phys. Rev. A* **88**, 063 633 (Dec 2013).

[146] S. Eckel, F. Jendrzejewski, A. Kumar, C. J. Lobb and G. K. Campbell, "Interferometric Measurement of the Current-Phase Relationship of a Superfluid Weak Link". *Phys. Rev. X* **4**, 031 052 (Sep 2014).

[147] A. Kumar, S. Eckel, F. Jendrzejewski and G. K. Campbell, "Temperature-induced decay of persistent currents in a superfluid ultracold gas". *Phys. Rev. A* **95**, 021 602 (Feb 2017).

[148] F. Jendrzejewski, S. Eckel, N. Murray, C. Lanier, M. Edwards, C. J. Lobb and G. K. Campbell, "Resistive Flow in a Weakly Interacting Bose-Einstein Condensate". *Phys. Rev. Lett.* **113**, 045 305 (Jul 2014).

[149] M. Aidelsburger, J. L. Ville, R. Saint-Jalm, S. Nascimbène, J. Dalibard and J. Beugnon, "Relaxation Dynamics in the Merging of N Independent Condensates". *Phys. Rev. Lett.* **119**, 190 403 (Nov 2017).

[150] S. Eckel, A. Kumar, T. Jacobson, I. B. Spielman and G. K. Campbell, "A Rapidly Expanding Bose-Einstein Condensate: An Expanding Universe in the Lab". *Phys. Rev. X* **8**, 021 021 (Apr 2018).

[151] Jean Dalibard, *Cohérence et superfluidité dans les gaz atomiques.* Course "Atomes et rayonnement ", Collège de France, year 2015-2016.

[152] Soheil Baharian and Gordon Baym, "Bose-Einstein condensates in toroidal traps: Instabilities, swallow-tail loops, and self-trapping". *Phys. Rev. A* **87**, 013 619 (Jan 2013).

[153] A. I. Yakimenko, S. I. Vilchinskii, Y. M. Bidasyuk, Y. I. Kuriatnikov, K. O. Isaieva and M. Weyrauch, "Generation and decay of persistent current in a toroidal Bose-Einstein condensate". *Romanian Reports in Physics* **67**, 249–272 (2015).

[154] F. Piazza, L. A. Collins and A. Smerzi, "Vortex-induced phase-slip dissipation in a toroidal Bose-Einstein condensate flowing through a barrier". *Phys. Rev. A* **80**, 021 601 (2009).

[155] R. Dubessy, T. Liennard, P. Pedri and H. Perrin, "Critical rotation of an annular superfluid Bose-Einstein condensate". *Phys. Rev. A* **86**, 011 602 (Jul 2012).

[156] Joachim Brand and William P. Reinhardt, "Generating ring currents, solitons and svortices by stirring a Bose–Einstein condensate in a toroidal trap". *J. Phys. B: At., Mol. Opt. Phys.* **34** (4), L113 (2001).

[157] A Kumar, N Anderson, W D Phillips, S Eckel, G K Campbell and S Stringari, "Minimally destructive, Doppler measurement of a quantized flow in a ring-shaped Bose–Einstein condensate". *New Journal of Physics* **18** (2), 025 001 (2016).

[158] J. L. Ville, T. Bienaimé, R. Saint-Jalm, L. Corman, M. Aidelsburger, L. Chomaz, K. Kleinlein, D. Perconte, S. Nascimbène, J. Dalibard and J. Beugnon, "Loading and compression of a single two-dimensional Bose gas in an optical accordion". *Phys. Rev. A* **95**, 013 632 (Jan 2017).

[159] S. P. Rath, *Production and investigation of quasi-two-dimensional Bose gases.* PhD thesis, Université Paris VI (2010).

[160] N. L. Smith, W. H. Heathcote, G. Hechenblaikner, E. Nugent and C. J. Foot, "Quasi-2D confinement of a BEC in a combined optical and magnetic potential". *J. Phys. B: At., Mol. Opt. Phys.* **38** (3), 223 (2005).

[161] R. Grimm, M. Weidemüller and Yu.B. Ovchinnikov, "Optical dipole traps for neutral atoms". *Adv. At. Mol. Opt. Phys.* **42**, 95–170 (2000).

[162] T.A. Savard, K.M. O'Hara and J.E. Thomas, "Laser-noise-induced heating in far-off resonance optical traps". *Phys. Rev. A* **56** (2), R1095–R1098 (1997).

[163] E. A. Burt, R. W. Ghrist, C. J. Myatt, M. J. Holland, E. A. Cornell and C. E. Wieman, "Coherence, Correlations, and Collisions: What One Learns about Bose-Einstein Condensates from Their Decay". *Phys. Rev. Lett.* **79**, 337–340 (Jul 1997).

[164] Matthias Wenzel, Fabian Böttcher, Jan-Niklas Schmidt, Michael Eisenmann, Tim Langen, Tilman Pfau and Igor Ferrier-Barbut, "Anisotropic Superfluid Behavior of a Dipolar Bose-Einstein Condensate". *Phys. Rev. Lett.* **121**, 030 401 (Jul 2018).

[165] J. S. Stiessberger and W. Zwerger, "Critcal velocity of superfluid flow past large obstacles in Bose-Einstein condensates". *Phys. Rev. A* **62**, 061 601 (Nov 2000).

[166] Woo Jin Kwon, Geol Moon, Sang Won Seo and Y. Shin, "Critical velocity for vortex shedding in a Bose-Einstein condensate". *Phys. Rev. A* **91**, 053 615 (May 2015).

[167] Avinash Kumar, Romain Dubessy, Thomas Badr, Camilla De Rossi, Mathieu de Goër de Herve, Laurent Longchambon and Hélène Perrin, "Producing superfluid circulation states using phase imprinting". *Phys. Rev. A* **97**, 043 615 (Apr 2018).

[168] D. M. Jezek, P. Capuzzi and H. M. Cataldo, "Dark-soliton collisions in a toroidal Bose-Einstein condensate". *Phys. Rev. A* **93**, 023 601 (Feb 2016).

[169] Gary A. Williams and Richard E. Packard, "Photographs of Quantized Vortex Lines in Rotating He II". *Phys. Rev. Lett.* **33**, 280–283 (Jul 1974).

[170] Alexander L. Fetter, "Rotating trapped Bose-Einstein condensates". *Rev. Mod. Phys.* **81** (2), 647–691 (May 2009).

[171] N. R. Cooper, "Rapidly rotating atomic gases". *Advances in Physics* **57** (6), 539–616 (2008).

[172] P. Engels, I. Coddington, P. C. Haljan, V. Schweikhard and E. A. Cornell, "Observation of Long-Lived Vortex Aggregates in Rapidly Rotating Bose-Einstein Condensates". *Phys. Rev. Lett.* **90**, 170 405 (May 2003).

[173] M. W. Zwierlein, J. R. Abo-Shaeer, A. Schirotzek, C. H. Schunck and W. Ketterle, "Vortices and superfluidity in a strongly interacting Fermi gas". *Nature* **435**, 1047 (2005).

[174] Z. Hadzibabic, P. Krüger, M. Cheneau, B. Battelier and J. Dalibard, "Berezinskii-Kosterlitz-Thouless crossover in a trapped atomic gas". *Nature* **441**, 1118 (2006).

[175] T. W. Neely, A. S. Bradley, E. C. Samson, S. J. Rooney, E. M. Wright, K. J. H. Law, R. Carretero-González, P. G. Kevrekidis, M. J. Davis and B. P. Anderson, "Characteristics of Two-Dimensional Quantum Turbulence in a Compressible Superfluid". *Phys. Rev. Lett.* **111**, 235 301 (Dec 2013).

[176] Simone Donadello, Simone Serafini, Marek Tylutki, Lev P. Pitaevskii, Franco Dalfovo, Giacomo Lamporesi and Gabriele Ferrari, "Observation of Solitonic Vortices in Bose-Einstein Condensates". *Phys. Rev. Lett.* **113**, 065 302 (Aug 2014).

[177] Mark J. H. Ku, Wenjie Ji, Biswaroop Mukherjee, Elmer Guardado-Sanchez, Lawrence W. Cheuk, Tarik Yefsah and Martin W. Zwierlein, "Motion of a Solitonic Vortex in the BEC-BCS Crossover". *Phys. Rev. Lett.* **113**, 065 301 (Aug 2014).

[178] Woo Jin Kwon, Joon Hyun Kim, Sang Won Seo and Y. Shin, "Observation of von Kármán Vortex Street in an Atomic Superfluid Gas". *Phys. Rev. Lett.* **117**, 245 301 (Dec 2016).

[179] Alexander L. Fetter, "Rotating vortex lattice in a Bose-Einstein condensate trapped in combined quadratic and quartic radial potentials". *Phys. Rev. A* **64**, 063 608 (Nov 2001).

[180] S. J. Rooney, P. B. Blakie, B. P. Anderson and A. S. Bradley, "Suppression of Kelvon-induced decay of quantized vortices in oblate Bose-Einstein condensates". *Phys. Rev. A* **84**, 023 637 (Aug 2011).

[181] A. Recati, F. Zambelli and S. Stringari, "Overcritical Rotation of a Trapped Bose-Einstein Condensate". *Phys. Rev. Lett.* **86**, 377–380 (Jan 2001).

[182] S. Stringari, "Phase Diagram of Quantized Vortices in a Trapped Bose-Einstein Condensed Gas". *Phys. Rev. Lett.* **82**, 4371–4375 (May 1999).

[183] A.A. Abrikosov, "On the Magnetic Properties of Superconductors of the Second Group". *J. Exp. Theor. Phys.* **22** (6), 1174 (1957).

[184] V.K. Tkachenko, "On Vortex Lattices". *J. Exp. Theor. Phys.* **22** (6), 1282 (1966).

[185] V. Schweikhard, I. Coddington, P. Engels, S. Tung and E. A. Cornell, "Vortex-Lattice Dynamics in Rotating Spinor Bose-Einstein Condensates". *Phys. Rev. Lett.* **93**, 210 403 (Nov 2004).

[186] David L. Feder and Charles W. Clark, "Superfluid-to-Solid Crossover in a Rotating Bose-Einstein Condensate". *Phys. Rev. Lett.* **87**, 190 401 (Oct 2001).

[187] Jean Dalibard, *Le magnétisme artificiel pour les gaz d'atomes froids.* Course "Atomes et rayonnement ", Collège de France, year 2013-2014.

[188] Keola Wierschem and Efstratios Manousakis, "Simulation of melting of two-dimensional Lennard-Jones solids". *Phys. Rev. B* **83**, 214 108 (Jun 2011).

[189] Jean Dalibard, *Fluides quantiques de basse dimension et transition de Kosterlitz-Thouless.* Course "Atomes et rayonnement ", Collège de France, year 2016-2017.

[190] I. Guillamón, H. Suderow, A. Fernández-Pacheco, J. Sesé, R. Córdoba, J. M. De Teresa, M. R. Ibarra and S. Vieira, "Direct observation of melting in a two-dimensional superconducting vortex lattice". *Nature Physics* **5**, 651 (2009).

[191] B. A. Huberman and S. Doniach, "Melting of Two-Dimensional Vortex Lattices". *Phys. Rev. Lett.* **43**, 950–952 (Sep 1979).

[192] S. Andrew Gifford and Gordon Baym, "Dislocation-mediated melting in superfluid vortex lattices". *Phys. Rev. A* **78**, 043 607 (Oct 2008).

[193] B. I. Halperin and David R. Nelson, "Theory of Two-Dimensional Melting". *Phys. Rev. Lett.* **41**, 121–124 (Jul 1978).

[194] Katherine J. Strandburg, "Two-dimensional melting". *Rev. Mod. Phys.* **60**, 161–207 (Jan 1988).

[195] S. I. Matveenko and G. V. Shlyapnikov, "Tkachenko modes and their damping in the vortex lattice regime of rapidly rotating bosons". *Phys. Rev. A* **83**, 033 604 (Mar 2011).

[196] M. Cozzini, A. L. Fetter, B. Jackson and S. Stringari, "Oscillations of a Bose-Einstein Condensate Rotating in a Harmonic Plus Quartic Trap". *Phys. Rev. Lett.* **94**, 100 402 (Mar 2005).

[197] V. Schweikhard, *Ultracold Bose gases under rotation, in lattice potentials, and both.* PhD thesis, University of Colorado (2008).

[198] G. Bismut, B. Pasquiou, E. Maréchal, P. Pedri, L. Vernac, O. Gorceix and B. Laburthe-Tolra, "Collective Excitations of a Dipolar Bose-Einstein Condensate". *Phys. Rev. Lett.* **105** (4), 040 404 (Jul 2010).

[199] Francesca Zambelli and Sandro Stringari, "Quantized Vortices and Collective Oscillations of a Trapped Bose-Einstein Condensate". *Phys. Rev. Lett.* **81**, 1754–1757 (Aug 1998).

[200] F. Chevy, K. W. Madison and J. Dalibard, "Measurement of the Angular Momentum of a Rotating Bose-Einstein Condensate". *Phys. Rev. Lett.* **85**, 2223–2227 (Sep 2000).

[201] S. Stringari, "Dynamics of Bose-Einstein condensed gases in highly deformed traps". *Phys. Rev. A* **58**, 2385–2388 (Sep 1998).

[202] S. Stock, V. Bretin, F. Chevy and J. Dalibard, "Shape oscillation of a rotating Bose-Einstein condensate". *Europhys. Lett.* **65** (5), 594–600 (2004).

[203] M. Cozzini, "Diffused vorticity approach to the oscillations of a rotating Bose-Einstein condensate confined in a harmonic plus quartic trap". *Pramana* **66** (1), 31–42 (Jan 2006).

[204] A. E. Leanhardt, A. Görlitz, A. P. Chikkatur, D. Kielpinski, Y. Shin, D. E. Pritchard and W. Ketterle, "Imprinting Vortices in a Bose-Einstein Condensate using Topological Phases". *Phys. Rev. Lett.* **89**, 190 403 (Oct 2002).

[205] David L. Feder, Anatoly A. Svidzinsky, Alexander L. Fetter and Charles W. Clark, "Anomalous Modes Drive Vortex Dynamics in Confined Bose-Einstein Condensates". *Phys. Rev. Lett.* **86**, 564–567 (Jan 2001).

[206] Carlos Lobo, Alice Sinatra and Yvan Castin, "Vortex Lattice Formation in Bose-Einstein Condensates". *Phys. Rev. Lett.* **92**, 020 403 (Jan 2004).

[207] C. Raman, J. R. Abo-Shaeer, J. M. Vogels, K. Xu and W. Ketterle, "Vortex Nucleation in a Stirred Bose-Einstein Condensate". *Phys. Rev. Lett.* **87**, 210 402 (Nov 2001).

[208] Y. Castin and R. Dum, "Bose-Einstein condensates in time dependent traps". *Phys. Rev. Lett.* **77** (27), 5315–5319 (1996).

[209] V. Bretin, *Rotations d'un condensat de Bose-Einstein*. PhD thesis, Université Paris VI (2004).

[210] F. Dalfovo and S. Stringari, "Shape deformations and angular-momentum transfer in trapped Bose–Einstein condensates". *Phys. Rev. A* **63**, 011 601(R) (2000).

[211] Sang Won Seo, Jae-yoon Choi and Yong-il Shin, "Free expansion of quasi-2D Bose-Einstein condensates with quantized vortices". *Journal of the Korean Physical Society* **64** (1), 53–57 (Jan 2014).

[212] V. Bretin, P. Rosenbusch, F. Chevy, G. V. Shlyapnikov and J. Dalibard, "Quadrupole Oscillation of a Single-Vortex Bose-Einstein Condensate: Evidence for Kelvin Modes". *Phys. Rev. Lett.* **90**, 100 403 (Mar 2003).

[213] F. Chevy, *Dynamique d'un condensat de Bose-Einstein*. PhD thesis, Université Pierre et Marie Curie – Paris VI (2001).

[214] J. Dalibard, "Collisional dynamics of ultra-cold atomic gases". In *Proceedings of the International School of Physics "Enrico Fermi", Course CXL*, edited by M. Inguscio, S. Stringari and C.E. Wieman, pages 321–349, IOS Press Ohmsha (1999).

[215] G. Hechenblaikner, J. M. Krueger and C. J. Foot, "Properties of quasi-two-dimensional condensates in highly anisotropic traps". *Phys. Rev. A* **71**, 013 604 (Jan 2005).

[216] Seji Kang, J. Choi, S. W. Seo, W. J. Kwon and Y. Shin, "Rotating a Bose-Einstein condensate by shaking an anharmonic axisymmetric magnetic potential". *Phys. Rev. A* **91**, 013 603 (Jan 2015).

[217] J. Billy, V. Josse, Z. Zuo, A. Bernard, B. Hambrecht, P. Lugan, D. Clément, L. Sanchez-Palencia, P. Bouyer and A. Aspect, "Direct observation of Anderson localization of matter waves in a controlled disorder". *Nature* **453**, 891 (2008).

[218] G. Roati, C. D'Errico, L. Fallani, M. Fattori, C. Fort, M. Zaccanti, G. Modugno, M. Modugno and M. Inguscio, "Anderson localization of a non-interacting Bose-Einstein condensate". *Nature* **453**, 895 (2008).

[219] Sang Won Seo, Jae-yoon Choi and Yong-il Shin, "Scaling behavior of density fluctuations in an expanding quasi-two-dimensional degenerate Bose gas". *Phys. Rev. A* **89**, 043 606 (Apr 2014).

[220] Tarik Yefsah, *Thermodynamics of the Bose gas in two dimensions*. Phd thesis, Université Pierre et Marie Curie - Paris VI (septembre 2011).

[221] Thomas Plisson, *Equilibrium and transport properties of two-dimensional Bose gase in the presence of disorder*. Phd thesis, Ecole Polytechnique X (septembre 2012).

Résumé

Le caractère irrotationnel des superfluides est à l'origine de propriétés de rotation spectaculaires. Pour que le fluide puisse tourner, sa densité doit s'annuler localement en une singularité appelée tourbillon quantique ou vortex. La géométrie annulaire présente un grand intérêt pour étudier la superfluidité car le gaz peut tourner autour d'un trou central sans présenter de singularité, permettant l'existence de courants permanents à la circulation quantifiée le long de l'anneau.

Nous confinons des atomes froids habillés par un champ radiofréquence dans un potentiel adiabatique reposant sur un piège magnétique quadrupolaire. Le potentiel résultant, en forme de bulle, à la fois très lisse et facilement modifiable, nous permet de réaliser deux types de condensats de Bose-Einstein en forme d'anneau. Une première stratégie consiste à utiliser une nappe de lumière très désaccordée pour confiner les atomes à l'intersection entre la bulle et le plan imposé par la lumière – un anneau. Nous présentons la mise en œuvre et l'optimisation de ce piège sur notre expérience et démontrons la possibilité de préparer et observer des courants superfluides dans l'anneau.

Une deuxième voie exploite la force centrifuge et l'anharmonicité du potentiel adiabatique pour créer un potentiel effectif en forme de chapeau mexicain en faisant tourner les atomes piégés au fond de la bulle plus vite que la fréquence du piège. Après avoir réalisé un tel système, nous en sondons les modes quadrupolaires pour caractériser sa rotation. L'étude de la distribution des vortex dans le gaz en rotation montre également un effet de fonte thermique des réseaux de vortex à température finie.

Mots-clefs : Condensation de Bose-Einstein, potentiel adiabatique, atomes habillés par la RF, superfluidité, courants permanents, vortex, anneaux, rotations rapides.

Abstract

The irrotational nature of superfluids leads to spectacular rotational properties. For the fluid to rotate, its density must locally vanish at a singular point called a quantum vortex. The annular geometry is of great interest for studying superfluidity as the gas can rotate in this geometry around a central hole without requiring any singularity, allowing the existence of persistent currents along the ring with a quantized circulation.

In out experiment, we confine cold atoms dressed by a radiofrequency field in an adiabatic potential based on a quadrupolar magnetic trap. The resulting bubble-shaped potential, both very smooth and easily tunable, allows us to produce two types of ring-shaped Bose-Einstein condensates. A first strategy consists in adding a far-detuned light sheet to confine the atoms at the intersection between the bubble and the horizontal plane imposed by the light field – i.e. a ring. We present the implementation and optimization of this trap and demonstrate the possibility to prepare and observe superfluid currents in the ring.

A second path exploits the centrifugal force and the anharmonicity of the adiabatic potential to create an effective Mexican hat potential by rotating the trapped atoms at the bottom of the bubble faster than the trap frequency. After having realized such a system, we probe its quadrupolar modes to characterize the rotation. The study of vortex distribution in the rotating gas also shows a thermal melting effect of the finite temperature vortex lattice.

Keywords: Bose-Einstein Condensates, adiabatic potentials, RF-dressed atoms, superfluidity, superfluid flow, vortex, rings, fast rotations.